Geïntegreerde siliciumnitridefotonica met sterk niet-lineaire dunne films en 2D-materialen: eigenschappen en componenten

Integrated Silicon Nitride Photonics with Highly Nonlinear Thin Films and 2D Materials: Properties and Devices

Koen Alexander

Promotoren: prof. dr. ir. D. Van Thourhout, prof. dr. ir. B. Kuyken
Proefschrift ingediend tot het behalen van de graad van
Doctor in de ingenieurswetenschappen: fotonica

UNIVERSITEIT
GENT

Vakgroep Informatietechnologie
Voorzitter: prof. dr. ir. B. Dhoedt
Faculteit Ingenieurswetenschappen en Architectuur
Academiejaar 2018 - 2019

ISBN 978-94-6355-188-5
NUR 959, 926
Wettelijk depot: D/2018/10.500/106

Universiteit Gent
Faculteit Ingenieurswetenschappen en Architectuur
Vakgroep Informatietechnologie

Promotoren:

prof. dr. ir. Dries Van Thourhout

prof. dr. ir. Bart Kuyken

Examencommissie:

em. prof. dr. ir. Daniël De Zutter (voorzitter)	Universiteit Gent
prof. dr. ir. Dries Van Thourhout (promotor)	Universiteit Gent
prof. dr. ir. Bart Kuyken (promotor)	Universiteit Gent
prof. dr. ir. Roel Baets (secretaris)	Universiteit Gent
prof. dr. ir. Johan Bauwelinck	Universiteit Gent
prof. dr. ir. Jeroen Beeckman	Universiteit Gent
prof. dr. ir. Pascal Kockaert	Université Libre de Bruxelles
dr. Giancarlo Soavi	University of Cambridge

Universiteit Gent
Faculteit Ingenieurswetenschappen en Architectuur
Vakgroep Informatietechnologie
Technologiepark-Zwijnaarde 15 iGent, B-9052 Gent, België
Tel.: +32 (0) 9264 3316
Fax.: +32 (0) 9264 3593

Dit werk kwam tot stand in het kader van een aspirantenbeurs van het Fonds voor Wetenschappenlijk Onderzoek - Vlaanderen.

Dankwoord *Acknowledgements*

Een doctoraat is een werk van lange adem, iets meer dan vier jaar in mijn geval. Maar gelukkig was ik gedurende deze zoektocht naar kennis niet alleen. Het werk in deze thesis zou er nooit zijn geweest zonder de begeleiding, het advies en de steun van een heel groot aantal mensen. Laat ik dus beginnen met hen de eer aan te doen die hen toekomt.

Laten we eerst een paar jaar teruggaan in de tijd. Eigenlijk begon het allemaal al ettelijke jaren voor mijn doctoraat, toen ik me, geïntrigeerd door Roel Baets' bachelorvak "Fotonica", inschreef voor de European Master of Science in Photonics (EMSP). Wat een avontuur was dat! In minder dan twee jaar tijd studeerde ik met een fantastische groep klasgenoten in België, Zweden en Schotland, en deed ik er nog eens een zomerstage in Spanje bovenop. Het was ook gedurende deze periode dat ik mijn masterthesis deed onder begeleiding van Peter Bienstman en Thomas Van Vaerenbergh en dat ik mede dankzij hen de smaak van het onderzoek te pakken kreeg. Al gauw ging ik op zoek naar het volgende avontuur. Geholpen door Roel behaalde ik een BAEF-beurs, waarmee ik de Atlantische Oceaan overtrok richting Cornell University om nog een jaartje bij te studeren. In the underground labs of Cornell, I met Stéphane Clemmen, who showed me around in the world of lasers, photonic crystal fibers and nonlinear optics.

Gedurende dat jaar in Amerika ontstond het idee om terug te gaan naar Gent om te doctoreren. Samen met Roel, Dries Van Thourhout en kersverse post-doc Bart Kuyken diende ik een applicatie in voor een FWO-doctoraatsbeurs. We kregen de beurs en ik zou onderzoek doen naar "niet-lineaire optica in 2D-materialen". Toen klonk dat allemaal nog wat vaag en de eerlijkheid gebiedt mij te zeggen dat de applicatie grotendeels door Bart en Dries geschreven was, maar het was het begin van weerom een groot avontuur. Laat ik hier meteen mijn promotoren uitvoerig bedanken. Eerst waren dat Dries en Roel, en later, nadat Bart het in een hallucinant tempo tot professor had geschopt, Dries en Bart. Zonder hun begeleiding, feedback en de vrijheid die ze me gegeven hebben was er van dit onderzoek niet veel in huis gekomen. Ik heb onderweg enorm veel van hen geleerd!

De Photonics Research Group (PRG) in Gent bleek al snel een heel aangename plaats om te werken, niet in het minst dankzij de vele collega's. In het Technicum kwam ik terecht in hetzelfde bureau als Bart, die naast getalenteerd fotonicus ook een intensief babbelaar bleek te zijn. De eindeloze gesprekken over de actualiteit en het occasioneel geroddel werden mede in stand gehouden door Kasper en Pieter. Ondertussen is de samenstelling van ons bureau danig veranderd. Kasper en ik worden tegenwoordig aan ons eiland vergezeld door Camiel en Isaac. De traditie om van tijd tot tijd eens goed te kletsen wordt door ons nog steeds in ere gehouden, snelfietsers Lukas en Stijn staan af en toe recht om van achter de grote kast ook hun duit in het zakje te doen. In addition, I want to thank Stéphane (yes, the same guy as in Cornell), Utsav, Herbert, Nina, Zuyang and Maximilien for making our office a great and stimulating place to work.

Niet in hetzelfde bureau, maar van even groot belang: Sören, meester-imitator die om 11.45u steevast klaarstaat om ons eraan te herinneren dat we best maar al aan de middagpauze beginnen. Alejandro, ever enthusiastic developer of next-generation microscopes, table tennis player and lan party organizer. My former EMSP-classmates, Haolan, Yufei and Alex, who just like me after many adventures eventually all returned to Ghent. Andres, lolbroek van dienst en sterkhouder van de Photonics Society Ghent. Artur, die naast collega niet-lineair fotonicus ook nog eens een fantastische reisgezel bleek te zijn op onze korte Californische roadtrip. Ali, the other awesome companion on the post-CLEO trip to Santa Barbara. En dan zijn er natuurlijk nog de collega's die ondertussen al andere oorden zijn gaan opzoeken: Michiel, kameraad sinds het eerste jaar burgie, die altijd wel te vinden was voor een koffiepauze. En niet te vergeten, hoogvliegers Frédéric 'pas op uw wiel draait' Peyskens en Raphaël Van Laer, de eerste is gepassioneerd maker van minuscule gouden strikjes en niet vies van af en toe een danspasje, en de tweede gevierd optomechanicus én onverslaanbaar pool-speler.

Als onhandige en chaotische onderzoekers zouden we nergens staan zonder een aantal fantastische mensen in de groep, die stuk voor stuk een applaus verdienen. Jasper, wiens handigheid me dag na dag weer verbaast (Een 3D-printer? Dat maak je toch gewoon zelf!). Michaël, Python-tovenaar van dienst in het labo. Liesbet, bij wie lange FIB-sessies eigenlijk vooral een gezellige babbel worden. Steven, ieders houvast in de cleanroom. Ilse, Ilse en Kristien, die alles, inclusief mijn tegenspruttelende laptop, met verve draaiende houden.

Samenwerken is belangrijk in het onderzoek. Our collaboration with the Liquid Crystals and Photonics group was exceptionally fruitful, and for this I especially want to thank John and Jeroen! It's also nice to see that some newer faces, Tessa, Gilles, Isaac and Irfan, are continuing the work. It was also a joy to collaborate with Prof. Sergey Mikhailov and Dr. Nadja Savostianova from the University of Augsburg. Their theoretical insights aligned perfectly with our experimental capabilities and they have contributed greatly to some of the most important publications related to this thesis.

De boog kan uiteraard niet altijd gespannen staan. In de onderzoeksgroep zat dat alvast goed. Naast occasionele drinkgelagen of caféquizzen werd er ook veel gesport. De PRG Squash Club was geen lang leven beschoren, maar toch heb ik me kostelijk geamuseerd met Floris, Daan, Ananth (who is absolutely unbeatable), Alejandro en alle anderen die wel eens kwamen meespelen. Sören en Frédéric vonden binnenspelen maar niets en waren eerder te vinden voor een potje tennis. Het PRG Cycling Team is een initiatief dat wel bleef bestaan, duizenden kilometers heb ik afgemaald samen met Pieter, Lukas, Liselotte, Bart Geers, Daan, Jasper en nieuwkomer Stijn. Met Kasper heb ik ten slotte een poging gedaan om onze skateboardcarrière nieuw leven in te blazen, niet zo succesvol, maar wel vree wijs! Iona en Michiel, en Tom en Pieter, bedankt om onze metgezel te zijn op zo vele uitstapjes, van Europa-Park tot India! For our occasional visits to Brussels, Leuven and the Netherlands, we were always more than welcome to hang out with Jens, Felicity, Vivek and Mathi. En dan zijn er natuurlijk nog the usual suspects: Jens, Stijn, Joachim, Michels, Oli, Kristof, Pieter, Sam, Loïc en Eli, merci voor alle avondjes uit en andere knotsgekke avonturen. Ik kijk op dit moment enorm uit naar ons aankomend Ardennenweekend. Ditmaal laat ik Zeeslag wel aan mij voorbijgaan.

Dat ik tot op dit punt ben geraakt, heb voor een heel groot deel te danken aan mijn familie, en vooral aan mama, papa en Jan, bedankt voor al jullie zorg, liefde en steun doorheen de jaren!

And of course, keeping the best for last, I want to thank Yoko. I could not have done this without you! Thanks for putting up with my mood swings and grumpiness while I was writing this book. Your support, understanding and love mean the world to me.

Ziezo, nu kan het echte leeswerk beginnen.

Gent, 9 December 2018
Koen Alexander

Table of Contents

Dankwoord *(Acknowledgements)* **i**

Samenvatting **xxix**
Referenties xxxvi

Summary **xxxvii**
References xliv

1 Introduction **1-1**
1.1 Silicon and silicon nitride photonics 1-1
1.2 Nonlinear optics 1-5
1.3 Enhancing silicon/silicon nitride photonics with novel nonlinear materials 1-8
1.4 Overview of the work presented in this thesis 1-10
1.5 Publications and awards 1-10
1.5.1 Publications in international journals 1-10
1.5.2 Publications in national and international conferences 1-11
1.5.3 Awards 1-12
References 1-14

2 Graphene as a material for nonlinear optics **2-1**
2.1 Introduction 2-1
2.2 A brief introduction to graphene 2-2
2.3 Graphene photonics 2-4
2.4 Graphene nonlinear optics 2-6
2.4.1 Quantifying the optical nonlinearity of graphene . . . 2-6
2.4.1.1 Nonlinear susceptibility 2-6
2.4.1.2 Nonlinear surface conductivity 2-7
2.4.1.3 Nonlinear refractive index 2-8
2.4.1.4 Which description should one use? 2-9
2.4.2 Theoretical models for optical nonlinearities in graphene 2-10

2.4.3 Experimental demonstrations of nonlinear optics in graphene . . . 2-12
2.5 Third order nonlinear optics in graphene-covered waveguides 2-15
2.6 Conclusion . . . 2-20
References . . . 2-21

3 Nonlinear optics in graphene-covered waveguides 3-1
3.1 Introduction . . . 3-1
3.2 Gate-tunable saturable absorption in graphene-covered Si waveguides . . . 3-2
3.2.1 Sample fabrication and measurement setup . . . 3-2
3.2.2 Experimental results . . . 3-4
3.2.3 Conclusion and comparison with literature . . . 3-8
3.3 Gate-tunable graphene-covered SiN waveguides . . . 3-9
3.3.1 Fabrication . . . 3-9
3.3.2 Electrostatic gating using a polymer electrolyte . . . 3-12
3.3.3 Theory of nonlinear optics in graphene-covered SiN waveguides . . . 3-15
3.4 Four-wave mixing in graphene-covered SiN waveguides . . . 3-15
3.4.1 Coupled-wave equations . . . 3-16
3.4.2 Experimental results . . . 3-19
3.4.3 Comparison with theoretical models . . . 3-24
3.5 Cross-amplitude and cross-phase modulation in graphene-covered SiN waveguides . . . 3-28
3.5.1 Coupled-wave equations . . . 3-28
3.5.2 Measurement setup and methodology . . . 3-30
3.5.3 Experimental results . . . 3-34
3.5.4 Comparison with theory . . . 3-39
3.5.5 Comparison with other experiments . . . 3-41
3.6 Third harmonic generation in graphene-covered SiN waveguides . . . 3-43
3.6.1 Coupled-wave equations . . . 3-43
3.6.2 Phase-matching techniques for third harmonic generation . . . 3-44
3.6.3 Simulations . . . 3-46
3.7 Conclusion and future outlook . . . 3-47
References . . . 3-51

4 PZT on silicon nitride 4-1
4.1 Introduction . . . 4-1
4.2 PZT . . . 4-3
4.3 Thin-film PZT deposition . . . 4-7
4.4 Second harmonic generation on thin-film PZT . . . 4-8
4.4.1 Measurement methodology and setup . . . 4-8
4.4.2 Measurement results for thin-film PZT . . . 4-9

4.5 PZT on silicon nitride waveguides 4-13
  4.5.1 Fabrication 4-14
  4.5.2 Waveguide losses 4-16
4.6 Second harmonic generation in PZT-covered waveguides . . . 4-18
  4.6.1 Second harmonic generation in a waveguide 4-18
  4.6.2 Experimental results 4-19
  4.6.3 Future work 4-23
4.7 Phase modulation on a PZT-covered waveguide 4-24
  4.7.1 Basic theory 4-24
  4.7.2 Preliminary phase modulation and poling 4-26
4.8 Electro-optic amplitude modulators on SiN 4-28
  4.8.1 Modulator types 4-28
  4.8.2 Static modulation 4-32
  4.8.3 Poling stability 4-34
  4.8.4 High-speed characterization 4-35
4.9 Further optimization of PZT-on-SiN phase modulators . . . 4-39
4.10 Conclusions and future prospects 4-43
References 4-46

5 Nonlinear optics in MoS_2 5-1
5.1 Introduction 5-1
5.2 2D materials beyond graphene 5-1
5.3 Nonlinear optics in TMDCs 5-2
5.4 Second harmonic generation in MOCVD-grown MoS_2 5-4
5.5 MoS_2 on integrated SiN waveguides 5-8
  5.5.1 Optical losses 5-9
  5.5.2 SHG on MoS_2-covered SiN waveguides 5-9
5.6 Conclusions and future prospects 5-14
References 5-15

6 Conclusions and future perspectives 6-1
6.1 Conclusions on the presented work 6-1
6.2 Future perspectives 6-4
References 6-7

A Phenomenological model for graphene nonlinear optics A-1
A.1 Introduction A-1
A.2 Linear conductivity of graphene A-2
A.3 Nonlinear conductivity of graphene A-2
A.4 High intensity behavior A-7
References A-9

List of Figures

1 **Met grafeen bedekte siliciumnitridegolfgeleiders. a** Optisch microscoopbeeld van enkele golfgeleiders. Het grafeen (onder de contacten) is niet zichtbaar maar de positie is aangeduid met stippellijnen. **b** Elektronenmicroscoopbeeld van een golfgeleider, het grafeen is duidelijk zichtbaar. **c** Elektronenmicroscoopbeeld van de dwarsdoorsnede van een golfgeleider. xxxi

2 **Gemeten niet-lineaire parameter van met grafeen bedekte siliciumnitridegolfgeleiders (γ) en de hieruit berekende derde-orde oppervlaktegeleidbaarheid van grafeen ($\sigma_s^{(3)}$). a**, **b** γ en $\sigma_s^{(3)}$ gemeten door vierbundelmenging (pomp met golflengte $\lambda_\mathrm{p} \approx 1550$ nm), in functie van de gatespanning en de geschatte Fermi-energie, voor verschillende signaalgolflengten λ_s (de legende toont $\lambda_\mathrm{s} - \lambda_\mathrm{p}$) (**a**) en als functie van het golflengteverschil $\lambda_\mathrm{s} - \lambda_\mathrm{p}$, voor verschillende gatespanningen V_GS (zie legende) (**b**). **c**, **d** γ en $\sigma_s^{(3)}$ gemeten door kruismodulatie tussen een pomp met golflengte $\lambda_\mathrm{pump} \approx 1550$ nm en een probe met verstelbare golflengte λ_probe, de legende toont het golflengteverschil $\lambda_\mathrm{probe} - \lambda_\mathrm{pump}$. **c** Im($\gamma$) en Re($\sigma_s^{(3)}$), die kruis-amplitudemodulatie beschrijven, in functie van de gatespanning en de geschatte Fermi-energie. **d** Re(γ) en Im($\sigma_s^{(3)}$), die kruis-fasemodulatie kwantificeren, ook als functie van de gatespanning. xxxii

3 **Siliciumnitride bedekt met PZT. a** Elektronenmicroscoopbeeld van de dwarsdoorsnede van een siliciumnitridegolfgeleider bedekt met PZT. **b** Optisch microscoopbeeld van één van de ringmodulatoren. xxxiii

4 **Metingen op PZT-op-siliciumnitridemodulatoren. a** Transmissiespectra van een C-band ringmodulator, voor verschillende aangelegde spanningen. **b** Elektro-optische kleinsignaalmeting ($|S_{21}|$-parameter) van verschillende modulatoren. **c** Voorbeeld van een oogdiagram met een bitrate van 28 Gbps. xxxiii

5 **Metingen met $\mathbf{MoS_2}$.** **a** Meting van frequentieverdubbeling op een met MoS_2 bedekt substraat, ofwel de s-gepolariseerde component (blauw), of de p-gepolariseerde component (rood) van de tweede harmonische wordt gemeten. De volle lijnen zijn de theoretische fits. **b** Verlies versus MoS_2-lengte voor met MoS_2 bedekte siliciumnitridegolfgeleiders met een breedte van 1200 nm, het propagatieverlies in deze meting is ongeveer 20 dB/cm. xxxiv

1 **Graphene-covered silicon nitride waveguides. a** Optical microscope image of a set of waveguides. The extent of the graphene (under the contacts) is shown by the dashed lines. **b** Scanning electron microscope image of one of the waveguides, the graphene is clearly visible. **c** Scanning electron microscope image of the cross-section of such a waveguide. . xxxix

2 **Measurements of the effective nonlinear parameter of graphene-covered silicon nitride waveguides (γ) and the corresponding third order nonlinear surface conductivity of the graphene ($\sigma_s^{(3)}$). a**, **b** γ and $\sigma_s^{(3)}$ characterized by degenerate four-wave mixing (pump wavelength $\lambda_\mathrm{p} \approx 1550$ nm), as function of gate voltage and estimated corresponding Fermi energy, for different values of signal-pump detuning $\lambda_\mathrm{s} - \lambda_\mathrm{p}$ (see legend) (**a**) and as a function of signal-pump detuning, for different gate voltages V_GS (see legend) (**b**). **c**, **d** γ and $\sigma_s^{(3)}$ characterized by cross-modulation between a pump at wavelength $\lambda_\mathrm{pump} \approx 1550$ nm and a tunable probe at wavelength λ_probe, see legends for the detuning $\lambda_\mathrm{probe} - \lambda_\mathrm{pump}$. **c** $\mathrm{Im}(\gamma)$ and $\mathrm{Re}(\sigma_s^{(3)})$, which quantify the cross-amplitude modulation, as a function of gate voltage and estimated Fermi energy. **d** $\mathrm{Re}(\gamma)$ and $\mathrm{Im}(\sigma_s^{(3)})$, which quantify the cross-phase modulation, also as a function of gate voltage. xl

3 **PZT-on-silicon nitride Pockels modulator. a** Scanning electron microscope image of the cross-section of a silicon nitride waveguide covered with a PZT film. **b** Microscope image of one of the ring modulators. xli

4 **Some measurement results obtained using the PZT-on-silicon nitride modulators.** **a** Normalized transmission spectra of a C-band ring modulator, for different applied DC voltages. **b** Electro-optic small signal ($|S_{21}|$ parameter) measurement of several modulators. **c** Example of an eye diagram obtained with a C-band ring modulator, using a non-return-to-zero modulation scheme at 28 Gbps. xli

5 **$\mathbf{MoS_2}$ measurements**. **a** Measured second harmonic power for an MoS_2-covered substrate, for the analyzer selecting either the s- (blue) or p-polarizations (red). The solid lines are the theoretical fits. **b** Loss versus MoS_2-covered length for MoS_2-covered silicon nitride waveguides with a width of 1200 nm, the propagation loss in this measurement is around 20 dB/cm. xlii

1.1 Different devices separating light into its different wavelengths. **a** Dispersive prism (image reproduced from Wikipedia). **b** Silica-based integrated optical arrayed waveguide grating (image from reference [2]). **c** Silicon-based planar concave grating, the colors conceptually show how white light can get split into its different components and do not represent actual colors (image from reference [3]). 1-2

1.2 **a** Commercially available optical parametric oscillator (Coherent Mira-OPO [39]). **b** Fiber-based supercontinuum source (NKT Photonics SuperK EVO OEM [40]). **c** Example of a supercontinuum generated on an integrated silicon nitride waveguide, the right-hand picture shows a scanning-electron micrograph of the waveguide cross-section (images from reference [41]). 1-6

2.1 **a** Crystal structure of graphene, consisting of a hexagonal lattice of carbon atoms (image reproduced reference [15]). **b** A hypothetical graphene hammock (image from reference [14]). 2-2

2.2 **a** Sketch of the band structure of graphene. E_F is the Fermi energy. **b** Demonstration of the electric field effect in graphene, sheet conductivity σ versus gate voltage V_g (image adapted from reference [13]). 2-3

2.3 **a** Real part of the intenstity-dependent change in linear conductivity $\sigma^{(1)}(|E_\omega|^2) - \sigma^{(1)}(0)$, as a function of $\tau_\mathcal{E}|E_\omega|^2$. The dotted lines represents the approximation using only the third order conductivity $\sigma^{(3)}$; $\sigma^{(1)}(|E_\omega|^2) = \sigma^{(1)}(0) + \frac{3}{2}\sigma^{(3)}|E_\omega|^2$. **b** Imaginary part of the same parameters. See Appendix A, Section A.4 for more details. These calculations are done for a wavelength of 1550 nm, assuming continuous-wave illumination. 2-14

2.4 Sketch of typical graphene-covered waveguide 2-16

3.1 **a** Fabrication steps for graphene-on-silicon waveguides. **b** Sketch of the cross-section of the final device, with applied gate voltage V_G (doping levels $n \approx 10^{18}\mathrm{cm}^{-3}$, $n+ \approx 10^{19}\mathrm{cm}^{-3}$, $n++ \approx 10^{20}\mathrm{cm}^{-3}$). **c** Examples of mode fields of a TE and a TM mode. **d** Optical micrograph (top) and SEM images (bottom) of the fabricated devices (taken from reference [7]). 3-3

3.2 Setup used for the saturable absorption measurements. Modelocked laser: Pritel, inc. FFL-1550-10, EDFA: erbium-doped fiber amplifier. VOA: variable optical attenuator. PD: photodiode. FPC: fiber polarization controller. In the measurement presented in figure 3.4, a modelocked laser of type Calmar FM-SA-306-SN was used, without EDFA. 3-4

3.3 **a** Transmission as a function of input peak power for the TM mode of a hybrid graphene-covered Si waveguide. Measurements for different gate voltages are shown (see legend), the solid lines represent a theoretical fit. Pulse duration: ≈ 8 ps, wavelength: 1550 nm, waveguide width: 650 nm, graphene-covered length: 150 µm. **b**, **c** Saturable loss (α'_S), nonsaturable loss (α'_NS) and saturation power for the fits shown in figure **a** (solid lines). Using the phenomenological model in equation (3.1), as a function of gate voltage. An effective two-photon absorption coefficient $\beta'_\mathrm{TPA} = 100\ \mathrm{m}^{-1}\mathrm{W}^{-1}$ was used. 3-5

3.4 **a** Transmission as a function of input peak power for the TE mode of a hybrid graphene-covered Si waveguide. Measurements for different gate voltages are shown (see legend), the solid lines represent a theoretical fit. Pulse duration: ≈ 4 ps, wavelength: 1550 nm, waveguide width: 500 nm, graphene-covered length: 150 µm. **b** Comparison between the measured saturable absorption modulation depth for this TE-waveguide and the TM-waveguide characterized in figure 3.3**a**. **c**, **d** Saturable loss (α'_S), nonsaturable loss (α'_NS) and saturation power for the fits shown in figure **a** (solid lines). Using the phenomenological model in equation (3.1), as a function of gate voltage. An effective two-photon absorption coefficient $\beta'_\mathrm{TPA} = 260\ \mathrm{m}^{-1}\mathrm{W}^{-1}$ was used. 3-7

3.5 Fabrication flow of the graphene-on-silicon nitride photonics structures. 3-10

3.6 SEM pictures of waveguides planarized using different recipes. **a** Only wet etching, top view. **b** Only wet-etching, cross-section. **c, d** Combination of RIE and wet etching, cross-section. 3-11

3.7 **a** Optical microscope image of a set of waveguides. The extent of the graphene (under the contacts) is shown by the dashed lines. **b** SEM image of one of the final devices. The patterned graphene can clearly be seen. Both images are taken on samples with no polymer electrolyte. 3-12

3.8 **a** A schematic illustration of the working principle of the polymer electrolyte gating. Li^{+} (magenta) and $\mathrm{ClO_4}^{-}$(cyan) ions and the Debye layers near the electrodes are shown (adapted from reference [18]). **b** Sketch of the cross-section of the graphene-on-SiN waveguides with polymer electrolyte. 3-12

3.9 **a** The measured electrical resistance over the graphene as function of the gate voltage V_{GS}. **b** The measured optical loss for a wavelength of 1550 nm and corresponding fit, proportional to the real part of the linear conductivity of graphene $\sigma_s^{(1)}$. For waveguides with a width of 1600 nm. **c** Estimated relation between gate voltage V_{GS} and Fermi energy E_{F} of the graphene covering the waveguides. 3-14

3.10 **a** Energy-level description of non-degenerate four-wave mixing. **b** Energy-level description of degenerate four-wave mixing. **c** Frequency components involved in degenerate four-wave mixing. 3-15

3.11 Setup used for the FWM experiments. EDFA: erbium-doped fiber amplifier, FBG: fiber Bragg grating, OSA: optical spectrum analyzer. 3-20

3.12 **a** Example of a FWM measurement on an ungated graphene-covered waveguide ($L = 500$ µm, waveguide width: 1200 nm). **b** FWM conversion efficiency versus detected pump power. The solid line represents a quadratic fit. 3-20

3.13 **a** Examples of the optical spectra ($V_{GS} = -0.5$ V). The pump peak (1550.18 nm) is filtered out by the FBG. The signal peaks can be seen on the left and the corresponding idler peaks on the right. Graphene section length: $L =$100 µm. **b** Effective length of the nonlinear interaction, calculated using the propagation loss in figure 3.9**b**, the black circles correspond to measured losses, the blue line is calculated using the fitted loss. **c** Conversion efficiency η as a function of V_{GS} and detuning $\lambda_{\mathrm{s}} - \lambda_{\mathrm{p}}$. 3-21

3.14 **a** Measured nonlinear parameter $|\gamma(\omega_\mathrm{i};\omega_\mathrm{p},\omega_\mathrm{p},-\omega_\mathrm{s})|$, and the corresponding graphene nonlinear conductivity $|\sigma_s^{(3)}(\omega_\mathrm{i};\omega_\mathrm{p},\omega_\mathrm{p},-\omega_\mathrm{s})|$, as a function of gate voltage and estimated Fermi energy for different values of signal-pump detuning $\Delta\lambda = \lambda_\mathrm{s} - \lambda_\mathrm{p}$ (see legend). **b** Measured $|\gamma(\omega_\mathrm{i};\omega_\mathrm{p},\omega_\mathrm{p},-\omega s)|$ and estimated $|\sigma_s^{(3)}(\omega_\mathrm{i};\omega_\mathrm{p},\omega_\mathrm{p},-\omega_\mathrm{s})|$ as a function of signal-pump detuning, both in wavelength difference (bottom axis) and angular frequency difference (top axis). 3-23

3.15 Simulated $|\sigma_s^{(3)}(\omega_\mathrm{i};\omega_\mathrm{p},\omega_\mathrm{p},-\omega_\mathrm{s})|$, using the phenomenological model discussed in Appendix A. **a** $|\sigma_s^{(3)}|$ versus Fermi energy for different values of signal-pump detuning $\Delta\lambda = \lambda_\mathrm{s} - \lambda_\mathrm{p}$ (see legend). **b** $|\sigma_s^{(3)}|$ versus detuning for different Fermi energies (see legend). Model parameters: $k_\mathrm{B}T_0 = 25$ meV, $E_i = 100$ meV, $\tau_\mathcal{E} = 0.5$ ps, the pump wavelength is 1550 nm ($\hbar\omega_\mathrm{p} \approx 0.8$ eV). 3-25

3.16 Simulated $|\sigma_s^{(3)}(\omega_\mathrm{i};\omega_\mathrm{p},\omega_\mathrm{p},-\omega_\mathrm{s})|$, using an adapted version of the model from references [29, 30]. The pump wavelength is 1550 nm. **a** $|\sigma_s^{(3)}|$ versus Fermi energy for different values of signal-pump detuning $\Delta\lambda = \lambda_\mathrm{s} - \lambda_\mathrm{p}$ (see legend). **b** $|\sigma_s^{(3)}|$ versus detuning for different Fermi energies (see legend). The simulations were performed by Sergey A. Mikhailov and Nadja A. Savostianova. 3-27

3.17 Sketch of the setup for the cross-amplitude/cross-phase modulation experiment. Red dotted arrow: path of the signal, blue dotted arrow: path of the pump. EDFA: erbium doped fiber amplifier, VNA: vector network analyzer, FBG: fiber Bragg grating, SMF: single mode fiber. 3-30

3.18 **a** The measured electrical resistance per unit of length (of the graphene section) over the graphene as function of the gate voltage V_GS. Measured on a device with an 800 µm long graphene section. **b** The measured optical loss for a wavelength of 1550 nm and corresponding fit, proportional to the real part of the linear conductivity of graphene $\sigma_s^{(1)}$. For waveguides with a width of 1400 nm. **c** Estimated relation between gate voltage V_GS and Fermi energy E_F of the graphene covering the waveguides. The range of gate voltages and corresponding Fermi energies for which the cross-modulation experiment was performed is shown by the shaded area. . . . 3-35

3.19 Examples of S-parameter measurements used in a cross-modulation experiment performed on a waveguide of width 1400 nm, covered with 50 µm of graphene. The traces shown here are for $\lambda_{\text{probe}} = 1551$ nm and $\lambda_{\text{pump}} = 1550.18$ nm. **a** Traces of $|S_{21}|$ and $|S_{31}|$ for $V_{\text{GS}} = 0$ V. The ratio $|S_{31}|/|S_{21}|$ can be used to estimate $|\text{Im}(\gamma)|$. **b** Trace of $\angle(S_{31}/S_{21})$ used to estimate the sign of $\text{Im}(\gamma)$, for two different gate voltages. **c** Traces of $|S_{41}|$ for two different gate voltages. The dashed lines show the corresponding sinusoidal fits ($\propto \left|\sin\left(\beta_2 L_{\text{SMF}}\Omega^2/2 + \angle\gamma\right)\right|$), used to estimate $\angle\gamma$. 3-36

3.20 **a** Measured $\text{Im}(\gamma)$ as function of V_{GS} for different probe wavelengths λ_{probe} (see legend). The top axis shows the estimated Fermi energy corresponding to the gate voltage, the right-hand axis shows the corresponding $\text{Re}(\sigma_s^{(3)})$. **b** Measured $\text{Re}(\gamma)$ and corresponding $\text{Im}(\sigma_s^{(3)})$, as function of gate voltage and estimated Fermi energy. The grey dashed lines in both **a** and **b** show the simulated results for $\lambda_{\text{probe}} = \lambda_{\text{pump}}$ (see Section 3.5.4). 3-37

3.21 **a** Measured $\text{Im}(\gamma)$ as a function of λ_{probe}, respectively, for different gate voltages V_{GS} (see legend). The top axes show the corresponding probe-pump detuning in radial frequency, the right-hand axis shows the corresponding $\text{Re}(\sigma_s^{(3)})$. **b** Measured $\text{Re}(\gamma)$ and corresponding $\text{Im}(\sigma_s^{(3)})$, as function of probe wavelength and frequency detuning. 3-38

3.22 Simulated real (**a**) and imaginary (**b**) parts of $\sigma_s^{(3)}$ as a function of Fermi energy at different probe wave frequencies ($\Delta\lambda \equiv \lambda_{\text{probe}} - \lambda_{\text{pump}}$). Real (**c**) and imaginary (**d**) parts of $\sigma_s^{(3)}$, as a function of λ_{probe} at different Fermi energies. Parameters: $k_B T_0 = 25$ meV, $E_i = 100$ meV, $\tau_{\mathcal{E}} = 0.165$ ps, the pump wavelength is 1550 nm ($\hbar\omega_{\text{pump}} \approx 0.8$ eV). 3-40

3.23 **a** Measured $|\sigma_s^{(3)}(\omega_{\text{probe}}; \omega_{\text{probe}}, \omega_{\text{pump}}, -\omega_{\text{pump}})|$, for $\lambda_{\text{probe}} = 1551.5$ nm. **b** Estimated nonlinear refractive index $n_2 + i\kappa_2$ as a function of estimated Fermi energy. The measurement of $\sigma_s^{(3)}$ using $\lambda_{\text{probe}} = 1551.5$ nm in figure 3.20 was used. The dotted lines are calculated values. **c** Estimated electron temperature as a function of illumination intensity for a wavelength of 1550 nm. **d** Theoretical calculations of n_2 for different electron temperatures. All calculations have been done using the phenomenological model described in Appendix A, with $\tau_{\mathcal{E}} = 0.16$ ps. 3-42

3.24 Simulated third harmonic conversion efficiency for a waveguide of thickness 300 nm and width 1400 nm, with nonlinear susceptibilities taken from different references. 3-47

4.1 **a** PZT unit cell with a tetragonal perovskite structure (adapted from Wikipedia). **b** STEM image of the cross-section of a PZT thin film, on top of a La-based intermediate layer. The overlay shows the relative EDX signal intensity measured along the cross-section, using representative elements La, Pb and Si (image taken from the PhD thesis of John P. George [26]). **c** HRTEM image of the cross-section. The inset shows the FFT power spectrum for the PZT layer (image taken from the PhD thesis of John P. George [26]). 4-4

4.2 **a** Setup used for the thin-film second harmonic generation experiments. $\lambda/2$: half-wave plate, LP: longpass filter, SP: shortpass filter, BP: bandpass filter. Adapted from reference [30]. **b** Principle of the thin-film second harmonic generation experiment. 4-8

4.3 Typical sample used for measuring the second harmonic response of thin-film PZT. 4-9

4.4 Measurement and fit for a blank BOROFLOAT® 33 substrate with known $\chi_s^{(2)}$ and thickness $L \approx 500$ µm. Used as a reference for other measurements. 4-10

4.5 Measurements (Meas.) and fits for two different PZT-covered glass samples after out-of-plane poling using comparable electric fields (≈ 9.3 V/µm), for two different PZT thicknesses L_{PZT} (see legend). 4-11

4.6 Second harmonic power at a fixed angle (48 °). **a** For two different PZT thicknesses. The dashed line is a fit based on equation (4.9). The dotted line is the theoretical curve in the absence of phase mismatch ($\Delta k = 0$), essentially a parabola. **b** After different poling steps, for $L_{\mathrm{PZT}} = 645$ nm. The arrow shows the order in which the different poling voltages are applied. 4-12

4.7 **a** Fabrication steps for the PZT-on-SiN waveguides, starting from a planarized SiN chip. **b-d** Examples of SEM cross-sections of different waveguides. For **b**, **c** the planarization was done through a combination of RIE and BOE etching (see Section 3.3.1 for a more detailed description) the inset shows the trench at the waveguide edge with enhanced contrast, caused by nonuniform etch rates. For **d** the planarization was performed using CMP. 4-14

4.8 Loss measurements on samples planarized through RIE and BOE-etching. **a** Transmission versus waveguide length for a PZT-covered rib and wire waveguide, with cross-section similar to figure 4.7**b** (width = 1400 nm, wavelength = 1550 nm, PZT thickness ≈ 125 nm). **b**, **c** Propagation loss of the respective rib and wire waveguides versus wavelength, before and after PZT deposition. The shaded area shows the standard deviation on the fitted slope. 4-16

4.9 Loss measurements on samples planarized through CMP. **a** Transmission versus waveguide length for a PZT-covered waveguide, with cross-section similar to figure 4.7**d** (width = 800 nm, wavelength = 1310 nm, PZT thickness = 150 nm). Measured on 3 different samples. **b** Propagation loss versus wavelength for these waveguide sets, including a sample with no PZT. 4-17

4.10 Setup used for the second harmonic generation measurements on PZT-covered waveguides. EDFA: erbium-doped fiber amplifier. The shortpass filter has a cutoff wavelength of 1000 nm. 4-19

4.11 **a** Detector voltage and corresponding estimated second harmonic power on the detector, as a function of fundamental wavelength, for different voltages applied over the waveguide. The dotted line shows the dark counts of the detector. **b** Estimated second harmonic power on the detector, as a function of power on the reference photodiode. For a voltage of 10 V and a wavelength of 1540 nm. The solid line represents a fit with slope 2.19. 4-21

4.12 Top-view of the PZT-covered waveguide in which SHG occurs, the waveguide lights up due to the scattering of the second harmonic. The probe needels used to apply the DC voltage can also be distinguished. 4-22

4.13 Top: camera image showing the SH light scattered from the waveguide. Bottom: estimated SH power in the waveguide based on the intensity of the scattered light observed with the camera (blue line). The dashed black line is an approximation based on equation (4.14), with α_f = 20 dB/cm and α_SH = 2000 dB/cm. 4-22

4.14 **a** TE00 mode of a PZT-covered waveguide at the fundamental wavelength (λ_f = 1550 nm). **b** Higher-order TE mode at the second harmonic wavelength (λ_SH = 775 nm). Both modes have an effective index of ≈ 1.83. The waveguide width, SiN thickness and PZT thickness are respectively 2000 nm, 335 nm and 150 nm. **c** Suggested solution to avoid coupling into slab modes. 4-23

4.15 Schematic of the PZT-covered SiN waveguide used as electro-optic phase modulator, the fundamental TE optical mode at is plotted in red. The quiver plot shows the applied electric field distribution between the electrodes. PZT thickness, waveguide width and gap between the electrodes are respectively 150 nm, 1200 nm and 4 µm. 4-24

4.16 Setup used for phase modulation measurements. FPC: fiber polarization controller, AOM: acousto-optic modulator, PD: photodiode, ESA: electrical spectrum analyzer. 4-26

4.17 **a** Example of an RF power spectrum used for preliminary characterization of a PZT-on-SiN phase modulator. **b** Estimated $V_\pi L$ value while applying a sequence of different poling voltages. The arrows show the order in which the voltages were applied. At 42 V the poling voltage is applied for 30 minutes (hence the two points, before and after). At 0 V, the same is done for 60 minutes. Waveguide width = 2400 nm, PZT thickness ≈ 150 µm, wavelength = 1550 nm, phase shifter length = 165 µm, electrode gap ≈ 6 µm, $\Omega = 10$ MHz. 4-27

4.18 **a** Top view of a C-band ring modulator. **b** Cross-section of a C-band ring modulator. **c** Top view of an O-band ring modulator. **d** Cross-section of an O-band ring modulator. **e** Top view of a C-band MZI modulator. **f** Cross-section of a C-band MZI modulator. The nominal thickness of the intermediate lanthanide layer (below the PZT) is 24 nm in all devices. 4-29

4.19 Normalized transmission spectra of a C-band ring modulator (**a**), an O-band ring modulator (**b**) and a C-band MZI modulator (**c**). 4-30

4.20 **a** Example of a slightly misaligned electrode pattern on a ring modulator, the misalignment is ≈ 1 µm. **b** Electrode-induced loss as a function of electrode misalignment, for different electrode spacings (see legend). For a wavelength of 1550 nm, a bend radius of 100 µm, a waveguide width of 1 µm and a PZT thickness of 120 nm, with an intermediate layer of 24 nm thick. Simulated with Lumerical FDTD. 4-31

4.21 **a** Normalized transmission spectra for different DC voltages of the C-band ring modulator. **b** Resonance wavelength shift of the C-band ring versus voltage, including a linear fit. **c** Normalized transmission spectra for different DC voltages of the O-band ring modulator. **d** Resonance wavelength shift of the O-band ring versus voltage, including a linear fit. **e** Normalized transmission spectra for different DC voltages of the C-band MZI modulator. **f** Optical phase shift as a function of voltage, including linear fit. 4-33

4.22 Tuning efficiency (in absolute value) of a C-band ring as a function of time after poling. The axis on the right shows the estimated corresponding $V_\pi L$. 4-34

4.23 Sketch of the setup used for the small signal measurements. VNA: vector network analyzer, EDFA: erbium-doped fiber amplifier, OTF: optical tunable filter. 4-35

4.24 Electro-optic small signal ($|S_{21}|$ parameter) measurement of several modulators. 4-36

4.25 Sketch of the setup used for the eye diagram measurements. AWG: arbitrary waveform generator, EDFA: erbium-doped fiber amplifier, OTF: optical tunable filter. 4-37

4.26 **a-c** Eye diagrams of a C-band ring modulator, measured with a non-return-to-zero scheme ($2^9 - 1$ pseudorandom binary sequence) and a peak-to-peak drive voltage of 4.2 V. Using respective modulation speeds of 10, 28 and 40 Gbps. **c** Eye diagram at 10Gbps, obtained using a DC-coupled optical receiver. 4-37

4.27 Bit error rates estimated on the basis of measured eye diagrams, the horizontal dotted line represents the HD-FEC limit with 7% overhead. 4-38

4.28 Simulation of the waveguide loss α (**a**), the half-wave voltage-length product $V_\pi L$ (**b**) and their product $V_\pi L\alpha$ (**c**) of a PZT-covered SiN waveguide modulator of the type shown in figure 4.15, for a wavelength of 1550 nm. Waveguide height, width and intermediate layer thickness are respectively 300 nm, 1.2 µm and 20 nm. The intrinsic waveguide loss (in the absence of electrodes) was taken to be 1 dB cm^{-1}, the effective electro-optic Pockels coefficient 67 pm V^{-1}. The circles show the approximate parameters used in this work, the diamonds show the optimal point with respect to $V_\pi L\alpha$. . 4-40

4.29 Optimization of the waveguide loss times the half-wave voltage-length product $V_\pi L\alpha$ of a PZT-covered SiN waveguide modulator as a function of waveguide width. **a** For each waveguide width $V_\pi L\alpha$ is minimized as function of both electrode spacing and PZT thickness (blue line). The red line plots the calculated $V_\pi L$ at this optimum. **b** Electrode spacing (blue) and PZT thickness (red) at the optimum. The light blue area shows the waveguide width/PZT thickness combinations for which the waveguide only supports a single TE mode. Wavelength, SiN height and intermediate layer thickness are respectively 1550 nm, 300 nm and 20 nm. The intrinsic waveguide loss (in the absence of electrodes) was taken to be 1 dB cm^{-1}, the effective electro-optic coefficient 67 pm V^{-1}. 4-41

5.1 **a** Structure of a monolayer TMDC, side view and top view. From the top it looks like a honeycomb structure with broken inversion symmetry (adapted from reference [2]). **b** Schematic of the side-view of 2H-MoS_2, adjacent layers have antiparallel orientations, restoring the inversion symmetry. The second order polarizations generated in different layers in a SHG experiment will destructively interfere (adapted from reference [3]). 5-3

5.2 **a** Setup used for the second harmonic generation experiments. $\lambda/2$: half-wave plate, LP: longpass filter, SP: shortpass filter, BP: bandpass filter. Adapted from reference [15]. The half-wave plate is mounted on a rotating stage in the vertical direction, the sample is mounted on a horizontally rotating stage. **b** Sketch of a measurement on an MoS_2 monolayer transferred to a silica-on-silicon substrate. **c** Sketch of the orientation of the MoS_2 monolayer on the substrate, x, y and z represent the 'lab' reference frame, X, Y and $Z = z$ the conventional reference frame of the MoS_2. 5-6

5.3 Measured SH power for the MoS_2-covered substrate, for respectively the analyzer selecting the s-(blue) and p-polarizations (red). The solid lines are the theoretical fits. 5-7

5.4 **a** Sketch of the cross-section of an MoS_2-covered SiN waveguide. **b** Microscope image of a set of waveguides covered with MoS_2 after patterning. The contrast was enhanced to make the MoS_2-patches clearly visible. 5-8

5.5 **a** Fiber-to-fiber loss for the MoS_2-covered waveguides, for different lengths of MoS_2. The measurements were performed on waveguides of different widths, see legend. The dashed lines show the linear fits. The wavelength is 1550 nm. **b** Estimated propagation loss of the MoS_2-covered section as a function of wavelength, from the linear fits. **c** Grating coupler loss as a function of wavelength. 5-10

5.6 Proposed waveguide structure for on-chip quasi-phase-matched second harmonic generation using MoS_2 and other TMDCs. . 5-12

5.7 Simulation results for quasi-phase-matched second harmonic generation using an MoS_2-covered SiN-waveguide, see figure 5.6. **a** Phase matching period for a fundamental wavelength of 1550 nm, as a function of waveguide thickness h and width w. **b** Calculated nonlinear coupling κ (using equation (5.6)), as a function of waveguide thickness h and width w, for $\chi^{(2)} = 5 \cdot 10^{-21}$ m^2/V. The dotted lines on figures **a** and **b** represent the approximate parameters of the currently available waveguides, the diamonds represent the point with optimal κ. **c** Calculated nonlinear conversion $\frac{P_{\mathrm{SH}}(L)}{P_{\mathrm{f}}(0)^2}$, for the values in line with what was measured ($\kappa = 0.1$ m^{-1} W$^{-\frac{1}{2}}$, propagation losses of 12.5 dB/cm for both fundamental and second harmonic) and for more optimistic values ($\kappa = 0.17$ m^{-1}W$^{-\frac{1}{2}}$, propagation losses of 2.5 dB/cm), respectively in blue and green. **d** Nonlinear coupling κ versus relative orientation of the MoS_2 crystal with respect to the waveguide, α is the angle between the waveguide cross-section plane and the 'armchair' (X) direction of the MoS_2 (see figure 5.2**c**), for $w = 1.65$ µm and $h = 190$ nm. 5-13

A.1 **a** Real part of the intensity-dependent linear conductivity $\sigma^{(1)}$, as a function of $\tau_{\mathcal{E}}|E_\omega|^2$. The dotted lines represents the approximation using only the third order conductivity $\sigma^{(3)}$; $\sigma^{(1)}(|E_\omega|^2) = \sigma^{(1)}(0) + \frac{3}{2}\sigma^{(3)}|E_\omega|^2$. **b** Imaginary part of the power-dependent linear conductivity $\sigma^{(1)}$, the dotted lines again express the $\sigma^{(3)}$-based approximation. A-8

List of Tables

1.1 Some key properties and available building blocks on some common nanophotonic platforms. The color code denotes whether the properties are desirable (green), moderately desirable (orange) or less desirable (red) for most applications. † Since these materials are centrosymmetric, their second order nonlinear coefficients are very small. Recently, several groups have however shown that second order nonlinearities can be induced through control of composition [31], strain [32] or the photogalvanic effect [33]. This is however not considered here. ‡ These devices can be fabricated through heterogeneous integration with III-V materials [34]. 1-4

2.1 Some earlier experimental values for $\chi^{(3)}$, $\sigma_s^{(3)}$ or n_2 from literature. λ is the wavelength of the measurement, Δt is the approximate pulse duration (CW denotes continuous wave illumination). I_p is the approximate (peak) intensity. 🟥 Four-wave mixing experiments. 🟩 Self- or cross- phase(or amplitude) modulation experiments. 🟦 Third harmonic generation experiments. ⬜ Nonlinear parameters as reported, the other values were extrapolated. † Dremetsika *et al.* [53] and Vermeulen *et al.* [54] were the first to independently report negative values for the intensity-dependent refractive index. ‡ In a second publication, Dremetsika *et al.* published complex values for the nonlinear parameters [50]. . 2-13

3.1 Rough estimates of $|\chi^{(3)}|$-values measured using third harmonic generation for fundamental wavelengths in the vicinity of 1550 nm, from different sources and with different Fermi energies. † Measurements performed with a fundamental wavelength of 1300 nm, values estimated from figure 4**c** in reference [42]. ‡ Measurement performed with a fundamental wavelength of 1738 nm for a Fermi energy of about 250 meV. The value at higher doping is rough estimate assuming a 4-fold enhancement of the $\chi^{(3)}$-parameter. 3-46

4.1 Second order susceptibility $\chi^{(2)}_{ijk}$ of different materials. Either calculated from the Pockels coefficient using equation (4.7), or measured using second order nonlinear processes such as second harmonic generation. n is the refractive index of the material. 4-6

List of Acronyms

2D	Two-dimensional
AFM	Atomic force microscopy
AOM	Acousto-optic modulator
ASE	Amplified spontaneous emission
a.u.	Arbitrary units
AWG	Arbitrary waveform generator
BER	Bit-error rate
BOE	Buffered oxide etch
BTO	Barium titanate ($BaTiO_3$)
CMOS	Complementary metal-oxide-semiconductor
CMP	Chemical mechanical polishing
CVD	Chemical vapor deposition
CSD	Chemical solution deposition
DC	Direct current
DFG	Difference-frequency generation
EDFA	Erbium-doped fiber amplifier
EDL	Electrical double layer
Eng.	English/Engels
EDX	Energy dispersive X-ray
ESA	Electrical spectrum analyzer
FBG	Fiber Bragg grating
FDTD	Finite-Difference Time-Domain method
FFT	Fast Fourier transform
FPC	Fiber polarization controller
FSR	Free-spectral range
FWM	Four-wave mixing
GC	Grating coupler
HRTEM	High-resolution transmission electron microscopy
HD-FEC	Hard-decision forward error coding
IR	Infrared
ITO	Indium tin oxide
ITRS	International Technology Roadmap for Semiconductors

LPCVD	Low pressure chemical vapor deposition
MEMS	Microelectromechanical systems
MMI	Multi-mode interferometer
MOCVD	Metal-organic chemical vapor deposition
MOS	Metal-oxide-semiconductor
MZI	Mach-Zehnder interferometer
NRZ	Non-return-to-zero
OHD	Optical heterodyne detection
OKE	Optical Kerr effect
OLED	Organic light-emitting diode
OPA	Optical parametric amplification
OPO	Optical parametric oscillator
OTF	Optical tunable filter
PD	Photodiode
PECVD	Plasma-enhanced chemical vapor deposition
PIC	Photonics integrated circuit
PMMA	Poly(methyl methacrylate)
PZT	Lead zirconate titanate ($PbZr_xTi_{1-x}O_3$)
Ref.	Reference
RF	Radio frequency
RIE	Reactive ion etching
RMS	Root-mean-square
rpm	Revolutions per minute
SEM	Scanning electron microscopy
SFG	Sum-frequency generation
SH	Second harmonic
SHG	Second harmonic generation
SHGE	Second harmonic generation efficiency
SMF	Single mode fiber
SOI	Silicon-on-insulator
SPDC	Spontaneous parametric down-conversion
STEM	Scanning transmission electron microscopy
TE	Transverse electric
THG	Third-harmonic generation
TM	Transverse magnetic
TMDC/TMD	Transition metal dichalcogenide
TPA	Two-photon absorption
UV	Ultraviolet
VNA	Vector network analyzer
VOA	Variable optical attenuator
XAM	Cross-amplitude modulation
XM	Cross modulation
XPM	Cross-phase modulation

Samenvatting

Doelstellingen en Motivatie

Geïntegreerde fotonica is een heel snel evoluerende tak van de ingenieurswetenschappen. Enkele decennia geleden waren optische chips nog academische curiositeiten, maar tegenwoordig worden ze steeds meer gebruikt voor veelbelovende toepassingen, zoals optische communicatie, sensoren voor industriële en medische toepassingen, of zelfs voor de implementatie van neurale netwerken. Verschillende materialen kunnen gebruikt worden om deze chips te maken. Silicium en in toenemende mate siliciumnitride zijn waarschijnlijk het meest veelbelovend [1]. Het grote voordeel van deze materialen is dat ze ook gebruikt worden in de micro-elektronica, en dat heel mature fabricatiemethoden makkelijk hergebruikt kunnen worden. Verder kunnen optische structuren bijzonder compact gemaakt worden door het hoge indexcontrast in deze platformen, en heeft vooral siliciumnitride een laag optisch verlies, een goede thermische stabiliteit en kan het gebruikt worden voor veel verschillende golflengtes. Er zijn echter ook nadelen. Op standaard siliciumplatformen kun je optische modulatoren en detectoren maken, maar geen lasers of versterkers. Actieve functionaliteiten zijn op nitride nog problematischer. Geen lasers of versterkers, noch detectoren of modulatoren, zijn voorhanden.

Een veelbelovende strategie om deze problemen aan te pakken is de integratie van andere materialen op silicium- of siliciumnitridechips. In deze thesis kijken we specifiek naar materialen die sterke optische niet-lineariteiten vertonen. Niet-lineaire effecten zijn aanwezig als de polarisatiedichtheid van een materiaal op een niet-lineaire manier afhangt van de sterkte van het optische veld. Zulke effecten zijn over het algemeen heel zwak en komen enkel tot uiting als hoge vermogens gebruikt worden. De komst van geïntegreerde fotonica heeft dit enigzins veranderd. Licht wordt geconcentreerd in hele kleine golfgeleiders, waardoor de lokale intensiteit enorm toeneemt. Hierdoor kunnen niet-lineaire effecten worden geobserveerd en zelfs gebruikt bij veel lagere vermogens. Wanneer de polarisatiedichtheid van het materiaal schaalt met het kwadraat van het elektrische veld, spreken we van tweedeorde niet-lineariteiten. Deze kunnen gebruikt worden voor het genereren van licht bij nieuwe golflengten, maar ook voor elektro-optische fasemodulatie. Dit laatste noemt men het Pockelseffect. Wanneer de polarisatiedichtheid schaalt met de derde macht van het elektrische veld, spreken we van derde-orde niet-lineaire effecten. Ook dit kan gebruikt worden voor de generatie van nieuwe golflengten van licht, of zelfs van buitengewoon breedbandige spectra. Silicium noch siliciumnitride kunnen gebruikt worden voor tweede-orde niet-lineaire optica. Derde-orde effecten komen voor in nitride, maar zijn relatief zwak. In silicium zijn ze heel wat sterker, maar hier maken andere effecten zoals twee-foton-absorptie ze moeilijk bruikbaar. In deze thesis onderzoeken we verschillende materialen. We gaan op zoek naar materialen waarvan we enerzijds verwachten dat ze sterk niet-lineair zijn, en die anderzijds relatief makkelijk en goedkoop met bestaande silicium- en siliciumnitridechips gecombineerd kunnen worden. Grafeen, het meest bekende van alle tweedimensionale kristallen, komt eerst aan de beurt. 2D-materialen kunnen relatief gemakkelijk geïntegreerd worden met nanofotonische componenten, bovendien hebben verschillende onderzoeksgroepen aangetoond dat de derde-orde niet-lineare respons van grafeen heel sterk kan zijn. Een tweede materiaal dat bestudeerd wordt is loodzirconaattitanaat (Eng.: lead zirconate titanate - PZT). PZT staat bekend voor zijn interessante materiaaleigenschappen, waaronder een sterke tweede-orde niet-lineaire respons en een sterk Pockelseffect. Recente ontwikkelingen in de depositie van PZT door de vaktroep Elektroncia en Informatiesystemen aan onze universiteit maken het voor het eerst mogelijk lichtdoorlatende dunne lagen van hoge kwaliteit te deponeren op onze fotonische chips [2]. Het laatste materiaal dat onder de loep wordt genomen is molybdeendisulfide (MoS_2), dit is een voorbeeld van een “transition metal dichalcogenide” (TMDC). TMDCs zijn tweedimensionele kristallen, en net als grafeen kunnen ze relatief gemakkelijk met bestaande fotonische chips gecombineerd worden. In hun monolaagvorm vertonen deze materialen tweede-orde niet-lineaire effecten.

Resultaten

Grafeen kan gecombineerd worden met zowel silicium- als siliciumnitridechips. Op figuur 1 staat zo een siliciumnitridechip afgebeeld. Het elektronenmicroscoopbeeld van de dwarsdoorsnede (figuur 1**c**) toont dat het grafeen op de oppervlakte van de chip in de directe nabijheid van de golfgeleider ligt. Het grafeen wordt ook elektrisch verbonden met metaalcontacten. Grafeen op deze chips kan elektrostatisch “gegate” worden, dit betekent dat de Fermi-energie kan aangepast worden door een gatespanning aan te leggen. Op onze siliciumchips doen we dit door een gatespanning aan te leggen tussen de kern van de golfgeleider zelf en het grafeen. Bij siliciumnitride is dit niet mogelijk, en gebruiken we een zogenaamd elektrolytisch polymeer. Als eerste experiment tonen we aan dat met grafeen bedekte siliciumgolfgelei-

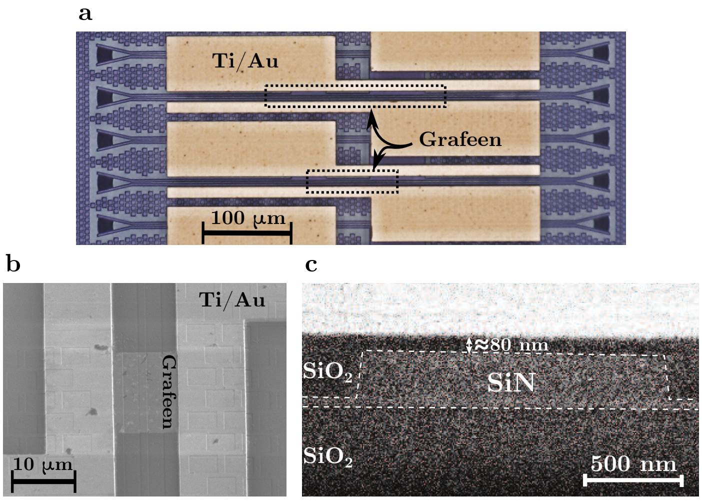

Figuur 1: **Met grafeen bedekte siliciumnitridegolfgeleiders.** **a** Optisch microscoopbeeld van enkele golfgeleiders. Het grafeen (onder de contacten) is niet zichtbaar maar de positie is aangeduid met stippellijnen. **b** Elektronenmicroscoopbeeld van een golfgeleider, het grafeen is duidelijk zichtbaar. **c** Elektronenmicroscoopbeeld van de dwarsdoorsnede van een golfgeleider.

ders kunnen gebruikt worden voor hun satureerbare absorptie. Dit betekent dat ze licht met een hoger vermogen minder absorberen. We meten saturatievermogens van ongeveer 1 W en tonen ook aan dat de mate van saturatie kan aangepast worden door middel van de gatespanning. Op siliciumnitridegolfgeleiders verrichten we twee andere experimenten, de resultaten zijn samengevat in figuur 2. Door middel van vierbundelmenging tonen we aan dat de niet-lineaire parameter $|\gamma|$ van de golfgeleiders en de derde-orde geleidbaarheid $|\sigma_s^{(3)}|$ van grafeen ook heel sterk afhangen van de gatespanning (figuur 2**a**). Door de signaalgolflengte aan te passen tonen we ook aan dat de sterkte van de vierbundelmenging sterk afhangt van het golflengteverschil tussen signaal en pomp (figuur 2**b**). Een kruismodulatie-experiment laat ook toe de niet-lineaire faserespons en amplituderespons van elkaar te onderscheiden. Figuren 2**c** en **d** tonen respectievelijk $\mathrm{Im}(\gamma) \propto \mathrm{Re}(\sigma_s^{(3)})$, die de kruis-amplitudemodulatie beschrijven, en $\mathrm{Re}(\gamma) \propto \mathrm{Im}(\sigma_s^{(3)})$, die hetzelfde doen voor de kruis-fasemodulatie, in functie van de gatespanning. Opnieuw zien we sterke variaties van de gemeten parameters met veranderende gatespanning. De variaties zijn zelfs drastischer dan wat we zien in het vierbundelmengingexperiment, met onder andere tekenveranderingen van zowel het reëele als het imaginaire deel van γ. Dit betekent dat verschillende regimes kunnen voorkomen, zoals een positieve of negatieve niet-lineaire breking, satureerbaare absorptie, of juist het tegenovergestelde. Beide experimenten kunnen we modeleren met redelijke overeenkomst. Ons model is gebaseerd

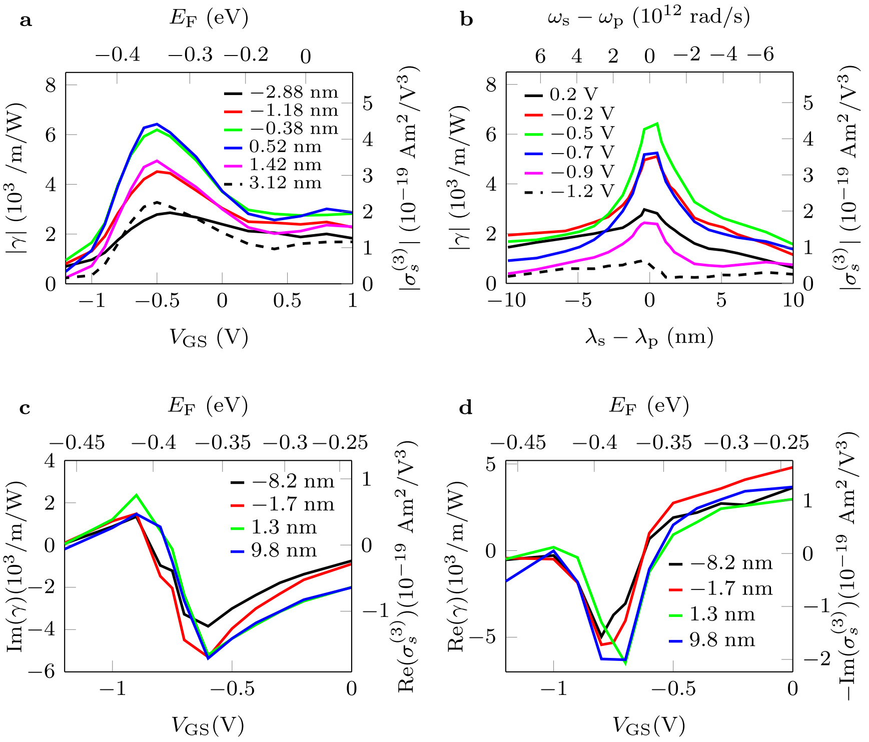

Figuur 2: **Gemeten niet-lineaire parameter van met grafeen bedekte siliciumnitridegolfgeleiders (γ) en de hieruit berekende derde-orde oppervlaktegeleidbaarheid van grafeen ($\sigma_s^{(3)}$).** **a**, **b** γ en $\sigma_s^{(3)}$ gemeten door vierbundelmenging (pomp met golflengte $\lambda_\mathrm{p} \approx 1550$ nm), in functie van de gatespanning en de geschatte Fermi-energie, voor verschillende signaalgolflengten λ_s (de legende toont $\lambda_\mathrm{s} - \lambda_\mathrm{p}$) (**a**) en als functie van het golflengteverschil $\lambda_\mathrm{s} - \lambda_\mathrm{p}$, voor verschillende gatespanningen V_GS (zie legende) (**b**). **c**, **d** γ en $\sigma_s^{(3)}$ gemeten door kruismodulatie tussen een pomp met golflengte $\lambda_\mathrm{pump} \approx 1550$ nm en een probe met verstelbare golflengte λ_probe, de legende toont het golflengteverschil $\lambda_\mathrm{probe} - \lambda_\mathrm{pump}$. **c** Im($\gamma$) en Re($\sigma_s^{(3)}$), die kruis-amplitudemodulatie beschrijven, in functie van de gatespanning en de geschatte Fermi-energie. **d** Re(γ) en Im($\sigma_s^{(3)}$), die kruis-fasemodulatie kwantificeren, ook als functie van de gatespanning.

op de excitatie van ladingsdragers in grafeen. Dit betekent dat de sterke niet-lineaire respons van grafeen niet voortkomt uit niet-resonante elektronische effecten, die wel domineren in diëlektrica met lage verliezen.

Door middel van frequentieverdubbeling tonen we aan dat dunne lagen PZT tweede-orde niet-lineaire susceptibiliteiten van minstens $\chi^{(2)} \approx 40$ pm/V kunnen hebben voor een pompgolflengte van 1550 nm. Figuur 3**a** toont dat PZT-lagen ook geïntegreerd kunnen worden met siliciumnitridegolfgeleiders. Het propagatieverlies van dergelijke golfgeleiders hangt sterk

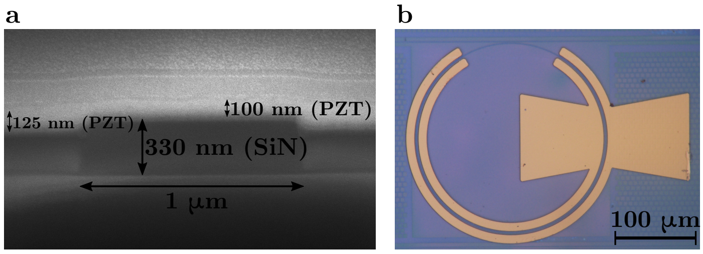

Figuur 3: **Siliciumnitride bedekt met PZT.** **a** Elektronenmicroscoopbeeld van de dwarsdoorsnede van een siliciumnitridegolfgeleider bedekt met PZT. **b** Optisch microscoopbeeld van één van de ringmodulatoren.

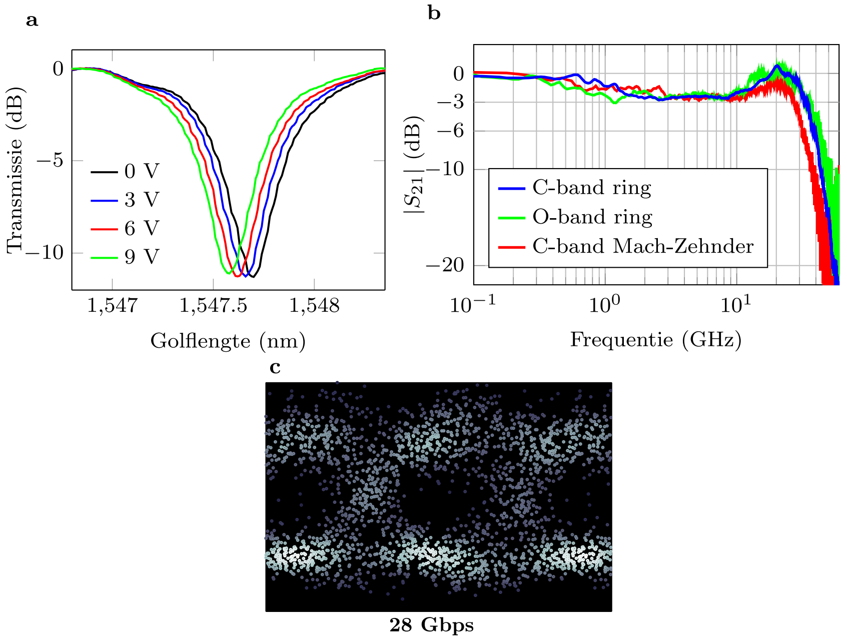

Figuur 4: **Metingen op PZT-op-siliciumnitridemodulatoren.** **a** Transmissiespectra van een C-band ringmodulator, voor verschillende aangelegde spanningen. **b** Elektro-optische kleinsignaalmeting ($|S_{21}|$-parameter) van verschillende modulatoren. **c** Voorbeeld van een oogdiagram met een bitrate van 28 Gbps.

af van de manier waarop de nitridechip wordt geplanariseerd voor de PZT-depositie. Wanneer dit gedaan wordt door middel van chemisch mechanisch polijsten kunnen verliezen van ongeveer 1 dB/cm gemeten worden. In deze golfgeleiders tonen we ook frequentieverdubbeling aan. Verder kunnen ze gebruikt worden voor elektro-optische fasemodulatie. Door een spanning aan te leggen dwars over de golfgeleider, verandert de effectieve index van de optische mode. Op figuur 3**b** wordt getoond hoe dit kan gebruikt worden in combinatie met een ringresonator om een amplitudemodulator te maken. Figuur 4**a** toont het transmissiespectrum van deze ring, voor verschillende spanningen. De resonantiegolflengte verschuift wanneer de spanning wordt aangepast. Deze ring is ontworpen voor gebruik in de optische C-band (1530 - 1565 nm), verder zijn er ringmodulatoren voor de O-band (1260 - 1360 nm) en Mach-Zehndermodulatoren voor de C-band gemaakt. Halve golf spanning-lengteproducten ($V_\pi L$) van 3.2 Vcm kunnen worden aangetoond. Hieruit kan een effectieve Pockelscoëfficient van 60-70 pm/V worden afgeleid. Deze modulatoren worden gepoold met hoge spanningen voor gebruik. Tests tonen aan dat de elektro-optische respons stabiel bijft voor minstens enkele dagen na het polen. De kleinsignaalrespons van onze modulatoren is te zien in figuur 4**b**. Bandbreedtes van meer dan 33 GHz wijzen erop dat dit materiaal geschikt is voor hoge-snelheidsmodulatie. Oogdiagrammen werden ook gemeten, en blijven open tot bij modulatiesnelheden van ongeveer 40 Gbps (zie figuur 4**c** voor een voorbeeld). Simulaties tonen aan dat simpele aanpassingen aan de dwarsdoorsnede van de golfgeleider nog voor sterke verbeteringen kunnen zorgen.

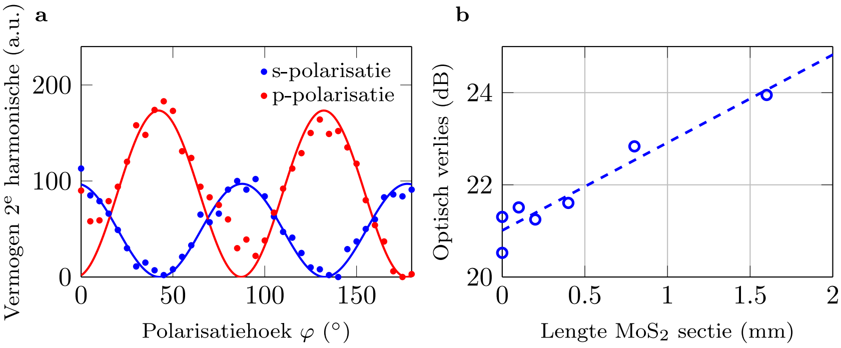

Figuur 5: **Metingen met MoS_2.** **a** Meting van frequentieverdubbeling op een met MoS_2 bedekt substraat, ofwel de s-gepolariseerde component (blauw), of de p-gepolariseerde component (rood) van de tweede harmonische wordt gemeten. De volle lijnen zijn de theoretische fits. **b** Verlies versus MoS_2-lengte voor met MoS_2 bedekte siliciumnitridegolfgeleiders met een breedte van 1200 nm, het propagatieverlies in deze meting is ongeveer 20 dB/cm.

Via imec (Leuven) hebben we toegang tot monolaag MoS_2. Figuur 5**a** toont het resultaat van een frequentieverdubbelingsexperiment op een met MoS_2 bedekt silica-op-siliciumsubstraat. Een lichtstraal met een fundamentele golflengte van 1550 nm valt in op het sample en is lineair gepolariseerd. De polarisatiehoek wordt tijdens de meting geroteerd. De blauwe en rode punten tonen het vermogen in respectievelijk de s- en de p-gepolariseerde component van de tweede harmonische. Uit deze meting kunnen we een tweede-orde oppervlaktesusceptibiliteit en bulksusceptibiliteit van respectievelijk $\chi_s^{(2)} \approx 5 \cdot 10^{-21}$ m^2/V en $\chi_b^{(2)} \approx 8$ pm/V afleiden. We kunnen MoS$_2$ ook combineren met optische golfgeleiders, gelijkaardig aan de golfgeleiders in figuur 1. De gemeten propagatieverliezen op deze bedekte golfgeleiders zijn echter relatief hoog (zie figuur 5**b**).

Conclusies

De experimenten met grafeen in deze thesis zijn een gote stap vooruit voor het ontrafelen van het complex niet-lineaire gedrag van dit materiaal. We tonen voor het eerst experimenteel aan dat een aantal niet-lineaire effecten sterk afhankelijk zijn van de Fermi-energie, en dat ze vooral te wijten zijn aan variaties in de distributie van de elektronen en gaten bij intense belichting. Satureerbare absorptie op een chip kan gebruikt worden voor bijvoorbeeld geïntegreerde gepulste lasers. De vierbundelmenging- en kruismodulatie-experimenten tonen aan dat de niet-lineariteiten in grafeen inderdaad heel sterk kunnen zijn. Anderzijds concluderen we ook dat ze veroorzaakt worden door excitatie van ladingsdragers. Dit betekent dat deze sterke niet-lineariteiten samengaan met sterke lineaire absorptie, dat ze waarschijnlijk zullen satureren bij hogere vermogens en dat fenomenen zoals vierbundelmenging smalbandig zijn. Omwille hiervan is het aangeraden geen onrealistisch grote hoop te koesteren voor het gebruik van grafeen voor niet-lineaire toepassingen. We tonen echter ook aan dat al deze effecten heel sterk aangepast kunnen worden door gating, wat dan weer een heel sterke troef kan zijn.

We tonen hoe dunne lagen PZT kunnen gecombineerd worden met fotonische chips voor frequentieverdubbeling en elektro-optische modulatie. Ons frequentieverdubbelingsexperiment toont aan dat dit mogelijk is, maar kan nog sterk verbeterd worden. Wel hebben we de eerste echte hogesnelheidsmodulatoren gemaakt op siliciumnitride, wat een mijlpaal betekent voor dit platform. Deze modulatoren kunnen nog verbeterd worden door optimalisatie van de dimensies van de doorsnede en op langere termijn zouden Mach-Zehnder modulatoren met langere fasesecties moeten gemaakt worden, zodat kleinere spanningen kunnen gebruikt worden. Het platform zou ook modulatie bij andere golflengtes mogelijk maken en PZT kan verder ook gebruikt worden op andere geïntegreerde platformen. De materiaalcontanten (de tweede-orde susceptibiliteit en de effectieve Pockels coëfficient) die we hier meten zijn kleiner dan wat kan verwacht worden op basis van andere metingen op bulk samples en dunne lagen [2]. Dit betekent dat het polen van onze dunne lagen nog niet optimaal is, beter polen (bijvoorbeeld bij hogere temperaturen) zou een directe weg naar betere modulatoren kunnen zijn.

De tweede-orde niet-lineaire respons van MoS$_2$ is niet buitengewoon sterk. In combinatie met de hoge verliezen die we meten op met MoS$_2$ bedekte golfgeleiders is dit niet zo veelbelovend. Er zijn echter een aantal pistes die nog kunnen verkend worden. Ten eerste is de oorsprong van de grote verliezen nog niet volledig gekend. Dit verlies kan te maken hebben met de materiaalkwaliteit. Het groeien van monolagen van TMDCs is complex en wordt voortdurend verbeterd. Kleinere verliezen zouden betekenen dat ondanks relatief kleine niet-lineariteiten toch sterke effecten gemeten kunnen worden. Toen de metingen uitgevoerd werden was bovendien enkel MoS_2 voorhanden. Meer TMDCs, bijvoorbeeld WS_2, kunnen tegenwoordig gegroeid worden en kunnen worden onderzocht.

Referenties

[1] A. Rahim, E. Ryckeboer, A. Z. Subramanian, S. Clemmen, B. Kuyken, A. Dhakal, A. Raza, A. Hermans, M. Muneeb, S. Dhoore, Y. Li, U. Dave, P. Bienstman, N. L. Thomas, G. Roelkens, D. V. Thourhout, P. Helin, S. Severi, X. Rottenberg, and R. Baets. *Expanding the silicon photonics portfolio with silicon nitride photonic integrated circuits.* Journal of Lightwave Technology, 35(4):639–649, 2017.

[2] J. P. George. *Integratie van ferro-elektrische dunne lagen op silicium voor toepassing in elektro-optische componenten (Eng.: Integration of ferroelectric thin films on silicon for electro-optic devices).* PhD thesis, Universiteit Gent, 2016.

Summary

Goals and Motivation

Integrated photonic technologies are rapidly coming of age. This is illustrated by the many applications that are being explored in both academia and industry. Examples range from optical interconnects, over various types of medical and industrial sensors, to neuromorphic photonic chips and much more. Different material platforms are being developed for these purposes, all with their own advantages and disadvantages. Particularly promising materials for photonic chips are silicon, and increasingly silicon nitride [1]. The main selling point of silicon- and silicon nitride-based integrated optics is that conventional CMOS-fabrication can be reused. This enables us to recycle very mature fabrication techniques stemming from more than half a century of research and development in the field of electronics. The high index contrast in these platforms makes very compact circuits possible. Especially silicon nitride exhibits low linear and nonlinear losses, a broad transparency window and good thermal stability. There are however some significant downsides. Although modulators and detectors can be made in standard silicon platforms, lasers and amplifiers can't. The situation for silicon nitride with respect to active functionalities is even more dire, since neither light modulation, detection nor generation or amplification is possible.

A promising strategy to solve these issues is the integration of other materials onto silicon or silicon nitride chips. In this work we look specifically into the co-integration with materials which show large optical nonlinearities. Nonlinear optical effects come into play when the polarization density of a material depends nonlinearly on the optical field strength. Typically these effects require very strong optical fields and thus very high optical powers. However with the advent of integrated optics, where the optical mode is confined into a very small cross-section, nonlinear effects can be observed and even used using much lower powers. In second order nonlinear optics the polarization density scales with the square of the electric fields. This can be used to generate new frequencies of light, for example through second harmonic generation, but it can also be used for electro-optic phase modulation, which is referred to as the Pockels effect. Third order nonlinearities, where the polarization density scales with the third power of the field, can also be used to generate light at specific wavelengths, or even to generate extremely broadband light. Neither silicon nor silicon nitride show significant second order nonlinear effects. Third order nonlinearities are typically weak in silicon nitride, and though they are relatively large in silicon, they are not so useful since nonlinear absorption processes limit the optical power that can be used. Several materials are studied in this thesis. We focus on materials which are expected to show high optical nonlinearities and can be integrated in a relatively straightforward and cheap way onto chips fabricated in the CMOS foundry. Graphene, the prime example of a two-dimensional material, is the first to be considered. 2D materials can relatively easily be integrated onto nanophotonic structures, moreover some groups have reported very strong third order nonlinear effects in this material. A second material which is extensively studied is thin film lead zirconate titanate (PZT). PZT is known for a variety of interesting properties, among which a strong second order nonlinear and Pockels response. This material has always been an attractive candidate for second order nonlinear optics. However only recent progress in PZT-deposition made by the Department of Electronics and Information Systems at our university enables the deposition of high-quality optically transparent thin films onto nanophotonic chips [2]. A final material which is studied, is molybdenum disulphide (MoS_2), this material belongs to the class of transition metal dichalcogenides (TMDCs). TMDCs are 2D materials like graphene. They can also be integrated onto nanophotonic structures in a relatively straightforward way. As single layers these materials can show significant second order nonlinear effects.

Results

Graphene can be integrated onto both silicon and silicon nitride photonic chips. On figure 1 such a silicon nitride chip is shown. On the electron microscope image of the cross-section (figure 1**c**), one can see that the waveguide core is in close proximity of the graphene on the chip's surface. The graphene is also contacted using metallic contacts. The graphene on these chips can be electrostatically gated, which means that the Fermi energy can be tuned by applying a voltage. On our silicon chips this is done by applying a gate voltage onto the waveguide core itself. On our silicon nitride chips this is done using a polymer electrolyte. As a first experiment, we demonstrate that the graphene-covered silicon chips can be used as saturable absorbers. This means that when injecting optical pulses the waveguide absorption decreases with increasing pulse power. The saturation power of this process is roughly 1 W. It is also demonstrated that the strength of the absorption saturation can be tuned by changing the gate voltage. On the silicon ni-

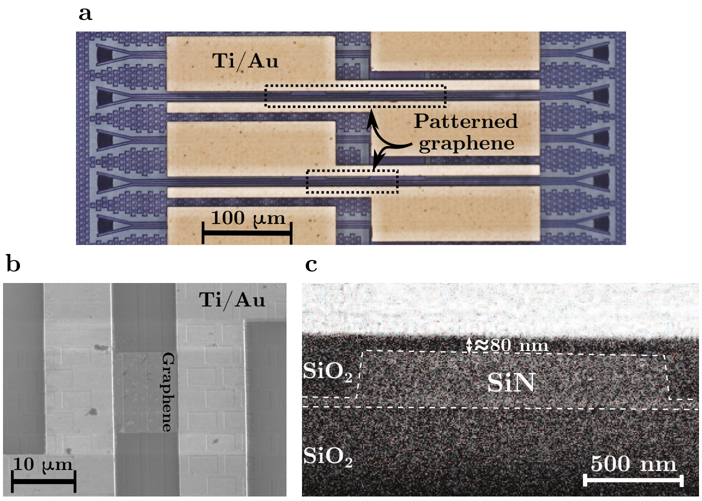

Figure 1: **Graphene-covered silicon nitride waveguides.** **a** Optical microscope image of a set of waveguides. The extent of the graphene (under the contacts) is shown by the dashed lines. **b** Scanning electron microscope image of one of the waveguides, the graphene is clearly visible. **c** Scanning electron microscope image of the cross-section of such a waveguide.

tride waveguides, we perform two other experiments, the results of which are summarized in figure 2. By means of degenerate four-wave mixing we show that the effective waveguide nonlinear parameter $|\gamma|$ and the corresponding third order nonlinear conductivity $|\sigma_s^{(3)}|$ of the graphene are strongly tunable when changing the gate voltage (figure 2**a**). By tuning the signal wavelength, we also show that the four-wave mixing response depends very strongly on the detuning between the signal and the pump (figure 2**b**). By doing a cross-modulation experiment, we can distinguish the nonlinear phase and amplitude response separately. Figures 2**c** and **d** show respectively $\mathrm{Im}(\gamma) \propto \mathrm{Re}(\sigma_s^{(3)})$, which quantifies cross-amplitude modulation, and $\mathrm{Re}(\gamma) \propto \mathrm{Im}(\sigma_s^{(3)})$, quantifying cross-phase modulation, as a function of the applied gate voltage. Again, we see strong variations in the nonlinear parameters. The tunability is even more drastic than when measured through four-wave mixing, including sign changes in both the real and imaginary part of γ. This implies that different regimes can exist, including both positive and negative nonlinear refraction, saturable absorption and its reverse effect. Both the four-wave mixing and cross-modulation experiment can be modeled with acceptable accuracy using a simple model based on carrier heating. This implies that the strong nonlinearity of graphene stems mainly from its carrier dynamics, and not from nonresonant electronic effects which dominate in most low-loss dielectrics.

Second harmonic generation experiments on thin-film PZT show that the

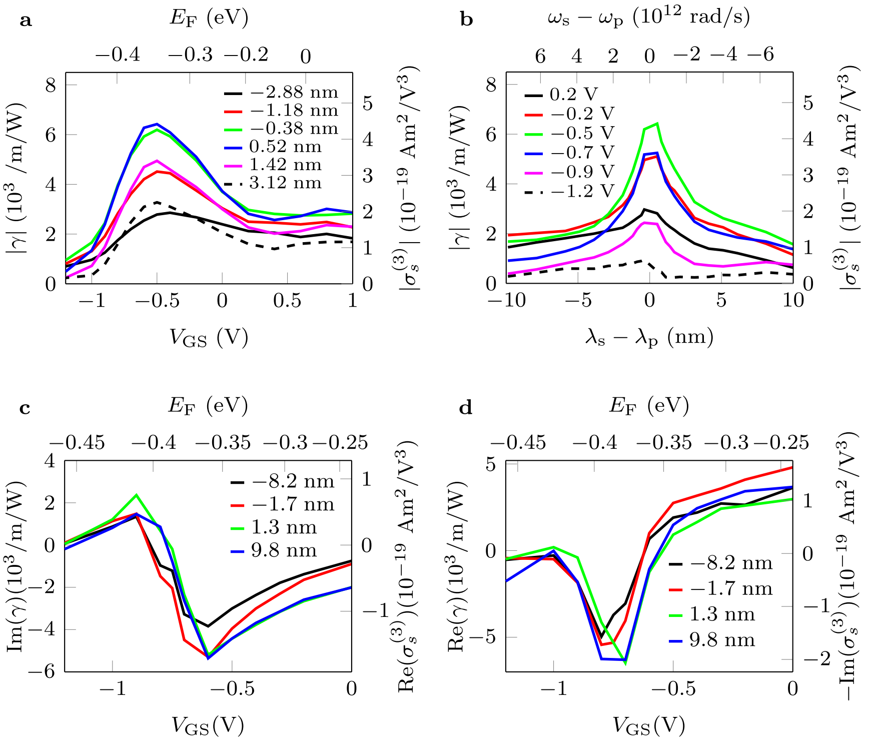

Figure 2: **Measurements of the effective nonlinear parameter of graphene-covered silicon nitride waveguides (γ) and the corresponding third order nonlinear surface conductivity of the graphene ($\sigma_s^{(3)}$).** **a**, **b** γ and $\sigma_s^{(3)}$ characterized by degenerate four-wave mixing (pump wavelength $\lambda_p \approx 1550$ nm), as function of gate voltage and estimated corresponding Fermi energy, for different values of signal-pump detuning $\lambda_s - \lambda_p$ (see legend) (**a**) and as a function of signal-pump detuning, for different gate voltages V_{GS} (see legend) (**b**). **c**, **d** γ and $\sigma_s^{(3)}$ characterized by cross-modulation between a pump at wavelength $\lambda_{pump} \approx 1550$ nm and a tunable probe at wavelength λ_{probe}, see legends for the detuning $\lambda_{probe} - \lambda_{pump}$. **c** Im($\gamma$) and Re($\sigma_s^{(3)}$), which quantify the cross-amplitude modulation, as a function of gate voltage and estimated Fermi energy. **d** Re(γ) and Im($\sigma_s^{(3)}$), which quantify the cross-phase modulation, also as a function of gate voltage.

material can have second order nonlinear susceptibilities of at least $\chi^{(2)} \approx 40$ pm/V for a pump at 1550 nm. We demonstrate that PZT thin-films can be integrated on silicon nitride waveguides, as can be seen in figure 3**a**. The losses of these PZT-covered waveguides depend strongly on the method used to planarize the underlying silicon nitride chip. When this is done by chemical mechanical polishing, losses on the order of 1 dB/cm are observed. In these waveguides also second harmonic generation through modal phase

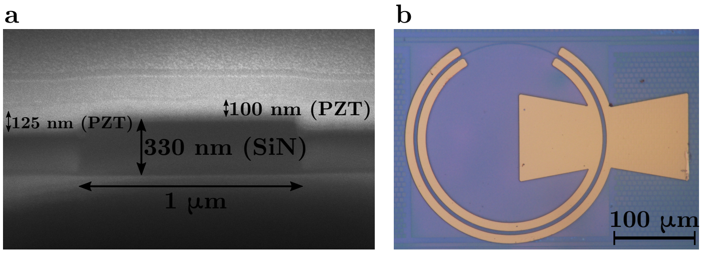

Figure 3: **PZT-on-silicon nitride Pockels modulator.** **a** Scanning electron microscope image of the cross-section of a silicon nitride waveguide covered with a PZT film. **b** Microscope image of one of the ring modulators.

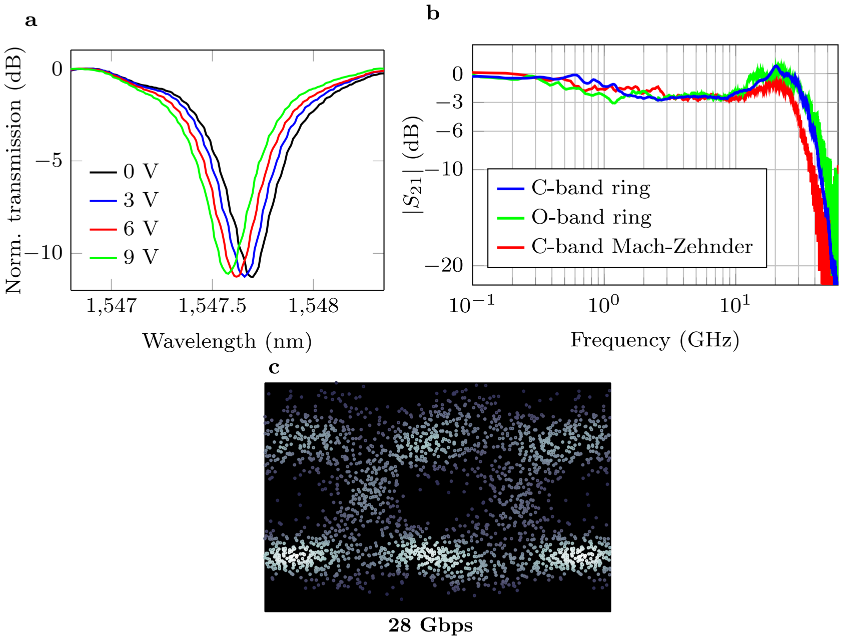

Figure 4: **Some measurement results obtained using the PZT-on-silicon nitride modulators.** **a** Normalized transmission spectra of a C-band ring modulator, for different applied DC voltages. **b** Electro-optic small signal ($|S_{21}|$ parameter) measurement of several modulators. **c** Example of an eye diagram obtained with a C-band ring modulator, using a non-return-to-zero modulation scheme at 28 Gbps.

matching is observed. However of most significance is the ability to use the Pockels effect in PZT for electro-optic phase modulation. By applying a voltage across the waveguide, the effective index of the optical mode can be changed. On figure 3**b** it is shown how this can be used in a ring resonator to make an amplitude modulator. Figure 4**a** shows the transmission spectrum of this ring, for different applied voltages. The shift of the resonance wavelength of these devices can be used for amplitude modulation. Besides this ring modulator for the C-band (1530 - 1565 nm), ring modulators for the O-band (1260 - 1360 nm) and Mach-Zehnder modulators for the C-band were also fabricated. Half-wave voltage-length products as low as 3.2 Vcm are measured. The extrapolated effective Pockels coefficients lie in the range of 60-70 pm/V. These modulators need to be poled using relatively high voltages before use, the stability of the material after poling is tested, and the response remains constant for at least several days at room temperature. The small-signal response in figure 4**b** indicates that these devices can be used for high-speed electro-optic modulation, with bandwidths beyond 33 GHz. Using a non-return-to zero modulation scheme, eye diagrams were also measured, which remained open until about 40 Gbps, an example is plotted in figure 4**c**. Simulations also show that the modulator efficiency can still be improved by optimization of for example the PZT thickness, electrode gap and waveguide width.

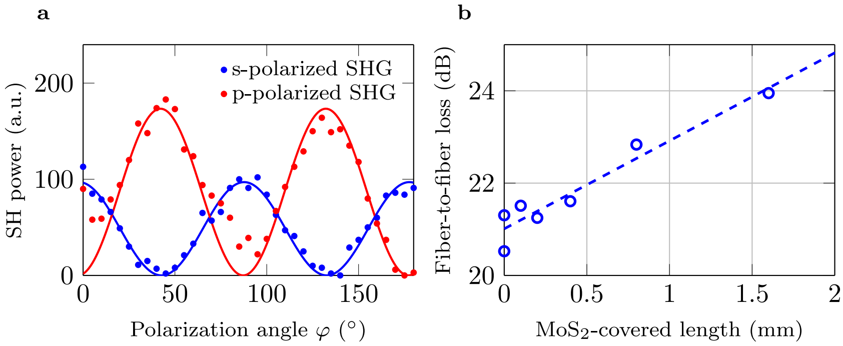

Figure 5: **MoS_2 measurements**. **a** Measured second harmonic power for an MoS_2-covered substrate, for the analyzer selecting either the s- (blue) or p-polarizations (red). The solid lines are the theoretical fits. **b** Loss versus MoS_2-covered length for MoS_2-covered silicon nitride waveguides with a width of 1200 nm, the propagation loss in this measurement is around 20 dB/cm.

Through imec (Leuven, Belgium), we have access to large area single layer MoS_2. Figure 5**a** shows a second harmonic generation measurement obtained with a silica-on-silicon substrate covered with monolayer MoS_2. The fundamental beam with a wavelength of 1550 nm is linearly polarized, and the polarization angle is rotated during the measurement. The blue and red line respectively correspond to the second harmonic power detected with the analyzer set to select either the s- and p- polarized component. From these measurements we extract respectively a surface and bulk second order nonlinear susceptibility of $\chi_s^{(2)} \approx 5 \cdot 10^{-21}$ m^2/V and $\chi_b^{(2)} \approx 8$ pm/V. This material can also be transferred on top of an integrated waveguide and patterned in a desirable shape. This was done using a silicon nitride waveguide similar to the one shown in figure 1. However the measured losses were on the order of 20-25 dB/cm (see figure 5**b**), which is relatively high.

Conclusions and Perspectives

For graphene, this work is a step towards better understanding the material's intricate nonlinear behavior. We show that the nonlinear effects we probe are strongly dependent on the Fermi energy, and that they are mainly caused by changes in the carrier distribution under strong illumination. Gate tunable saturable absorption could be used in integrated modelocked lasers. In the four-wave mixing and cross-modulation experiment, very high nonlinear parameters were measured. However since they are caused by carrier excitation, they inevitably coincide with a large linear absorption, they will probably suffer from saturation at higher optical powers and effects such as four-wave mixing are intrinsically narrowband. These reasons make me less hopeful when it comes to actually using these effects in nonlinear devices. However we have also shown that these effects are readily tunable using a gate voltage, which might be a very strong advantage.

We show that thin-film PZT can be combined with integrated photonics for second harmonic generation and electro-optic modulation. Our demonstration of on-chip second harmonic generation is very preliminary and still needs to be improved, for example by looking into quasi phase-matching by periodic poling. The modulators we fabricated are however the first true high-speed modulators on silicon nitride. The most straightforward next steps are the improvement of the modulator efficiency by optimizing the cross-section and the design of Mach-Zehnder modulators with longer phase shifters. Demonstrations of modulation in other wavelength ranges, and perhaps the use of PZT on other integrated platforms, can also be considered. It should be noted that the second order susceptibility and effective Pockels coefficient that were measured were lower than what can be expected based on bulk values and other thin-film measurements [2]. This might be an indication that the poling of the material was not yet optimal, better poling (for example by raising the temperature) would be a direct way towards more efficient modulation.

The second harmonic response of the MoS_2 is not extremely high. In combination with the high losses of MoS_2-covered waveguides this does not give a very positive outlook. However some future avenues can be explored. First of all, the high loss is not yet understood. Absorption or scattering might be related to the quality of the monolayer which is under constant improvement. If the loss can be reduced then the relatively small nonlinearity can in principle be compensated for. At the time of the measurement, only MoS_2 was available, however more TMDCs, for example WS_2, are available now and could also be tested.

References

[1] A. Rahim, E. Ryckeboer, A. Z. Subramanian, S. Clemmen, B. Kuyken, A. Dhakal, A. Raza, A. Hermans, M. Muneeb, S. Dhoore, Y. Li, U. Dave, P. Bienstman, N. L. Thomas, G. Roelkens, D. V. Thourhout, P. Helin, S. Severi, X. Rottenberg, and R. Baets. *Expanding the silicon photonics portfolio with silicon nitride photonic integrated circuits*. Journal of Lightwave Technology, 35(4):639–649, 2017.

[2] J. P. George. *Integration of ferroelectric thin films on silicon for electro-optic devices*. PhD thesis, Ghent University, 2016.

Chapter 1

Introduction

1.1 Silicon and silicon nitride photonics

Optics is the branch of physics in which *light* is studied. The average high-school curriculum does not go much further than covering lenses, microscopes and telescopes, which have been around since at least the 17th century. As a consequence this topic perhaps has the reputation of being somewhat old-fashioned among the broader public. In the past decades this perception has however become completely unjust. Several key developments have transformed the science of light and its applications into a hugely dynamic field, with increasing importance in modern society. At the basis of this rejuvenation lie the invention of the laser, the introduction of low-loss optical fiber, the development of semiconductor optical devices and recently the advent of integrated optical circuits [1].

To underline the increasing use of semiconductor materials for generating and manipulating light, and the growing link between electronics and optics, the term *photonics* has largely replaced the term *optics* [1]. One of the main evolutions photonics has gone through has been the drastic miniaturization. Making ever smaller components has already drastically transformed the performance and economics of electronic systems. For photonic systems, the same general laws are valid. If you can make the building blocks smaller, production volumes and yields tend to go up, driving prices down. Photonic circuits can also become more complex, with improved functionality. Figure 1.1 illustrates this evolution. Light can be a mixture of different wavelengths, which for visible light correspond to different colors. An important functionality of an optical system could be the ability to separate these different colors. In the days of Isaac Newton, and in your high-school physics class, this was done by using centimeter-scale glass com-

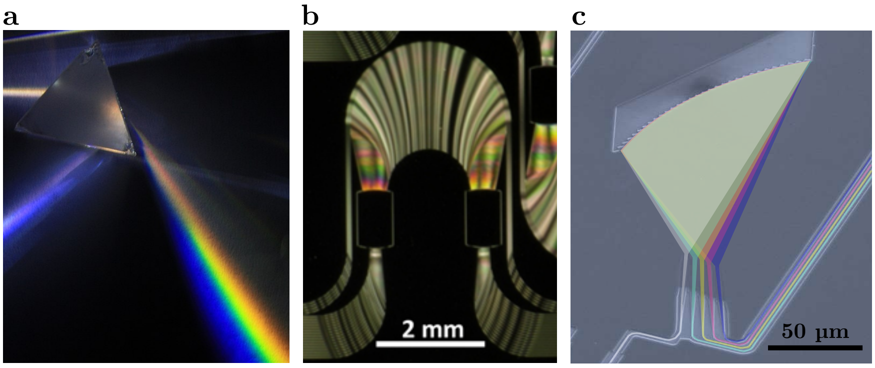

Figure 1.1: Different devices separating light into its different wavelengths. **a** Dispersive prism (image reproduced from Wikipedia). **b** Silica-based integrated optical arrayed waveguide grating (image from reference [2]). **c** Silicon-based planar concave grating, the colors conceptually show how white light can get split into its different components and do not represent actual colors (image from reference [3]).

ponents such as dispersive prisms. This is shown in figure 1.1**a**. However with the advent of novel photonic technologies, such as silica-based photonics (figure 1.1**b**) and silicon photonics (figure 1.1**c**), devices with essentially the same functionality on the order of tens to hundreds of micrometer can be made.

The term "photonic integrated circuit" (PIC) refers to optical systems implemented on a chip, as can be seen in for example figures 1.1**b** and **c**. These chips are fabricated using very similar techniques as the ones used for electronic chips. That photonic chips are here to stay is illustrated by the many applications which are currently being explored, both in academia and industry. On the forefront are the many commercial products for optical interconnects, which have replaced long-distance electrical interconnects, and are increasingly replacing interconnects within datacenters [4]. Silicon photonics-based optical tranceivers for these markets are being developed by both tech giants like Intel [5], and younger companies like Luxtera [6]. In recent years, important progress has been made towards combining photonic interconnects with conventional electronic processors and memory on the same chip, which could be hugely beneficial for operating speeds and power consumption of computing devices [7]. Other applications are currently appearing at a rapid pace. PICs are especially useful for biosensing and medical applications. Companies such as Genalyte are working on silicon photonics-based lab-on-a-chip devices which promise to provide cheaper, faster and better diagnostics [8]. Indigo, a spin-off of our research group, works towards next-generation needle-free glucose monitoring systems, promising to improve the quality of life of numerous diabetes patients [9]. Not only biosensors are being developed, but also sensors for industrial applications, such as the silicon photonics-based solutions for monitoring the structural health of windmills and other large infrastructure which are currently being developed by Sentea [10]. In the wake of extremely fast proliferation of machine learning and neural networking, neuromorphic photonic chips are also in the pipeline. Important steps towards hardware-based neural networks using light are being made [11], which is illustrated by the recent appearance of startups Lightmatter and Lightelligence [12, 13]. Driven by the needs of future self-driving cars, companies like Analog Photonics are developing integrated photonic-based next generation Light Detection and Ranging (LiDAR) sensors [14]. These are only some of the examples of what integrated photonics has in store for us. The list could go on, for example considering recent developments in the use of integrated photonics for quantum information processing [15] or the many potential applications of on-chip optical frequency combs, such as spectroscopy or extremely precise optical clocks [16].

Unlike electronics, where silicon is the predominant material system for making integrated circuits, PICs are still being fabricated in a variety of platforms. Some notable examples are III-V materials such as InP, silicon-on-insulator, silicon nitride, chalcogenide glasses, polymers and recently nanophotonic lithium niobate-based platforms [35]. All of the aforementioned applications have different requirements, but generally an ideal platform provides low-loss waveguides, good passive components such as filters and splitters, optical sources, detectors and some kind of active control like amplitude or phase modulators. Preferably this would be at a low cost, and for a large range of optical wavelengths. Table 1.1 compares some key properties of commonly used material systems. Indium phosphide (InP) is probably the most mature platform, which is illustrated by the long-standing success of companies using this technology like Infinera [36]. A fundamental advantage of III-V semiconductors is that they have a direct bandgap and can be used for light generation in lasers and optical amplifiers. This is for example not possible in silicon. However, silicon photonics has some notable advantages as well, an important one is the much larger index contrast between the waveguide core and cladding. As a consequence silicon-based PICs are significantly more compact. Another advantage is the much larger transparency range, which for example makes mid-IR spectroscopy possible [37]. Although lasers and amplifiers cannot be made within the platform itself, detectors and modulators can [38]. One of the most significant advantages of silicon is the fact that the technology is CMOS-compatible. The

	InP	Silicon	Silicon nitride
Transparency window (µm)	1.3 → 1.7 [17]	1.1 → 4 [18]	0.4 → 4 [18]
Index contrast (%)	<10 [19]	140 [18]	38 [18]
Waveguide loss (dB/cm)	2 → 4 [20]	1 → 1.5 [18]	0.001 → 0.5 [18]
TPA Coefficient (m/W)	$3 \cdot 10^{-10}$ [21]	10^{-11} [22]	0 [23]
Thermo-optic coefficient (K^{-1})	$2 \cdot 10^{-4}$ [24]	$1.8 \cdot 10^{-4}$ [25]	$2.5 \cdot 10^{-5}$ [26]
$\chi^{(2)}$ (pm/V)	286 [27]	✗†	✗†
$\chi^{(3)}$ (m^2/V^2)	$7 \cdot 10^{-18}$ [28]	$2.8 \cdot 10^{-18}$ [29]	$3.4 \cdot 10^{-21}$ [30]
Waveguides and passives	✓	✓	✓
Detectors	✓	✓	✗
Fast modulators	✓	✓	✗
Amplifiers	✓	✗‡	✗
Lasers	✓	✗‡	✗
CMOS-compatible fabrication	✗	✓	✓

Table 1.1: Some key properties and available building blocks on some common nanophotonic platforms. The color code denotes whether the properties are desirable (green), moderately desirable (orange) or less desirable (red) for most applications.
† Since these materials are centrosymmetric, their second order nonlinear coefficients are very small. Recently, several groups have however shown that second order nonlinearities can be induced through control of composition [31], strain [32] or the photogalvanic effect [33]. This is however not considered here.
‡ These devices can be fabricated through heterogeneous integration with III-V materials [34].

PICs can be produced using standard CMOS processes, and decades of research and investment from the field of electronics can be recycled. This has a huge impact on fabrication cost and yield. Silicon nitride is a material which appeared more recently [18] and is also CMOS-compatible. This material is excellent for passive structures, and offers far reduced waveguide losses, still with a reasonably high index contrast. Contrary to InP and Si, high optical powers can be tolerated in the telecom bands (around wavelengths of 1.3 µm and 1.55 µm) due to the absence of two-photon absorption (TPA). The lower thermo-optic coefficient implies much better temperature stability. This however comes at a cost, being an insulator with a very large bandgap, the use of SiN is limited to passives. Neither amplifiers, lasers, modulators nor detectors can be directly fabricated in this platform.

It is now clear that the existing platforms all have specific advantages and disadvantages, and that the choice of the material platform will depend strongly on the envisaged application. A promising strategy is to heterogeneously integrate other materials on silicon or silicon nitride. Co-integration of III-V semiconductors on silicon PICs has been done routinely by our research group, enabling amplifiers and light sources [34]. This thesis follows a similar strategy. However, instead of looking into the co-integration of direct-bandgap materials with silicon or silicon nitride, we look at the integration of several materials which exhibit large optical nonlinearities, namely several two-dimensional crystals and the thin-film ferroelectric material lead zirconate titanate. These phenomena will be discussed in more detail in the next section. They can be used for different types of light generation or amplification, and other more exotic applications such as all-optical signal processing. Second order optical nonlinear materials are also prime candidates for optical phase modulators. We have chosen to work mainly with silicon nitride nanophotonic structures, and occasionally with silicon. As was discussed before silicon nitride is a very good material for integrated photonics, but it has some notorious flaws which in part can be alleviated by the co-integration of highly nonlinear materials. One however has to note that due to the specific deposition processes used in this work, these materials can be readily integrated on other nanophotonic platforms as well.

1.2 Nonlinear optics

Nonlinear optics is typically defined as the study of optical phenomena which are nonlinear in the sense that the material polarization depends nonlinearly on the optical field strength. Such a nonlinear relation can in most cases be expressed using a Taylor expansion [29]:

$$\begin{aligned} P(t) =& P^{(1)}(t) + P^{(2)}(t) + P^{(3)}(t) + \dots \\ =& \varepsilon_0(\chi^{(1)}E(t) + \chi^{(2)}E^2(t) + \chi^{(3)}E^3(t) + \dots), \end{aligned} \tag{1.1}$$

where $E(t)$ is the time-varying electric field and $P(t)$ is the material polarization density. $\chi^{(1)}$ is the linear susceptibility and $\chi^{(2)}$ and $\chi^{(3)}$ are respectively the second and third order nonlinear susceptibilities, ε_0 is the vacuum permittivity. The consequences of having significant nonlinear terms $P^{(2)}$ and/or $P^{(3)}$ can be far-reaching. Let's first consider a material where the nonlinear terms are not present. In that case light, which is a sinusoidal wave of frequency ω (say $E(t) \propto \sin(\omega t)$), will induce a polarization of the same frequency. This in turn will radiate electromagnetic waves at frequency ω. Interference between the incident and emitted waves will merely induce phase changes, which can be quantified by the refractive index of the material. In this case no new frequencies/wavelengths of light are generated. When the nonlinear terms are strong however, the polarization and radiated electric field contain components which scale as $E^2(t) \propto \sin^2(\omega t) = [1 - \cos(2\omega)]/2$ and/or $E^3(t) \propto \sin^3(\omega t) = [3\sin(\omega) - \sin(3\omega)]/4$. Electromagnetic waves of new frequencies, 0, 2ω and/or 3ω, are now generated in the material. When two waves of different frequencies ω_1 and ω_2 are incident, the frequencies can even mix into different combinations of these incident frequencies ($\omega_1+\omega_2$, $\omega_1-\omega_2$, $2\omega_1-\omega_2$...). In other words, nonlinear optics can be used to generate new wavelengths/colors of light.

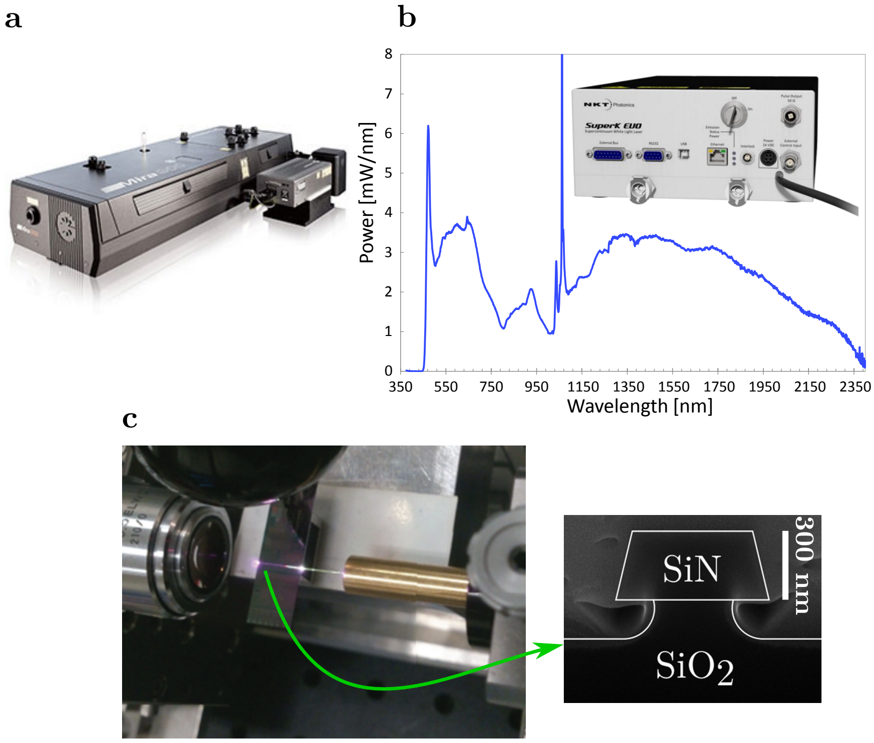

Figure 1.2: **a** Commercially available optical parametric oscillator (Coherent Mira-OPO [39]). **b** Fiber-based supercontinuum source (NKT Photonics SuperK EVO OEM [40]). **c** Example of a supercontinuum generated on an integrated silicon nitride waveguide, the right-hand picture shows a scanning-electron micrograph of the waveguide cross-section (images from reference [41]).

A strong second order nonlinearity, $\chi^{(2)}$, can be used to generate new frequencies through second harmonic generation (SHG, $\omega \rightarrow 2\omega$), sum frequency generation (SFG, $\omega_1, \omega_2 \rightarrow \omega_1+\omega_2$), difference frequency generation (DFG, $\omega_1, \omega_2 \rightarrow \omega_1 - \omega_2$) and optical rectification ($\omega \rightarrow \omega - \omega = 0$) [29].

These phenomena are routinely used to obtain optical gain at specific wavelengths (Optical Parametric Amplification, OPA). This gain can then be used to amplify modes of an optical cavity which is then called an optical parametric oscillator (OPO). OPOs are similar to lasers in that they produce highly monochromatic, coherent and directional beams. Typically these sources have a very large tuning range. OPOs are commercially available, see for example figure 1.2**a**, but they contain sensitive free-space optics and are very expensive, bulky and cumbersome to operate. Spontaneous parametric downconversion (SPDC), which is essentially the reverse process of SFG ($\omega_1 + \omega_2 \rightarrow \omega_1, \omega_2$) is used in the field of quantum optics to make entangled photon pair sources [42]. Finally, when one of the input fields is not optical, but is an externally applied DC (or RF) field E_{DC}, then the induced polarization will contain the following terms $P(t) = \varepsilon_0 \left[(\chi^{(1)} + \chi^{(2)} E_{\mathrm{DC}}) E(t) + \ldots \right]$. The applied field changes the linear susceptibility and hence the refractive index of the material. This phenomenon is called the linear electro-optic or the Pockels effect and is very useful for making optical phase modulators. Unfortunately, as can be seen in table 1.1, $\chi^{(2)}$ is not present in silicon or silicon nitride (although there are exceptions [31–33]). This is because in centrosymmetric materials second order effects are negligible [29].

Third order optical nonlinearities ($\chi^{(3)}$) are however present in all materials. Again these effects can be used to generate new frequencies, for example through third harmonic generation (THG, $\omega \rightarrow 3\omega$). As a matter of fact, any possible addition or subtraction of three incident frequencies can be generated (for example $\omega_1, \omega_2, \omega_3 \rightarrow \omega_1 + \omega_2 - \omega_3$), these processes are typically called four-wave mixing (FWM) and can also be used for amplification, photon pair generation, etc. The optical Kerr effect, where the incident field imposes an intensity-dependent phase change upon itself or on another probe beam (self-phase modulation or cross-phase modulation), is another important effect. The combination of the Kerr effect and cascaded four-wave mixing effects can be used to drastically broaden the spectrum of short optical pulses, and create extremely bright broadband sources called supercontinua, an example of a commercially available supercontinuum source and its spectrum are shown in figure 1.2**b**.

These many applications show that nonlinear optics can be a very powerful tool, however under most circumstances either the electric fields or the nonlinear susceptibilities are too small for them to have any measurable effect. In fact, it was only after the laser was invented that strong enough optical fields were available to observe these effects [43]. The advent of guided-wave optics has also been a game-changer for nonlinear optics. By confining a light beam of a given power into a smaller cross-section, electric field strengths go up drastically. Moreover by having long interaction lengths, the newly generated optical frequencies can add up coherently and become much stronger. This has lead to optical fiber-based broadband sources of the kinds shown in figure 1.2**b**, which were the first actual plug-and-play products based on nonlinear optics (much less cumbersome than for example OPOs). Integrated optical devices consist of waveguides with cross-sections that are more than an order of magnitude smaller than the cores of optical fibers. This extra confinement enhances nonlinear processes even more. This is for example demonstrated in figure 1.2**c**, which shows a supercontinuum generated in an integrated silicon nitride waveguide, bright white light is visible, even after only several millimeters of interaction length. Modulators based on the Pockels effect typically consist of centimeter-long nonlinear crystals. The advent of nanophotonics has recently also enabled the fist demonstrations of strongly miniaturized $\chi^{(2)}$-based optical modulators [44, 45], where the device footprints are on the order of several 100s of micrometer. Other demonstrations of nanophotonic nonlinear devices, for example producing entangled photon pairs or frequency combs, are appearing at a rapid pace.

1.3 Enhancing silicon/silicon nitride photonics with novel nonlinear materials

In the previous sections, we introduced integrated photonics and discussed some of the material platforms which are particularly promising. Silicon nitride (and to a slightly lesser extent silicon) photonics has some clear-cut advantages, mainly stemming from the convenience and cost-effectiveness of CMOS-fabrication, low losses, high-quality passives, small device footprint, etc. However, especially silicon nitride is a notoriously unsuitable platform for active devices for light generation, modulation, detection, etc.

$\chi^{(2)}$ and $\chi^{(3)}$ nonlinear optics can be used to fill some of these voids, as discussed in the previous chapter, these processes can provide a flexible tool for light generation and manipulation. Since both silicon and silicon nitride have negligible $\chi^{(2)}$, and relatively limited $\chi^{(3)}$ [1] we will look into heterogeneous integration with other materials. There are several candidate materials. Utsav D. Dave has studied the co-integration of InGaP onto several platforms [46]. The fabricated waveguides exhibit third order nonlinearities similar to silicon waveguides, in the absence of two photon absorption.

---

[1] Silicon actually has a rather large $\chi^{(3)}$, however two-photon absorption limits the amount of optical power than can be injected in a waveguide, hampering the overall effect.

Moreover the material also has a relatively strong $\chi^{(2)}$-coefficient. However the fabrication is based on bonding and is relatively cumbersome and expensive. Lithium niobate, a material typically used for bulk modulators, can also be integrated, for example for on-chip second harmonic generation [47] or electro-optic modulation [48]. However in these examples, the waveguides are patterned in SiN layers deposited on top of a lithium niobate layer, and not using standard CMOS-processes. Using organic materials, some promising modulator designs have been made on silicon [49], although questions can be asked about the long-term stability of these materials.

Integration of all the aforementioned materials onto silicon or silicon nitride photonic chips is still in its infancy. It is certainly worth the effort to be on the lookout for new materials which have high optical nonlinearities, and perhaps are easier/cheaper to integrate. In this thesis, we investigate several of such materials. First of all there is the class of 2D materials, of which graphene is the most famous exponent. Our research was triggered by some early reports [50, 51] suggesting that the $\chi^{(3)}$ of graphene is extremely high. Besides that, research around graphene is booming, and relatively cheap high-quality large-area graphene is already commercially available. Graphene is also considered to be one of the candidates for post-Si electronics [52], so it is expected to be available in standard fabrication facilities at some point. 2D materials in general also have the advantage that they are naturally passivated, with no dangling bonds. This facilitates integration with all kinds of integrated platforms. Another class of 2D materials, the transition metal dichalcogenides (TMDCs), is also considered. The motivation for this is largely the same as for graphene: the ease of integration and the large interest in these materials as a whole. Unlike graphene, TMDCs have a nonzero second order nonlinearitiy $\chi^{(2)}$. At the time of the start of this PhD project, several groups had done preliminary studies of these effects, some of which again published extraordinary high values of the material nonlinearity [53]. At the beginning of this project we were for a big part driven by curiosity, wondering whether the hopeful numbers that had been published would turn into something practically useful, or whether it all would turn out to be a bit more complicated (let's leave this question open for now). Apart from 2D materials, we also studied integration of thin film lead zirconate titanate (PZT) onto our chips. This was of course driven by the fact that this is a ferroelectric material known to exhibit strong second order nonlinear effects. Moreover, we have the ability to deposit this material onto our chips, thanks to the research performed by John P. George [54], with who we closely collaborated. The deposition method is unique in the sense that high-quality and optically transparent thin films can be deposited onto any sufficiently planar surface, including silicon or silicon nitride chips fabricated in a CMOS-fab.

1.4 Overview of the work presented in this thesis

The thesis is structured so that different materials are covered in different chapters. Graphene, which was most extensively studied, comes first. Chapter 2 first introduces this unique material, and then goes on discussing the state of the art of graphene photonics and nonlinear optics, important concepts for understanding nonlinear optics in graphene and graphene-covered waveguides are introduced. Chapter 3 goes on discussing our experimental work on graphene-covered waveguides. Most notable are a study of grate-tunable saturable absorption and tunable four-wave mixing and cross-modulation in graphene-covered waveguides. PZT comes next, in Chapter 4 we explore both the necessary theory, the second harmonic generation experiments performed both on thin films on a blank substrate and in PZT-covered waveguides, and the fabrication and optimization of high-speed phase and amplitude modulators. From the class of the TMDCs, we studied the material molybdenum disulphide (MoS_2). We chose to cover this material last because it has properties in common with both graphene (it is also a 2D crystal) and PZT (it has a large second order optical nonlinearity). In chapter 5, we introduce this material and discuss the existing literature on second order nonlinear optics using TMDCs. After this we discuss a second harmonic generation experiment on the MoS_2-samples available to us through our collaborators at imec, Leuven. Finally a preliminary loss measurement of MoS_2-covered silicon nitride waveguides is presented. In Chapter 6 some general conclusions and future prospects are given.

1.5 Publications and awards

1.5.1 Publications in international journals

Koen Alexander, Nadja A. Savostianova, Sergey A. Mikhailov, Dries Van Thourhout and Bart Kuyken. *Gate-tunable nonlinear refraction and absorption in graphene-covered silicon nitride waveguides.* ACS Photonics, Article ASAP, Published online on November 12, 2018.
`https://pubs.acs.org/doi/10.1021/acsphotonics.8b01132`

Koen Alexander, John P. George, Jochem Verbist, Kristiaan Neyts, Bart Kuyken, Dries Van Thourhout and Jeroen Beeckman. *Nanophotonic Pockels modulators on a silicon nitride platform.* Nature Communications, vol.

9, no. 1, pp. 3444, 2018.
`www.nature.com/articles/s41467-018-05846-6`

Koen Alexander, Nadja A. Savostianova, Sergey A. Mikhailov, Bart Kuyken and Dries Van Thourhout. *Electrically tunable optical nonlinearities in graphene-covered SiN waveguides characterized by four-wave mixing.* ACS Photonics, vol. 4, no. 12, pp. 3039-3044, 2017.
`https://pubs.acs.org/doi/10.1021/acsphotonics.7b00559`

1.5.2 Publications in national and international conferences

John P. George, **Koen Alexander**, Bart Kuyken, Dries Van Thourhout and Jeroen Beeckman. *Advances in PZT-on-SiN electro-optic modulator platform.* Advanced Photonics 2018 (Integrated Photonics Research, Silicon and Nanophotonics), Switzerland, 2018.
`www.osapublishing.org/abstract.cfm?uri=IPRSN-2018-ITh3B.2`

Utsav D. Dave, Nicolas Poulvellarie, **Koen Alexander**, Simon-Pierre Gorza, Fabrice Raineri, Sylvain Combrié, Alfredo De Rossi, Günther Roelkens, Bart Kuyken, and François Leo. *Second Harmonic Generation by Mixing Longitudinal and Transverse Electric Field Components in Indium Gallium Phosphide-on-insulator Wire Waveguides.* Advanced Photonics 2018 (Nonlinear Photonics), Switzerland, 2018.
`www.osapublishing.org/abstract.cfm?uri=NP-2018-NpTh1C.2`

Koen Alexander, Bart Kuyken, and Dries Van Thourhout. *Electrically Tunable Nonlinear Refraction and Absorption in Graphene-covered SiN Waveguides.* Conference on Lasers and Electro-Optics (CLEO), United States, 2018.
`www.osapublishing.org/abstract.cfm?uri=CLEO_QELS-2018-FF2E.3`

Koen Alexander, John P. George, Bart Kuyken, Jeroen Beeckman and Dries Van Thourhout. *Broadband electro-optic modulation using low-loss PZT-on-silicon nitride integrated waveguides.* Conference on Lasers and Electro-Optics (CLEO), United States, 2017. **(Post-deadline)**
`www.osapublishing.org/abstract.cfm?uri=CLEO_AT-2017-JTh5C.7`

Koen Alexander, Muhammad Mohsin, Utsav D. Dave, Stéphane Clemmen, Daniel Neumaier, Bart Kuyken and Dries Van Thourhout. *Electrically Tunable Optical Nonlinearity of Graphene-Covered SiN Waveguides.* Con-

ference on Lasers and Electro-Optics (CLEO), United States, 2017.
`www.osapublishing.org/abstract.cfm?uri=CLEO_QELS-2017-FM2F.3`

Dries Van Thourhout, Marianna Pantouvaki, Herbert D'heer, **Koen Alexander**, Bart Kuyken, Inge Asselberghs, Steven Brems, Cédric Huyghebaert, Leili Abdollahi Shiramin, Chiara Alessandri, John P. George, Jeroen Beeckman, Min-Hsiang Hsu, Clement Merckling and Joris Van Campenhout. *New materials for modulators and switches in silicon photonics.* Silicon Photonics XII, United States, 2017.
`spie.org/Publications/Proceedings/Paper/10.1117/12.2253679`

Dries Van Thourhout, Leili Abdollahi Shiramin, Chiara Alessandri, **Koen Alexander**, Bart Kuyken, Marianna Pantouvaki, Inge Asselberghs, Steven Brems, Joris Van Campenhout and Cédric Huygebaert. *Hybrid Graphene-Silicon Photonics Devices for Telecom and Datacom.* Graphene2017, Spain, 2017.
`www.photonics.intec.ugent.be/download/pub_3967.pdf`

Koen Alexander, Bart Kuyken and Dries Van Thourhout. *Characterization of graphene-covered SiN waveguide using four-wave mixing.* Annual Symposium of the IEEE Photonics Benelux Chapter, IEEE Photonics Society, Belgium, 2016.
`www.photonics.intec.ugent.be/download/pub_3903.pdf`

Dries Van Thourhout, Yingtao Hu, Marianna Pantouvaki, **Koen Alexander**, Bart Kuyken, Steven Brems, Inge Asselberghs, Cédric Huyghebaert, Chiara Alessandri, Philippe Absil and Joris Van Campenhout. *Hybrid graphene-silicon photonics devices.* European Conference on Optical Communication (ECOC), Spain, 2015.
`https://ieeexplore.ieee.org/document/7341887/`

Koen Alexander, Yingtao Hu, Marianna Pantouvaki, Steven Brems, Inge Asselberghs, Simon-Pierre Gorza, Cedric Huyghebaert, Joris Van Campenhout, Bart Kuyken and Dries Van Thourhout. *Electrically controllable saturable absorption in hybrid graphene-silicon waveguides.* Conference on Lasers and Electro-Optics (CLEO), United States, 2015.
`www.osapublishing.org/abstract.cfm?uri=CLEO_SI-2015-STh4H.7`

1.5.3 Awards

Incubic/Milton Chang Travel Grant at the Conference on Lasers and Electro-Optics 2018 for the paper *Electrically Tunable Nonlinear Refraction*

and Absorption in Graphene-covered SiN Waveguides.
`www.osa.org/en-us/foundation/programs/incubic/`

References

[1] B. E. Saleh and M. C. Teich. *Fundamentals of photonics*, 1991.

[2] K. Yamada, T. Tsuchizawa, H. Nishi, R. Kou, T. Hiraki, K. Takeda, H. Fukuda, Y. Ishikawa, K. Wada, and T. Yamamoto. *High-performance silicon photonics technology for telecommunications applications.* Science and Technology of Advanced Materials, 15(2):024603, 2014.

[3] R. Baets, A. Z. Subramanian, S. Clemmen, B. Kuyken, P. Bienstman, N. Le Thomas, G. Roelkens, D. Van Thourhout, P. Helin, and S. Severi. *Silicon Photonics: silicon nitride versus silicon-on-insulator.* In Optical Fiber Communication Conference, pages Th3J–1. Optical Society of America, 2016.

[4] A. F. Benner, M. Ignatowski, J. A. Kash, D. M. Kuchta, and M. B. Ritter. *Exploitation of optical interconnects in future server architectures.* IBM Journal of Research and Development, 49(4.5):755–775, 2005.

[5] *https://www.intel.com/content/www/us/en/architecture-and-technology/silicon-photonics/silicon-photonics-overview.html*.

[6] *http://www.luxtera.com/silicon-photonics-technology/*.

[7] C. Sun, M. T. Wade, Y. Lee, J. S. Orcutt, L. Alloatti, M. S. Georgas, A. S. Waterman, J. M. Shainline, R. R. Avizienis, S. Lin, B. R. Moss, R. Kumar, F. Pavanello, A. H. Atabaki, H. M. Cook, A. J. Ou, J. C. Leu, Y.-H. Chen, K. Asanovic, R. J. Ram, M. A. Popovic, and V. M. Stojanovic. *Single-chip microprocessor that communicates directly using light.* Nature, 528:534–538, 2015.

[8] *https://www.genalyte.com/*.

[9] *https://indigomed.com/*.

[10] *http://www.senteatech.com/*.

[11] Y. Shen, N. C. Harris, S. Skirlo, M. Prabhu, T. Baehr-Jones, M. Hochberg, X. Sun, S. Zhao, H. Larochelle, D. Englund, and M. Soljacic. *Deep learning with coherent nanophotonic circuits.* Nature Photonics, 11(7):441–446, 2017.

[12] *https://www.lightmatter.ai/*.

[13] *https://www.lightelligence.ai/*.

[14] `http://www.analogphotonics.com/products/`.

[15] X. Qiang, X. Zhou, J. Wang, C. M. Wilkes, T. Loke, S. O'Gara, L. Kling, G. D. Marshall, R. Santagati, T. C. Ralph, J. B. Wang, J. L. O'Brien, M. G. Thompson, and J. C. F. Matthews. *Large-scale silicon quantum photonics implementing arbitrary two-qubit processing.* Nature Photonics, 12(9):534–539, 2018.

[16] N. R. Newbury. *Searching for applications with a fine-tooth comb.* Nature Photonics, 5(4):186–188, 2011.

[17] `http://www.jeppix.eu/technology/`.

[18] A. Rahim, E. Ryckeboer, A. Z. Subramanian, S. Clemmen, B. Kuyken, A. Dhakal, A. Raza, A. Hermans, M. Muneeb, S. Dhoore, Y. Li, U. Dave, P. Bienstman, N. L. Thomas, G. Roelkens, D. V. Thourhout, P. Helin, S. Severi, X. Rottenberg, and R. Baets. *Expanding the silicon photonics portfolio with silicon nitride photonic integrated circuits.* Journal of Lightwave Technology, 35(4):639–649, 2017.

[19] C. R. Doerr. *Integrated photonic platforms for telecommunications: InP and Si.* In IEICE Transactions on Electronics, volume 96, 2013.

[20] M. Smit, X. Leijtens, H. Ambrosius, E. Bente, J. Van der Tol, B. Smalbrugge, T. De Vries, E.-J. Geluk, J. Bolk, R. Van Veldhoven, and L. Augustin. *An introduction to InP-based generic integration technology.* Semiconductor Science and Technology, 29(8):083001, 2014.

[21] D. Vignaud, J. Lampin, and F. Mollot. *Two-photon absorption in InP substrates in the 1.55 μ m range.* Applied Physics Letters, 85(2):239–241, 2004.

[22] A. D. Bristow, N. Rotenberg, and H. M. Van Driel. *Two-photon absorption and Kerr coefficients of silicon for 850–2200 nm.* Applied Physics Letters, 90(19):191104, 2007.

[23] D. J. Moss, R. Morandotti, A. L. Gaeta, and M. Lipson. *New CMOS-compatible platforms based on silicon nitride and Hydex for nonlinear optics.* Nature Photonics, 7(8):597–607, 2013.

[24] F. G. Della Corte, G. Cocorullo, M. Iodice, and I. Rendina. *Temperature dependence of the thermo-optic coefficient of InP, GaAs, and SiC from room temperature to 600 K at the wavelength of 1.5 μm.* Applied Physics Letters, 77(11):1614–1616, 2000.

[25] J. Komma, C. Schwarz, G. Hofmann, D. Heinert, and R. Nawrodt. *Thermo-optic coefficient of silicon at 1550 nm and cryogenic temperatures.* Applied Physics Letters, 101(4):041905, 2012.

[26] A. W. Elshaari, I. E. Zadeh, K. D. Jöns, and V. Zwiller. *Thermo-optic characterization of silicon nitride resonators for cryogenic photonic circuits.* IEEE Photonics Journal, 8(3):1–9, 2016.

[27] M. J. Weber. *Handbook of optical materials.* CRC press, 2002.

[28] J.-K. Seo and T. Mizumoto. *Measurement of nonlinear index changes in an InGaAsP/InP waveguide using an optical loop mirror interferometer.* In Conference on Lasers and Electro-Optics, page CThJ5. Optical Society of America, 2004.

[29] R. W. Boyd. *Nonlinear Optics.* Academic Press, 2003.

[30] K. Ikeda, R. E. Saperstein, N. Alic, and Y. Fainman. *Thermal and Kerr nonlinear properties of plasma-deposited silicon nitride/silicon dioxide waveguides.* Optics Express, 16(17):12987–12994, 2008.

[31] K. Koskinen, R. Czaplicki, A. Slablab, T. Ning, A. Hermans, B. Kuyken, V. Mittal, G. Murugan, T. Niemi, R. Baets, and M. Kauranen. *Enhancement of bulk second-harmonic generation from silicon nitride films by material composition.* Optics Letters, 42(23):5030–5033, 2017.

[32] M. Cazzanelli, F. Bianco, E. Borga, G. Pucker, M. Ghulinyan, E. Degoli, E. Luppi, V. Véniard, S. Ossicini, D. Modotto, and S. Wabnitz. *Second-harmonic generation in silicon waveguides strained by silicon nitride.* Nature Materials, 11(2):148–154, 2012.

[33] A. Billat, D. Grassani, M. H. Pfeiffer, S. Kharitonov, T. J. Kippenberg, and C.-S. Brès. *Large second harmonic generation enhancement in Si_3N_4 waveguides by all-optically induced quasi-phase-matching.* Nature Communications, 8(1):1016, 2017.

[34] Z. Wang, A. Abbasi, U. Dave, A. Groote, S. Kumari, B. Kunert, C. Merckling, M. Pantouvaki, Y. Shi, B. Tian, K. Gasse, J. Verbist, R. Wang, W. Xie, J. Zhang, Y. Zhu, J. Bauwelinck, X. Yin, Z. Hens, J. Campenhout, B. Kuyken, R. Baets, G. Morthier, D. Thourhout, and G. Roelkens. *Novel light source integration approaches for silicon photonics.* Laser & Photonics Reviews, 11(4):1700063, 2017.

[35] M. Zhang, C. Wang, R. Cheng, A. Shams-Ansari, and M. Lončar. *Monolithic ultra-high-Q lithium niobate microring resonator.* Optica, 4(12):1536–1537, 2017.

[36] *https://www.infinera.com/.*

[37] A. Vasiliev, A. Malik, M. Muneeb, B. Kuyken, R. Baets, and G. Roelkens. *On-chip mid-infrared photothermal spectroscopy using suspended silicon-on-insulator microring resonators.* ACS Sensors, 1(11):1301–1307, 2016.

[38] *https://www.imec-int.com/en/silicon-photonic-ICs-prototyping.*

[39] *http://lasers.coherent.com/lasers/optical-parametric-oscillator.*

[40] *https://www.nktphotonics.com/lasers-fibers/product/superk-evo-oem-supercontinuum-laser/.*

[41] H. Zhao. *Coherent Raman Spectroscopy Enabled by Photonic Integrated Circuits.* PhD thesis, Ghent University, 2017.

[42] M. Bock, A. Lenhard, C. Chunnilall, and C. Becher. *Highly efficient heralded single-photon source for telecom wavelengths based on a PPLN waveguide.* Optics Express, 24(21):23992–24001, 2016.

[43] e. P. Franken, A. E. Hill, C. e. Peters, and G. Weinreich. *Generation of optical harmonics.* Physical Review Letters, 7(4):118, 1961.

[44] C. Xiong, W. H. Pernice, J. H. Ngai, J. W. Reiner, D. Kumah, F. J. Walker, C. H. Ahn, and H. X. Tang. *Active silicon integrated nanophotonics: ferroelectric $BaTiO_3$-devices.* Nano Letters, 14(3):1419–1425, 2014.

[45] C. Wang, M. Zhang, B. Stern, M. Lipson, and M. Lončar. *Nanophotonic lithium niobate electro-optic modulators.* Optics Express, 26(2):1547–1555, 2018.

[46] U. D. Dave. *Nonlinear optics in a-Si: H-on-insulator and InGaP-on-insulator waveguide circuits.* PhD thesis, Ghent University, 2017.

[47] L. Chang, Y. Li, N. Volet, L. Wang, J. Peters, and J. E. Bowers. *Thin film wavelength converters for photonic integrated circuits.* Optica, 3(5):531–535, 2016.

[48] A. Rao, A. Patil, P. Rabiei, A. Honardoost, R. DeSalvo, A. Paolella, and S. Fathpour. *High-performance and linear thin-film lithium niobate Mach–Zehnder modulators on silicon up to 50 GHz.* Optics Letters, 41(24):5700–5703, 2016.

[49] S. Koeber, R. Palmer, M. Lauermann, W. Heni, D. L. Elder, D. Korn, M. Woessner, L. Alloatti, S. Koenig, P. C. Schindler, H. Yu, W. Bogaerts, L. R. Dalton, W. Fruede, J. Leuthold, and C. Koos. *Femtojoule electro-optic modulation using a silicon–organic hybrid device.* Light: Science & Applications, 4(2):e255, 2015.

[50] E. Hendry, P. J. Hale, J. Moger, A. K. Savchenko, and S. A. Mikhailov. *Coherent nonlinear optical response of graphene.* Physical Review Letters, 105(9):097401, 2010.

[51] H. Zhang, S. Virally, Q. Bao, L. K. Ping, S. Massar, N. Godbout, and P. Kockaert. *Z-scan measurement of the nonlinear refractive index of graphene.* Optics Letters, 37(11):1856–1858, 2012.

[52] *http://www.itrs2.net/*.

[53] N. Kumar, S. Najmaei, Q. Cui, F. Ceballos, P. M. Ajayan, J. Lou, and H. Zhao. *Second harmonic microscopy of monolayer MoS_2.* Physical Review B, 87(16):161403, 2013.

[54] J. P. George. *Integration of ferroelectric thin films on silicon for electro-optic devices.* PhD thesis, Ghent University, 2016.

Chapter 2

Graphene as a material for nonlinear optics

The material presented in this chapter has in part been published in references [1, 2].

2.1 Introduction

Based on several promising experimental and theoretical results, graphene has been described as a material with great potential for nonlinear optics. To underline the strength of the third order optical nonlinearity in graphene, authors of some of the pioneering experimental studies have not shied away from using terms like "very strong" [3], "remarkably huge" [4] or "giant" [5]. An often discussed advantage of graphene is the potential tunability of the optical properties through electrostatic gating [6–8]. At the onset of this PhD project however, not much more was known than the rather vague description given here. Measured values of nonlinear parameters were orders of magnitude apart, and the assumed tunability had not yet been demonstrated experimentally. Within this PhD project, we have combined graphene with silicon and silicon nitride photonic structures, to characterize its nonlinearity through different experiments. The experimental results will be discussed in-depth in Chapter 3. In this chapter, the context is sketched, some important literature is reviewed and necessary theoretical concepts are introduced.

To start, in Section 2.2, a brief introduction to graphene and its short history is given. In Section 2.3, we describe how graphene has been used so far in the field of photonics. Section 2.4 introduces graphene nonlinear optics, including an overview of the different units that are used and with a strong focus on some issues with the existing experimental demonstrations. In Section 2.5, the theory describing third-order nonlinear optics in graphene-covered waveguides is developed. This section provides important tools for the interpretation of the experiments in Sections 3.4 and 3.5.

2.2 A brief introduction to graphene

For almost 70 years, it was assumed that purely two-dimensional (2D) crystals could simply not exist, that they would be thermodynamically unstable and would disintegrate at even the lowest temperatures [9–11]. As a consequence, interest in graphene and other 2D crystals was for many years purely academical, as a model system for theoretical physicist [11]. In 2004 however, this assumption was fundamentally challenged, when Konstantin S. Novoselov, Andre K. Geim and their collaborators published the first experimental findings on single layer graphene [12, 13]. They had isolated single crystals using a technique called micromechanical cleaving or the 'scotch-tape method', since it involves repeated peeling from bulk graphite using adhesive tape [12, 13]. Soon it was recognized that graphene, and the many other 2D materials that since have followed, showed many extraordinary properties and novel physics. This has lead to a surge in research interest from researchers from a variety of different backgrounds, and eventually the contributions of Novoselov and Geim were recognized with the 2010 Nobel Prize in Physics [14].

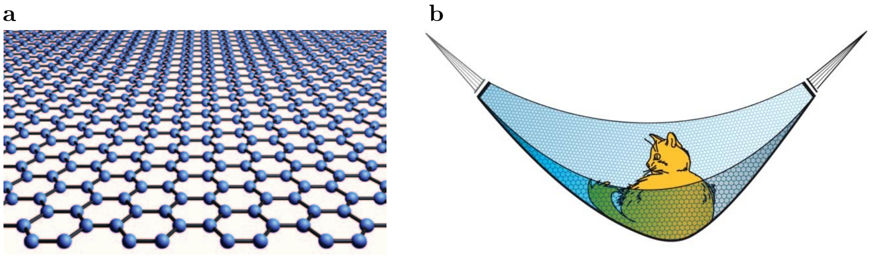

Figure 2.1: **a** Crystal structure of graphene, consisting of a hexagonal lattice of carbon atoms (image reproduced reference [15]). **b** A hypothetical graphene hammock (image from reference [14]).

Figure 2.1**a** shows an artist's impression of a graphene sheet. It consists of a single layer of sp^2 hybridized carbon atoms in a hexagonal crystal lattice. The combination of this crystal structure with the exceptional strength of the carbon-carbon bonds [15], gives rise to extraordinary mechanical properties. Graphene is extremely strong (with a breaking strength over 100 times higher than that of steel), though remarkably stretchable and flexible [14, 16]. This was intuitively illustrated by the Royal Swedish Academy of Sciences when awarding the 2010 Nobel Prize with the analogy shown in figure 2.1**b**: if one was to make a hypothetical 1 m^2-large hammock of single crystalline graphene (which is not possible at the time of writing), then this hammock would be able to support a full-grown cat, whilst weighing less than one of its whiskers [14]. As is discussed below, the hammock would furthermore be colorless and (almost) invisible. Graphene is being heavily researched for the use in composite materials, where it can not only strongly improve the mechanical properties, but also can contribute to the gas barrier properties, electrical and thermal conductivity, and more [16].

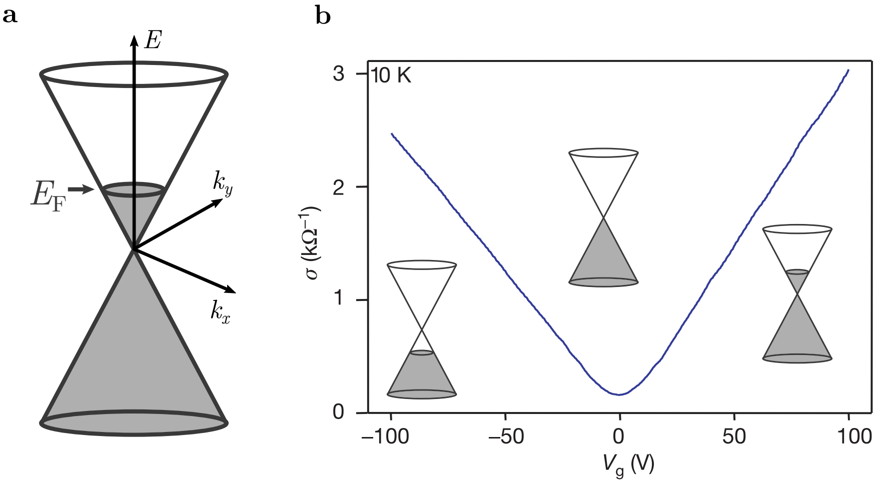

Figure 2.2: **a** Sketch of the band structure of graphene. E_F is the Fermi energy. **b** Demonstration of the electric field effect in graphene, sheet conductivity σ versus gate voltage V_g (image adapted from reference [13]).

The electrical properties of graphene are equally remarkable. Graphene is a zero-overlap semimetal, with valence and conductance bands touching at the K- and K'-points in the Brillouin zone [15], also known as the Dirac points. At low energies (< 1 eV), the bands are almost perfectly conical [17], following the dispersion relation $E = \hbar v_F |k|$, with $v_F \approx 10^6$ m/s the Fermi velocity [11]. The conical part of the band structure of graphene is sketched in figure 2.2**a**. One of the first notable electrical properties of graphene that was studied was its strong electric field effect: using a gate electrode, the charge carrier density, and correspondingly the conductivity in graphene can be strongly tuned [11, 12]. An early demonstration of this is shown in figure 2.2**b**. Graphene is characterized by a very high carrier mobility μ, which moreover remains high at elevated carrier concentrations [11]. Carrier mobilities at room temperature exceeding $\mu = 10^5$ cm^{2}V^{-1}s^{-1} and ballistic transport over several micrometers have been demonstrated [18].

Graphene has attracted interest for many electronic applications, the International Technology Roadmap for Semiconductors (ITRS) considers it as one of the candidates for post-Si electronics [19]. On the long run, graphene is expected to enable novel RF and logic transistors [16]. However, the zero bandgap of graphene causes a non-zero off state drain current, currently severely limiting the on-off ratio of graphene transistors [16]. Methods to artificially open a band gap in graphene, such as the use of bilayers, nanoribbons or chemical modification, are actively being researched, and functional device prototypes using graphene transistors are only projected to appear in the next decade [16]. On a shorter term, graphene is an ideal candidate as a conductive film in flexible electronics, for example for touch screens, rollable e-paper, foldable OLEDs, flexible sensors and more [16, 20].

Expectations for graphene are high in many other fields, such as energy generation and storage, sensing and metrology, bioapplications (for example for drug delivery) and photonics [21].

2.3 Graphene photonics

The importance of the optical properties of graphene could hardly be underestimated. This was already illustrated by the very first experimental isolation of monolayer graphene [11, 12]. The ‘scotch tape method’, where a piece of graphite is repeatedly peeled with adhesive tape until monolayers of graphene are found, had been used before [22]. However single or few layer graphene flakes had not been discovered. Even though single layers were almost certainly present, finding them is like finding a needle in a haystack. This was not even feasible using advanced methods such as atomic force microscopy (AFM) or scanning electron microscopy (SEM). The key to discovering the first monolayer flakes was the simple observation that these become visible in an optical microscope on top of a Si wafer with with a very specific thickness of SiO_2, due to interference effects [11, 12]. If it wasn’t for this method, graphene would have probably remained undiscovered. In a sense simple optics was key in enabling graphene science as a whole.

Likewise, graphene is starting to play an enabling role in optics and photonics. This material shows very strong light-matter interaction and has an almost perfectly wavelength-independent absorption spectrum (≈ 2.3 % for normal incidence) for wavelengths ranging from ≈ 500 nm to the mid-infrared (the upper wavelength limit depends on the doping level) [17, 23]. Photodetectors using graphene have been demonstrated [24, 25]. The broadband nature is for example illustrated by recent work from Goossens *et al.*, who demonstrated a graphene-CMOS image sensor array covering the 300-2000 nm wavelength range [26]. Moreover, the high carrier mobility allows for ultra-fast carrier extraction, in principle making photodetectors with bandwidths exceeding 500 GHz possible [27]. Graphene photodetectors rely on different physical mechanisms, such as the photovoltaic effect, the photo-thermoelectric effect or the bolometric effect, for a comprehensive review see reference [28]. Closely related to photodetectors are optical modulators. A major asset of graphene is that its Fermi energy can be changed to a large extent by electrostatic gating, this gives rise to strong tunability of its electromagnetic properties, for example causing its strong electric field effect [12]. Similarly, both absorption and refraction at optical frequencies can be tuned drastically. This enabled the demonstration of integrated electro-absorption modulators on silicon [29–31] and silicon nitride waveguides [32]. More recently, Sorianello *et al.* demonstrated that graphene can also be used to make highly efficient integrated phase modulators [33, 34]. In a somewhat different context, Yao *et al.* have shown that gated graphene can be used to control the properties of a frequency comb by tuning the chromatic dispersion of the ring resonator in which it is generated [35]. Graphene can furthermore support plasmons. This seems especially promising for applications in the terahertz and mid-infrared wavelength range, such as imaging, sensing, or even active metamaterial development [36]. Again tunability of the plasmon resonance through gating or doping is a crucial advantage of graphene [36].

Finally, graphene is a very strong saturable absorber, a phenomenon that can be used to make ultrafast modelocked lasers [37, 38]. When light gets absorbed by graphene, electrons get excited from the valence to the conductance band, between the energy levels at $-\hbar\omega/2$ and $\hbar\omega/2$ (with ω the photon frequency). After this they will relax, due to carrier-carrier intraband collisions and phonon emission, into a hot Fermi-Dirac distribution (on a timescale of about 100 fs [38]). On a timescale of picoseconds, they further relax due to interband relaxation and cooling of hot phonons [38]. At high illumination intensities, the band-filling becomes large enough to induce a significant decrease in the absorption of the material (no two electrons can occupy the same state), this phenomenon is called Pauli blocking. In graphene, saturable absorption in the near-infrared wavelength range occurs at relatively low powers. As a consequence of the combination of a linear dispersion relation and the vanishing density of states at the Dirac point, optical fields can produce particularly large changes in the charge carrier distributions and the corresponding absorption [39]. It is moreover a fast process due to the small relaxation times involved, and it is intrinsically broadband. Initial demonstrations were modelocked fiber lasers with wavelengths around 1560 nm [37, 38]. However other laser types at other wavelengths soon followed, such as in vertical-external-cavity surface emitting lasers at 935-981 nm [40] or modelocked lasers in the mid-IR [41, 42]. Pulse durations down to 29 fs have been demonstrated [43]. Saturable absorption is an example of a nonlinear optical process, and it was the first to be experimentally observed in graphene.

2.4 Graphene nonlinear optics

Nonlinear optics can be defined as the study of optical phenomena which are "nonlinear" in the sense that the material response (for example polarization or current) depends nonlinearly on the optical field strength [44]. Light-matter interaction in graphene is remarkably strong, and the material shows a variety of nonlinear phenomena at even moderate powers. This part focuses on experimental results that can be found in literature (Section 2.4.3) and on some models that are being used to explain these phenomena (Section 2.4.2). First however, a section is devoted to the different ways in which nonlinear optical phenomena are quantified in graphene, since a variety of approaches have been used.

2.4.1 Quantifying the optical nonlinearity of graphene

Graphene nonlinear optics has been studied for about a decade [45]. This quickly lead to the consensus that the third order nonlinearity of graphene is "strong", often quantified by a single scalar real valued material parameter (nonlinear index or susceptibility). However a very large large spread in the measured nonlinear parameters has been published (table 2.1), hence before giving a brief overview of these results in the next section, it is helpful to discuss the different material parameters typically used to quantify nonlinear optical phenomena in graphene, and how they can be compared.

2.4.1.1 Nonlinear susceptibility

Historically, nonlinear optical processes have been studied in the context of dielectrics, the nonlinear optical response is described by an optical polarization $P(t)$ with a nonlinear dependency on the electric field strength $E(t)$. This is often expressed by a power series [44],

$$\begin{aligned} P(t) =& P^{(1)}(t) + P^{(2)}(t) + P^{(3)}(t) + \dots \\ =& \varepsilon_0(\chi^{(1)}E(t) + \chi^{(2)}E^2(t) + \chi^{(3)}E^3(t) + \dots), \end{aligned} \tag{2.1}$$

where ε_0 is the vacuum permittivity and $\chi^{(1)}$, $\chi^{(2)}$, $\chi^{(3)}$,... are respectively the linear susceptibility and the second and third order nonlinear susceptibilities. Equation (2.1) works very well for many isotropic dielectrics, for which certain approximations are valid [44]. Graphene, being a two-dimensional semi-metal, behaves differently and several of these approximations need to be revisited. Mainly, graphene is extremely anisotropic, and the material response is non-instantaneous. Taking this into account, the m^{th} term of the polarization series expansion can be written as [46],

$$\mathbf{P}^{(m)}(t) = \varepsilon_0 \int_0^\infty d\tau_1 \cdots \int_0^\infty d\tau_m \mathbf{R}^{(m)}(\tau_1, \ldots, \tau_m) \vdots \mathbf{E}(t-\tau_1) \ldots \mathbf{E}(t-\tau_m) \ , \tag{2.2}$$

where $\mathbf{R}^{(m)}(\tau_1, \ldots, \tau_m)$ is the polarization response function of the m^{th} order [46]. The time-dependence reflects the non-instantaneous nature of the nonlinear response, and $\mathbf{R}^{(m)}$ being a tensor reflects the anisotropy of the medium. If we decompose the electric field and the polarization in a set of monochromatic waves, with frequencies ω_j and complex amplitudes $\mathbf{E}(\omega_j)$ and $\mathbf{P}^{(m)}(\omega_j)$. Then the relationship between the nonlinear polarization and electric complex field amplitudes can be written as [1],

$$\mathbf{P}^{(m)}(\omega_j) = \frac{\varepsilon_0}{2^{m-1}} \sum_{\omega_j = \omega_1 + \cdots + \omega_m} \chi^{(m)}(\omega_j; \omega_1, \ldots, \omega_m) \vdots \mathbf{E}(\omega_1) \ldots \mathbf{E}(\omega_m) \ , \tag{2.3}$$

with $\chi^{(m)}(\omega_j; \omega_1, \ldots, \omega_m)$ the m^{th} order Fourier transform of $\mathbf{R}^{(m)}$ [46]. The sum is taken for all combinations of m frequencies for which $\omega_j = \omega_1 + \cdots + \omega_m$. Note that for a non-instantaneous response, $\chi^{(m)}(\omega_j; \omega_1, \ldots, \omega_m)$ is in general dependent on the exact frequencies involved[2].

Being the parameter-of-choice in dielectrics, $\chi^{(m)}$ is often used for graphene [3, 4, 47–50]. Due to symmetry considerations only the odd orders $\chi^{(1)}$, $\chi^{(3)}$, $\chi^{(5)}$, ... are present in centrosymmetric materials such as graphene [44]. Often it is assumed that $\chi^{(3)}$ is the only non-negligible nonlinear term.

2.4.1.2 Nonlinear surface conductivity

Graphene is known to be a conductor, rather than a dielectric. Moreover $\chi^{(m)}$ is usually defined as a bulk parameter, whereas graphene is inherently a 2D material. It is much more natural to describe graphene as an infinitesimally thin surface, and to quantify its response to electromagnetic radiation (both linear and nonlinear) using surface conductivities $\sigma_s^{(m)}$, so that,

---

[1] A similar approach can be taken for more general fields, replacing the sum in equation (2.3) by an appropriate integral [46].

[2] ω_j is not an argument of this function, it is a common convention to write the "generated" frequency (the sum of all the actual frequency arguments [44]) before the frequency arguments $\omega_1, \ldots, \omega_m$.

$$\mathbf{J}_s^{(m)}(\omega_j) = \frac{1}{2^{m-1}} \sum_{\omega_j=\omega_1+\cdots+\omega_m} \sigma_s^{(m)}(\omega_j;\omega_1,\ldots,\omega_m)\vdots\mathbf{E}(\omega_1)\ldots\mathbf{E}(\omega_m)\ , \tag{2.4}$$

is the m^{th} order surface current density. Both descriptions are equivalent using the relation,

$$\mathbf{J}^{(m)}(t) = \frac{\mathbf{J}_s^{(m)}(t)}{\delta} = \frac{\partial \mathbf{P}^{(m)}(t)}{\partial t}, \tag{2.5}$$

where δ is the graphene thickness and $\mathbf{J}^{(m)}$ is the m^{th} order *bulk* current density. This leads to,

$$\sigma_s^{(m)}(\omega_j;\omega_1,\ldots,\omega_m) = -i\varepsilon_0\delta\omega_j\chi^{(m)}(\omega_j;\omega_1,\ldots,\omega_m). \tag{2.6}$$

Using symmetry considerations one can also prove that the third order conductivity tensor of graphene has only the following nonzero elements [6] (with x and y coordinates within the graphene sheet, the out-of-plane components are negligibly small [50]):

$$\sigma^{(3)}_{s,\,xxxx} = \sigma^{(3)}_{s,\,yyyy}\ , \tag{2.7}$$

$$\sigma^{(3)}_{s,\,xxyy} = \sigma^{(3)}_{s,\,yyxx}\ , \tag{2.8}$$

$$\sigma^{(3)}_{s,\,xyxy} = \sigma^{(3)}_{s,\,yxyx}\ , \tag{2.9}$$

$$\sigma^{(3)}_{s,\,xyyx} = \sigma^{(3)}_{s,\,yxxy}\ , \tag{2.10}$$

$$\sigma^{(3)}_{s,\,xxxx} = \sigma^{(3)}_{s,\,xxyy} + \sigma^{(3)}_{s,\,xyxy} + \sigma^{(3)}_{s,\,xyyx}\ . \tag{2.11}$$

2.4.1.3 Nonlinear refractive index

Alternatively, the nonlinear response of graphene is often quantified by simply assuming that the refractive index $n+i\kappa$ of the material depends linearly on the illumination intensity I,

$$n + i\kappa = n_0 + i\kappa_0 + (n_2 + i\kappa_2)I \tag{2.12}$$

where $n_2 + i\kappa_2$ is called the intensity-dependent refractive index. n_2 and κ_2 represent the nonlinear refraction and absorption, respectively. When the optical absorption is negligible, $\kappa \ll n$, and the relations $n_2 \propto \mathrm{Re}(\chi^{(3)})$ and $\kappa_2 \propto \mathrm{Im}(\chi^{(3)})$ can be used. In a strongly absorbing medium such as graphene however, the nonlinear refraction and absorption are the result of a more complex functions of real and imaginary parts of $\chi^{(1)}$ ($\sigma_s^{(1)}$) and $\chi^{(3)}$ ($\sigma_s^{(3)}$) [51],

$$\begin{aligned} n_2 =& \frac{3}{4\epsilon_0 c(n_0^2+\kappa_0^2)}\left[\mathrm{Re}(\chi^{(3)})+\frac{\kappa_0}{n_0}\mathrm{Im}(\chi^{(3)})\right] \\ =& \frac{3}{4\epsilon_0^2 c\omega\delta(n_0^2+\kappa_0^2)}\left[-\mathrm{Im}(\sigma_s^{(3)})+\frac{\kappa_0}{n_0}\mathrm{Re}(\sigma_s^{(3)})\right], \end{aligned} \tag{2.13}$$

$$\begin{aligned} \kappa_2 =& \frac{3}{4\epsilon_0 c(n_0^2+\kappa_0^2)}\left[\mathrm{Im}(\chi^{(3)})-\frac{\kappa_0}{n_0}\mathrm{Re}(\chi^{(3)})\right] \\ =& \frac{3}{4\epsilon_0^2 c\omega\delta(n_0^2+\kappa_0^2)}\left[\mathrm{Re}(\sigma_s^{(3)})+\frac{\kappa_0}{n_0}\mathrm{Im}(\sigma_s^{(3)})\right]. \end{aligned} \tag{2.14}$$

In absorbing media, the complex linear refractive index is related to the linear susceptibility and conductivity through the relation $(n_0+i\kappa_0)^2 = 1+\chi^{(1)} = 1+i\sigma_s^{(1)}/(\omega\delta\varepsilon_0)$.

As mentioned before, graphene is often used as a saturable absorber [37, 38]. In this context usually only nonlinear absorption is considered and a somewhat different phenomenological model is used [37],

$$\alpha(I) = \alpha_{\mathrm{NS}} + \frac{\alpha_{\mathrm{S}}}{1+I/I_{\mathrm{S}}}, \tag{2.15}$$

where α_{S} and α_{NS} are the saturable and the nonsaturable contributions to the absorption, and I_{S} is the saturation intensity. For the limit $I \ll I_{\mathrm{S}}$ this converges to the intensity dependent refractive index model ($\alpha(I) \equiv (4\pi/\lambda)(\kappa_0+\kappa_2 I)$, with λ the optical wavelength), with,

$$\kappa_2 \approx -\frac{\lambda}{4\pi}\frac{\alpha_{\mathrm{S}}}{I_{\mathrm{S}}}. \tag{2.16}$$

2.4.1.4 Which description should one use?

Historically, third order nonlinear optical properties have been described in terms of a nonlinear index or a nonlinear susceptibility [44]. For graphene, these conventions have been taken over by most experimentalists [3–5, 47, 48, 52–54].

However to unambiguously quantify third order processes in graphene, the third order surface conductivity tensor $\sigma_s^{(3)}$ is the best option. It naturally reflects graphene's high conductance, its 2D nature and can encompass frequency dependence.

Using a third order susceptibility tensor $\chi^{(3)}$ is in practice equivalent and will yield the same results. However it is intrinsically a bulk value and hence somewhat unnatural for graphene (we effectively assume graphene is a uniform slab of thickness δ). Using this quantity also leads to some unfair and even deceptive comparisons. Extremely large $\chi^{(3)}$ values for graphene compared to bulk materials such as glass or silicon are often used as a selling point. However these large nonlinearities are characteristic to monolayers and the interaction volumes/lengths are henceforth orders of magnitude smaller than when shining light through bulk materials (think for example about a $\approx$ 0.3 nm thick layer of graphene covering a 300 nm thick SiN waveguide and the correspondingly small overlap between graphene and the optical mode).

The nonlinear refractive index is the least appropriate. It is again a parameter defined for bulk media. Anisotropy as well as frequency dispersion are often not included. Moreover the conversion to the other parameters is nontrivial, equations (2.13) and (2.14) were initially derived for lossy isotropic bulk media [51] and should only be used for order-of-magnitude estimates when comparing experimental values for a material such as graphene. More detailed studies show that experimentally reported n_2 (κ_2) values depend on different combinations of the $\sigma_s^{(3)}$ tensor components, depending on the measurement technique and the pump/probe polarizations used [55].

As a general rule, the use of bulk parameters such as linear and nonlinear refractive indices should be avoided for monolayer 2D materials, linear and nonlinear optical processes can be appropriately modelled using surface conductivities.[3]

2.4.2 Theoretical models for optical nonlinearities in graphene

The strong nonlinear response of graphene to electromagnetic radiation was, from a theoretical point of view, first noted by Mikhailov in 2007 [45]. Qualitatively, his argumentation was based on the linear carrier dispersion relation of graphene. He noted that in the presence of a sinusoidal electric field $E_x \propto \cos\Omega t$, the momentum of an electron follows the equation of motion $dp_x/dt = -eE_x$, hence $p_x \propto \sin\Omega t$ and the velocity $v_x = \partial\epsilon/\partial p_x \propto \mathrm{sgn}(\sin\Omega t)$, where ϵ is the electron energy. As a consequence the induced current does not only oscillate at frequency Ω, but also strong higher harmonics of frequencies $m\Omega$, m = 3,5,7,... are present. This first quasi-classical theory only takes into account intraband transitions and is valid for frequencies typically below 5-10 THz [45].

---

[3] A parameter which is equally appropriate, but was not mentioned here, is the surface susceptibility $\chi_s^{(m)} \equiv \delta\chi^{(m)} = i\sigma_s^{(m)}/(\varepsilon_0\omega)$. For low loss 2D materials or interfaces this parameter is often used, see for example Chapter 5.

Since then, Mikhailov and other authors have published more extensive theoretical models for the nonlinear conductivity of graphene, also taking into account interband transitions, and extending their models to the optical domain [6–8]. Analytical expressions are obtained using perturbative approaches, be it of large complexity. These models have been successfully linked to several experimental results, such as recent demonstrations of gate-tunable third harmonic generation [56, 57] and the four-wave mixing experiment presented in Section 3.4.

A more intuitive approach is developed in Appendix A. We apply a simple phenomenological model which takes into account the heating of the electron-hole gas by the incident electromagnetic radiation and its cooling due to interaction with the environment, with a phenomenological time constant $\tau_{\mathcal{E}}$. Based on some simplifying assumptions, we calculate the intensity I (or electric field E_ω) dependence of the charge carrier distribution in the graphene. Since the linear conductivity of graphene (and hence the linear optical properties) depend strongly on this distribution, an estimate can be made of the intensity-dependence of the conductivity, $\sigma_s^{(1)}(|E_\omega|^2)$ (see Appendix A for more information). A $\sigma_s^{(3)}$-based description of the nonlinearities assumes that the function $\sigma_s^{(1)}(|E_\omega|^2)$ is approximately linear with respect to $|E_\omega|^2$, so that $\sigma^{(1)}(|E_\omega|^2) \approx \sigma^{(1)}(0) + \frac{3}{2}\sigma^{(3)}|E_\omega|^2$. Our model is based on the assumption that the electron distribution can at all times be described by a Fermi-Dirac-type function. The chemical potential μ and hot electron temperature T describing this distribution are dependent on the local optical intensity. It must be clear that this approach can only be used to describe phenomena for which the fluctuations in the local intensity occur at a longer time-scale than the time needed to reach a steady-state Fermi-Dirac distribution. This model can be used to describe self- and cross-modulation experiments, as long as sub-THz modulation frequencies are used, or pulses with ps durations or more. The model is validated by cross-modulation experiments in Section 3.5. Four-wave mixing experiments can also be described using this model, be it for a relatively small signal-pump wavelength detuning, this is discussed further in Section 3.4. The model is also used to explore the limitations of a purely $\sigma_s^{(3)}$-based description of the optical nonlinearities in graphene in terms of optical intensity, see Section 2.4.3 (and Appendix A.4 for more details).

2.4.3 Experimental demonstrations of nonlinear optics in graphene

In 2009, the first demonstration of strong optical nonlinearities in graphene was published, in the context of saturable absorption for modelocked lasers [37]. The first demonstration of frequency conversion through four-wave mixing was published by Hendry *et al.* in 2010 [3]. Soon many other experimental demonstrations of nonlinear optical processes in graphene followed. Gu *et al.* also observed four-wave mixing in graphene, this time after incorporating it in an integrated silicon photonic crystal cavity [47]. Wu *et al.* studied self-phase modulation in solution dispersions of chemically exfoliated graphene. The same phenomenon was later also studied on CVD-grown single layer graphene using the Z-scan method [5, 52, 53]. Dremetsika *et al.* used an optical heterodyne detection technique for measuring the optical Kerr effect (OHD-OKE), concluding that the nonlinear refractive index n_2 had a negative value in their measurements [53]. They later refined their method and reported complex values of the nonlinear index, conductivity and susceptibility [50]. The observation that graphene can induce negative nonlinear refraction was also made by Vermeulen *et al.*, who covered integrated silicon waveguides with graphene and performed a self-phase modulation experiment using chirped pulses [54]. Strong third harmonic generation has furthermore been demonstrated on graphene by several groups [48, 49].

Table 2.1 summarizes the nonlinear parameters reported in some of these earlier experimental studies (mostly pre-2017), along with some of the experimental parameters. The nonlinear parameters as they are reported in the paper are denoted by a grey background, the others are estimated based on the relations from the previous section. These values are often only crude order-of-magnitude estimates, because not all information is available to do a proper conversion. For example conversion between the nonlinear index and the nonlinear conductivity/susceptibility requires full knowledge of the complex nonlinear index, as can be seen in equations (2.13) and (2.14).

When comparing these different experimental studies, one cannot but notice the enormous spread in reported values. This can have several different causes. As was mentioned in the previous section, n_2 values measured using different experimental methods are generally not the same, as they are functions of different components of the $\sigma_s^{(3)}$ tensor. An other explanation for this is the variety of different phenomena that have been experimentally studied, at different wavelengths. The nonlinear conductivity is very dependent on its frequency arguments, and we for example cannot expect third harmonic generation and self-phase modulation experiments to yield the same values. Theoretical models further indicate that sample dependent

Ref.	λ (nm)	Δt (ps)	I_p (W/m^2)	$\lvert\chi^{(3)}\rvert$ (m^2/V^2)	$\lvert\sigma_s^{(3)}\rvert$ (Am^2/V^3)	n_2 (m^2/W)
🟥 [3]	760-1200	6	$\approx 10^{13}$	$2.1 \cdot 10^{-15}$	$1.5 \cdot 10^{-20}$	$\approx 10^{-13}$
🟥 [47]	1560	CW	-	$\approx 10^{-15}$	$\approx 10^{-20}$	$\approx 10^{-13}$
🟩 [4]	532	CW	$< 10^{6}$	$\approx 10^{-15}$	$\approx 10^{-20}$	$\approx 10^{-13}$
🟩 [5]	1550	3.8	$< 10^{13}$	$\approx 10^{-12}$	$\approx 10^{-18}$	$\approx 10^{-11}$
🟩 [52]	733	0.1	$\approx 10^{15}$	$\approx 10^{-15}$	$\approx 10^{-20}$	$\approx 10^{-13}$
🟩 [54]†	1550	1.2	$\approx 10^{13}$	$\approx 10^{-14}$	$\approx 10^{-20}$	$\approx -10^{-13}$
🟩 [53]†	1600	0.18	$5 \cdot 10^{12}$	$\approx 10^{-14}$	$\approx 10^{-20}$	$-1.1 \cdot 10^{-13}$
🟩 [53]†	1550	3.8	$5 \cdot 10^{12}$	$\approx 10^{-13}$	$\approx 10^{-19}$	$-2 \cdot 10^{-12}$
🟩 [50]‡	1600	0.18	$5 \cdot 10^{12}$	$(-6 - 9.6i) \cdot 10^{-16}$	$(-3.3 + 2.1i) \cdot 10^{-21}$	$(-1 - 1.6i) \cdot 10^{-13}$
🟦 [48]	$789 \rightarrow 263$	0.05	$2 \cdot 10^{14}$	$2 \cdot 10^{-19}$	$5 \cdot 10^{-24}$	-
🟦 [49]	$1550 \rightarrow 520$	0.15	$3 \cdot 10^{15}$	$4 \cdot 10^{-15}$	$5 \cdot 10^{-20}$	-

Table 2.1: Some earlier experimental values for $\chi^{(3)}$, $\sigma_s^{(3)}$ or n_2 from literature. λ is the wavelength of the measurement, Δt is the approximate pulse duration (CW denotes continuous wave illumination). I_p is the approximate (peak) intensity.
🟥 Four-wave mixing experiments.
🟩 Self- or cross- phase(or amplitude) modulation experiments.
🟦 Third harmonic generation experiments.
⬜ Nonlinear parameters as reported, the other values were extrapolated.
† Dremetsika *et al.* [53] and Vermeulen *et al.* [54] were the first to independently report negative values for the intensity-dependent refractive index.
‡ In a second publication, Dremetsika *et al.* published complex values for the nonlinear parameters [50].

parameters such as the Fermi energy E_F or the carrier lifetime (material quality) strongly influence the nonlinear conductivity of graphene [6–8]. Finally, in most experimental studies, the third order nonlinearity is assumed to be dominant, and higher order terms are neglected. However when using high optical powers the validity of this assumption is not so trivial. Demetriou *et al.* recently showed that higher order nonlinearities become significant at intensities on the order of 10^{12} Wm^{-2} and higher [58]. It has even been argued that at very high powers, the whole series expansion of the type in equation (2.1) becomes incorrect [59] and an exact solution for the

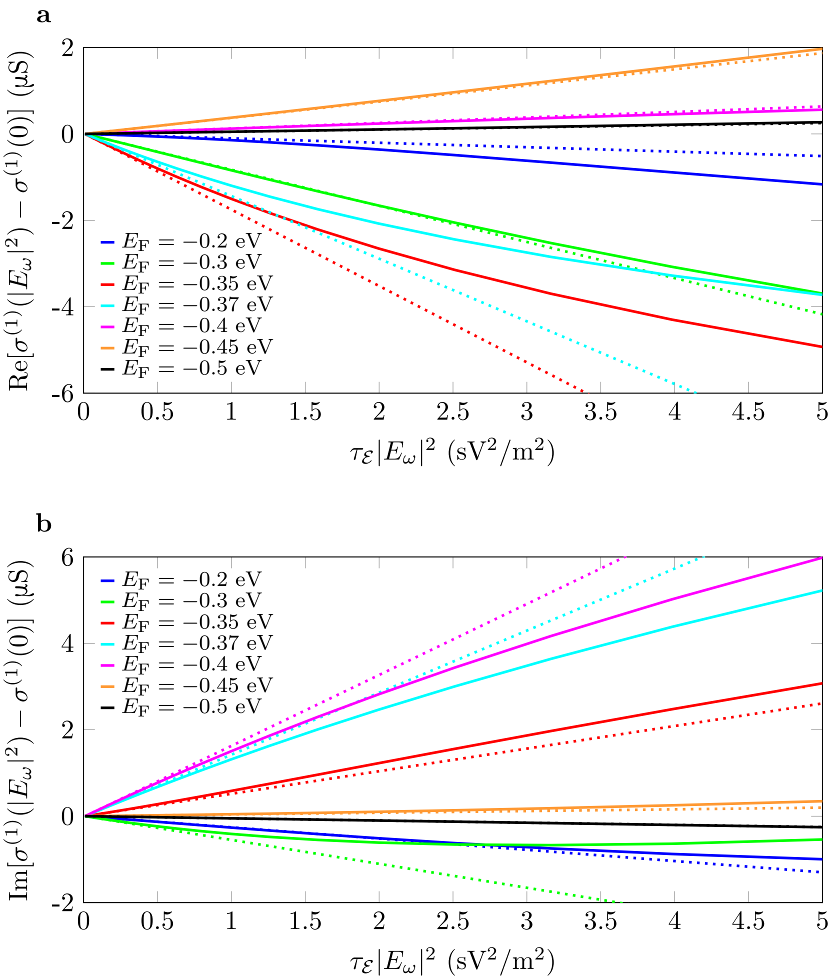

Figure 2.3: **a** Real part of the intenstity-dependent change in linear conductivity $\sigma^{(1)}(|E_\omega|^2) - \sigma^{(1)}(0)$, as a function of $\tau_\mathcal{E}|E_\omega|^2$. The dotted lines represents the approximation using only the third order conductivity $\sigma^{(3)}$; $\sigma^{(1)}(|E_\omega|^2) = \sigma^{(1)}(0) + \frac{3}{2}\sigma^{(3)}|E_\omega|^2$. **b** Imaginary part of the same parameters. See Appendix A, Section A.4 for more details. These calculations are done for a wavelength of 1550 nm, assuming continuous-wave illumination.

intensity dependent conductivity $\sigma_s(I)$ has to be calculated. Using the simple phenomenological model for the optical nonlinearities in graphene which was introduced in Section 2.4.2 and is described in detail in Appendix A, this issue can be explored in some more detail. This is done in Section A.4. As discussed, this model takes into account the heating of the electron and hole distributions in graphene under strong illumination. An estimate can then be made of the intensity-dependent linear conductivity of graphene, $\sigma_s^{(1)}(|E_\omega|^2)$ and the third order nonlinear conductivity by introducing the linearization, $\sigma^{(1)}(|E_\omega|^2) \approx \sigma^{(1)}(0) + \frac{3}{2}\sigma^{(3)}|E_\omega|^2$. Figure 2.3 shows the *variation* in linear conductivity as a function of electric field strength, using both the full model (solid lines) and this linearization (dotted lines), for a variety of Fermi energies E_F. According to these estimates the $\sigma^{(3)}$-based model is a reasonably good representation for $\tau_\mathcal{E}|E_\omega|^2 \lesssim 1$ sV^2/m^2. For increasing intensities, the linearization starts to deviate strongly from the exact calculations. For $\tau_\mathcal{E}|E_\omega|^2 > 10$ sV^2/m^2, even order-of-magnitude estimates become problematic. Our experimental results in Sections 3.4 and 3.5 show reasonable correspondence with this model for time constants within the range 0.1 ps $< \tau_\mathcal{E} <$ 1 ps. For these values, we expect the third order description to lose its validity somewhere within the local intensity range of $10^{10} \ldots 10^{12}$ Wm^{-2}, depending upon the exact time constant, the Fermi energy and the amount of error that can be tolerated. This is comparable with, or even slightly more pessimistic than, the conclusions made by Demetriou *et al.* [58].

With the experiments presented in Sections 3.4 and 3.5, we try to resolve some of these issues. We measure different nonlinear phenomena on graphene (four-wave mixing and cross-amplitude/phase modulation) and we explicitly map the frequency dependence of the corresponding nonlinear conductivity $\sigma_s^{(3)}$. By using SiN waveguides we moreover strongly improve the efficiency of the nonlinear interactions, allowing us to work in the continuous-wave regime with limited local intensities. Finally, we have also gated the graphene, which enabled us to map $\sigma_s^{(3)}$ over a range of Fermi energies E_F. Recently, several other groups have also performed more elaborate studies on gated graphene. Soavi *et al.* reported a change of almost two orders of magnitude in the third harmonic generation efficiency when tuning the Fermi level in gated graphene [56]. Jiang *et al.* reported similar dependencies, for third harmonic generation, and four-wave mixing [57].

2.5 Third order nonlinear optics in graphene-covered waveguides

For the experiments presented in the next chapter, graphene will be deposited on integrated waveguides. This has some advantages compared to more traditional experiments performed on single-layer graphene. Firstly, the optical mode is strongly confined, which is beneficial for nonlinear experiments which scale nonlinearly with the local intensity. Secondly, the interaction length can be tailored and can easily amount to hundreds of

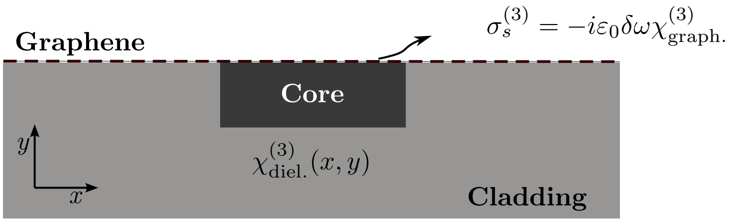
$\sigma_s^{(3)} = -i\varepsilon_0\delta\omega\chi^{(3)}_{\text{graph.}}$
Graphene
Core
y
$\chi^{(3)}_{\text{diel.}}(x,y)$
x
Cladding

Figure 2.4: Sketch of typical graphene-covered waveguide

micrometer, in contrast to experiments where the light passes through a layer of graphene with a nominal thickness of only several Ångström. A disadvantage however is that by using a waveguide the nonlinearity in the graphene is measured *indirectly*. Instead of the nonlinear conductivity of the graphene $\sigma_s^{(3)}$, an effective nonlinear parameter of the whole waveguide, typically called γ, is measured. The relation between the nonlinear conductivity and this waveguide parameter is complicated and depends on the exact waveguide cross-section. In this section we derive the conversion between these parameters.

Figure 2.4 shows a typical graphene-covered waveguide. It consists of a dielectric core and cladding, which have an overall nonlinearity quantified by a position-dependent nonlinear susceptibility $\chi^{(3)}_{\text{diel.}}(x,y)$. The graphene layer covers the waveguide. Its contribution to the overall nonlinearity of the waveguide can be taken into account by assuming that the graphene is an infinitesimally thin layer with nonlinear surface conductivity $\sigma_s^{(3)}$, or equivalently by assuming it is a uniform layer with thickness δ and nonlinear susceptibility $\chi^{(3)}_{\text{graph.}}$. The conversion between these parameters is shown on figure 2.4.

We will start our derivation by using the latter assumption, in that case the overall nonlinear susceptibility $\chi^{(3)}(x,y)$ is just the sum of the dielectric contribution and the contribution by the graphene. Another assumption is that we consider the nonlinear interaction between a discrete number of monochromatic waves. This allows us to express the nonlinear polarization density at frequency ω_j within the cross-section using the following expression,

$$\mathbf{P}_{\text{NL}}(\omega_j) = \frac{\varepsilon_0}{4} \sum_{\substack{\omega_j=\omega_k+\\ \omega_l+\omega_m}} \chi^{(3)}(\omega_j;\omega_k,\omega_l,\omega_m)\vdots\mathbf{E}(\omega_k)\mathbf{E}(\omega_l)\mathbf{E}(\omega_m). \tag{2.17}$$

In the derivation of the effective nonlinear parameters of the graphene-covered waveguides, we will assume that this nonlinear polarization causes only a small perturbation to the waveguide modes calculated using the linear material parameters. The complex amplitude of an unperturbed waveguide mode at frequency ω_j can be written as:

$$\mathbf{E}_0(\omega_j, \mathbf{r}) = A_0(\omega_j) \frac{\mathbf{e}(\omega_j, \mathbf{r}_\perp)}{\sqrt{\mathscr{P}_j}} e^{i\beta_j z}, \tag{2.18}$$

$$\mathbf{H}_0(\omega_j, \mathbf{r}) = A_0(\omega_j) \frac{\mathbf{h}(\omega_j, \mathbf{r}_\perp)}{\sqrt{\mathscr{P}_j}} e^{i\beta_j z}. \tag{2.19}$$

Where $\mathbf{e}(\omega_j, \mathbf{r}_\perp)$ and $\mathbf{h}(\omega_j, \mathbf{r}_\perp)$ are the vectorial electric and magnetic mode profiles, in what follows, we will often omit the arguments $\mathbf{r}$ and $\mathbf{r}_\perp$ for brevity. $A_0(\omega_j)$ is the complex amplitude of the mode. β_j is the mode propagation constant and $\mathscr{P}_j$ is the power normalization constant, defined so that the total power of the mode equals $|A_0(\omega_j)|^2$:

$$\begin{aligned} &\iint_{A_\infty} \frac{1}{2} \mathrm{Re}\{|A_0(\omega_j)|^2 \frac{\mathbf{e}(\omega_j)}{\sqrt{\mathscr{P}_j}} \times \frac{\mathbf{h}^*(\omega_j)}{\sqrt{\mathscr{P}_j}}\} \cdot \hat{\mathbf{e}}_z dA \equiv |A_0(\omega_j)|^2 \\ &\Rightarrow \mathscr{P}_j = \frac{1}{4} \iint_{A_\infty} \{\mathbf{e}(\omega_j) \times \mathbf{h}^*(\omega_j) + \mathbf{e}^*(\omega_j) \times \mathbf{h}(\omega_j))\} \cdot \hat{\mathbf{e}}_z dA. \end{aligned} \tag{2.20}$$

A_∞ is the plane perpendicular to the waveguide propagation direction. $\hat{\mathbf{e}}_z$ is the unit vector in the propagation direction z. By definition, these modes obey the Maxwell curl equations,

$$\nabla \times \mathbf{E}_0(\omega_j) = i\omega_j \mu_0 \mathbf{H}_0(\omega_j), \tag{2.21}$$

$$\nabla \times \mathbf{H}_0(\omega_j) = -i\omega_j \epsilon_0 n^2 \mathbf{E}_0(\omega_j), \tag{2.22}$$

$n(\mathbf{r}_\perp)$ is the refractive index of the unperturbed waveguide cross-section. One can include the effect of perturbations, such as linear losses and nonlinearities, by introducing complex slowly varying amplitudes $A(\omega_j, z)$. The perturbed waveguide modes are then written as:

$$\mathbf{E}(\omega_j, \mathbf{r}) = A(\omega_j, z) \frac{\mathbf{e}(\omega_j, \mathbf{r}_\perp)}{\sqrt{\mathscr{P}_j}} e^{i\beta_j z}\ , \tag{2.23}$$

$$\mathbf{H}(\omega_j, \mathbf{r}) = A(\omega_j, z) \frac{\mathbf{h}(\omega_j, \mathbf{r}_\perp)}{\sqrt{\mathscr{P}_j}} e^{i\beta_j z}. \tag{2.24}$$

In practice, we will consider the total time-varying fields to be superpositions of a number of monochromatic waves:

$$\widetilde{\mathbf{E}}(\mathbf{r}, t) = \sum_j \mathrm{Re}\{A(\omega_j, z) \frac{\mathbf{e}(\omega_j, \mathbf{r}_\perp)}{\sqrt{\mathscr{P}_j}} e^{-i(\omega_j t - \beta_j z)}\}\ , \tag{2.25}$$

$$\widetilde{\mathbf{H}}(\mathbf{r}, t) = \sum_j \mathrm{Re}\{A(\omega_j, z) \frac{\mathbf{h}(\omega_j, \mathbf{r}_\perp)}{\sqrt{\mathscr{P}_j}} e^{-i(\omega_j t - \beta_j z)}\}. \tag{2.26}$$

These perturbed modes should also obey the Maxwell curl equations, where the influence of third order nonlinearities can be incorporated as a nonlinear polarization density, $\mathbf{P}_{\mathrm{NL}}(\omega_j)$,

$$\begin{aligned} \nabla \times \mathbf{E}(\omega_j) =& i\omega_j \mu_0 \mathbf{H}(\omega_j)\ , && (2.27) \\ \nabla \times \mathbf{H}(\omega_j) =& - i\omega_j \epsilon_0 n^2 \mathbf{E}(\omega_j) - i\omega_j \mathbf{P}_{\mathrm{NL}}(\omega_j)\ . && (2.28) \end{aligned}$$

To derive the coupled-wave equations, we can start from the conjugated form of the Lorentz reciprocity theorem [60]:

$$\iint_{A_\infty} \nabla \cdot \mathbf{F} = \frac{\partial}{\partial z} \iint_{A_\infty} \mathbf{F} \cdot \hat{\mathbf{e}}_z dA. \tag{2.29}$$

A_∞ is the surface perpendicular to the propagation direction. The **F**-field can be constructed from the perturbed and unperturbed waveguide mode fields as $\mathbf{F} \equiv \mathbf{E}_0^*(\omega_j) \times \mathbf{H}(\omega_j) + \mathbf{E}(\omega_j) \times \mathbf{H}_0^*(\omega_j)$. Substituting this in equation (2.29) yields:

$$\begin{aligned} &\iint_{A_\infty} \{(\nabla \times \mathbf{E}_0^*(\omega_j)) \cdot \mathbf{H}(\omega_j) - \mathbf{E}_0^*(\omega_j) \cdot (\nabla \times \mathbf{H}(\omega_j)) \\ &\qquad + (\nabla \times \mathbf{E}(\omega_j)) \cdot \mathbf{H}_0^*(\omega_j) - \mathbf{E}(\omega_j) \cdot (\nabla \times \mathbf{H}_0^*(\omega_j))\} dA \\ &= \frac{\partial}{\partial z} \iint_{A_\infty} \frac{A_0(\omega_j)^* A(\omega_j, z)}{\mathscr{P}_j} \{\mathbf{e}(\omega_j) \times \mathbf{h}^*(\omega_j) + \mathbf{e}^*(\omega_j) \times \mathbf{h}(\omega_j))\} \cdot \hat{\mathbf{e}}_z dA. \end{aligned} \tag{2.30}$$

The left hand side of equation (2.30) can be simplified by substituting equations (2.21)-(2.22) and (2.27)-(2.28). The right hand side can be simplified by using the normalization condition (equation (2.20)). Eventually this gives

$$\frac{\partial}{\partial z} A(\omega_j, z) = i\omega_j \frac{e^{-i\beta_j z}}{4\sqrt{\mathscr{P}_j}} \iint_{A_\infty} \mathbf{e}^*(\omega_j) \cdot \mathbf{P}_{\mathrm{NL}}(\omega_j) dA, \tag{2.31}$$

substituting equations (2.23) and (2.24) in equation (2.17), and subsequently in equation (2.31), one gets a general coupled-wave equation for the set of slowly varying amplitudes:

$$\begin{aligned} \frac{\partial}{\partial z} A(\omega_j, z) =& i\varepsilon_0 \omega_j \sum_{\substack{\omega_j = \omega_k \\ +\omega_l + \omega_m}} \frac{A(\omega_k, z) A(\omega_l, z) A(\omega_m, z) e^{i(\beta_k + \beta_l + \beta_m - \beta_j) z}}{16\sqrt{\mathscr{P}_j \mathscr{P}_k \mathscr{P}_l \mathscr{P}_m}} \cdot \\ & \iint_{A_\infty} \mathbf{e}^*(\omega_j) \cdot \chi^{(3)}(\omega_j; \omega_k, \omega_l, \omega_m) \vdots \mathbf{e}(\omega_k) \mathbf{e}(\omega_l) \mathbf{e}(\omega_m) dA, \end{aligned} \tag{2.32}$$

here the summation goes over *all possible combinations of 3 frequencies that add up to ω_j, including the negative frequencies*. Moreover, since the time-dependent electrical fields are real-valued, one can make use of the equalities $\mathbf{e}(-\omega) = \mathbf{e}^*(\omega)$ and $A(-\omega_j) = A(\omega_j)^*$ [44].

The integral in equation (2.32) can now be split into the dielectric contribution containing $\chi^{(3)}_{\text{diel.}}$, and the graphene contribution $\chi^{(3)}_{\text{graph.}}$. Moreover, we can switch to the description using the nonlinear sheet conductivity for graphene using the conversion $\sigma_s^{(3)} = -i\varepsilon_0\delta\omega\chi^{(3)}_{\text{graph.}}$,

$$\begin{aligned}
\frac{\partial}{\partial z}A(\omega_j, z) = \sum_{\substack{\omega_j=\omega_k\\+\omega_l+\omega_m}} & \frac{A(\omega_k, z)A(\omega_l, z)A(\omega_m, z)e^{i(\beta_k+\beta_l+\beta_m-\beta_j)z}}{16\sqrt{\mathscr{P}_j\mathscr{P}_k\mathscr{P}_l\mathscr{P}_m}} \cdot \\
& \Bigg[i\varepsilon_0\omega_j \iint_{A_\infty} \mathbf{e}^*(\omega_j)\cdot\chi^{(3)}_{\text{diel.}}(\omega_j;\omega_k,\omega_l,\omega_m)\vdots\mathbf{e}(\omega_k)\mathbf{e}(\omega_l)\mathbf{e}(\omega_m)dA \\
& \quad - \int_G \mathbf{e}^*(\omega_j)\cdot\sigma_s^{(3)}(\omega_j;\omega_k,\omega_l,\omega_m)\vdots\mathbf{e}(\omega_k)\mathbf{e}(\omega_l)\mathbf{e}(\omega_m)d\ell \Bigg] \\
& \overset{\text{SiN}}{\approx} - \sum_{\substack{\omega_j=\omega_k\\+\omega_l+\omega_m}} \frac{A(\omega_k, z)A(\omega_l, z)A(\omega_m, z)e^{i(\beta_k+\beta_l+\beta_m-\beta_j)z}}{16\sqrt{\mathscr{P}_j\mathscr{P}_k\mathscr{P}_l\mathscr{P}_m}} \cdot \\
& \qquad \int_G \mathbf{e}^*(\omega_j)\cdot\sigma_s^{(3)}(\omega_j;\omega_k,\omega_l,\omega_m)\vdots\mathbf{e}(\omega_k)\mathbf{e}(\omega_l)\mathbf{e}(\omega_m)d\ell,
\end{aligned} \tag{2.33}$$

where for the graphene contribution, the surface integral over the cross-section of the waveguide has become a line integral over the graphene. The final approximation is in the assumption that the nonlinear interactions in the dielectrics are negligible compared to the ones in the graphene. This the case for our graphene-covered SiN waveguides discussed in the next chapter. A simple SiN waveguide without graphene has a nonlinear parameter of $\gamma_{\text{SiN}} \approx 1.4\ \text{cm}^{-1}\text{W}^{-1}$ [61], more than 3 orders of magnitude smaller than our experimental values for graphene-covered waveguides presented in the next chapter. This is *not* necessarily the case for silicon waveguides, for example in reference [54].

Note that in the above derivation, we have not taken into account linear losses, although these are very important when considering graphene. Linear losses in these waveguides can be obtained by calculating the unperturbed modes with a mode-solver (by making $n(\mathbf{r}_\perp)^2$ complex, or by adding a conductive boundary representing the graphene). The propagation loss is then $\alpha(\omega_j) = 2\text{Im}(\beta_j)$. The most intuitive way to describe loss is to incorporate a loss term, $-\frac{\alpha(\omega_j)}{2}A(\omega_j, z)$, in the right-hand side of equations (2.32) and (2.33) and to assume the propagation constant is real. For graphene-covered waveguides, it is also intuitive to treat the linear loss due to the graphene absorption as a perturbation, namely by adding a term representing the linear surface current density $\sigma_s^{(1)}(\omega_j)\mathbf{E}(\omega_j)$ to equation (2.28). A similar derivation as the one given before will then give,

$$\alpha(\omega_j) = \frac{1}{2\mathscr{P}_j} \int_G \mathbf{e}^*(\omega_j) \cdot \sigma_s^{(1)}(\omega_j)\mathbf{e}(\omega_j) d\ell, \tag{2.34}$$

with $\sigma_s^{(1)}$ the linear surface conductivity of graphene.

2.6 Conclusion

In this chapter we started by introducing graphene from a general perspective (Section 2.2), then we have focused more on the potential of graphene as a material for photonics (Section 2.3) and more specifically nonlinear optics (Section 2.4). In Section 2.4.1, the issue of quantifying the optical nonlinearities in graphene was addressed. This is a seemingly tedious exercise, however necessary because several units have been used in literature and the interpretation and comparison is not straightforward. In Section 2.4.2, a brief overview of different theoretical approaches to model the optical nonlinearities in graphene is given. A phenomenological model discussed in detail in Appendix A, is also introduced here. Section 2.4.3 gives an overview of some important experimental demonstrations of graphene nonlinear optics. A comparison between the numerical values given in these different publications is made, to the extent that this is possible. The main conclusion is that there is a very large discrepancy between different published parameters. Several possible explanations of these large differences are given. For example the different wavelengths used, differences in doping levels and graphene quality, etc. The possibility that the third-order description of the optical nonlinearities, which is generally used, is just not adequate for the high optical powers used in many experiments, is also explored in more detail. These large differences between existing experimental values and the potential experimental issues serve as a motivation for the experiments discussed in Chapter 3, more specifically Sections 3.4 and 3.5. In these experiments the nonlinear properties of graphene incorporated on integrated waveguides are probed, while carefully tuning parameters such as the carrier density and while keeping the local optical intensities modest. In Section 2.5, a general theoretical model describing third-order nonlinear optics in graphene-covered waveguides is developed. This theory will serve as a stepping stone for the interpretation of the experiments in Sections 3.4 and 3.5.

References

[1] K. Alexander, N. A. Savostianova, S. A. Mikhailov, B. Kuyken, and D. Van Thourhout. *Electrically tunable optical nonlinearities in graphene-covered SiN waveguides characterized by four-wave mixing.* ACS Photonics, 4(12):3039–3044, 2017.

[2] K. Alexander, N. A. Savostianova, S. A. Mikhailov, D. Van Thourhout, and B. Kuyken. *Gate-tunable nonlinear refraction and absorption in graphene-covered silicon nitride waveguides.* ACS Photonics, 2018.

[3] E. Hendry, P. J. Hale, J. Moger, A. K. Savchenko, and S. A. Mikhailov. *Coherent nonlinear optical response of graphene.* Physical Review Letters, 105(9):097401, 2010.

[4] R. Wu, Y. Zhang, S. Yan, F. Bian, W. Wang, X. Bai, X. Lu, J. Zhao, and E. Wang. *Purely coherent nonlinear optical response in solution dispersions of graphene sheets.* Nano Letters, 11(12):5159–5164, 2011.

[5] H. Zhang, S. Virally, Q. Bao, L. K. Ping, S. Massar, N. Godbout, and P. Kockaert. *Z-scan measurement of the nonlinear refractive index of graphene.* Optics Letters, 37(11):1856–1858, 2012.

[6] J. Cheng, N. Vermeulen, and J. E. Sipe. *Third order optical nonlinearity of graphene.* New Journal of Physics, 16(5):053014, 2014.

[7] J. Cheng, N. Vermeulen, and J. E. Sipe. *Third-order nonlinearity of graphene: Effects of phenomenological relaxation and finite temperature.* Physical Review B, 91(23):235320, 2015.

[8] S. A. Mikhailov. *Quantum theory of the third-order nonlinear electrodynamic effects of graphene.* Physical Review B, 93(8):085403, 2016.

[9] R. E. Peierls. *Quelques proprietes typiques des corpses solides.* Annales de l'institut Henri Poincaré, 5:177–222, 1935.

[10] L. D. Landau. *Zur Theorie der phasenumwandlungen II.* Physikalische Zeitschrift der Sowjetunion, 11(545):26–35, 1937.

[11] A. K. Geim and K. S. Novoselov. *The rise of graphene.* Nature Materials, 6(3):183 – 191, 2007.

[12] K. S. Novoselov, A. K. Geim, S. V. Morozov, D. Jiang, Y. Zhang, S. V. Dubonos, I. V. Grigorieva, and A. A. Firsov. *Electric field effect in atomically thin carbon films.* Science, 306(5696):666–669, 2004.

[13] K. S. Novoselov, A. K. Geim, S. V. Morozov, D. Jiang, M. I. Katsnelson, I. V. Grigorieva, S. V. Dubonos, and A. A. Firsov. *Two-dimensional gas of massless Dirac fermions in graphene.* Nature, 438:197–200, 2005.

[14] *Scientifc Background on the Nobel Prize in Physics 2010 - Graphene.* The Royal Swedish Academy of Sciences (Nobelprize.org), 2010.

[15] K. S. Novoselov. *Nobel Lecture: Graphene: Materials in the Flatland.* Reviews of Modern Physics, 83:837–849, 2011.

[16] A. C. Ferrari et al. *Science and technology roadmap for graphene, related two-dimensional crystals, and hybrid systems.* Nanoscale, 7(11):4598–4810, 2015.

[17] R. R. Nair, P. Blake, A. N. Grigorenko, K. S. Novoselov, T. J. Booth, T. Stauber, N. M. R. Peres, and A. K. Geim. *Fine structure constant defines visual transparency of graphene.* Science, 320(5881):1308–1308, 2008.

[18] A. S. Mayorov, R. V. Gorbachev, S. V. Morozov, L. Britnell, R. Jalil, L. A. Ponomarenko, P. Blake, K. S. Novoselov, K. Watanabe, T. Taniguchi, and A. K. Geim. *Micrometer-scale ballistic transport in encapsulated graphene at room temperature.* Nano Letters, 11(6):2396–2399, 2011.

[19] *http://www.itrs2.net/*.

[20] M. Alahbakhshi, A. Fallahi, E. Mohajerani, M.-R. Fathollahi, F. A. Taromi, and M. Shahinpoor. *High-performance Bi-stage process in reduction of graphene oxide for transparent conductive electrodes.* Optical Materials, 64:366–375, 2017.

[21] K. S. Novoselov, V. I. Fal'ko, L. Colombo, P. R. Gellert, M. G. Schwab, and K. Kim. *A roadmap for graphene.* Nature, 490(7419):192–200, 2012.

[22] Y. Ohashi, T. Koizumi, T. Yoshikawa, T. Hironaka, and K. Shiiki. *Size Effect inthe In-plane Electrical Resistivity of Very Thin Graphite Crystals.* TANSO, 1997(180):235–238, 1997.

[23] X. He, W. Gao, Q. Zhang, L. Ren, and J. Kono. *Carbon-based terahertz devices.* In Automatic Target Recognition XXV, volume 9476, page 947612. International Society for Optics and Photonics, 2015.

[24] A. Pospischil, M. Humer, M. M. Furchi, D. Bachmann, R. Guider, T. Fromherz, and T. Mueller. *CMOS-compatible graphene photodetector covering all optical communication bands.* Nature Photonics, 7(11):892–896, 2013.

[25] X. Gan, R.-J. Shiue, Y. Gao, I. Meric, T. F. Heinz, K. Shepard, J. Hone, S. Assefa, and D. Englund. *Chip-integrated ultrafast graphene photodetector with high responsivity.* Nature Photonics, 7(11):883 – 887, 2013.

[26] S. Goossens, G. Navickaite, C. Monasterio, S. Gupta, J. J. Piqueras, R. Pérez, G. Burwell, I. Nikitskiy, T. Lasanta, T. Galán, and E. Puma. *Broadband image sensor array based on graphene–CMOS integration.* Nature Photonics, 11(6):366–371, 2017.

[27] F. Xia, T. Mueller, Y.-m. Lin, A. Valdes-Garcia, and P. Avouris. *Ultrafast graphene photodetector.* Nature nanotechnology, 4(12):839–843, 2009.

[28] F. H. L. Koppens, T. Mueller, P. Avouris, A. C. Ferrari, M. S. Vitiello, and M. Polini. *Photodetectors based on graphene, other two-dimensional materials and hybrid systems.* Nature Nanotechnology, 9(10):780–793, 2014.

[29] M. Liu, X. Yin, E. Ulin-Avila, B. Geng, T. Zentgraf, L. Ju, F. Wang, and X. Zhang. *A graphene-based broadband optical modulator.* Nature, 474(7349):64–67, 2011.

[30] Y. Hu, M. Pantouvaki, J. Van Campenhout, S. Brems, I. Asselberghs, C. Huyghebaert, P. Absil, and D. Van Thourhout. *Broadband 10 Gb/s operation of graphene electro-absorption modulator on silicon.* Laser & Photonics Reviews, 10(2):307–316, 2016.

[31] M. Liu, X. Yin, and X. Zhang. *Double-layer graphene optical modulator.* Nano Letters, 12(3):1482–1485, 2012.

[32] C. T. Phare, Y.-H. D. Lee, J. Cardenas, and M. Lipson. *Graphene electro-optic modulator with 30 GHz bandwidth.* Nature Photonics, 9(8):511–514, 2015.

[33] M. Mohsin, D. Neumaier, D. Schall, M. Otto, C. Matheisen, A. L. Giesecke, A. A. Sagade, and H. Kurz. *Experimental verification of electro-refractive phase modulation in graphene.* Scientific Reports, 5:10967, 2015.

[34] V. Sorianello, M. Midrio, G. Contestabile, I. Asselberghs, J. Van Campenhout, C. Huyghebaert, I. Goykhman, A. K. Ott, A. C. Ferrari, and M. Romagnoli. *Graphene–silicon phase modulators with gigahertz bandwidth.* Nature Photonics, 12(1):40–44, 2018.

[35] B. Yao, G. Soavi, T. Ma, X. Zhang, B. Fu, D. Yoon, S. A. Hussain, A. Lombardo, D. Popa, and A. C. Ferrari. *Gate controllable ultrafast fiber lasers based on graphene.* In CLEO: Science and Innovations, pages SF3K–6. Optical Society of America, 2018.

[36] T. Low and P. Avouris. *Graphene plasmonics for terahertz to mid-infrared applications.* ACS Nano, 8(2):1086–1101, 2014.

[37] Q. Bao, H. Zhang, Y. Wang, Z. Ni, Y. Yan, Z. X. Shen, K. P. Loh, and D. Y. Tang. *Atomic-layer graphene as a saturable absorber for ultrafast pulsed lasers.* Advanced Functional Materials, 19(19):3077–3083, 2009.

[38] Z. Sun, T. Hasan, F. Torrisi, D. Popa, G. Privitera, F. Wang, F. Bonaccorso, D. M. Basko, and A. C. Ferrari. *Graphene mode-locked ultrafast laser.* ACS Nano, 4(2):803–810, 2010.

[39] A. Marini, J. Cox, and F. G. De Abajo. *Theory of graphene saturable absorption.* Physical Review B, 95(12):125408, 2017.

[40] C. A. Zaugg, Z. Sun, V. J. Wittwer, D. Popa, S. Milana, T. S. Kulmala, R. S. Sundaram, M. Mangold, O. D. Sieber, M. Golling, Y. Lee, A. C. Ferrari, and U. Keller. *Ultrafast and widely tuneable vertical-external-cavity surface-emitting laser, mode-locked by a graphene-integrated distributed Bragg reflector.* Optics Express, 21(25):31548–31559, 2013.

[41] N. Tolstik, E. Sorokin, and I. T. Sorokina. *Graphene mode-locked Cr: ZnS laser with 41 fs pulse duration.* Optics Express, 22(5):5564–5571, 2014.

[42] G. Zhu, X. Zhu, F. Wang, S. Xu, Y. Li, X. Guo, K. Balakrishnan, R. A. Norwood, and N. Peyghambarian. *Graphene Mode-Locked Fiber Laser at 2.8 μm.* IEEE Photonics Technology Letters, 28(1):7–10, 2016.

[43] D. Purdie, D. G.and Popa, V. J. Wittwer, Z. Jiang, G. Bonacchini, F. Torrisi, S. Milana, E. Lidorikis, and A. C. Ferrari. *Few-cycle pulses from a graphene mode-locked all-fiber laser.* Applied Physics Letters, 106(25):253101, 2015.

[44] R. W. Boyd. *Nonlinear Optics.* Academic Press, 2003.

[45] S. A. Mikhailov. *Non-linear electromagnetic response of graphene.* Europhysics Letters, 79(2):27002, 2007.

[46] B. Kuyken, G. Roelkens, and R. Baets. *Nonlinear Optics (Course notes at Ghent University).* 2017.

[47] T. Gu, N. Petrone, J. F. McMillan, A. van der Zande, M. Yu, G.-Q. Lo, D.-L. Kwong, J. Hone, and C. W. Wong. *Regenerative oscillation and four-wave mixing in graphene optoelectronics.* Nature Photonics, 6(8):554 – 559, 2012.

[48] S.-Y. Hong, J. I. Dadap, N. Petrone, P.-C. Yeh, J. Hone, and R. M. Osgood Jr. *Optical third-harmonic generation in graphene.* Physical Review X, 3(2):021014, 2013.

[49] A. Säynätjoki, A.tjoki, L. Karvonen, J. Riikonen, W. Kim, S. Mehravar, R. A. Norwood, N. Peyghambarian, H. Lipsanen, and K. Kieu. *Rapid large-area multiphoton microscopy for characterization of graphene.* ACS Nano, 7(10):8441–8446, 2013.

[50] E. Dremetsika and P. Kockaert. *Enhanced optical Kerr effect method for a detailed characterization of the third-order nonlinearity of two-dimensional materials applied to graphene.* Physical Review B, 96(23):235422, 2017.

[51] R. Del Coso and J. Solis. *Relation between nonlinear refractive index and third-order susceptibility in absorbing media.* JOSA B, 21(3):640–644, 2004.

[52] W. Chen, G. Wang, S. Qin, C. Wang, J. Fang, J. Qi, X. Zhang, L. Wang, H. Jia, and S. Chang. *The nonlinear optical properties of coupling and decoupling graphene layers.* AIP Advances, 3(4):042123, 2013.

[53] E. Dremetsika, B. Dlubak, S.-P. Gorza, C. Ciret, M.-B. Martin, S. Hofmann, P. Seneor, D. Dolfi, S. Massar, P. Emplit, and P. Kockaert. *Measuring the nonlinear refractive index of graphene using the optical Kerr effect method.* Optics Letters, 41(14):3281–3284, 2016.

[54] N. Vermeulen, D. Castelló-Lurbe, J. Cheng, I. Pasternak, A. Krajewska, T. Ciuk, W. Strupinski, H. Thienpont, and J. Van Erps. *Negative Kerr nonlinearity of graphene as seen via chirped-pulse-pumped self-phase modulation.* Physical Review Applied, 6(4):044006, 2016.

[55] N. A. Savostianova and S. A. Mikhailov. *Optical Kerr effect in graphene: Theoretical analysis of the optical heterodyne detection technique.* Physical Review B, 97(16):165424, 2018.

[56] G. Soavi, G. Wang, H. Rostami, D. G. Purdie, D. De Fazio, T. Ma, B. Luo, J. Wang, A. K. Ott, D. Yoon, S. A. Bourelle, J. E. Muench, I. Goykhman, S. Dal Conte, M. Celebrano, A. Tomadin, M. Polini, G. Cerullo, and A. C. Ferrari. *Broadband, electrically tunable third-harmonic generation in graphene.* Nature Nanotechnology, 13:583–588, 2018.

[57] T. Jiang, D. Huang, J. Cheng, X. Fan, Z. Zhang, Y. Shan, Y. Yi, Y. Dai, L. Shi, K. Liu, C. Zeng, J. Zi, J. E. Sipe, Y.-R. Shen, W.-T. Liu, and S. Wu. *Gate-tunable third-order nonlinear optical response of massless Dirac fermions in graphene.* Nature Photonics, 12:430–436, 2018.

[58] G. Demetriou, F. Biancalana, E. Abraham, W. ji, Y. Wang, and A. K. Kar. *Negative Irradiance-Dependent Nonlinear Refraction in Single-Layer Graphene.* In Conference on Lasers and Electro-Optics, page JTu2A.115. Optical Society of America, 2018.

[59] S. A. Mikhailov. *Nonperturbative quasiclassical theory of the nonlinear electrodynamic response of graphene.* Physical Review B, 95(8):085432, 2017.

[60] R. M. Osgood, N. C. Panoiu, J. I. Dadap, X. Liu, X. Chen, I.-W. Hsieh, E. Dulkeith, W. Green, and Y. A. Vlasov. *Engineering nonlinearities in nanoscale optical systems: physics and applications in dispersion-engineered silicon nanophotonic wires.* Advances in Optics and Photonics, 1(1):162–235, 2009.

[61] D. J. Moss, R. Morandotti, A. L. Gaeta, and M. Lipson. *New CMOS-compatible platforms based on silicon nitride and Hydex for nonlinear optics.* Nature Photonics, 7(8):597–607, 2013.

Chapter 3

Nonlinear optics in graphene-covered waveguides

The material presented in this chapter has in part been published in references [1–6].

3.1 Introduction

In Chapter 2, graphene was introduced as a material for nonlinear optics. The context and literature were discussed and some theoretical background was provided. In this chapter, the experiments performed using graphene-covered waveguides within this PhD project will be discussed. The first experiment, a demonstration of gate-tunable saturable absorption in graphene-covered silicon (Si) waveguides, is presented in Section 3.2. In a sense this experiment stands somewhat separate for the other experiments discussed in this chapter. Firstly, because it is the only experiment using Si waveguides, secondly, because saturable absorption is *not* a simple third order nonlinear effect if measured with high-power pulses. Hence the theory developed in Section 2.5 is not adequate and a different model will be used. The remaining experiments have been performed using graphene covered silicon nitride (SiN) waveguides, the development of this platform is described in Section 3.3. The main reason for switching from Si to SiN is the strong optical nonlinearity (Kerr and two-photon absoprtion) in Si, which make it more difficult to intperpret the nonlinear measurements of graphene-covered silicon waveguides. Gate-tunable four-wave mixing and cross-modulation were demonstrated on this platform, the experiments and their interpretations are discussed in Sections 3.4 and 3.5. The possibility of using this platform for gate-tunable third harmonic generation is discussed in Section 3.6. Some conclusions are drawn in Section 3.7. Appendix A is closely related to this chapter, it contains a theoretical model which is used to interpret some of the experimental results.

3.2 Gate-tunable saturable absorption in graphene-covered Si waveguides

The first experiment that was performed in the context of this thesis was the demonstration of gate-tunable saturable absorption in graphene. As was mentioned above, saturable absorption is a well-known phenomenon in graphene, at high optical intensities the absorption of the material decreases due to band-filling and Pauli blocking. This experiment is distinct from the experiments presented later in this chapter (four-wave mixing and cross-modulation) in that it is performed using a picosecond pulsed laser, and that only nonlinear absorption, and no nonlinear refraction effects are probed.

3.2.1 Sample fabrication and measurement setup

The samples for this experiment were originally designed and fabricated by Yingtao Hu, in the context of the development of graphene electro-absorption modulators [7]. The device fabrication is summarized in figure 3.1**a**. The waveguides, grating couplers etc. are first defined and patterned using deep UV lithography. Phosphorous ion implantation is used to lower the electrical resistance of the Si (while keeping the optical loss acceptable, hence the different doping levels). A thermal oxide layer of ≈ 5 nm thick is then grown on the surface. The graphene is grown by chemical vapor deposition (CVD) on a $Si/SiO_2/Cu$ substrate and transferred using an elastomer stamp at Graphenea [8]. After this it is patterned through an oxygen plasma etch at Ghent University. Finally the doped silicon and the graphene were contacted in two different steps. More details on the fabrication can be found in reference [7]. Figure 3.1**b** shows a sketch of the final device. The silicon waveguide itself can be used as a gate for the graphene, due to the thin layer of thermal gate oxide. When applying a gate voltage V_{G} the charge carrier density in the graphene can be drastically tuned, changing its optical absorption. These waveguides have been used as efficient electro-absorption modulators [7]. In figure 3.1**c** typical mode profiles of a TE and a TM mode are plotted and figure 3.1**d** shows optical microscope and SEM images of the fabricated devices, note that monolayer graphene is clearly visible in the SEM. Waveguides are either optimized for TE or TM modes

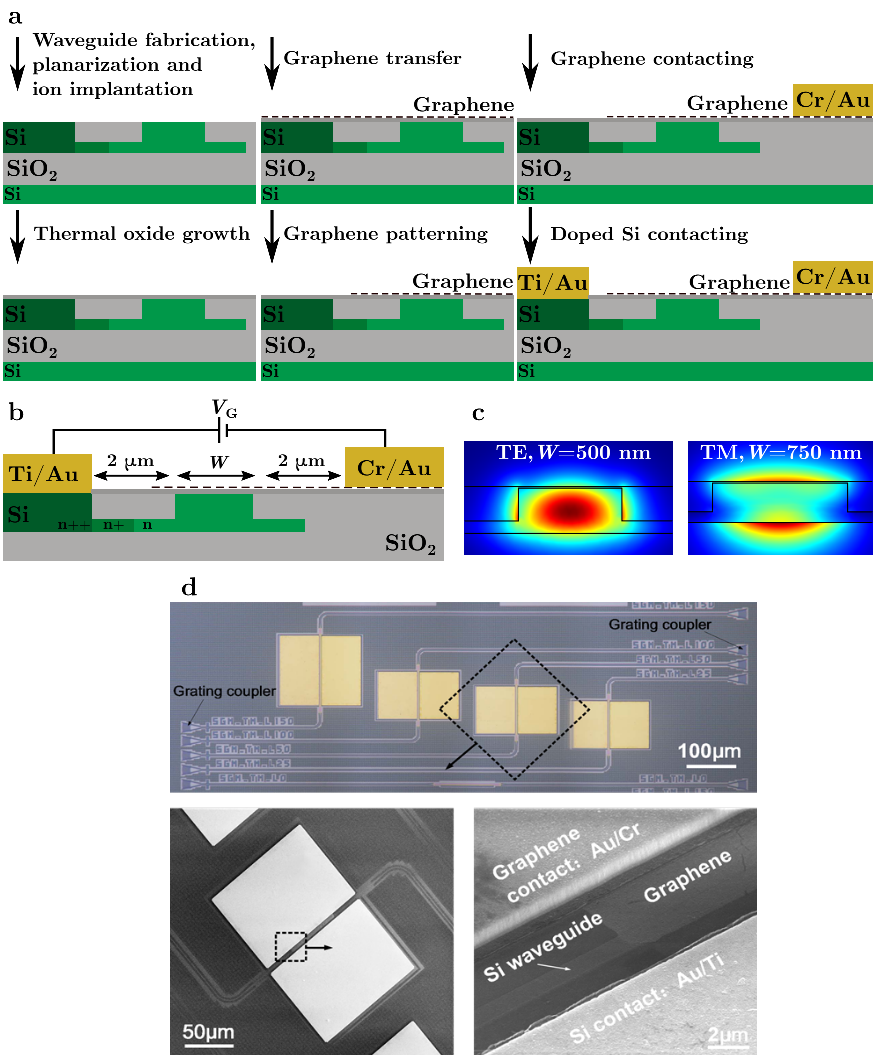
a
Waveguide fabrication, planarization and ion implantation
Graphene transfer
Graphene contacting
Graphene
Graphene
Cr/Au
Si
SiO₂
Si
Thermal oxide growth
Graphene patterning
Doped Si contacting
Graphene
Ti/Au
Graphene
Cr/Au
b
V_G
Ti/Au
2 µm
W
2 µm
Cr/Au
Si
n++
n+
n
SiO₂
c
TE, W=500 nm
TM, W=750 nm
d
Grating coupler
Grating coupler
100µm
50µm
Graphene contact: Au/Cr
Graphene
Si waveguide
Si contact: Au/Ti
2µm

Figure 3.1: **a** Fabrication steps for graphene-on-silicon waveguides. **b** Sketch of the cross-section of the final device, with applied gate voltage V_{G} (doping levels $n \approx 10^{18}\mathrm{cm}^{-3}$, $n+ \approx 10^{19}\mathrm{cm}^{-3}$, $n++ \approx 10^{20}\mathrm{cm}^{-3}$). **c** Examples of mode fields of a TE and a TM mode. **d** Optical micrograph (top) and SEM images (bottom) of the fabricated devices (taken from reference [7]).

depending on the grating couplers used.

The setup used for the saturable absorption measurements is shown in figure 3.2. Pulses from a Pritel, inc. FFL-1550-10 modelocked laser are amplified using a Pritel, inc. HPP-PMFA-20 high peak-power erbium doped

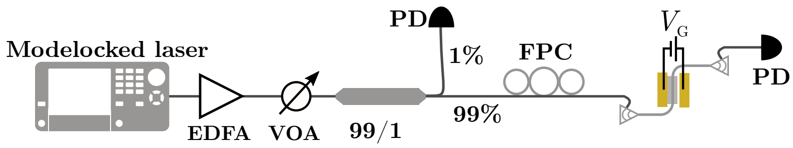

Figure 3.2: Setup used for the saturable absorption measurements. Modelocked laser: Pritel, inc. FFL-1550-10, EDFA: erbium-doped fiber amplifier. VOA: variable optical attenuator. PD: photodiode. FPC: fiber polarization controller. In the measurement presented in figure 3.4, a modelocked laser of type Calmar FM-SA-306-SN was used, without EDFA.

fiber amplifier (EDFA), producing pulses of about 8 ps long at 10 MHz repetition rate, with a central wavelength of 1550 nm. The pulses are then attenuated using a JDS Fitel HA9 variable optical attenuator (VOA), enabling us to tune the optical power without significantly changing the pulse shape. A splitter and photodiode are used to have a reference measurement of the optical power injected into the chip and a fiber polarization controller (FPC) is used to optimize the amount of light coupled into the waveguide. The power coupled out of the waveguide is detected with another photodiode (PD). Hence the transmission of the graphene-covered waveguide can be estimated as a function of voltage and input power. Using picosecond pulses and a relatively low repetition rate, the influence of free carriers generated by two-photon absorption in Si is minimized.

3.2.2 Experimental results

In figure 3.3**a**, the measured transmission as a function of the input peak power is plotted for different voltages, for a TM-waveguide of width 650 nm, with a graphene-covered section of 150 µm long. At low optical powers the transmission is independent of input power and the device behaves linearly. One can see that the absorption decreases when the gate voltage decreases. The graphene becomes increasingly p-doped and the occupation probability at $-\hbar\omega/2$ gradually decreases, reducing the number of available electrons and thus reducing the low-power absorption. In this regime the device operates as an electro-absorption modulator. At high input powers nonlinear effects play a significant role. On one hand one can see a clear initial decrease of optical loss, especially for the high positive voltages. This is a clear signature of saturable absorption. At higher powers however, the transmission drops drastically, this is a known complication of silicon waveguides and is due to very strong two-photon absorption (TPA) in silicon at telecommunication wavelengths [9]. Saturable absorption is caused by band-filling and subsequent Pauli-blocking in graphene (less electrons in the valence band

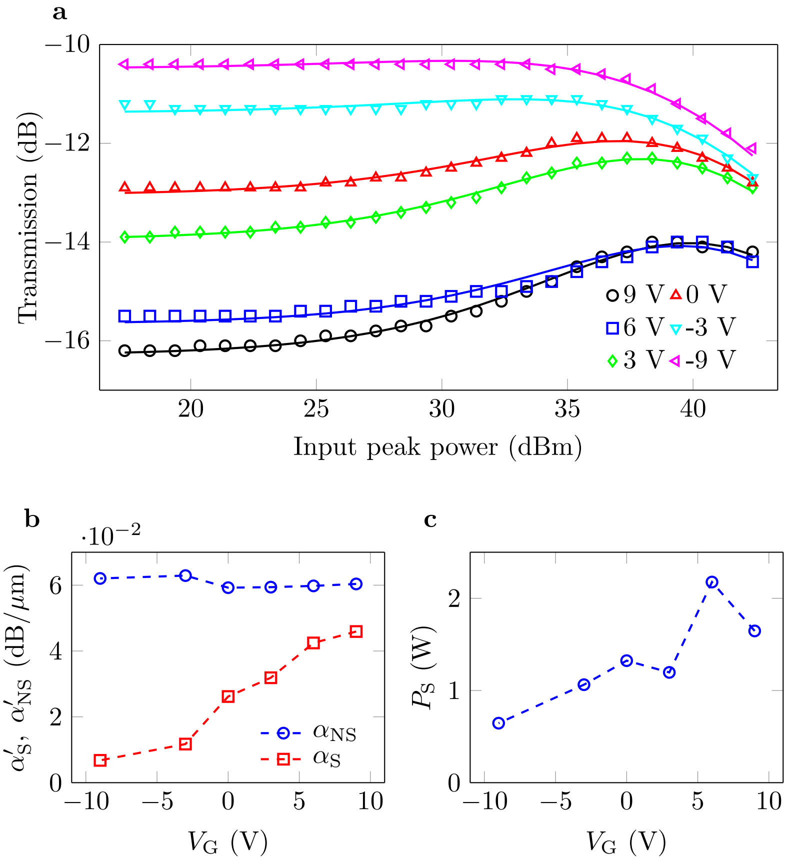

Figure 3.3: **a** Transmission as a function of input peak power for the TM mode of a hybrid graphene-covered Si waveguide. Measurements for different gate voltages are shown (see legend), the solid lines represent a theoretical fit. Pulse duration: ≈ 8 ps, wavelength: 1550 nm, waveguide width: 650 nm, graphene-covered length: 150 μm. **b**, **c** Saturable loss (α'_S), nonsaturable loss (α'_NS) and saturation power for the fits shown in figure **a** (solid lines). Using the phenomenological model in equation (3.1), as a function of gate voltage. An effective two-photon absorption coefficient $\beta'_\mathrm{TPA} = 100\ \mathrm{m}^{-1}\mathrm{W}^{-1}$ was used.

and unoccupied states in the conduction band are available for absorption). The saturable absorption modulation depth, defined as the ratio between the peak transmission and the the low-power transmission, amounts to 2.2 dB for $V_\mathrm{G} = 9$ V. At lower voltages, as the linear absorption drops, the relative effect of absorption saturation due to band-filling also becomes less pronounced. This causes TPA to dominate and brings the modulation depth down to 0 dB.

A simple phenomenological model based on equation (2.15) can be fitted to these results[1]. The power transmission through a section of graphene-covered waveguide can be modelled by the following differential equation,

$$\frac{\partial P(z)}{\partial z} = -\left[\alpha'_{\mathrm{NS}} + \frac{\alpha'_{\mathrm{S}}}{1+\frac{P(z)}{P_{\mathrm{S}}}} + \beta'_{\mathrm{TPA}} P(z)\right] P(z), \tag{3.1}$$

where $P(z)$ represents the optical power as a function of position along the waveguide z. α'_{NS} and α'_{S} represent respectively the contribution to the waveguide loss which does not saturate, and the contribution which saturates. P_{S} is the saturation power and β'_{TPA} the effective two-photon absorption coefficient of the waveguide. The primes in α'_{NS}, α'_{S} and β'_{TPA} denote that these parameters are effective waveguide parameters and not material parameters (as opposed the parameters in equation (2.15)). The devices discussed here also have significant sections of silicon waveguides which are not covered with graphene (see figure 3.1**d**), these can be modelled with acceptable accuracy by only maintaining the two-photon absorption term in equation (3.1). In figure 3.3**a**, the solid lines represent fits to the different measurements, using this model. In figure 3.3**b** and **c**, the corresponding fitting parameters are plotted. An effective two-photon absorption coefficient of $\beta'_{\mathrm{TPA}} = 100\ \mathrm{m}^{-1}\mathrm{W}^{-1}$ was used. This is a realistic value considering the (approximate) relation $\beta'_{\mathrm{TPA}} = \beta_{\mathrm{TPA}}/A_{\mathrm{eff}}$ [10] (where $\beta_{\mathrm{TPA}} \approx 0.5$ cm/GW [9] is the two-photon absorption coefficient of silicon and A_{eff} is the nonlinear effective area [10]).

In figure 3.4**a**, a measurement of the transmission versus peak power for a TE-waveguide of width 500 nm, also with a graphene-covered section of 150 µm long, is shown. For this measurement, the source was a different modelocked laser (Calmar FM-SA-306-SN) without EDFA, generating an estimated on-chip pulse duration of 4 ps, with central wavelenght of 1548 nm. The fits based on the equation (3.1) are represented by solid lines. In figures 3.4**c** and **d**, the corresponding fitting parameters are plotted, an effective TPA coefficient of $\beta'_{\mathrm{TPA}} = 260\ \mathrm{m}^{-1}\mathrm{W}^{-1}$ was used to obtain a good fit.

Comparing the nonlinear response of the TM and TE waveguides (figures 3.3**a** and 3.4**a**), one can clearly see that the saturable absorption is much less pronounced for the TE waveguide. This is illustrated by figure 3.4**b**. In this graph, the saturable absorption modulation depth is plotted for different voltages, for the TE and TM waveguide. The difference is due to the very distinct field profiles of the TE and TM modes. As can

---

[1] Note that the purely third-order model developed in Section 2.5 is not adequate for this experiment, since high peak-power pulses are used.

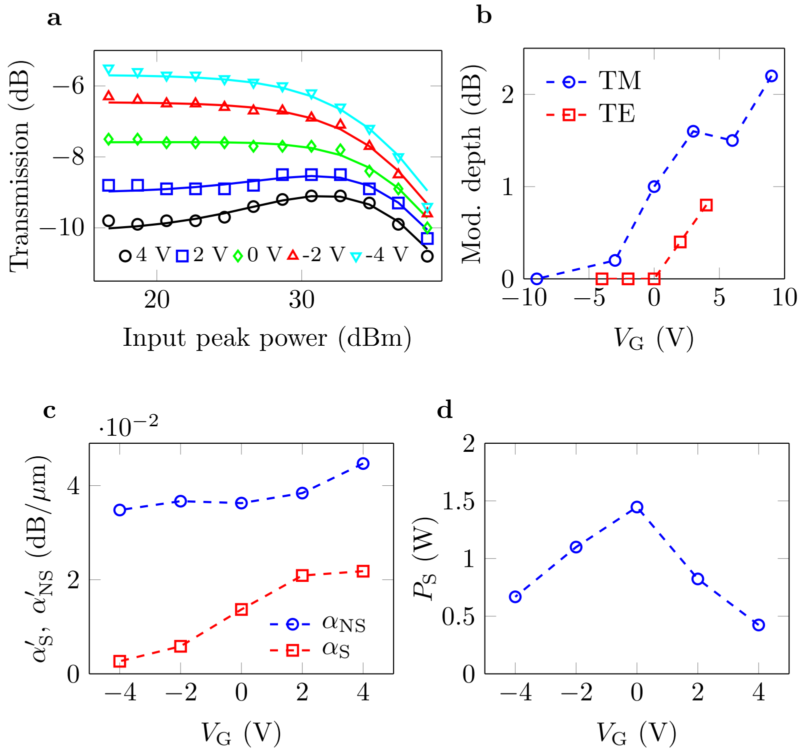

Figure 3.4: **a** Transmission as a function of input peak power for the TE mode of a hybrid graphene-covered Si waveguide. Measurements for different gate voltages are shown (see legend), the solid lines represent a theoretical fit. Pulse duration: ≈ 4 ps, wavelength: 1550 nm, waveguide width: 500 nm, graphene-covered length: 150 μm. **b** Comparison between the measured saturable absorption modulation depth for this TE-waveguide and the TM-waveguide characterized in figure 3.3**a**. **c**, **d** Saturable loss (α'_S), nonsaturable loss (α'_{NS}) and saturation power for the fits shown in figure **a** (solid lines). Using the phenomenological model in equation (3.1), as a function of gate voltage. An effective two-photon absorption coefficient $\beta'_{TPA} = 260\ \mathrm{m}^{-1}\mathrm{W}^{-1}$ was used.

be seen on figure 3.1**c**, the TE mode is much more confined in the waveguide core. The contribution of the TPA in silicon will as a consequence be much higher. Hence a β'_{TPA} of almost 3 times higher was used for the TE mode, and the 'roll-off' in the transmission curves due to TPA occurs at lower powers. Secondly, the interaction between the optical mode and the graphene is different for both modes. The interaction between the optical mode and the graphene is larger for TM than for TE modes. Intuitively, but incorrectly, one might attribute this to this high out-of-plane electric field component just outside the waveguide core for TM modes (see figure 3.1**c**). This is however incorrect as graphene is highly anisotropic and only interacts strongly with field components parallel to its plane. This high interaction is mainly caused by the longitudinal component of the electric field, which for silicon waveguides is almost as strong (though continuous) as the out-of-plane component in the vicinity of the interface.

3.2.3 Conclusion and comparison with literature

In conclusion we have demonstrated that the saturable absorption properties of graphene-covered silicon waveguides can be drastically tuned through electrostatic gating. We are not the first to demonstrate a change in the saturable absorption properties of graphene as a function of charge carrier density. Lee *et al.* have studied such effects for chemically doped graphene [11], and Baylam *et al.* using electrostatic gating [12]. We are the first however to demonstrate this effect on integrated waveguides. By making use of the high confinement and long interaction lengths inherent to such waveguides, the nonlinear interactions are strong and saturable absorption modulation depths exceeding 2 dB are demonstrated. An important material parameter of graphene as a saturable absorber is its saturation intensity I_S. By simulating the electric field components in-plane with the graphene and converting this to a local intensity, we estimate the saturation intensity in our measurements to be on the order of 100–200 MW/cm^2. This fits within the saturation intensities found in literature (0.71 MW/cm^2 in reference [13], ≈1-30 MW/cm^2 in reference [14], >100 MW/cm^2 in reference [15], 250 MW/cm^2 in reference [11], etc.). The spread of these published saturation intensities is very large, this might have to do with differences in quality of the used graphene samples. Higher quality graphene has a longer carrier lifetime so will saturate easier. Bao *et al.* also work with multilayer graphene [13] and Sun *et al.* use a graphene suspension. These might all behave differently. An other possible explanation of the discrepancies could be mistakes in the previously publised results, Lee *et al.* for example question the correctness of the very low saturation intensity published by Bao *et al.*. Yao *et al.* have recently demonstrated that gate-tunability of graphene-coated fibers can be used for tuning the operational regime (continuous-wave, Q-switching or mode-locking) of a modelocked fiber laser, as well as for stabilization of the timing jitter and tuning of the repetition rate (by tuning the linear properties through gating) [14]. By studying gate-tunable saturable absorption on an integrated waveguide platform, the results in this section can be the basis for the design of integrated modelocked lasers with similar properties. A notable disadvantage of silicon is the competition between the graphene saturable absorption and two-photon absorption in silicon. For the experiments discussed in the remainder of this chapter, we have switched to graphene-covered silicon nitride waveguides, in which two-photon absorption is negligible.

3.3 Gate-tunable graphene-covered SiN waveguides

Saturable absorption measurements were performed on graphene-covered silicon waveguides, as discussed in Section 3.2. It is clear that these waveguides can indeed be used to study graphene nonlinear optics, but that the silicon itself shows strong optical nonlinearities. For the experiments presented below (in Sections 3.4 and 3.5), we have also deposited graphene on integrated waveguides. Using a guided-wave approach we benefit from the high optical confinement and long interaction lengths, this enables us to perform our experiments at low powers, which assures that third order nonlinear effects are dominant. However we preferred not to use silicon waveguides because the strong third order nonlinear effects in silicon would introduce extra uncertainties in our measurements. As an alternative we used silicon nitride waveguides, third order nonlinear effects in these waveguides are over two orders of magnitude weaker than in silicon [16]. As the goal was to study the Fermi-energy dependence of the nonlinearities in graphene, we gated the graphene using a polymer electrolyte. This was an extra complication compared to silicon waveguides, since silicon can be made conductive and the waveguide itself can be used as a back-gate (see Section 3.2). Here, we elaborate on the fabrication of the graphene-on-SiN structures and the gating with the polymer electrolyte.

3.3.1 Fabrication

The initial fabrication steps were performed in a CMOS pilot line. The SiN waveguides and other integrated structures were patterned in a 330 nm thick SiN layer deposited by low pressure chemical vapor deposition (LPCVD) on top of a 3 µm buried oxide layer on a silicon handle wafer. The sample was then covered with LPCVD oxide and planarized by means of chemical mechanical polishing (CMP). Resulting in SiN structures covered by ≈ 1 µm of top-oxide. To obtain strong interaction between the light in the waveguide and a monolayer of gate-tunable graphene several subsequent processing steps are performed, they are summarized in figure 3.5 and described in more detail below.

Oxide thinning First, the top oxide needs to be thinned down significantly. Ideally, we want to obtain structures with a smooth surface, where

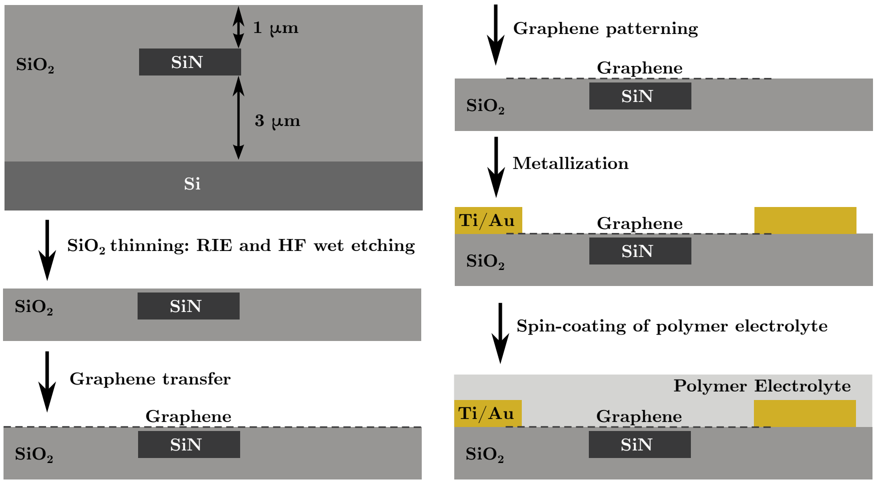
1 µm
SiO$_2$
SiN
3 µm
Si
SiO$_2$ thinning: RIE and HF wet etching
SiO$_2$
SiN
Graphene transfer
Graphene
SiO$_2$
SiN
Graphene patterning
Graphene
SiO$_2$
SiN
Metallization
Ti/Au
Graphene
SiO$_2$
SiN
Spin-coating of polymer electrolyte
Polymer Electrolyte
Ti/Au
Graphene
SiO$_2$
SiN

Figure 3.5: Fabrication flow of the graphene-on-silicon nitride photonics structures.

the oxide surface lies in the same plane as the waveguide top surface. Initially, this was attempted through wet etching using buffered oxide etch (BOE). The results are shown in figures 3.6**a**, **b**. It is clear that this results in very deep and irregular trenches next to the waveguide. This results in increased scattering losses and significant topology in the chip's surface. An alternative way of thinning down the oxide is through reactive ion etching (RIE) using a combination of SF_6 and O_2. However, as opposed to wet etching, the SiN structures themselves would also be significantly damaged when exposed to this etch recipe. This means that for the case of accidental over-etching, the chips would become useless. Moreover we get no feedback during the etch process and there tends to be quite some variability in the exact initial oxide thicknesses and the etch-rates of different chips. For our final devices, we opted to use a combination of the two etch recipes. First, we remove most of the top oxide through RIE, aiming for a remaining thickness of 100-200 nm. Subsequently, we use wet etching to thin down the oxide further. Before the second step, we perform an optical lithography step in which we cover the whole chip in resist, apart from some test structures (usually some alignment markers). We first etch the oxide on these structures in a step-wise manner, while carefully monitoring the surface with a profilometer (Dektak 150). This way we can estimate the exact residual thickness of the oxide, the etch rate and the appropriate etch time needed to planarize the whole chip. Figures 3.6**c**, **d** show the cross-sections of two waveguides planarized using this method. It is clear that there is

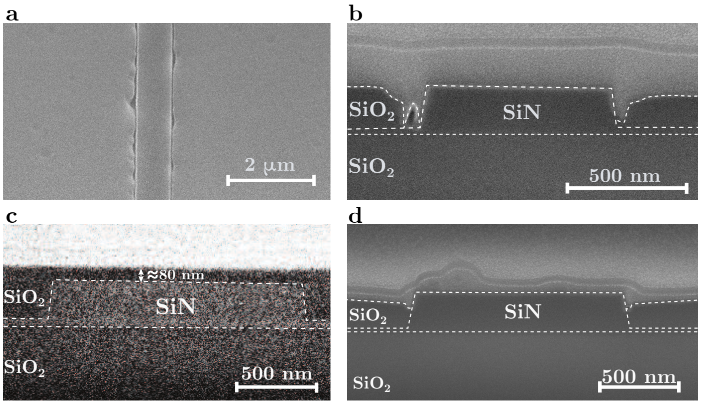

Figure 3.6: SEM pictures of waveguides planarized using different recipes. **a** Only wet etching, top view. **b** Only wet-etching, cross-section. **c, d** Combination of RIE and wet etching, cross-section.

still quite some variability in this process, both in the RIE and in the wet etching step, added variability is caused by slight non-uniformities in the initial oxide thickness. In figure 3.6**c**, a thin layer of oxide remains on top of the waveguide, resulting in a very flat surface, but a weaker interaction between the optical mode and materials deposited on the top surface. Figure 3.6**d** shows an example of slight over-etching, trenches of the kind seen in figures 3.6**a**, **b** are also present, be it to a much smaller extent.

Graphene transfer and patterning A graphene monolayer grown with chemical vapor deposition (CVD) is transferred to the samples by Graphenea [8]. After this, the graphene is patterned using a photolithography step and an etch step based on O_2 plasma (more details can be found in reference [17]).

Metallic contacts Metallic contacts (Ti/Au; typically ≈ 5 nm/300 nm) were deposited through a subsequent lithography step, metal evaporation and lift-off.

Polymer electrolyte deposition Finally the structures were covered with a polymer electrolyte. The electrolyte is dissolved in water and was spin-coated for 2 minutes at 6000 rpm. After this the remaining water was evaporated using a hotplate (1 min. at 100 °C). How the polymer electrolyte allows us to gate the sample is described in more detail below (Section 3.3.2).

Figure 3.7**a** shows an optical microscope image of a set of contacted graphene-covered waveguides, prior to the deposition of the polymer electrolyte. The SiN waveguides can be seen, as well as the grating couplers used to couple to the optical fibers. The graphene is not visible, therefore

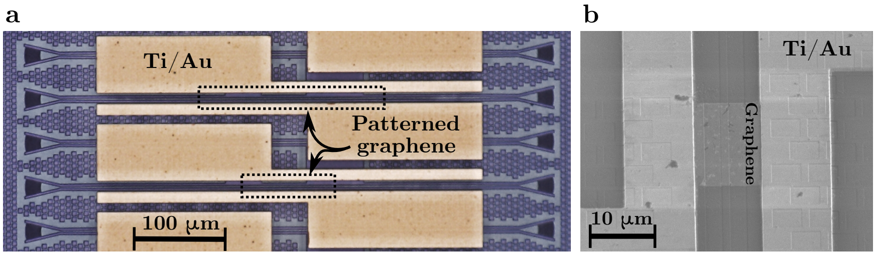

Figure 3.7: **a** Optical microscope image of a set of waveguides. The extent of the graphene (under the contacts) is shown by the dashed lines. **b** SEM image of one of the final devices. The patterned graphene can clearly be seen. Both images are taken on samples with no polymer electrolyte.

its extent is shown by the dashed lines. A more detailed picture is given by the SEM image in figure 3.7**b**, here the patterned graphene is clearly visible.

3.3.2 Electrostatic gating using a polymer electrolyte

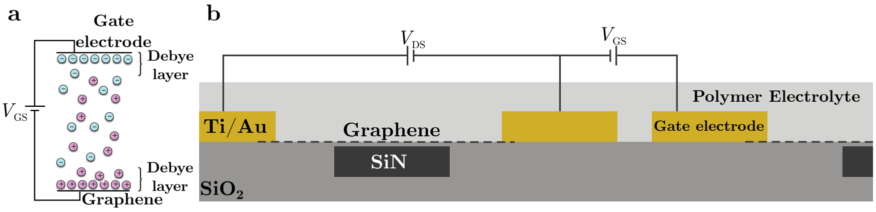

Figure 3.8: **a** A schematic illustration of the working principle of the polymer electrolyte gating. Li^+ (magenta) and $ClO_4{}^-$(cyan) ions and the Debye layers near the electrodes are shown (adapted from reference [18]). **b** Sketch of the cross-section of the graphene-on-SiN waveguides with polymer electrolyte.

A polymer electrolyte or ion gel (consisting of $LiClO_4$ and polyethylene oxide (PEO) in a weight ratio of 0.1:1) is used to gate the graphene, i.e. to electrostatically change its carrier density or Fermi energy. The working principle of the polymer electrolyte is schematically illustrated in figure 3.8**a**. After spin-coating and drying, the electrolyte consists of a polymer matrix with free ions, Li^+ and $ClO_4{}^-$. If a gate voltage is applied, as is shown in figure 3.8**a**, these ions will move through the matrix and accumulate at the ionic gel/gate electrode and ionic gel/graphene interfaces to counteract the applied electric field, forming so-called Debye layers [18]. A corresponding accumulation of charge carriers occurs in the electrode and the graphene layer and electrical double layers (EDL) are formed [19]. After reaching the equilibrium, most of the potential drop is situated within a few nanometers of the interfaces. The electric double layers effectively behave like two capacitor structures in series, with a spacing between the capacitor 'plates' of only a few nanometers [19]. This allows us to gate the graphene significantly with only moderate voltages, using a gate electrode which is not in the direct vicinity of the graphene. The dependence of the Fermi energy E_F on the gate voltage V_GS can be approximated by the following formula [18, 19]:

$$V_\mathrm{GS} - V_\mathrm{D} = \mathrm{sgn}(E_\mathrm{F}) \frac{eE_\mathrm{F}^2}{\hbar^2 v_\mathrm{F}^2 \pi C_\mathrm{EDL}} + \frac{E_\mathrm{F}}{e}, \tag{3.2}$$

with e the electron charge, $v_\mathrm{F} \approx 10^6$ m/s the Fermi velocity and C_EDL the electric double layer capacitance. V_D is the Dirac voltage, the voltage at which the graphene becomes intrinsic ($E_\mathrm{F} = 0$). The first term in equation (3.2) is due to the regular geometrical capacitance, it equates to $\phi = ne/C_\mathrm{EDL}$ using the relation beteen Fermi energy and electron density n; $E_\mathrm{F} = \hbar v_\mathrm{F}\sqrt{\pi n}$ [18, 19].[2] The second term is caused by the significant impact of band-filling/band-emptying in the graphene upon charging/discharging, which is non-negligible due to the large electric double layer capacitance and the small density-of-states of graphene, sometimes this contribution is described using the concept of an extra 'quantum' capacitance C_Q in series with the electric double layer [18, 19].

Figure 3.8**b** shows a sketch of the cross-section of the SiN waveguides. Each waveguide is covered with a certain length of patterned graphene, which is contacted at both sides. The whole sample is covered with the polymer electrolyte, this allows us to apply the gate voltage V_GS on one of the contacts of an adjacent waveguide structure, hereby tuning the charge carrier density in the graphene. By applying a small 'drain-source'[3] voltage V_DS across the graphene we can measure the resistance over the graphene sheet as a function of V_GS. Figure 3.9**a** shows such a resistance measurement. Since the resistivity of graphene is known to peak at $E_\mathrm{F} = 0$ [21], we can estimate the Dirac voltage through this measurement ($V_D \approx 0.64$ V in this specific case).

Figure 3.9**b** shows the optical loss as a function of the gate voltage, for a wavelength of 1550 nm. For this measurement, the propagation loss without

---

[2] These are the expressions are for n-doped graphene ($E_\mathrm{F} > 0$) at low temperatures, for p-doping, $\phi = -pe/C_\mathrm{EDL}$ and $E_\mathrm{F} = -\hbar v_\mathrm{F}\sqrt{\pi p}$ can be used, with p the hole density. Simulations have furthermore shown that this approach is to good approximation applicable at room temperature [20].

[3] We measure the 'field effect'; the change of conductance of a channel in response to applying a gate voltage, we thus reuse terminology used for semiconductor field-effect transistors.

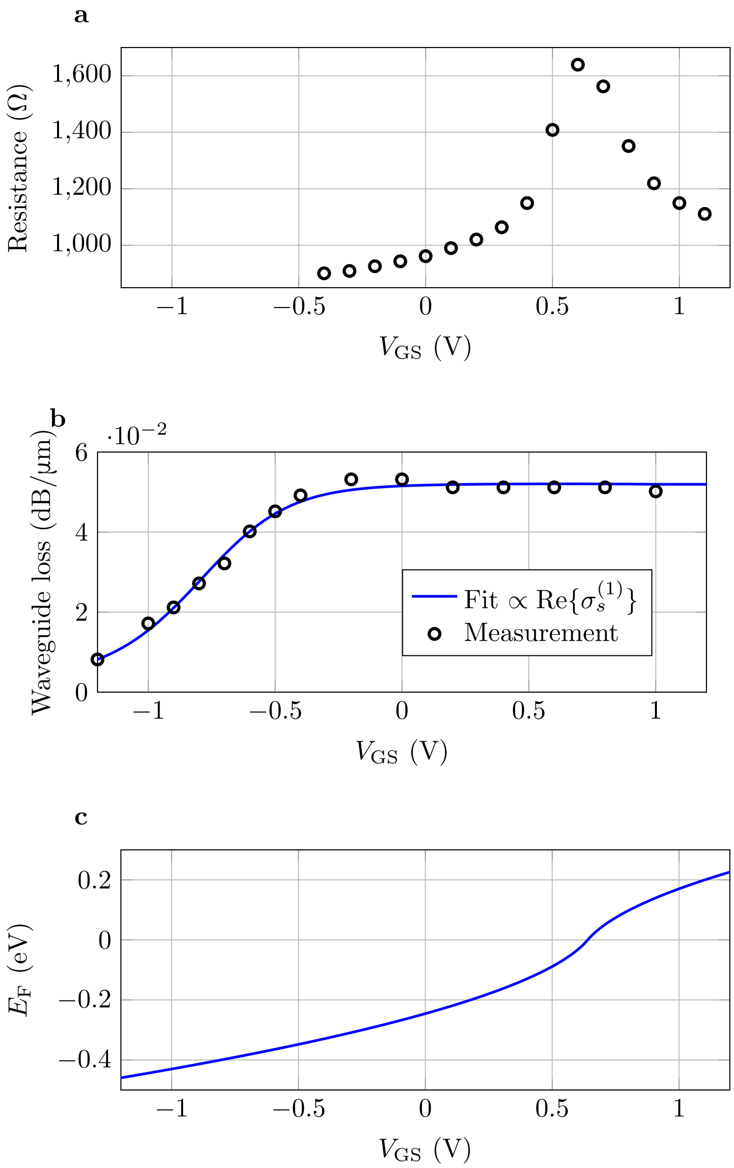

Figure 3.9: **a** The measured electrical resistance over the graphene as function of the gate voltage V_{GS}. **b** The measured optical loss for a wavelength of 1550 nm and corresponding fit, proportional to the real part of the linear conductivity of graphene $\sigma_s^{(1)}$. For waveguides with a width of 1600 nm. **c** Estimated relation between gate voltage V_{GS} and Fermi energy E_{F} of the graphene covering the waveguides.

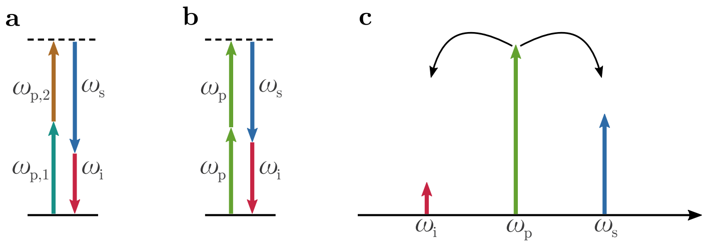

Figure 3.10: **a** Energy-level description of non-degenerate four-wave mixing. **b** Energy-level description of degenerate four-wave mixing. **c** Frequency components involved in degenerate four-wave mixing.

applying a gate voltage was first measured on a set of waveguides covered with different lengths of graphene. Then the voltage-dependent loss was measured on a single waveguide, from this the voltage-dependence of the propagation loss was extrapolated. The optical loss is proportional to the real part of the linear conductivity $\sigma_s^{(1)}$, which can be calculated using the equations (A.1, A.2) in Appendix A. By fitting this model to the measured propagation loss and using the relation between the gate voltage and Fermi energy in equation (3.2) $C_{\mathrm{EDL}} \approx 1.8 \cdot 10^{-2}$ F m^{-2} can be estimated (other used parameters for this fit were $\hbar\Gamma = 10$ meV and $T = 293$ K). The fit is also plotted in figure 3.9**b**. The resulting relation between Fermi energy and gate voltage using the fitted V_{D} and C_{EDL} values is shown in figure 3.9**c**.

3.3.3 Theory of nonlinear optics in graphene-covered SiN waveguides

For the experiments performed on the graphene-covered silicon nitride waveguides, we will assume that third order nonlinear effects are dominant. As discussed in Section 2.4, this is not trivial. However the on-chip optical powers are on the order of 10 mW or smaller, resulting in local intensities on the order of 10^{10} Wm^{-2}. For these intensities a third-order description should still be reasonably adequate (see Section 2.4.3 and reference [22]). In this case, the relevant coupled-wave equations for the nonlinear interaction between a set of monochromatic waves can be found in Section 2.5.

3.4 Four-wave mixing in graphene-covered SiN waveguides

Four-wave mixing (FWM) is one of the most commonly studied third order nonlinear processes. A FWM experiment typically involves two pump frequencies ($\omega_{\mathrm{p},1}$ and $\omega_{\mathrm{p},2}$), of which energy is transferred to two other frequencies of light, typically called the signal and idler, ω_{s} and ω_{i}. Energy conservation dictates that $\omega_{\mathrm{p},1} + \omega_{\mathrm{p},2} = \omega_{\mathrm{s}} + \omega_{\mathrm{i}}$. The energy-level description of this process is shown in figure 3.10**a**. In practice, four-wave mixing experiments are often performed in a degenerate regime, in this case a single pump wave ($\omega_{\mathrm{p},1} = \omega_{\mathrm{p},2} \equiv \omega_{\mathrm{p}}$) is used, the energy level description is shown in figure 3.10**b**, two identical pump photons are annihilated, and a signal and idler photon are created. The frequency components involved are sketched in figure 3.10**c**. Typically, both the pump and the signal beam are externally injected, in this case the signal experiences parametric amplification [23].

Intuitively, this process can be understood in terms of the intensity-dependent refractive index $n_2 + i\kappa_2$ (see Section 2.4.1). The pump and idler beam interfere and the total optical intensity contains a corresponding beat note at frequency $|\Delta\omega| = |\omega_{\mathrm{s}} - \omega_{\mathrm{p}}|$. Through the nonlinear index, the refractive index (and possibly the absorption, through a non-zero κ_2) of the medium is modulated with he same frequency. This modulation will generate sidebands on the pump, one generating the idler, and one constructively interfering with the already existing signal. It is clear that the signal and generated idler will also experience modulation and more sidebands can be created. Cascaded four-wave mixing is an important phenomenon in the generation of frequency combs in microresonators [24]. From this intuitive explanation it is also clear that FWM is a phase sensitive process, and that coherent built-up of the idler only occurs efficiently as long as phase-matching is ensured, $|2\beta(\omega_{\mathrm{p}}) - \beta(\omega_{\mathrm{s}}) - \beta(\omega_{\mathrm{i}})|L \approx |\beta_2(\Delta\omega)^2|L \ll \pi$, where β is the propagation constant of the mode, $\beta_2 \equiv \frac{\partial^2\beta}{\partial\omega^2}$ represents the group-velocity dispersion and L is the interaction length. In practice this means that four-wave mixing occurs efficiently over a limited band around the pump frequency (unless specific care is taken to engineer the dispersion [25]).

To indirectly characterize the nonlinear conductivity of graphene, we performed a degenerate four-wave mixing experiment on our graphene-covered SiN waveguides. In the following section, a mathematical description of the problem is given. Then the experiment and experimental results are described and finally the result are briefly compared with existing theoretical models.

3.4.1 Coupled-wave equations

For the case of degenerate four-wave mixing, only three monochromatic waves are involved, the pump, signal and idler, respectively at frequencies

ω_p, ω_s and ω_i at equally spaced intervals ($\Delta\omega = \omega_\mathrm{s} - \omega_\mathrm{p} = \omega_\mathrm{p} - \omega_\mathrm{i}$).

For this specific case, the coupled wave equations (equation (2.33)) can be simplified to:

$$\begin{aligned}\frac{\partial A_\mathrm{p}}{\partial z} &= i\{\gamma(\omega_\mathrm{p};\omega_\mathrm{p},\omega_\mathrm{p},-\omega_\mathrm{p})|A_\mathrm{p}|^2A_\mathrm{p} + 2\gamma(\omega_\mathrm{p};\omega_\mathrm{p},\omega_\mathrm{s},-\omega_\mathrm{s})|A_\mathrm{s}|^2A_\mathrm{p}\\ &+ 2\gamma(\omega_\mathrm{p};\omega_\mathrm{p},\omega_\mathrm{i},-\omega_\mathrm{i})|A_\mathrm{i}|^2A_\mathrm{p} + 2\gamma(\omega_\mathrm{p};\omega_\mathrm{s},\omega_\mathrm{i},-\omega_\mathrm{p})A_\mathrm{s}A_\mathrm{i}A_\mathrm{p}^*e^{-i\Delta\beta z}\}\\ &- \frac{\alpha(\omega_\mathrm{p})}{2}A_\mathrm{p},\end{aligned} \tag{3.3}$$

$$\begin{aligned}\frac{\partial A_\mathrm{s}}{\partial z} &= i\{\gamma(\omega_\mathrm{s};\omega_\mathrm{s},\omega_\mathrm{s},-\omega_\mathrm{s})|A_\mathrm{s}|^2A_\mathrm{s} + 2\gamma(\omega_\mathrm{s};\omega_\mathrm{s},\omega_\mathrm{p},-\omega_\mathrm{p})|A_\mathrm{p}|^2A_\mathrm{s}\\ &+ 2\gamma(\omega_\mathrm{s};\omega_\mathrm{s},\omega_\mathrm{i},-\omega_\mathrm{i})|A_\mathrm{i}|^2A_\mathrm{s} + \gamma(\omega_\mathrm{s};\omega_\mathrm{p},\omega_\mathrm{p},-\omega_\mathrm{i})A_\mathrm{p}A_\mathrm{p}A_\mathrm{i}^*e^{i\Delta\beta z}\}\\ &- \frac{\alpha(\omega_\mathrm{s})}{2}A_\mathrm{s},\end{aligned} \tag{3.4}$$

$$\begin{aligned}\frac{\partial A_\mathrm{i}}{\partial z} &= i\{\gamma(\omega_\mathrm{i};\omega_\mathrm{i},\omega_\mathrm{i},-\omega_\mathrm{i})|A_\mathrm{i}|^2A_\mathrm{i} + 2\gamma(\omega_\mathrm{i};\omega_\mathrm{i},\omega_\mathrm{p},-\omega_\mathrm{p})|A_\mathrm{p}|^2A_\mathrm{i}\\ &+ 2\gamma(\omega_\mathrm{i};\omega_\mathrm{i},\omega_\mathrm{s},-\omega_\mathrm{s})|A_\mathrm{s}|^2A_\mathrm{i} + \gamma(\omega_\mathrm{i};\omega_\mathrm{p},\omega_\mathrm{p},-\omega_\mathrm{s})A_\mathrm{p}A_\mathrm{p}A_\mathrm{s}^*e^{i\Delta\beta z}\}\\ &- \frac{\alpha(\omega_\mathrm{i})}{2}A_\mathrm{i},\end{aligned} \tag{3.5}$$

where $A_\mathrm{p}(z) \equiv A(\omega_\mathrm{p}, z)$, $A_\mathrm{s}(z) \equiv A(\omega_\mathrm{s}, z)$ and $A_\mathrm{i}(z) \equiv A(\omega_\mathrm{i}, z)$ are shorthand notations for the complex amplitudes of respectively the pump, signal and idler. $\Delta\beta = 2\beta(\omega_\mathrm{p}) - \beta(\omega_\mathrm{s}) - \beta(\omega_\mathrm{i})$ is the phase mismatch term. $\alpha(\omega)$ represents the linear loss and $\gamma(\omega_\mathrm{p} + \omega_q + \omega_r; \omega_\mathrm{p}, \omega_q, \omega_r)$ is the frequency dependent nonlinear parameter of the waveguide. Comparing with equation (2.33) and using equation (2.34) for the linear loss, these parameters become:

$$\alpha(\omega_j) = \frac{1}{2\mathscr{P}_j}\int_G \mathbf{e}^*(\omega_j)\cdot\sigma_s^{(1)}(\omega_j)\mathbf{e}(\omega_j)d\ell, \tag{3.6}$$

$$\begin{aligned}\gamma(\omega_j = \omega_\mathrm{p} + \omega_q + \omega_r; \omega_\mathrm{p}, \omega_q, \omega_r) =& i\frac{3}{N_{(p,q,r)}}\cdot\\ \sum_{k,l,m}\frac{1}{16\sqrt{\mathscr{P}_j\mathscr{P}_k\mathscr{P}_l\mathscr{P}_m}}&\int_G \mathbf{e}^*(\omega_j)\cdot\sigma_s^{(3)}(\omega_j;\omega_k,\omega_l,\omega_m)\vdots\mathbf{e}(\omega_k)\mathbf{e}(\omega_l)\mathbf{e}(\omega_m)d\ell.\end{aligned} \tag{3.7}$$

In equation (3.7), the summation parameters (k, l, m) take all different permutations of the set (p, q, r). $N_{(p,q,r)}$ is the number of permutations of the set (p, q, r).

For the four-wave mixing experiments presented in this section, the coupled-wave equations (3.3)-(3.5) can be further simplified. Firstly, the pump carries a much higher power than the signal, moreover the idler will be orders of magnitude weaker ($|A_\mathrm{p}| > |A_\mathrm{s}| \gg |A_\mathrm{i}|$). Secondly, in the experiments presented here the on-chip power levels were kept on the order of 10 mW or lower. Hence the assumption can be made that the nonlinear terms describing self- and cross-modulation are negligible compared to the linear loss terms, $|\gamma||A_\mathrm{p,s,i}|^2 \ll |\frac{\alpha(\omega)}{2}|$. As will become clear from the experiments that $|\gamma| < 10^4$ W^{-1}m^{-1}, and from figure 3.9**b** we know that $\frac{\alpha(\omega_\mathrm{pump})}{2} \sim 10^3 \ldots 10^4$ m^{-1}). This is also in line with our saturable absorption measurements on silicon (Section 3.2), where we concluded that significant saturation of the absorption only occurs for powers of the order of 1 W or higher. Thirdly, the phase mismatch is negligible ($L\beta_2\Delta\omega^2 \ll 1$, $L = \mathcal{O}(100\ \mu\mathrm{m})$, $\Delta\omega < 10^{13}$ rad/s and $\beta_2 \equiv \frac{\partial^2\beta}{\partial\omega^2}$ of a SiN waveguide is on the order of 10^{-25} s^2/m [16]). All these assumptions lead to heavily simplified coupled-wave equations:

$$\frac{\partial A_\mathrm{p}}{\partial z} \approx -\frac{\alpha(\omega_\mathrm{p})}{2}A_\mathrm{p}, \tag{3.8}$$

$$\frac{\partial A_\mathrm{s}}{\partial z} \approx -\frac{\alpha(\omega_\mathrm{s})}{2}A_\mathrm{s}, \tag{3.9}$$

$$\frac{\partial A_\mathrm{i}}{\partial z} \approx i\gamma(\omega_\mathrm{i};\omega_\mathrm{p},\omega_\mathrm{p},-\omega_\mathrm{s})A_\mathrm{p}A_\mathrm{p}A_\mathrm{s}^* - \frac{\alpha(\omega_\mathrm{i})}{2}A_\mathrm{i}. \tag{3.10}$$

Under these conditions the conversion efficiency η, defined as the ratio of the idler power to the signal power, has a quadratic dependence on the nonlinear parameter γ [26]:

$$\begin{aligned}\eta \equiv \frac{P_\mathrm{i}(L)}{P_\mathrm{s}(L)} = \frac{|A_\mathrm{i}(L)|^2}{|A_\mathrm{s}(L)|^2} \\ \approx |\gamma(\omega_\mathrm{i};\omega_\mathrm{p},\omega_\mathrm{p},-\omega_\mathrm{s})|^2 P_\mathrm{p}(0)^2 L_\mathrm{eff}^2 e^{\{\alpha(\omega_\mathrm{s})-\alpha(\omega_\mathrm{i})\}L} \\ \approx |\gamma(\omega_\mathrm{i};\omega_\mathrm{p},\omega_\mathrm{p},-\omega_\mathrm{s})|^2 P_\mathrm{p}(0)^2 L_\mathrm{eff}^2,\end{aligned} \tag{3.11}$$

where the effective interaction length is defined as:

$$L_\mathrm{eff} \equiv \frac{1-e^{-\{\alpha(\omega_\mathrm{p})+\alpha(\omega_\mathrm{s})/2-\alpha(\omega_\mathrm{i})/2\}L}}{\alpha(\omega_\mathrm{p})+\alpha(\omega_\mathrm{s})/2-\alpha(\omega_\mathrm{i})/2} \approx \frac{1-e^{-\alpha L}}{\alpha}. \tag{3.12}$$

The final expressions in equations (3.11) and (3.12) are only valid when the approximation $\alpha(\omega_\mathrm{p}) \approx \alpha(\omega_\mathrm{s}) \approx \alpha(\omega_\mathrm{i}) \equiv \alpha$ holds, i.e. when the frequencies detuning is small ($\Delta\omega \ll \omega_\mathrm{p}$). For the four-wave mixing experiments presented here, the expressions for α and γ can be further simplified. It is assumed that a flat sheet of graphene lies in the xz plane (this can easily be generalized to arbitrary graphene shapes). Firstly, the linear conductivity has only two nonzero elements, which are equal: $\sigma_{xx}^{(1)} = \sigma_{zz}^{(1)}$. Now we can treat the linear conductivity as a scalar parameter and calculate the linear loss as:

$$\alpha(\omega_j) = \frac{\sigma^{(1)}_{s,xx}(\omega_j)}{2\mathscr{P}_j} \int_G |\mathbf{e}(\omega_j)_{\parallel}|^2 d\ell, \tag{3.13}$$

where $\mathbf{e}(\omega_j)_{\parallel}$ is the electric field component tangential to the graphene sheet.

Moreover, simulations show that the modes in the SiN waveguides used here are quasi-TE, meaning that $\mathrm{e}_x \gg \mathrm{e}_z$. This implies that the term containing $\sigma^{(3)}_{s,\,xxxx}$ in equation (3.7) is about two orders of magnitude larger than any of all other terms. The expression for the nonlinear parameter can be simplified to:

$$\begin{aligned} &\gamma(\omega_\mathrm{i};\omega_\mathrm{p},\omega_\mathrm{p},-\omega_\mathrm{s}) \\ &\quad\approx i\frac{3\sigma^{(3)}_{s,\,xxxx}(\omega_\mathrm{i};\omega_\mathrm{p},\omega_\mathrm{p},-\omega_\mathrm{s})}{16\mathscr{P}_\mathrm{p}\sqrt{\mathscr{P}_\mathrm{i}\mathscr{P}_\mathrm{s}}} \int_G \mathrm{e}^*(\omega_\mathrm{i})_x \mathrm{e}(\omega_\mathrm{p})_x \mathrm{e}(\omega_\mathrm{p})_x \mathrm{e}^*(\omega_\mathrm{s})_x d\ell \\ &\quad\approx i\frac{3\sigma^{(3)}_{s,\,xxxx}(\omega_\mathrm{i};\omega_\mathrm{p},\omega_\mathrm{p},-\omega_\mathrm{s})}{16\mathscr{P}_\mathrm{p}^2} \int_G |\mathrm{e}(\omega_\mathrm{p})_x|^4 d\ell. \end{aligned} \tag{3.14}$$

To arrive to the second expression, we have used the assumption that $\mathrm{e}(\omega_\mathrm{p}) \approx \mathrm{e}(\omega_\mathrm{s}) \approx \mathrm{e}(\omega_\mathrm{i})$, which is the case when one considers the same spatial modes and small detunings ($\Delta\omega \ll \omega_\mathrm{p}$). Note that we also do not take the 'sum over different permutations of (ω_p, ω_p, $-\omega_\mathrm{s}$)', as was done in equation (3.7), this because the convention of intrinsic permutation symmetry implies that $\sigma^{(3)}_{s,\,xxxx}(\omega_\mathrm{i};\omega_\mathrm{p},\omega_\mathrm{p},-\omega_\mathrm{s}) = \sigma^{(3)}_{s,\,xxxx}(\omega_\mathrm{i};\omega_\mathrm{p},-\omega_\mathrm{s},\omega_\mathrm{p}) = \sigma^{(3)}_{s,\,xxxx}(\omega_\mathrm{i};-\omega_\mathrm{s},\omega_\mathrm{p},\omega_\mathrm{p})$ [23] [4].

We can further generalize this expression to arbitrary graphene shapes:

$$\gamma(\omega_\mathrm{i};\omega_\mathrm{p},\omega_\mathrm{p},-\omega_\mathrm{s}) \approx i\frac{3\sigma^{(3)}_{s,\,xxxx}(\omega_\mathrm{i};\omega_\mathrm{p},\omega_\mathrm{p},-\omega_\mathrm{s})}{16\mathscr{P}_\mathrm{p}^2} \int_G |\mathbf{e}(\omega_\mathrm{p})_{\parallel} \times \hat{\mathbf{e}}_z|^4 d\ell. \tag{3.15}$$

3.4.2 Experimental results

The setup used for the FWM experiment is shown in figure 3.11. A pump laser (Syntune S7500, $\lambda_\mathrm{p} \approx 1550$ nm) is amplified using an Erbium-doped fiber amplifier (EDFA), a tunable band-pass filter suppresses the Amplified Spontaneous Emission (ASE) of the EDFA. The signal is provided by a Santec Tunable Laser TSL-510. Pump and signal are coupled into the waveguide through a grating coupler. At the output a fiber Bragg grating (FBG) filters out the strong pump light and the signal and idler are visualized on an Anritsu MS9740A optical spectrum analyzer (OSA).

---

[4] Note that this equality is not valid for non-diagonal terms of the $\sigma_s^{(3)}$-tensor!

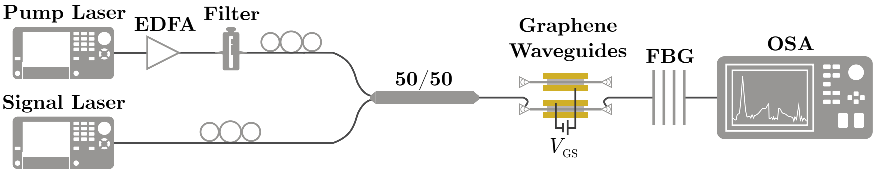

Figure 3.11: Setup used for the FWM experiments. EDFA: erbium-doped fiber amplifier, FBG: fiber Bragg grating, OSA: optical spectrum analyzer.

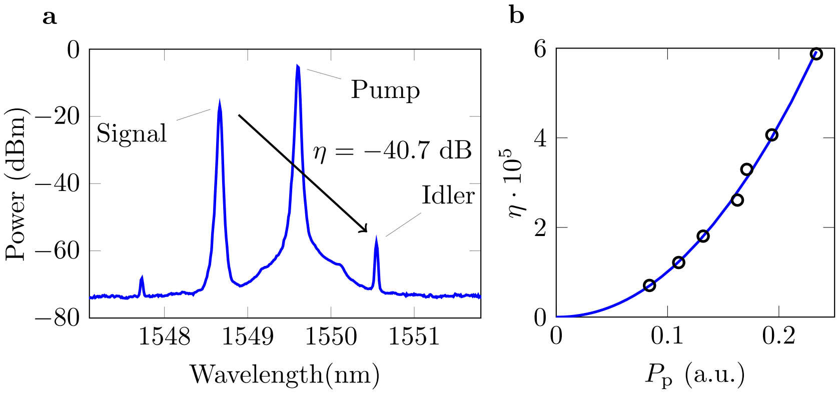

Figure 3.12: **a** Example of a FWM measurement on an ungated graphene-covered waveguide (L = 500 µm, waveguide width: 1200 nm). **b** FWM conversion efficiency versus detected pump power. The solid line represents a quadratic fit.

Figure 3.12**a** shows an example of a FWM measurement, for this measurement the FBG that filters out the pump has been removed for illustrative purposes. The measurement was also performed on an ungated sample. A strong pump (1549.61 nm) and a weaker signal (1548.67 nm) are injected. A clear peak at the idler wavelength (1550.55 nm) arises. Note that another small peak arises at 1547.73 nm, this is the result of a FWM process where the roles of the pump and the signal have been switched. The FWM conversion efficiency η can be easily read from this spectrum. On figure 3.12**b**, a plot of η as a function of pump power is shown. As is expected from equation (3.11), we observe a quadratic dependence.

To map the graphene nonlinearity in more detail, we performed an experiment where we measured the conversion efficiency as function of the signal-pump detuning $\Delta\lambda = \lambda_s - \lambda_p$ and gate voltage V_{GS}. Figure 3.13 summarizes the experimental results obtained for a 1600 nm wide waveguide covered with 100 µm of graphene and for a pump wavelength of $\lambda_p = 1550.18$

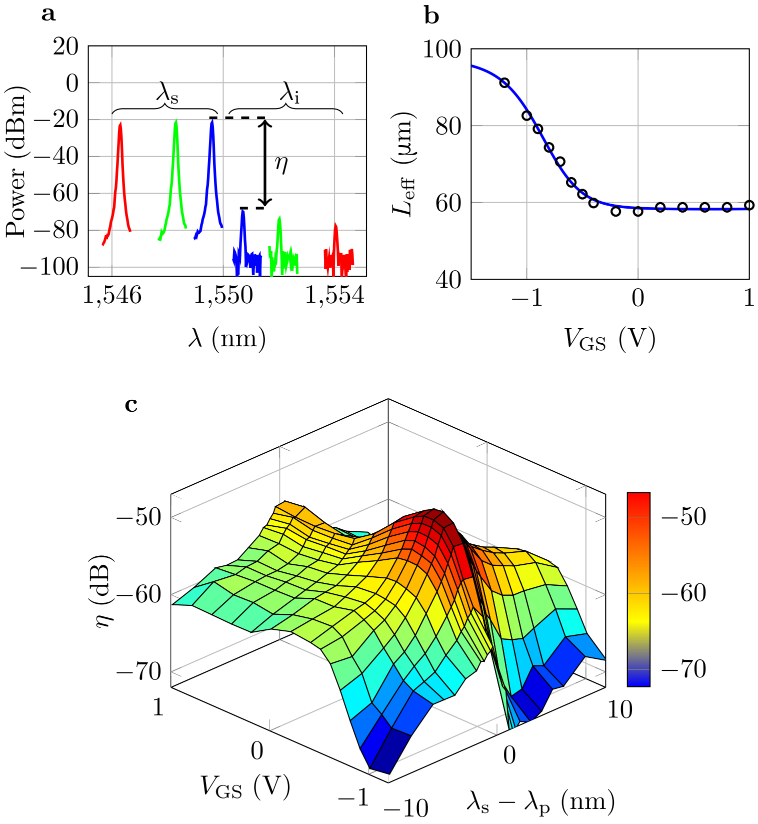

Figure 3.13: **a** Examples of the optical spectra ($V_{GS} = -0.5$ V). The pump peak (1550.18 nm) is filtered out by the FBG. The signal peaks can be seen on the left and the corresponding idler peaks on the right. Graphene section length: L =100 µm. **b** Effective length of the nonlinear interaction, calculated using the propagation loss in figure 3.9**b**, the black circles correspond to measured losses, the blue line is calculated using the fitted loss. **c** Conversion efficiency η as a function of V_{GS} and detuning $\lambda_s - \lambda_p$.

nm. In figure 3.13**a**, some of the measured spectra are plotted ($V_{\text{GS}} = -0.5$ V). The spectra are corrected for variations in the transmission of the grating couplers with changing wavelength. The propagation loss as a function of gate voltage for this waveguide can be found in figure 3.9**b**. Note that the absorption drops sharply for negative voltages, and that the interband absorption edge, $E_F = -\hbar\omega/2$ is reached for $V_{\text{GS}} \approx -0.8$ V. The corresponding effective interaction length L_{eff} of the FWM process is plotted in figure 3.13**b**. The measured conversion efficiencies are plotted in figure

3.13**c**, as a function of gate voltage and signal wavelengths. The estimated on-chip pump power for this measurement was $P_\mathrm{p}(0) = 10.5$ dBm. The FWM conversion efficiency depends strongly on both the detuning and the gate voltage. Note that the increase of η for a given detuning can be almost 10 dB between $V_\mathrm{GS} = 0$ V and $V_\mathrm{GS} \approx -0.6$ V, an increase that can not be explained by the slight increase in L_eff alone (figure 3.9**b**). Hence the nonlinear response itself changes drastically.

Using the derived expression for η (equation (3.11)), the known effective length (figure 3.9**b**) and the on-chip pump power, the magnitude of the nonlinear parameter $|\gamma(\omega_\mathrm{i}; \omega_\mathrm{p}, \omega_\mathrm{p}, -\omega_\mathrm{s})|$ can be readily estimated. One can then use equation (3.14) to relate this noninear parameter to the magnitude of the third order conductivity $|\sigma_s^{(3)}(\omega_i; \omega_p, \omega_p, -\omega_s)|$. The integral and power normalization constant $\mathscr{P}_\mathrm{p}$ in equation (3.14) are calculated using a COMSOL Multiphysics®-model of the cross-section of the waveguide. The graphene is located in the evanescent field of the optical mode, which decays approximately exponentially with distance from the waveguide core. Moreover, the conversion between γ and $\sigma_s^{(3)}$ scales with the fourth power of the local electric field in graphene (equation (3.14)). Getting a good estimate of the cross-sectional dimensions of the waveguides, and especially the thickness of the residual oxide that might still cover the nitride, is of utmost importance. For this the dimensions were estimated using a SEM image of the waveguide on which the nonlinear experiment was performed. This cross-section can be found in figure 3.6**c**. Figures 3.14**a** and 3.14**b** show the results of these conversions. The measured values for $|\gamma|$ and $|\sigma_s^{(3)}|$ have a sharp resonance as a function of detuning and a broad asymmetric resonance as a function of E_F. $|\gamma|$ is about 2800 $\mathrm{m}^{-1}\mathrm{W}^{-1}$ at small $|E_\mathrm{F}|$ (for minimum detuning) and about 6400 $\mathrm{m}^{-1}\mathrm{W}^{-1}$ at its absolute peak. The uncertainty on the measured $|\gamma| \approx \sqrt{\eta}/(P_\mathrm{p}(0)L_\mathrm{eff})$ results from the separate uncertainties on η, $P_\mathrm{p}(0)$ and L_eff. The biggest errors are introduced by $P_\mathrm{p}(0)$, through uncertainty or drift in the coupling. A conservative guess for this uncertainty would be ±1 dB. Likewise the uncertainty on the effective length (see figure 3.13**b**) is at worst only a couple of micrometer, so on the order of ±0.5 dB ≈ ±12%. This would lead to a total uncertainty of ≈ ±40%.

The estimated values for $|\sigma_s^{(3)}|$ can be as high as $4.3 \cdot 10^{-19}$ $\mathrm{Am}^2/\mathrm{V}^3$ for small detunings and $V_\mathrm{GS} \approx -0.5$ V ($E_\mathrm{F} \approx -0.35$ eV). However for low doping and larger detuning values, $|\sigma_s^{(3)}|$ seems to decay to values of the order 10^{-20} $\mathrm{Am}^2/\mathrm{V}^3$. These strong variations in the nonlinear response can already explain some of the variations than can be found in literature (see table 2.1). Hendry *et al.* reported a nonlinear susceptibility corresponding to $|\sigma_s^{(3)}| \approx 1.5 \cdot 10^{-20}$ $\mathrm{Am}^2/\mathrm{V}^3$ for a FWM experiment at large

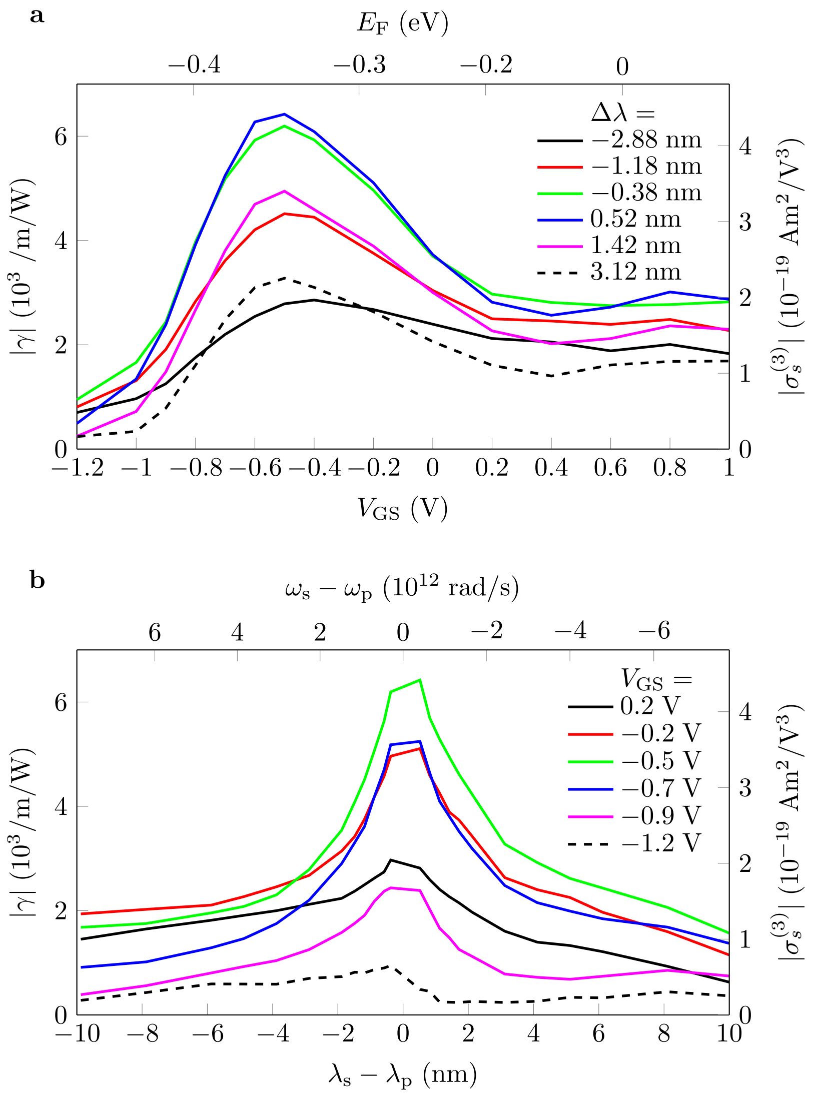

Figure 3.14: **a** Measured nonlinear parameter $|\gamma(\omega_\mathrm{i};\omega_\mathrm{p},\omega_\mathrm{p},-\omega_\mathrm{s})|$, and the corresponding graphene nonlinear conductivity $|\sigma_s^{(3)}(\omega_\mathrm{i};\omega_\mathrm{p},\omega_\mathrm{p},-\omega_\mathrm{s})|$, as a function of gate voltage and estimated Fermi energy for different values of signal-pump detuning $\Delta\lambda = \lambda_\mathrm{s} - \lambda_\mathrm{p}$ (see legend). **b** Measured $|\gamma(\omega_\mathrm{i};\omega_\mathrm{p},\omega_\mathrm{p},-\omega s)|$ and estimated $|\sigma_s^{(3)}(\omega_\mathrm{i};\omega_\mathrm{p},\omega_\mathrm{p},-\omega_\mathrm{s})|$ as a function of signal-pump detuning, both in wavelength difference (bottom axis) and angular frequency difference (top axis).

detuning (> 100 nm). The values we measure for $\Delta\lambda \to 0$ converge to $|\gamma(\omega_p;\omega_p,\omega_p,-\omega_p)|$ which is also the dominant term in self-phase modulation experiments using pulses of bandwidths smaller than the peaks in figure 3.14**b** (corresponding to pulse durations longer than about a ps). Two such experiments can for example be found in Zhang *et al.* [27] and Vermeulen *et al.* [28]. They respectively report values that are about one order of magnitude higher ($\approx 10^{-18}$ Am^2/V^3) and one order of magnitude lower ($\approx 10^{-20}$ Am^2/V^3) than what we measure. Here however, as explained in Section 2.4.3, there are several issues with some of the measurements in these papers which might explain order of magnitude differences (for example saturation of the nonlinear response at high peak powers) also differences in sample quality and environmental influences can cause some difference. These experiments are compared in more detail with the cross-modulation experiments presented in Section 3.5. Again we can make a rough estimate of the uncertainty of our $|\sigma_s^{(3)}|$-measurement. As discussed above a crude estimate of the error on the $|\gamma|$-measurement is $\approx \pm 40\%$. On top of this we have the potential error in the conversion between $|\gamma|$ and $|\sigma_s^{(3)}|$. The biggest contribution to this error is the uncertainty with respect to the cross-section of the waveguide, namely the thickness of the oxide on top of the waveguide. Simulations show that a change of 20 nm of this thickness changes the conversion with roughly 20%. This seems like a reasonable estimate for the error. This brings the total uncertainty of the measurement to about $\pm 60 - 70\%$.

3.4.3 Comparison with theoretical models

As was explained in Section 2.4.2, several theoretical models can be used to interpret these experimental results. Here, we try to use both the simple model introduced in Appendix A, as well as more advanced models from literature, to interpret our results.

Simple phenomenological model A first option is to use the simple model developed in Appendix A. This model takes into account the heating of the charge carrier distribution in graphene under strong illumination and the cooling due to the interaction with the environment, the nonlinearities stem from the intensity dependent changes in the linear optical response due to this change in charge carrier distribution. With a phenomenological energy relaxation time $\tau_{\mathcal{E}} = 500$ fs, we get the results plotted in figure 3.15. Figure 3.15**a** shows $|\sigma_s^{(3)}|$ as a function of Fermi energy, for different signal-pump detuning values. It is immediately clear that, despite being very simple, this model is able to grasp some of the main features of the four-wave mixing experiment. We see qualitatively similar behavior as function of Fermi energy, with a peak when approaching the interband absorption edge $E_\mathrm{F} = -\hbar\omega/2 \approx -0.4$ eV, and strong decay for higher doping levels. There are however differences, the model predicts a sharper resonance, and

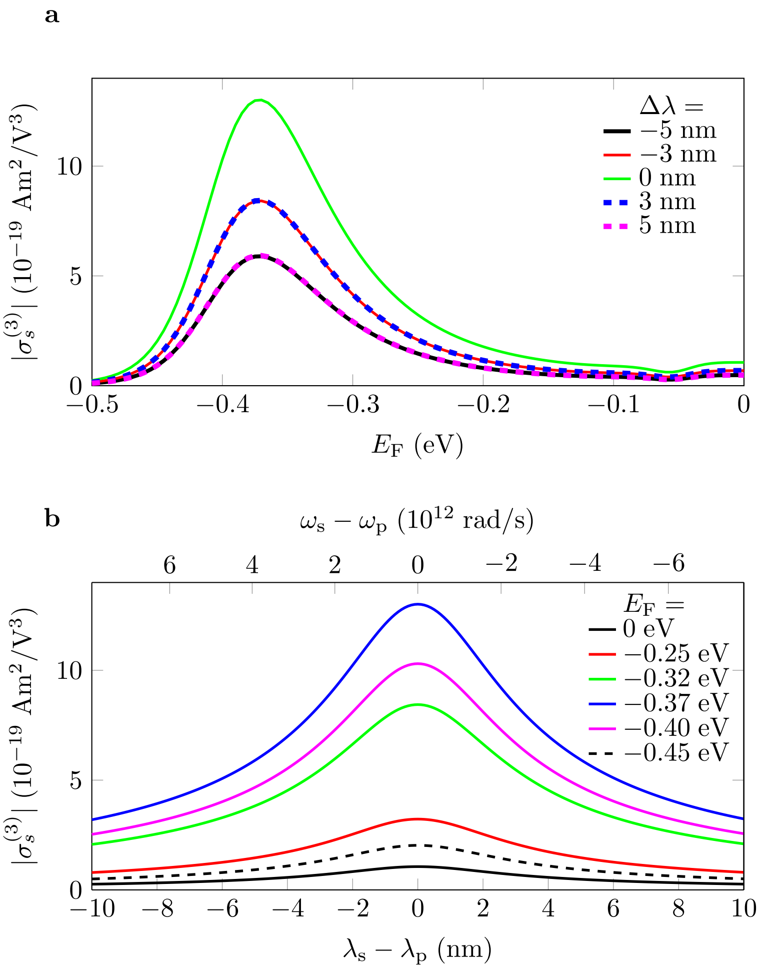

Figure 3.15: Simulated $|\sigma_s^{(3)}(\omega_\mathrm{i}; \omega_\mathrm{p}, \omega_\mathrm{p}, -\omega_\mathrm{s})|$, using the phenomenological model discussed in Appendix A. **a** $|\sigma_s^{(3)}|$ versus Fermi energy for different values of signal-pump detuning $\Delta\lambda = \lambda_\mathrm{s} - \lambda_\mathrm{p}$ (see legend). **b** $|\sigma_s^{(3)}|$ versus detuning for different Fermi energies (see legend). Model parameters: $k_\mathrm{B}T_0 = 25$ meV, $E_i = 100$ meV, $\tau_\mathcal{E} = 0.5$ ps, the pump wavelength is 1550 nm ($\hbar\omega_\mathrm{p} \approx 0.8$ eV).

a much smaller response at low doping. There can be multiple reasons for this, the model might be too approximate (for example the assumption that the carrier distribution can be modelled by a Fermi-Dirac distribution with a single chemical potential might not always hold), or might fail to take some of the contributions to the nonlinearity into account. Another cause of the differences can be variations in the Fermi energy along the waveguide length, causing us to measure a 'smeared out' (heterogeneously broadened) version of the actual E_F-dependence. Quantitatively, there is a difference at the peak of about a factor 3. This might be due to the same reasons mentioned before, or due to measurement uncertainties, for example on the estimate of $P_\mathrm{pump}(0)$ or the waveguide loss. Figure 3.15**b** shows $|\sigma_s^{(3)}|$ versus detuning, for different Fermi energies. Note that this is just a simple Lorentzian lineshape with damping rate $\tau_\mathcal{E}^{-1}$. Despite this simplicity and limited validity (probably for less than only a couple of nanometers of detuning, see Appendix A), it seems to describe the measured behavior quite well.

More advanced models[5] More elaborate models for the third order conductivity of graphene exist (see Section 2.4.2). We can compare our experimental results with a slightly modified version of the theory published in references [29, 30]. In these papers analytical expressions for the third order conductivity $\sigma^{(3)}_{s,\,\alpha\beta\gamma\delta}(\omega_1+\omega_2+\omega_3;\omega_1,\omega_2,\omega_3,E_\mathrm{F},\Gamma)$ were derived at $T=0$, where the relaxation rate Γ was assumed to be energy independent. Here we however assume that $\Gamma(E)$ is a function of the electron energy. This assumption is supported by both theoretical [31] and experimental [32] studies. An appropriate model is,

$$\Gamma(E) = \frac{\Gamma_0}{\left(1+E^2/E_0^2\right)^{\alpha/2}}, \tag{3.16}$$

where $0.5 \lesssim \alpha \lesssim 1$ is determined by the scattering mechanism ($\alpha = 1$ for impurity scattering) and E_0 is related to the density of impurities [31]. The quantities Γ_0, E_0 and α in equation (3.16) are treated as fitting parameters. In addition, to take into account the effects of nonzero temperatures, we can use the formula (the frequency arguments are omitted for clarity) [30]:

$$\begin{aligned}&\sigma^{(3)}_{s,\,\alpha\beta\gamma\delta}(E_\mathrm{F},\Gamma_0,E_0,\alpha,T) = \\ &\frac{1}{4T}\int_{-\infty}^{+\infty}\frac{\sigma^{(3)}_{s,\,\alpha\beta\gamma\delta}(E'_\mathrm{F},\Gamma_0,E_0,\alpha,T=0)}{\cosh^2\left(\frac{E_\mathrm{F}-E'_\mathrm{F}}{2T}\right)}dE'_\mathrm{F}.\end{aligned} \tag{3.17}$$

Figures 3.16**a** and 3.16**b** show the obtained theoretical dependencies of the absolute value of the third order conductivity $|\sigma^{(3)}_{s,\,xxxx}(\omega_\mathrm{i};\omega_\mathrm{p},\omega_\mathrm{p},-\omega_\mathrm{s})|$ on the Fermi energy and the detuning $\lambda_\mathrm{s}-\lambda_\mathrm{p}$. The parameters $\hbar\Gamma_0 = 2.5$ meV, $E_0 = 250$ meV and $\alpha = 0.8$ have been chosen so that good qualitative agreement was obtained with the experimental plots shown in figure 3.14.

---

[5] The simulations and adaptations to the theory summarized in this paragraph and in figure 3.16 were done by Sergey A. Mikhailov and Nadja A. Savostianova. More information can be found in reference [4].

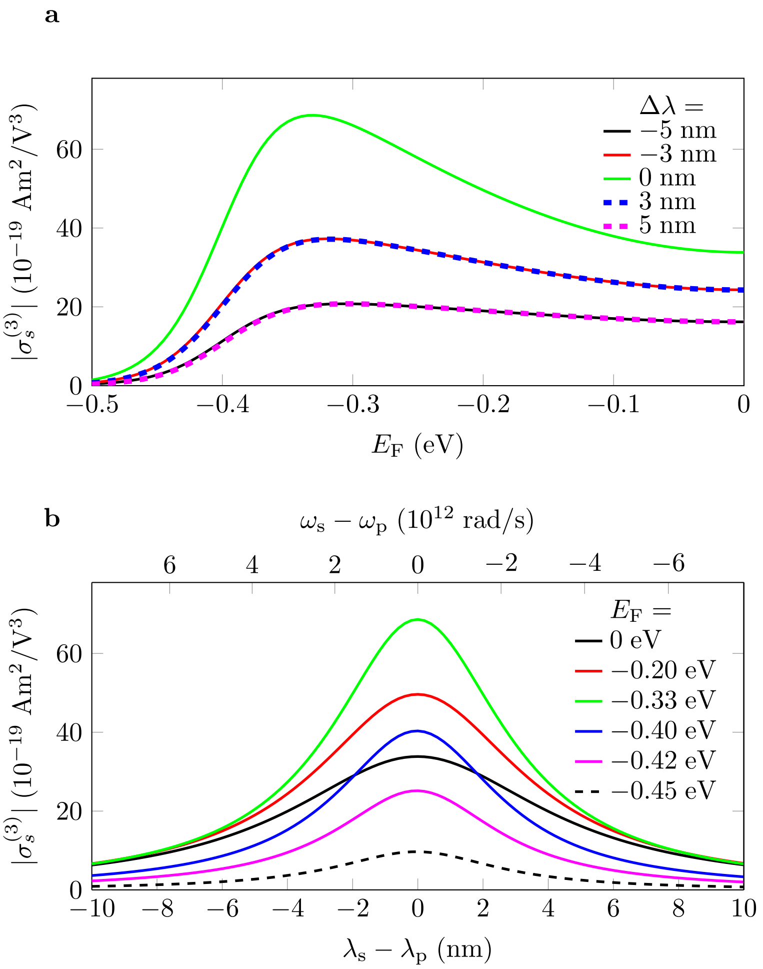

Figure 3.16: Simulated $|\sigma_s^{(3)}(\omega_\mathrm{i}; \omega_\mathrm{p}, \omega_\mathrm{p}, -\omega_\mathrm{s})|$, using an adapted version of the model from references [29, 30]. The pump wavelength is 1550 nm. **a** $|\sigma_s^{(3)}|$ versus Fermi energy for different values of signal-pump detuning $\Delta\lambda = \lambda_\mathrm{s} - \lambda_\mathrm{p}$ (see legend). **b** $|\sigma_s^{(3)}|$ versus detuning for different Fermi energies (see legend). The simulations were performed by Sergey A. Mikhailov and Nadja A. Savostianova.

One can see that, just like for the simpler phenomenological model, the theory indeed describes the most important features of the FWM response: a narrow resonance as a function of $\lambda_\mathrm{s} - \lambda_\mathrm{p}$ and a broad strongly asymmetric shape as a function of E_F; the inflection point in the vicinity of the interband absorption edge is also observed. The relative difference between peak and low-doping levels is in better correspondence with the measurements than for the simpler model. Quantitatively however, the theory again predicts higher values than what was measured, with a discrepancy of about an order of magnitude. In part, this discrepancy can have the same causes mentioned in the previous paragraph, such as measurement uncertainties, inhomogeneities in doping level and imperfections in the graphene the theory fails to take into account. This discrepancy, and the discrepancy in magnitude between the two different models, should be subject to further investigation.

3.5 Cross-amplitude and cross-phase modulation in graphene-covered SiN waveguides

The four-wave mixing experiment presented in the previous section gave detailed insight in some aspects of the nonlinear behavior of graphene. Namely strong variations with signal-pump detuning, as well as gate-tunability of the nonlinear response, were observed. However, the experiment can only be used to measure the magnitude of the nonlinear conductivity $|\sigma_s^{(3)}|$ ($\angle\sigma_s^{(3)}$ influences the phase of the generated idler, which is not easily observable). However, $\sigma_s^{(3)}$ is a complex parameter. Its real part ($\mathrm{Re}(\sigma_s^{(3)}) \propto \mathrm{Im}(\chi^{(3)})$) expresses power dependent changes in the optical absorption, whereas its imaginary part ($\mathrm{Im}(\sigma_s^{(3)}) \propto \mathrm{Re}(\chi^{(3)})$) expresses nonlinear changes in optical refraction. For many applications, such as all-optical signal processing, full knowledge of $\sigma_s^{(3)}$ is imperative.

In this section, our SiN waveguides covered with gated graphene are used to perform a simultaneous measurement of cross-amplitude and cross-phase modulation (XAM/XPM) between a relatively strong modulated pump and a weaker probe. Through this measurement we extract the full complex value of the waveguide nonlinear parameter γ, and a corresponding estimate of $\sigma_s^{(3)}$, as a function of gate voltage and pump-probe detuning.

First, a mathematical description of cross-modulation in waveguides will be given, then the experimental method will be described in detail. Finally the results will be analyzed and compared with theoretical calculations and related experiments from literature.

3.5.1 Coupled-wave equations

For the cross-modulation experiments presented in this part of the thesis, there are 2 quasi-monochromatic waves involved. The pump and the probe have respective frequencies ω_{pump} and ω_{probe}. The coupled wave equations (equation (2.33), with inclusion of a loss term) can be written as:

$$\begin{aligned}\frac{\partial A_{\text{pump}}}{\partial z} &= i\{\gamma(\omega_{\text{pump}};\omega_{\text{pump}},\omega_{\text{pump}},-\omega_{\text{pump}})|A_{\text{pump}}|^2 \\ &\quad + 2\gamma(\omega_{\text{pump}};\omega_{\text{pump}},\omega_{\text{probe}},-\omega_{\text{probe}})|A_{\text{probe}}|^2\}A_{\text{pump}} \\ &\quad - \frac{\alpha(\omega_{\text{pump}})}{2}A_{\text{pump}},\end{aligned} \tag{3.18}$$

$$\begin{aligned}\frac{\partial A_{\text{probe}}}{\partial z} &= i\{\gamma(\omega_{\text{probe}};\omega_{\text{probe}},\omega_{\text{probe}},-\omega_{\text{probe}})|A_{\text{probe}}|^2 \\ &\quad + 2\gamma(\omega_{\text{probe}};\omega_{\text{probe}},\omega_{\text{pump}},-\omega_{\text{pump}})|A_{\text{pump}}|^2\}A_{\text{probe}} \\ &\quad - \frac{\alpha(\omega_{\text{probe}})}{2}A_{\text{probe}},\end{aligned} \tag{3.19}$$

where $A_{\text{pump}}(z) \equiv A(\omega_{\text{pump}}, z)$ and $A_{\text{probe}}(z) \equiv A(\omega_{\text{probe}}, z)$ are the complex amplitudes of respectively the pump and probe. As was the case for four-wave mixing, these equations can be strongly simplified. Again on-chip powers are limited to about 10 mW, so the cross- and self modulation terms can in general be neglected. However the cross-modulation term in the equation of the probe ($2i\gamma|A_{\text{pump}}|^2 A_{\text{probe}}$) should be kept. This is because in the experiments presented below, the pump will be modulated at frequency Ω. Hence the cross-modulation term will add extra frequency components to the probe, which will be small in amplitude but can be distinguished from the unmodulated terms using the right techniques. The coupled-wave equations now look like:

$$\frac{\partial A_{\text{pump}}}{\partial z} \approx -\frac{\alpha(\omega_{\text{pump}})}{2}A_{\text{pump}}\ , \tag{3.20}$$

$$\begin{aligned}\frac{\partial A_{\text{probe}}}{\partial z} &\approx i2\gamma(\omega_{\text{probe}};\omega_{\text{probe}},\omega_{\text{pump}},-\omega_{\text{pump}})|A_{\text{pump}}|^2 A_{\text{probe}} \\ &\quad - \frac{\alpha(\omega_{\text{probe}})}{2}A_{\text{probe}}\ .\end{aligned} \tag{3.21}$$

The equation for the pump amplitude/power can be solved easily, leading to:

$$A_{\text{pump}}(z) = A_{\text{pump}}(0)e^{-\frac{\alpha(\omega_{\text{pump}})}{2}z}\ , \tag{3.22}$$

$$P_{\text{pump}}(z) \equiv |A_{\text{pump}}(z)|^2 = P_{\text{pump}}(0)e^{-\alpha(\omega_{\text{pump}})z}\ . \tag{3.23}$$

Substituting this in the differential equation for the probe, we get the following expression for the probe field as a function of z:

$$\begin{aligned}&A_{\text{probe}}(z) = \\ &\quad A_{\text{probe}}(0)e^{-\frac{\alpha(\omega_{\text{probe}})}{2}z}e^{i2\gamma(\omega_{\text{probe}};\omega_{\text{probe}},\omega_{\text{pump}},-\omega_{\text{pump}})P_{\text{pump}}(0)L_{\text{eff}}},\end{aligned} \tag{3.24}$$

where the effective length is defined as $L_{\text{eff}} \equiv \frac{1-e^{-\alpha(\omega_{\text{pump}})z}}{\alpha(\omega_{\text{pump}})}$. The expression for the propagation loss $\alpha(\omega_j)$ is given by equation (3.13), alternatively the linear loss can be calculated using a mode-solver. The nonlinear parameter $\gamma(\omega_{\text{probe}};\omega_{\text{probe}},\omega_{\text{pump}},-\omega_{\text{pump}})$ is, analogously to equation (3.14), given by,

$$\gamma(\omega_{\text{probe}};\omega_{\text{probe}},\omega_{\text{pump}},-\omega_{\text{pump}}) \approx i\frac{3\sigma^{(3)}_{s,\,xxxx}(\omega_{\text{probe}};\omega_{\text{probe}},\omega_{\text{pump}},-\omega_{\text{pump}})}{16\mathscr{P}^2_{\text{pump}}}\int_G |\mathbf{e}(\omega_{\text{pump}})_{\parallel}\times\hat{\mathbf{e}}_z|^4 d\ell\,. \tag{3.25}$$

Note that this is in general *not* the same γ-parameter as in the four-wave mixing case (equation (3.14)) for $\omega_{\text{p}} = \omega_{\text{pump}}$ and $\omega_{\text{s}} = \omega_{\text{probe}}$, since we are measuring the $\sigma_s^{(3)}$-function for different frequency arguments!

3.5.2 Measurement setup and methodology

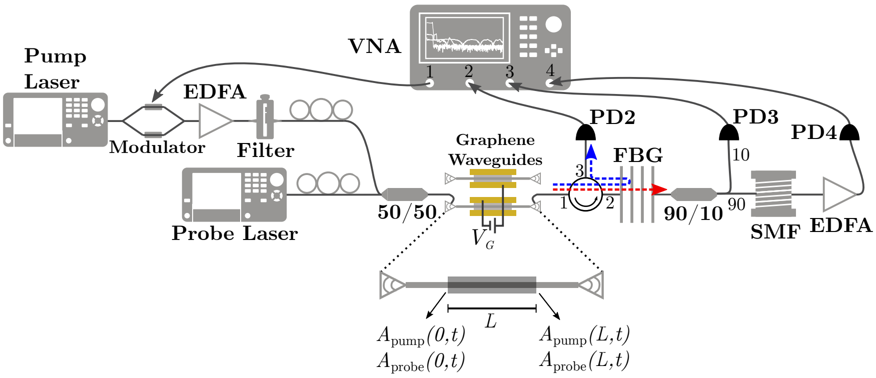

Figure 3.17: Sketch of the setup for the cross-amplitude/cross-phase modulation experiment. Red dotted arrow: path of the signal, blue dotted arrow: path of the pump. EDFA: erbium doped fiber amplifier, VNA: vector network analyzer, FBG: fiber Bragg grating, SMF: single mode fiber.

In the cross-modulation experiment, the pump is modulated at RF frequencies, we use a vector network analyzer (VNA) to sweep the modulation frequency and a dispersive fiber to distinguish amplitude from phase modulation. The method was in part based on reference [33][6]. The setup for this experiment is shown in figure 3.17. Through the modulator, the VNA will sinusoidally modulate the pump power, we will now assume the pump power at the start of the graphene-covered waveguide section to be:

---

[6] Wathen *et al.* have used a similar technique to measure the *ratio* between the real and imaginary part of γ [33], which serves as a commonly used figure-of-merit for nonlinear optics in dielectrics with significant two-photon absorption, such as silicon. We expanded their method to also get quantitative information on the *magnitude* of γ.

$$P_{\text{pump}}(0,t) = P_{\text{pump},0} + P_{\text{pump},\Omega}\cos(\Omega t). \tag{3.26}$$

Using equation (3.24), we can now write the complex amplitude of the probe field, at the end of the graphene-covered waveguide section, as:

$$\begin{aligned} &A_{\text{probe}}(L,t) = \\ &\qquad A_{\text{probe}}(0)e^{-\frac{\alpha(\omega_{\text{probe}})}{2}L}e^{i2\gamma L_{\text{eff}}[P_{\text{pump},0}+P_{\text{pump},\Omega}\cos(\Omega t)]}, \end{aligned} \tag{3.27}$$

where we have omitted the frequency arguments of γ for clarity, and where $A_{\text{probe}}(0)$ is the probe field at the waveguide input. In the experiment, the optical power is being measured at 3 different locations, using high-speed optical receivers, the resulting electrical signals are then fed to the ports of the VNA. The fiber Bragg grating (FBG) is chosen so that the probe wavelength is in its pass-band, and the pump wavelength ($\approx$ 1550 nm) is reflected, hence the total time-dependent optical power received by photodiode 2 (**PD2**) is:

$$\begin{aligned} P_{\text{PD2}}(t) &= T_2 \cdot P_{\text{pump}}(L, t-\tau_{g,2}) \\ &= T_2 \cdot [P_{\text{pump},0} + P_{\text{pump},\Omega}\cos(\Omega(t-\tau_{g,2}))] \cdot e^{-\alpha(\omega_{\text{pump}})L}, \end{aligned} \tag{3.28}$$

$\tau_{g,2}$ is the total group delay between the waveguide (at the end of the graphene-covered section) and the photodiode, approximately equal to $\beta_1\times$ (total fiber length), with $\beta_1 \equiv \frac{\partial\beta}{\partial\omega} = \frac{n_g}{c}$ and β and n_g are respectively the propagation constant and group index of the fiber. We assume that the total fiber length is on the order of several meters, moreover we are only interested in relatively low frequencies at this port, hence the group velocity dispersion $\beta_2 \equiv \frac{\partial^2\beta}{\partial\omega^2}$ can be ignored. T_2 is the total power loss between the waveguide (after the graphene section) and the photodiode: $T_2 = T_{\text{GC}}(\omega_{\text{pump}})T_{\text{circ.;1,2}}(\omega_{\text{pump}})T_{\text{circ.;2,3}}(\omega_{\text{pump}})R_{\text{FBG}}(\omega_{\text{pump}})$. With T_{GC}, R_{FBG} and $T_{\text{circ.;i,j}}$ the transmission (T) and reflection (R) functions of the grating coupler (GC), FBG and circulator (circ.).

The FBG transmits only the probe field. We can calculate the time-dependent probe field amplitude at photodiode 3 (**PD3**):

$$A_{\text{PD3}}(t) \approx t_3 A_{\text{probe}}(0)e^{-\frac{\alpha(\omega_{\text{probe}})}{2}L}e^{i2\gamma L_{\text{eff}}[P_{\text{pump},0}+P_{\text{pump},\Omega}\cos(\Omega(t-\tau_{g,3}))]}, \tag{3.29}$$

from this the power can be calculated as:

$$
\begin{aligned}
P_{\mathrm{PD3}}(t) &= |A_{\mathrm{PD3}}(t)|^2 \\
&= T_3 P_{\mathrm{probe}}(0) e^{-\alpha(\omega_{\mathrm{probe}})L} e^{-4\mathrm{Im}(\gamma) L_{\mathrm{eff}}[P_{\mathrm{pump},0} + P_{\mathrm{pump},\Omega}\cos(\Omega(t-\tau_{g,3}))]} \\
&\approx T_3 P_{\mathrm{probe}}(0) e^{-\alpha(\omega_{\mathrm{probe}})L} e^{-4\mathrm{Im}(\gamma) L_{\mathrm{eff}} P_{\mathrm{pump},0}} \cdot \\
&\qquad [1 - 4\mathrm{Im}(\gamma) L_{\mathrm{eff}} P_{\mathrm{pump},\Omega} \cos(\Omega(t-\tau_{g,3}))],
\end{aligned} \tag{3.30}
$$

where $T_3 = T_{\mathrm{GC}}(\omega_{\mathrm{probe}}) T_{\mathrm{circ.;1,2}}(\omega_{\mathrm{probe}}) T_{\mathrm{FBG}}(\omega_{\mathrm{probe}}) T_{\mathrm{splitter,10\%}}(\omega_{\mathrm{probe}})$ ($\equiv |t_3|^2$), T_{FBG} is the FBG transmission spectrum and $T_{\mathrm{splitter,10\%}}$ is the power transmission to the 10 % port of the splitter. $\tau_{g,3}$ is the total group delay in the path to **PD3**.

To calculate the field at photodiode (**PD4**), we have to take into account group velocity dispersion due to the long length of single mode fiber (SMF). For this we start by approximating the field amplitude at the end of the waveguide (equation (3.24)) by:

$$
\begin{aligned}
&A_{\mathrm{probe}}(L,t) \approx \\
&\qquad A_{\mathrm{probe}}(0) e^{-\frac{\alpha(\omega_{\mathrm{probe}})}{2}L} e^{i2\gamma L_{\mathrm{eff}} P_{\mathrm{pump},0}} [1 + i2\gamma L_{\mathrm{eff}} P_{\mathrm{pump},\Omega} \cos(\Omega t)].
\end{aligned} \tag{3.31}
$$

This approximation is based on the assumption that $\gamma L_{\mathrm{eff}} P_{\mathrm{pump},\Omega} \ll 1$, which is the case for our experiments. The optical field amplitude at the photodiode is,

$$
\begin{aligned}
A_{\mathrm{PD4}}(t) &\approx t_4 A_{\mathrm{probe}}(0) e^{-\frac{\alpha(\omega_{\mathrm{probe}})}{2}L} e^{i2\gamma L_{\mathrm{eff}} P_{\mathrm{pump},0}} \cdot \\
&\qquad [1 + i2\gamma L_{\mathrm{eff}} P_{\mathrm{pump},\Omega} \cos(\Omega(t-\tau_{g,4})) e^{\frac{i\beta_2 L_{\mathrm{SMF}}\Omega^2}{2}}],
\end{aligned} \tag{3.32}
$$

where $\tau_{g,4}$ is again the total group delay for the path to the photodiode, and $\beta_2 \equiv \frac{\partial^2\beta}{\partial\omega^2}$ represents the group velocity dispersion of the fiber, L_{SMF} is the total single mode fiber length. $T_4 = |t_4|^2 = T_{\mathrm{GC}}(\omega_{\mathrm{probe}})$ $T_{\mathrm{circ.;1,2}}(\omega_{\mathrm{probe}}) T_{\mathrm{FBG}}(\omega_{\mathrm{probe}}) T_{\mathrm{splitter,90\%}}(\omega_{\mathrm{probe}})$ $T_{\mathrm{SMF}}(\omega_{\mathrm{probe}}) G_{\mathrm{EDFA}}(\omega_{\mathrm{probe}})$, were $T_{\mathrm{splitter,90\%}}$ is the transmission to the 90 % port of the splitter, T_{SMF} the power transmission of the SMF and G_{EDFA} the gain of the EDFA. The power on **PD4** is then,

$$
\begin{aligned}
P_{\mathrm{PD4}}(t) &= |A_{\mathrm{PD4}}(t)|^2 \\
&\approx T_4 P_{\mathrm{probe}}(0) e^{-\alpha(\omega_{\mathrm{probe}})L} e^{-4\mathrm{Im}(\gamma) L_{\mathrm{eff}} P_{\mathrm{pump},0}} \cdot \\
&\qquad [1 + 2|\gamma|^2 L_{\mathrm{eff}}^2 P_{\mathrm{pump},\Omega}^2 \\
&\qquad - 4|\gamma| L_{\mathrm{eff}} P_{\mathrm{pump},\Omega} \sin\left(\frac{\beta_2 L_{\mathrm{SMF}}\Omega^2}{2} + \angle\gamma\right) \cos\left(\Omega(t-\tau_{g,4})\right) \\
&\qquad + 2|\gamma|^2 L_{\mathrm{eff}}^2 P_{\mathrm{pump},\Omega}^2 \cos\left(2\Omega(t-\tau_{g,4})\right)].
\end{aligned} \tag{3.33}
$$

From the perspective of the vector network analyzer (VNA), the whole optical system between the RF-port of the modulator and the RF-ports of the receivers is treated as a black-box. All the VNA does is measure the frequency dependent scattering parameters between input and output. For this specific experiment we only apply a drive signal through port 1 of the VNA, and measure scattering parameters S_{21}, S_{31} and S_{41}. Subsequently we can calculate **(a)**, $\mathrm{Im}(\gamma)$ from S_{31} and S_{21} and **(b)**, $\angle\gamma$ from S_{41}.

(a) We can estimate $|\mathrm{Im}\gamma|$ from $|S_{31}|/|S_{21}|$,

$$\begin{aligned}\frac{|S_{31}|}{|S_{21}|} &= 4\frac{R_{\mathrm{PD3}}T_3P_{\mathrm{probe}}(0)|\mathrm{Im}(\gamma)|L_{\mathrm{eff}}e^{-\alpha(\omega_{\mathrm{probe}})L}e^{-4\mathrm{Im}(\gamma)L_{\mathrm{eff}}P_{\mathrm{pump},0}}}{R_{\mathrm{PD2}}T_2e^{-\alpha(\omega_{\mathrm{pump}})L}} \\ &\approx 4\frac{R_{\mathrm{PD3}}T_3}{R_{\mathrm{PD2}}T_2}|\mathrm{Im}(\gamma)|L_{\mathrm{eff}}P_{\mathrm{probe}}(0),\end{aligned} \tag{3.34}$$

for the last approximation we make use of the observations that $\mathrm{Im}(\gamma)$ $L_{\mathrm{eff}}P_{\mathrm{pump},0} \ll 1$ and that the pump-probe detuning is usually small, so we can neglect dispersion in the optical absorption term $\alpha(\omega_{\mathrm{probe}}) \approx \alpha(\omega_{\mathrm{pump}})$. R_{PDi} is the responsivity of the respective i^{th} photodiode.

To derive the sign of $\mathrm{Im}(\gamma)$ we can use the observation that:

$$\angle S_{31} - \angle S_{21} = \begin{cases} -(\tau_{g,3} - \tau_{g,2})\Omega & \text{if} \quad \mathrm{Im}(\gamma) < 0 \\ -(\tau_{g,3} - \tau_{g,2})\Omega + \pi & \text{if} \quad \mathrm{Im}(\gamma) > 0 \end{cases}, \tag{3.35}$$

and consequently that,

$$\lim_{\Omega\to 0}(\angle S_{31} - \angle S_{21}) = \begin{cases} 0 & \text{if} \quad \mathrm{Im}(\gamma) < 0 \\ \pi & \text{if} \quad \mathrm{Im}(\gamma) > 0 \end{cases}. \tag{3.36}$$

(b) On the other hand, we can use S_{41} to estimate $\angle\gamma$,

$$|S_{41}| \propto \left|\sin\left(\frac{\beta_2 L_{\mathrm{SMF}}\Omega^2}{2} + \angle\gamma\right)\right|. \tag{3.37}$$

By measuring the S_{41} parameter with a high enough bandwidth and using a long enough fiber, $\angle\gamma$ can be estimated through a sinusoidal fit, provided the sign of β_2 is known (which is the case for standard SMF) and $\mathrm{sgn}(\mathrm{Im}(\gamma))$ has been estimated as described in **(a)**.

It is now clear that these observations can be used to estimate the complex value of γ, through estimation of its imaginary part and phase. In principle this method can also be used by only using 3 ports of the VNA, as $\mathrm{Im}(\gamma)$ can also be estimated from $\lim_{\Omega\to 0}\frac{S_{41}}{S_{21}}$, however then a good knowledge of the EDFA amplification is necessary.

Influence of fiber nonlinearities

In the above derivation, we have assumed for simplicity that we could neglect nonlinear effects in the input fiber. This is for example the case for experiments presented in reference [33], where the pump and probe were combined in free-space. In our experiments, in particular the influence of the fiber section between the 50/50 splitter and the chip has a non-negligible influence that has to be taken into account. The fiber section between splitter and grating coupler has length $L_{\mathrm{SMF,in}}$ and a nonlinear coefficient γ_{SMF}. The pump power in this fiber section is, $\frac{P_{\mathrm{pump}}(0,t)}{T_{\mathrm{GC}}(\omega_{\mathrm{pump}})}$, hence we have to substitute $A_{\mathrm{probe}}(0)$ in equation (3.24) by $A_{\mathrm{probe}}(0)\exp\left(i2\frac{\gamma_{\mathrm{SMF}}P_{\mathrm{pump}}(0,t)L_{\mathrm{SMF,in}}}{T_{\mathrm{GC}}(\omega_{\mathrm{pump}})}\right)$. This implies that using the method described above, rather than $\gamma(\omega_{\mathrm{probe}};\omega_{\mathrm{probe}},\omega_{\mathrm{pump}},-\omega_{\mathrm{pump}})$ of the graphene-covered waveguide alone, we measure:

$$\gamma = \gamma(\omega_{\mathrm{probe}};\omega_{\mathrm{probe}},\omega_{\mathrm{pump}},-\omega_{\mathrm{pump}}) + \gamma_{\mathrm{SMF}}\frac{L_{\mathrm{SMF,in}}}{L_{\mathrm{eff}}T_{\mathrm{GC}}(\omega_{\mathrm{pump}})}, \tag{3.38}$$

hence we have to correct the obtained values accordingly. In the the experiments described in this paper, $L_{\mathrm{SMF,in}} \approx 1.77$ m and $\gamma_{\mathrm{SMF}} = \frac{2\pi n_2}{\lambda A_{\mathrm{eff}}} = 0.0013$ /W/m [34] (for a standard SMF, $\frac{n_2}{A_{\mathrm{eff}}} = 3.18\cdot 10^{-10}$ /W [35]). In the measurements presented in this work, this correction is small but non-negligible, on the order of 800 $\mathrm{m}^{-1}\mathrm{W}^{-1}$ (varies slightly with gating/effective length).

3.5.3 Experimental results

The cross-modulation experiment described here was performed on a waveguide with a width of 1400 nm, covered with graphene over a length of 50 µm. As was the case for the FWM experiment, the graphene is gated through a polymer electrolyte. On figure 3.18, measurements of the graphene resistance (figure 3.18**a**) and waveguide loss (figure 3.18**b**) are shown. Following the procedure described in Section 3.3.2, the Dirac voltage and electric double layer capacitance of this sample are respectively estimated to be $V_{\mathrm{D}} \approx 0.6$ eV and $C_{\mathrm{EDL}} \approx 1.82\cdot 10^{-2}$ F m^{-2}. The resulting relation between Fermi energy and voltage is plotted in figure 3.18**c**. The grey area in this figure denotes the parameter range for which the cross-modulation experiment discussed below is performed.

Using the methodology introduced in the previous section, the complex value of $\gamma(\omega_{\mathrm{probe}};\omega_{\mathrm{probe}},\omega_{\mathrm{pump}},-\omega_{\mathrm{pump}})$ was estimated for a range of different gate voltages and probe wavelengths ($\lambda_{\mathrm{pump}} = 1550.18$ nm). For every single one of these parameter combinations a measurement of the S-parameters was performed and analyzed. It is not possible to show all the

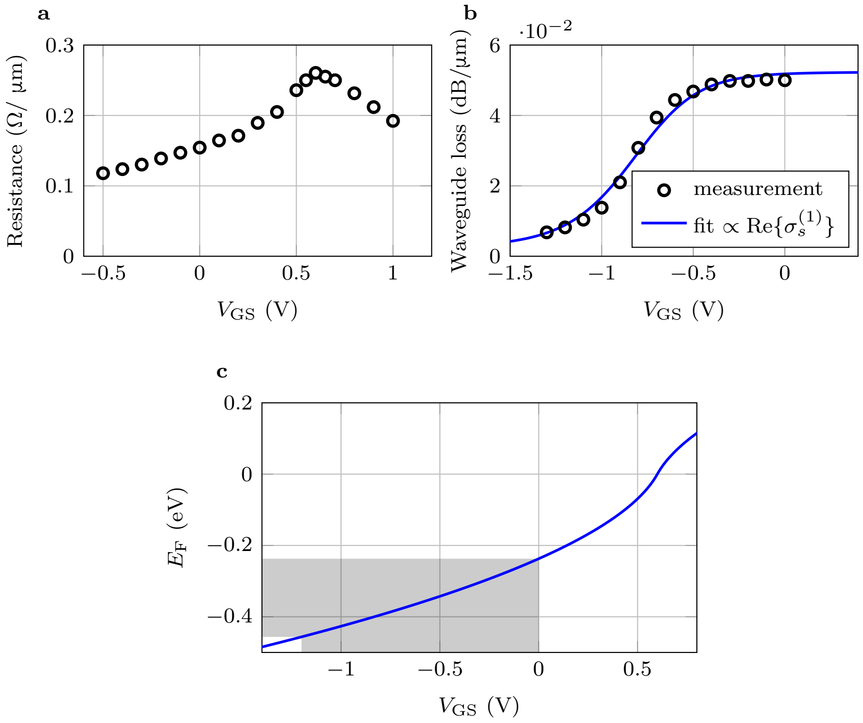

Figure 3.18: **a** The measured electrical resistance per unit of length (of the graphene section) over the graphene as function of the gate voltage V_{GS}. Measured on a device with an 800 µm long graphene section. **b** The measured optical loss for a wavelength of 1550 nm and corresponding fit, proportional to the real part of the linear conductivity of graphene $\sigma_s^{(1)}$. For waveguides with a width of 1400 nm. **c** Estimated relation between gate voltage V_{GS} and Fermi energy E_{F} of the graphene covering the waveguides. The range of gate voltages and corresponding Fermi energies for which the cross-modulation experiment was performed is shown by the shaded area.

data, however figure 3.19 shows some examples of measured S-parameters as an illustration.

In figure 3.19**a**, $|S_{21}|$ and $|S_{31}|$ are plotted, for $V_{\mathrm{GS}} = 0$ V and $\lambda_{\mathrm{probe}} = 1551$ nm. From equation (3.34) we know that $|S_{31}|/|S_{21}|$ is proportional to $|\mathrm{Im}(\gamma)|$ in the low-frequency limit. At these ports, two Thorlabs PDB480C-AC receivers were used, with bandwidths limited to ≈ 1.8 GHz. Note that since we only look at low frequencies the limited bandwidth is not an issue. From equation (3.34) one can see that, to obtain proper normalization, the only necessary parameters are the on-chip probe power $P_{\mathrm{probe}}(0)$ and

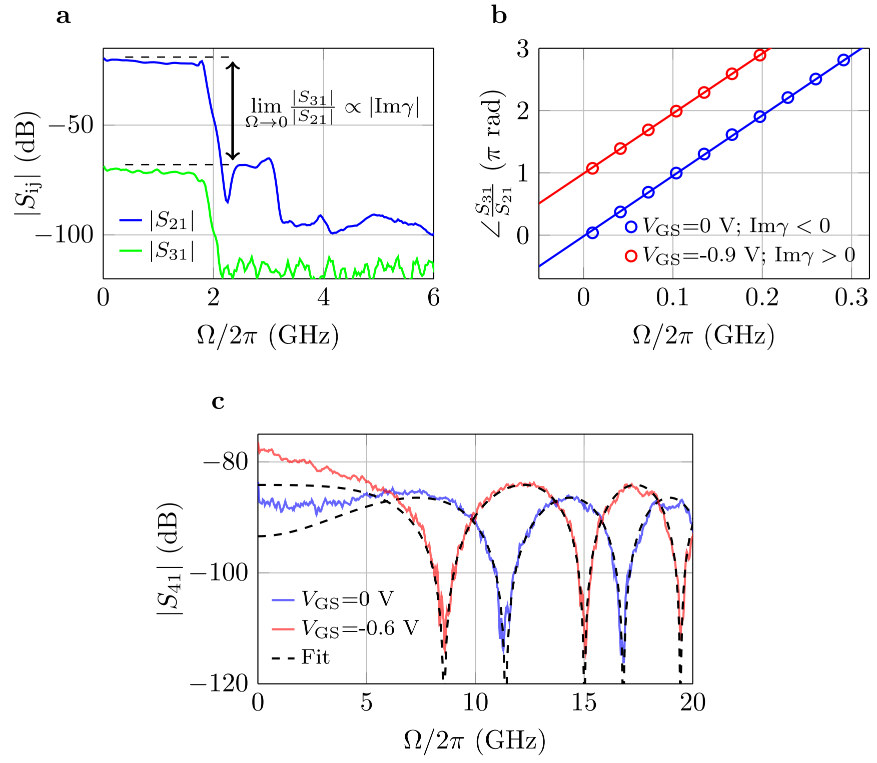

Figure 3.19: Examples of S-parameter measurements used in a cross-modulation experiment performed on a waveguide of width 1400 nm, covered with 50 µm of graphene. The traces shown here are for $\lambda_{\text{probe}} = 1551$ nm and $\lambda_{\text{pump}} = 1550.18$ nm. **a** Traces of $|S_{21}|$ and $|S_{31}|$ for $V_{\text{GS}} = 0$ V. The ratio $|S_{31}|/|S_{21}|$ can be used to estimate $|\text{Im}(\gamma)|$. **b** Trace of $\angle(S_{31}/S_{21})$ used to estimate the sign of $\text{Im}(\gamma)$, for two different gate voltages. **c** Traces of $|S_{41}|$ for two different gate voltages. The dashed lines show the corresponding sinusoidal fits ($\propto \left|\sin\left(\beta_2 L_{\text{SMF}}\Omega^2/2 + \angle\gamma\right)\right|$), used to estimate $\angle\gamma$.

the effective lenth L_{eff}. For this experiment, the on-chip probe powers vary between −5 and 0 dBm with variations caused by the wavelength dependence of the grating couplers. The effective length was calculated using a loss measurement similar to the one shown in figure 3.9**b**.

To obtain the sign of $\text{Im}(\gamma)$, we can use the phase difference $\angle S_{31} - \angle S_{21}$, as can be seen in equation (3.36). When this phase difference converges to 0, in the limit $\Omega \to 0$, then $\text{Im}(\gamma) < 0$. This essentially means that we are observing saturable absorption, which causes the pump and probe to oscillate in phase (increasing the pump power decreases the absorption of the probe, and hence increases the probe power at the output). If the phase

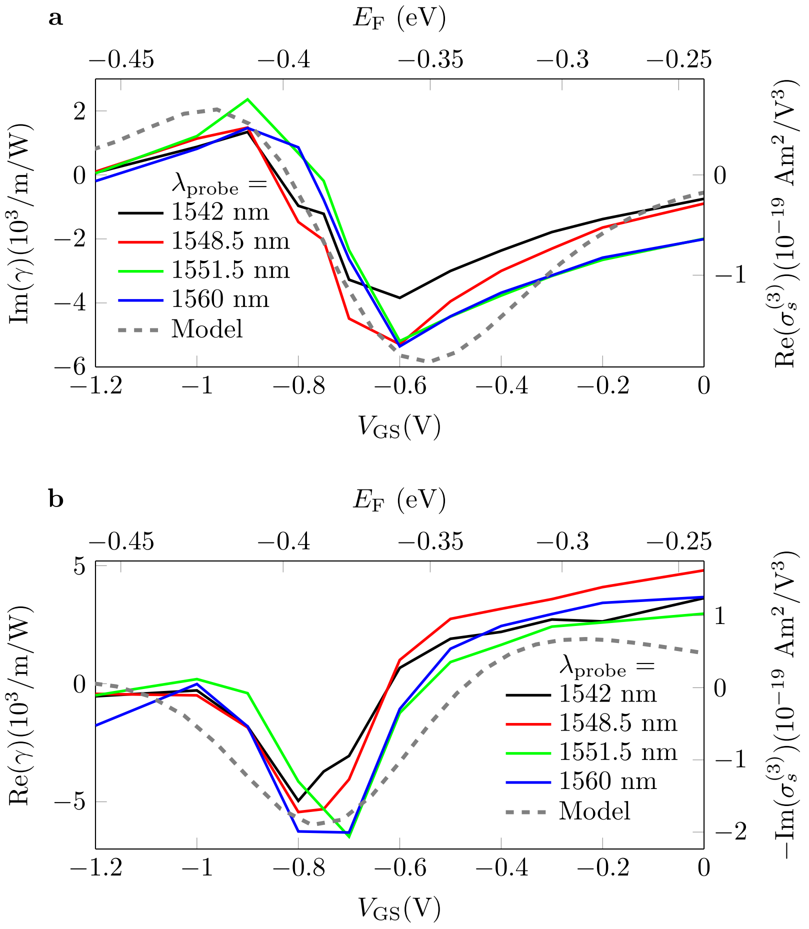

Figure 3.20: **a** Measured Im(γ) as function of V_{GS} for different probe wavelengths λ_{probe} (see legend). The top axis shows the estimated Fermi energy corresponding to the gate voltage, the right-hand axis shows the corresponding Re($\sigma_s^{(3)}$). **b** Measured Re(γ) and corresponding Im($\sigma_s^{(3)}$), as function of gate voltage and estimated Fermi energy. The grey dashed lines in both **a** and **b** show the simulated results for $\lambda_{\mathrm{probe}} = \lambda_{\mathrm{pump}}$ (see Section 3.5.4).

difference converges to $\pm\pi$, the opposite happens and the pump and probe oscillate out of phase, which is a signature of increasing probe absorption with increasing pump power, hence Im(γ) > 0. The blue circles on figure 3.19**b** show this phase difference for the measurement shown in figure 3.19**a**, the linear fit shows that $\lim_{\Omega\to 0}(\angle S_{31} - \angle S_{21}) \approx 0$, indicating saturable absorption. A measurement for a different gate voltage ($V_{\mathrm{GS}} = -0.9$ V,

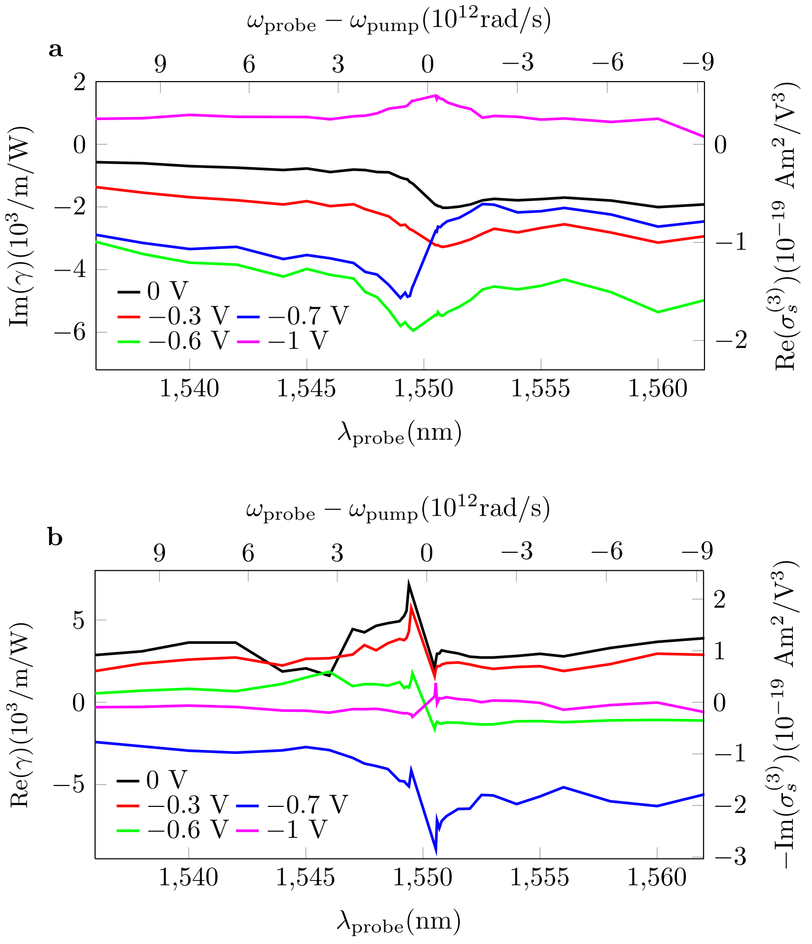

Figure 3.21: **a** Measured $\text{Im}(\gamma)$ as a function of λ_{probe}, respectively, for different gate voltages V_{GS} (see legend). The top axes show the corresponding probe-pump detuning in radial frequency, the right-hand axis shows the corresponding $\text{Re}(\sigma_s^{(3)})$. **b** Measured $\text{Re}(\gamma)$ and corresponding $\text{Im}(\sigma_s^{(3)})$, as function of probe wavelength and frequency detuning.

$\lambda_{\text{probe}} = 1551$ nm) is plotted in red, this time the phase difference converges to π, indicating that the opposite to saturable absorption, an increase of absorption with power, occurs for certain gating voltages.

Finally, as described by equation (3.37), the phase $\angle\gamma$ can be estimated using the $|S_{41}|$-trace, which is proportional to $|\sin\left(\frac{\beta_2 L_{\text{SMF}}\Omega^2}{2} + \angle\gamma\right)|$. As an example, figure 3.19**d** shows two of these measurements, accompanied by the sinusoidal fits. Hence a sinusoidal fit of the $|S_{41}|$-measurement, in combination with the knowledge of $|\mathrm{Im}(\gamma)|$ and $\mathrm{sgn}(\mathrm{Im}(\gamma))$ acquired as described above, can be used to fully characterize the nonlinear parameter γ. In practice, the fibers used to couple light into the chip also cause non-negligible cross-phase modulation. This contribution is corrected for in the measurements presented below, as is described in the previous section.

Figures 3.20 and 3.21 summarize the final results of this measurement. The measured values for $\mathrm{Im}(\gamma)$ and $\mathrm{Re}(\gamma)$ are plotted. The right-hand axes show the corresponding $\mathrm{Re}(\sigma_s^{(3)})$ and $\mathrm{Im}(\sigma_s^{(3)})$. In analogy to the FWM experiment the conversion was done through equation (3.25), using a realistic cross-section of the waveguide based on a SEM-image (a different sample than for the FWM experiment was used). In figure 3.20, these parameters are plotted as a function of the gate voltage. On the top axes, the estimated corresponding Fermi energies are plotted. It is clear from these measurements that $\gamma(\omega_{\mathrm{probe}};\omega_{\mathrm{probe}},\omega_{\mathrm{pump}},-\omega_{\mathrm{pump}})$, and the corresponding $\sigma_s^{(3)}(\omega_{\mathrm{probe}};\omega_{\mathrm{probe}},\omega_{\mathrm{pump}},-\omega_{\mathrm{pump}})$ of graphene, are very Fermi energy-dependent, and that both its real and imaginary part show strong resonance-like features around $|E_{\mathrm{F}}| \approx \hbar\omega/2$. At lower doping levels ($|E_{\mathrm{F}}| \ll \hbar\omega/2$), the negative sign of $\mathrm{Im}(\gamma)$ ($\mathrm{Re}(\sigma_s^{(3)})$) corresponds to saturable absorption, a well-known phenomenon in graphene (see references [13, 15, 36] and Section 3.2). However, in the vicinity of $|E_{\mathrm{F}}| \approx \hbar\omega/2$, the opposite effect is observed! The measured $\mathrm{Re}(\gamma)$ ($\propto -\mathrm{Im}(\sigma_s^{(3)})$) is positive for low doping, but becomes strongly negative around $|E_{\mathrm{F}}| \approx \hbar\omega/2$, after which it decays to zero. In figure 3.21, the same parameters are plotted as a function of λ_{probe}, for different gating voltages V_{GS}. γ is relatively insensitive to pump-probe detuning, apart from a small resonant feature around $\lambda_{\mathrm{probe}} \approx \lambda_{\mathrm{pump}}$.

3.5.4 Comparison with theory

Again, these experimental values can be compared with predictions made by theoretical models. We will focus on the phenomenological model described in Appendix A.

In figures 3.22**a** and 3.22**b** we show the real and imaginary parts of the calculated third order conductivity as a function of Fermi energy. The pump wavelength is 1550 nm and several different values of the probe wavelength are used. The equilibrium (before irradiation) temperature $k_{\mathrm{B}}T_0 = 25$ meV corresponds to room temperature. For the parameter E_i we took a value of 100 meV (see Appendix A). Our simulated results are moreover practically insensitive to the exact value of E_i used. The overall Fermi-energy dependence qualitatively corresponds to the experimental data. Approximate quantitative agreement is achieved using a phenomenological relaxation time $\tau_{\mathcal{E}} \approx 0.165$ ps. The difference between the curves for different

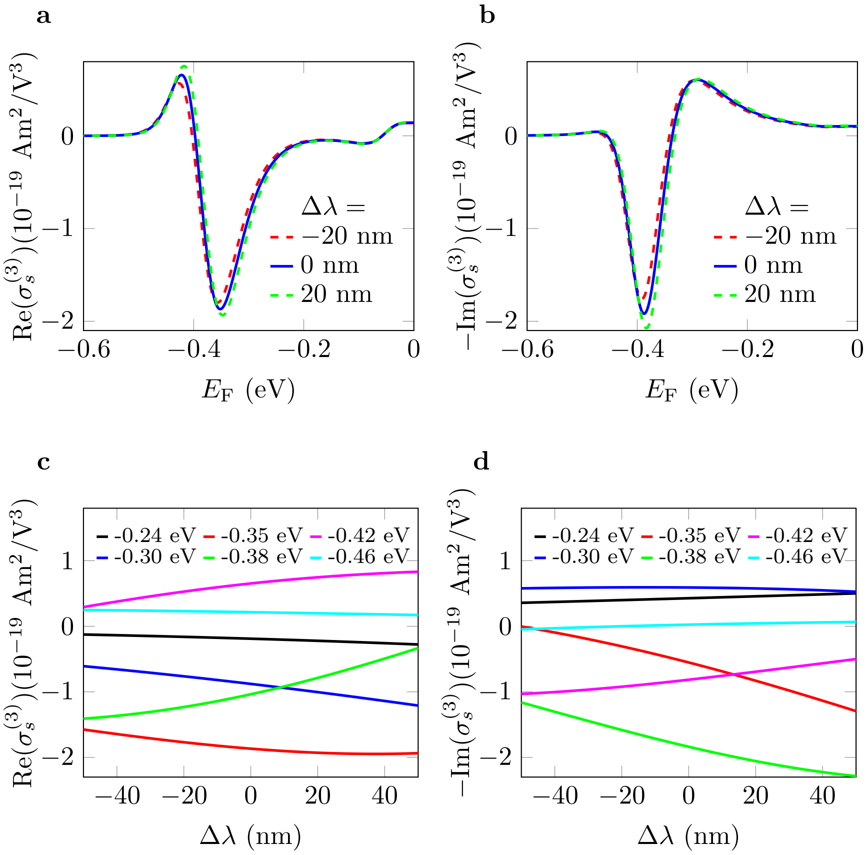

Figure 3.22: Simulated real (**a**) and imaginary (**b**) parts of $\sigma_s^{(3)}$ as a function of Fermi energy at different probe wave frequencies ($\Delta\lambda \equiv \lambda_\mathrm{probe} - \lambda_\mathrm{pump}$). Real (**c**) and imaginary (**d**) parts of $\sigma_s^{(3)}$, as a function of λ_probe at different Fermi energies. Parameters: $k_\mathrm{B}T_0 = 25$ meV, $E_i = 100$ meV, $\tau_\mathcal{E} = 0.165$ ps, the pump wavelength is 1550 nm ($\hbar\omega_\mathrm{pump} \approx 0.8$ eV).

probe wavelengths is small and the overall behavior agrees with the experimental findings in figure 3.20. The calculated values for $\Delta\lambda = 0$ nm are displayed on figure 3.20 (grey lines) to highlight this correspondence.

In figures 3.22**c** and 3.22**d** the real and imaginary parts are plotted as a function of probe wavelength detuning $\Delta\lambda = \lambda_\mathrm{probe} - \lambda_\mathrm{pump}$. The curves follow qualitatively similar trends as the experimental curves (figure 3.21), however we do not see any resonant feature at $\lambda_\mathrm{probe} \approx \lambda_\mathrm{pump}$. We believe that this deviation around λ_pump between the model and experiment is due to a slight deviation of the actual carrier distribution function from the assumed Fermi-Dirac distribution in the vicinity of energy levels $\pm\hbar\omega_{\mathrm{pump}}/2$, due to spectral hole burning. This local perturbation to the distribution is believed to give rise to the resonant features in the measured $\sigma_s^{(3)}$ values.

For the simulations here we used a relaxation rate $\tau_{\mathcal{E}}$ which was smaller than the one used for the simulations in the context of the four-wave mixing experiments (see Section 3.4 – 165 ps versus 500 ps). Partly, this can be due to experimental errors. But note that for the FWM experiments the relaxation rate was chosen in order to get a similar width of the Lorentzian line-shapes between figures 3.14**b** and 3.15**b**. This value resulted in simulated nonlinear conductivities of about a factor 3 higher than the measured ones. Since from Appendix A it is clear that $\sigma_s^{(3)}(\omega;\omega,\omega,-\omega) \propto \tau_{\mathcal{E}}$, we would get the comparable discrepancies between experiment and model if we would use $\tau_{\mathcal{E}} = 500$ ps for the experiments described here. In other words, the quantitative difference between model and experiment is similar for both the FWM and cross-modulation experiment.

3.5.5 Comparison with other experiments

We can now compare these experimental results with other nonlinear measurements in graphene. First and foremost, we do this for the four-wave mixing experiment in Section 3.4. Through FWM only the magnitude of the nonlinear conductivity can be estimated, hence to have a fair comparison, we have to estimate $|\sigma_s^{(3)}|$ for the cross-modulation experiment as well, this is plotted in figure 3.23**a**, for $\lambda_{\mathrm{probe}} = 1551.5$ nm. Comparing with figure 3.14**a** we see a similar peak in the vicinity of the interband absorption edge, quantitatively the values are also comparable. Note that we only expect the values to converge in the limit $\lambda_{\mathrm{probe}} \to \lambda_{\mathrm{pump}}$ for cross-modulation and $\lambda_{\mathrm{s}} \to \lambda_{\mathrm{p}}$ for FWM, and that the measurements were performed on different samples, so the graphene quality and conversion between γ and $\sigma_s^{(3)}$ might differ.

In figure 3.23**b**, the estimated real and imaginary part of the nonlinear refractive index are plotted. They are calculated using equations (2.13, 2.14), the linear refractive index is computed using the expressions for the linear conductivity given in Appendix A. The dotted lines give a theoretical estimation, calculated using the model in Appendix A with phenomenological relaxation time $\tau_{\mathcal{E}} = 0.16$ ps. Despite our belief that these units are not the most appropriate for graphene (see discussion in Section 2.4.1 and reference [37]), this conversion makes it possible to compare with other experiments available in literature (see table 2.1). Figure 3.23**b** shows that the nonlinear index fluctuates strongly in the vicinity of $E_{\mathrm{F}} = -\hbar\omega/2$. In terms of magnitude, the low-doping limit of $n_2 \approx 10^{-13}$ m^2/W is compara-

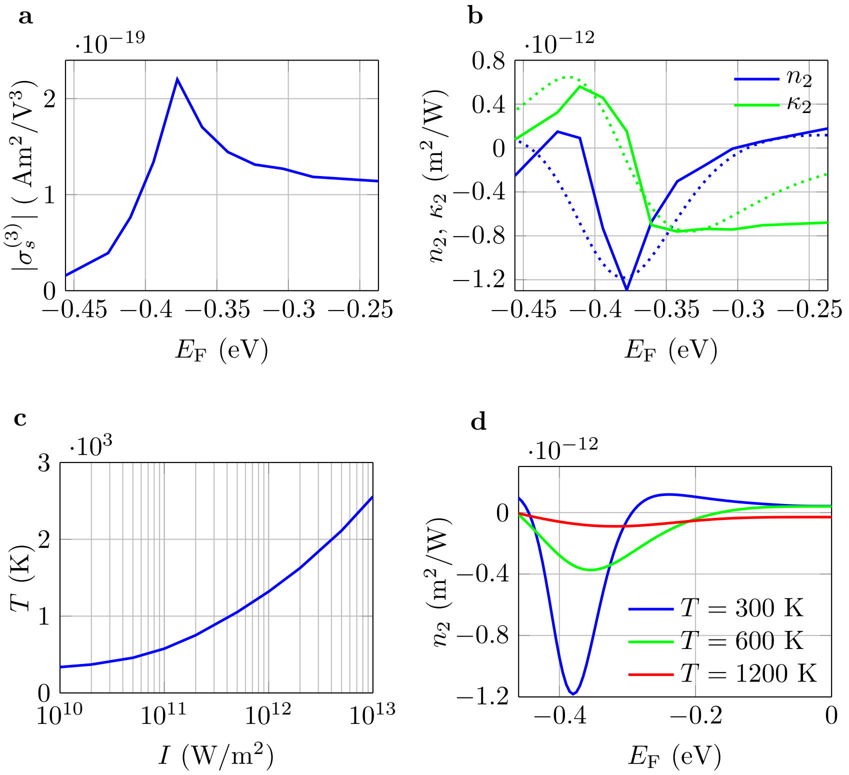

Figure 3.23: **a** Measured $|\sigma_s^{(3)}(\omega_{\text{probe}};\omega_{\text{probe}},\omega_{\text{pump}},-\omega_{\text{pump}})|$, for $\lambda_{\text{probe}} = 1551.5$ nm. **b** Estimated nonlinear refractive index $n_2 + i\kappa_2$ as a function of estimated Fermi energy. The measurement of $\sigma_s^{(3)}$ using $\lambda_{\text{probe}} = 1551.5$ nm in figure 3.20 was used. The dotted lines are calculated values. **c** Estimated electron temperature as a function of illumination intensity for a wavelength of 1550 nm. **d** Theoretical calculations of n_2 for different electron temperatures. All calculations have been done using the phenomenological model described in Appendix A, with $\tau_{\mathcal{E}} = 0.16$ ps.

ble with what has been measured in references [28, 38–41]. Dremetsika *et al.* [40, 41] and Vermeulen *et al.* [28] however reported negative values for n_2, for Fermi energies of around -0.2 eV. A possible explanation for this is the high optical peak intensity typically used in these experiments ($10^{12} \ldots 10^{13}$ W/m^2). Using the model in Appendix A, we can estimate how the electron temperature increases for increasing illumination intensity, by enforcing the electroneutrality condition, equation (A.4), and the energy balance condition, equation (A.10). In figure 3.23**c** the estimated electron temperature versus intensity is plotted. Note that for the illumination intensities used in references [28, 40, 41], the electron temperature is probably significantly increased. On figure 3.23**d**, the nonlinear index n_2 is calculated for different electron temperatures. According to the model, an elevated electron temperature can indeed switch the sign of the nonlinear index. Note that the explanation given here is probably not entirely correct for the experiments in references [28, 40, 41], as short pulses are used for which the model in Appendix A is no longer valid. However the simulations illustrate how the use of high peak intensities can perturb the carrier distribution in graphene to the extent that very different values of n_2 are observed.

3.6 Third harmonic generation in graphene-covered SiN waveguides

Gate-tunable third harmonic generation using graphene has recently been demonstrated by several groups. In this section we explore the possibility of doing this on an integrated waveguides. Experimental work on third harmonic generation was not performed within the PhD project. We merely give a mathematical framework, suggest an approach for quasi-phase-matching and perform some preliminary simulations.

3.6.1 Coupled-wave equations

When performing third harmonic generation in a graphene-covered waveguide, two optical frequencies should be considered, the fundamental ω_f, and its third harmonic $\omega_\mathrm{TH} = 3\omega_\mathrm{f}$. Both can be in very distinctive optical modes, with electric field profiles $\mathbf{e}_\mathrm{f} \equiv \mathbf{e}(\omega_\mathrm{f}, \mathbf{r}_\perp)$ and $\mathbf{e}_\mathrm{TH} \equiv \mathbf{e}(\omega_\mathrm{TH}, \mathbf{r}_\perp)$ and with slowly varying amplitudes $A_\mathrm{f}(z) \equiv A(\omega_\mathrm{f}, z)$ and $A_\mathrm{TH}(z) \equiv A(\omega_\mathrm{TH}, z)$. The coupled wave equations for the nonlinear interactions (equation (2.33)) can be written as:

$$\frac{\partial A_\mathrm{f}}{\partial z} = i\gamma(\omega_\mathrm{f}; \omega_\mathrm{TH}, -\omega_\mathrm{f}, -\omega_\mathrm{f}) A_\mathrm{TH} A_\mathrm{f}^{*2} e^{-i\Delta\beta z} - \frac{\alpha(\omega_\mathrm{f})}{2} A_\mathrm{f}, \tag{3.39}$$

$$\frac{\partial A_\mathrm{TH}}{\partial z} = i\frac{1}{3}\gamma(\omega_\mathrm{TH}; \omega_\mathrm{f}, \omega_\mathrm{f}, \omega_\mathrm{f}) A_\mathrm{f}^3 e^{i\Delta\beta z} - \frac{\alpha(\omega_\mathrm{TH})}{2} A_\mathrm{TH}, \tag{3.40}$$

where $\Delta\beta = 3\beta_\mathrm{f} - \beta_\mathrm{TH}$. Here we have, as was done for the four-wave mixing experiments, assumed that the cross- and self-modulation terms are negligible. The propagation loss is again given by equation (3.13). If we assume that the coupling between the transversal components of the electric fields is dominant, we get the approximate expressions for the γ-parameters:

$$\gamma(\omega_{\mathrm{f}};\omega_{\mathrm{TH}},-\omega_{\mathrm{f}},-\omega_{\mathrm{f}}) \approx i\frac{3\sigma^{(3)}_{s,\,xxxx}(\omega_{\mathrm{f}};\omega_{\mathrm{TH}},-\omega_{\mathrm{f}},-\omega_{\mathrm{f}})}{16\mathscr{P}_{\mathrm{f}}^{\frac{3}{2}}\mathscr{P}_{\mathrm{TH}}^{\frac{1}{2}}}\int_G (\mathrm{e}_{\mathrm{TH}})_x[(\mathrm{e}_{\mathrm{f}})^*_x]^3 d\ell \tag{3.41}$$

$$\gamma(\omega_{\mathrm{TH}};\omega_{\mathrm{f}},\omega_{\mathrm{f}},\omega_{\mathrm{f}}) \approx i\frac{3\sigma^{(3)}_{s,\,xxxx}(\omega_{\mathrm{TH}};\omega_{\mathrm{f}},\omega_{\mathrm{f}},\omega_{\mathrm{f}})}{16\mathscr{P}_{\mathrm{f}}^{\frac{3}{2}}\mathscr{P}_{\mathrm{TH}}^{\frac{1}{2}}}\int_G (\mathrm{e}_{\mathrm{TH}})^*_x[(\mathrm{e}_{\mathrm{f}})_x]^3 d\ell \tag{3.42}$$

For a third harmonic generation experiment, we can typically assume that the down-conversion term in equation (3.39) can be ignored. The amplitude of the fundamental field is then given by $A_{\mathrm{f}}(z) = A_{\mathrm{f}}(0)\exp[-\alpha(\omega_{\mathrm{f}})z/2]$. Substituting this in equation (3.40), we can get the following expression for the third harmonic amplitude (assuming that the field at $z = 0$ is 0):

$$\begin{aligned} A_{\mathrm{TH}}(z) &= \frac{iA^3_{\mathrm{f},0}e^{-\frac{\alpha_{\mathrm{TH}}}{2}z}}{3}\int_0^z \gamma e^{[\frac{1}{2}(\alpha_{\mathrm{TH}}-3\alpha_{\mathrm{f}})+i\Delta\beta]z'}dz' \\ &= \frac{i\gamma A^3_{\mathrm{f},0}e^{-\frac{\alpha_{\mathrm{TH}}}{2}z}}{3}\frac{(e^{[\frac{1}{2}(\alpha_{\mathrm{TH}}-3\alpha_{\mathrm{f}})+i\Delta\beta]z}-1)}{\frac{1}{2}(\alpha_{\mathrm{TH}}-3\alpha_{\mathrm{f}})+i\Delta\beta}, \end{aligned} \tag{3.43}$$

where we have introduced the short-hand notations $\gamma \equiv \gamma(\omega_{\mathrm{TH}};\omega_{\mathrm{f}},\omega_{\mathrm{f}},\omega_{\mathrm{f}})$, $\alpha_{\mathrm{f}} \equiv \alpha(\omega_{\mathrm{f}})$, $\alpha_{\mathrm{TH}} \equiv \alpha(\omega_{\mathrm{TH}})$ and $A_{\mathrm{f},0} \equiv A_{\mathrm{f}}(0)$.

3.6.2 Phase-matching techniques for third harmonic generation

Integrated waveguide modes are strongly dispersive. This implies that when two fundamental TE modes are coupled through THG, the generated third harmonic field (equation 3.43) strongly oscillates as a function of z. In other words a nonzero phase mismatch term $\Delta\beta$ is detrimental for efficient wavelength conversion. There are two commonly used solutions for this problem, modal phase-matching and quasi-phase-matching. In the former, one looks for two distinctly different modes, often the fundamental TE mode for the fundamental frequency and some higher-order mode at higher frequencies. Once such a pair of modes is found, equation (3.43) can be readily used to estimate the power conversion. However this approach typically results in a strongly reduced γ-parameter due to the relatively small overlap integral in equation (3.42). The second approach assumes that the nonlinear parameter γ itself is a periodic function of z. A periodic γ-function with period Λ can be written as a Fourier series [23]:

$$\gamma(z) = \sum_{m=-\infty}^{\infty} g_m e^{imKz}, \tag{3.44}$$

where $K = 2\pi/\Lambda$. Equivalent to equation (3.43) we can write,

$$\begin{aligned} A_{\mathrm{TH}}(z) &= \sum_{m=-\infty}^{\infty} \frac{iA_{\mathrm{f},0}^3 e^{-\frac{\alpha_{\mathrm{TH}}}{2}z}}{3} \int_0^z g_m e^{[\frac{1}{2}(\alpha_{\mathrm{TH}}-3\alpha_{\mathrm{f}})+i(\Delta\beta+mK)]z'} dz' \\ &= \sum_{m=-\infty}^{\infty} \frac{ig_m A_{\mathrm{f},0}^3 e^{-\frac{\alpha_{\mathrm{TH}}}{2}z}}{3} \frac{(e^{[\frac{1}{2}(\alpha_{\mathrm{TH}}-3\alpha_{\mathrm{f}})+i(\Delta\beta+mK)]z}-1)}{\frac{1}{2}(\alpha_{\mathrm{TH}}-3\alpha_{\mathrm{f}})+i(\Delta\beta+mK)}. \end{aligned} \tag{3.45}$$

It is now clear that most of the terms in this series expansion will oscillate with a period comparable to or smaller than Λ, the period can be chosen so that at most one term is phase-matched ($|\Delta\beta + mK| \ll K$). Only this term will build up coherently over multiple phase-matching periods. If we neglect the other terms, keep this term and assume perfect phase-matching, $mK = -\Delta\beta$ ($\Delta\beta$ is negative for the typical case $n_{\mathrm{TH}} > n_{\mathrm{f}}$), we can approximate:

$$A_{\mathrm{TH}}(z) \approx \frac{ig_m A_{\mathrm{f},0}^3 e^{-\frac{\alpha_{\mathrm{TH}}}{2}z}}{3} \frac{(e^{\frac{1}{2}(\alpha_{\mathrm{TH}}-3\alpha_{\mathrm{f}})z}-1)}{\frac{1}{2}(\alpha_{\mathrm{TH}}-3\alpha_{\mathrm{f}})}. \tag{3.46}$$

In a waveguide covered with graphene, or any other 2D material, a trivial way to modulate the nonlinear parameter γ is to selectively etch away a the graphene in a periodic pattern. If we assume that we periodically remove half of each period, then $\gamma(z)$ can be expressed as,

$$\gamma(z) = \gamma_{\max} \left\{ \frac{1}{2} + \frac{1}{2}\mathrm{sgn}[\cos(Kz)] \right\}, \tag{3.47}$$

for which the Fourier coefficients are,

$$g_m = \begin{cases} \gamma_{\max}/2 & \text{if} \quad m = 0 \\ (-1)^{(m-1)/2}\gamma_{\max}/m\pi & \text{if} \quad m \text{ is odd and } m \neq 0 \\ 0 & \text{if} \quad m \text{ is even and } m \neq 0 \end{cases} . \tag{3.48}$$

One can see that only odd values of m yield a nonzero effect, moreover as m increases, the efficiency drops drastically. The third harmonic power conversion efficiency in a perfectly quasi-phase-matched waveguide (with phase-mathing order $m = 1$) of length L can be estimated from equation (3.45),

$$\frac{P_{\mathrm{TH}}(L)}{P_{\mathrm{f}}(0)^3} \approx \frac{4|\gamma_{\max}|^2}{9\pi^2} \left| \frac{e^{-\frac{3}{2}\alpha_{\mathrm{f}}L+i(\Delta\beta+K)L} - e^{-\frac{1}{2}\alpha_{\mathrm{TH}}L}}{(\alpha_{\mathrm{TH}}-3\alpha_{\mathrm{f}})+i(\Delta\beta+K)} \right|^2, \tag{3.49}$$

For higher-order odd phase matching schemes the efficiency drops with a factor $1/m^3$, however this corresponds to longer phase-matching periods which might be technologically easier to achieve.

Note that in our derivation another approximation was made, namely that the modulation of the waveguide losses $\alpha(\omega)$ (with period Λ) is neglected. However if the loss per period is small, we can use an average value for the loss and expect no significant influence on the outcome.

3.6.3 Simulations

There are two recent experimental studies on gate tunable THG in graphene, by Jiang *et al.* [42] and Soavi *et al.* [43]. Both give estimates of the $\chi^{(3)}$ of graphene for fundamental wavelengths in the vicinity of 1550 nm and for different doping levels, which are shown in table 3.1. For a typical waveguide (width 1400 nm and height 300 nm), γ was estimated using a COMSOL Multiphysics®-model and equation (3.42). An estimate of the average waveguide losses is also given. Figure 3.24 shows the calculated conversion efficiency (equation (3.49)) as a function of distance corresponding to these parameter sets.

Ref.	E_F (meV)	$\lvert\chi^{(3)}\rvert$ ($\frac{\mathrm{m}^2}{\mathrm{V}^2}$)	γ ($\frac{1}{\mathrm{m\ W}}$)	α_f ($\frac{\mathrm{dB}}{\mathrm{cm}}$)	α_TH ($\frac{\mathrm{dB}}{\mathrm{cm}}$)
Jiang *et al.* [42] †	-250	$2 \cdot 10^{-19}$	0.0449	0.0338	0.012
Jiang *et al.* [42] †	-500	$6 \cdot 10^{-19}$	0.1347	0.0013	0.012
Soavi *et al.* [43] ‡	-250	$5 \cdot 10^{-18}$	1.1224	0.0338	0.012
Soavi *et al.* [43] ‡	-500	$1 \cdot 10^{-17}$	2.2450	0.0013	0.012

Table 3.1: Rough estimates of $|\chi^{(3)}|$-values measured using third harmonic generation for fundamental wavelengths in the vicinity of 1550 nm, from different sources and with different Fermi energies.
† Measurements performed with a fundamental wavelength of 1300 nm, values estimated from figure 4**c** in reference [42].
‡ Measurement performed with a fundamental wavelength of 1738 nm for a Fermi energy of about 250 meV. The value at higher doping is rough estimate assuming a 4-fold enhancement of the $\chi^{(3)}$-parameter.

As can be seen on figure 3.24 there is a large uncertainty given the different susceptibilities published in literature. In order to measure conversion efficiencies of these orders of magnitude, pulsed sources with high peak powers will probably have to be used.

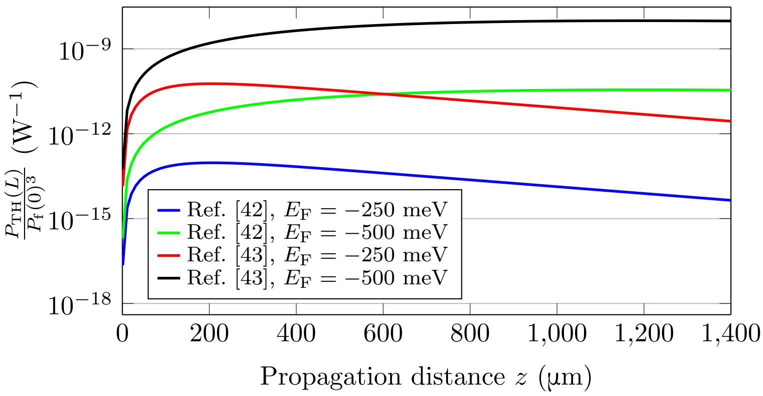

Figure 3.24: Simulated third harmonic conversion efficiency for a waveguide of thickness 300 nm and width 1400 nm, with nonlinear susceptibilities taken from different references.

3.7 Conclusion and future outlook

In this chapter, different experimental results obtained on graphene-covered waveguides were discussed. Where possible they were interpreted using relevant theoretical models.

In the first experiment (Section 3.2), gate-tunable saturable absorption in graphene-covered silicon waveguides was demonstrated. This was the first demonstration on integrated waveguides and can form the basis of studies of integrated lasers using graphene as a saturable absorber. Especially in light of a recent demonstration in which the properties of gate-tunable graphene are exploited to adjust the operational regime of a fiber modelocked laser [14], this idea can be promising. A simple model for saturable absorption was fitted to the measurements and saturation intensities in reasonable comparison of what has been measured by other groups were obtained. These measurements also show that when measuring the nonlinearities in a graphene-covered *silicon* waveguide, the nonlinear effects of the graphene and the silicon both play a significant role. From a practical point of view, this can be unwanted, the absorption saturation in the graphene for example competes with the two-photon absorption in the silicon, which could be an issue for modelocked lasers. Also, from a characterization perspective this is undesirable, as the nonlinearity in the silicon obscures the contribution of the graphene.

Therefore we developed a platform in which we incorporated graphene on *silicon nitride* waveguides. The details of this platform are given in Section 3.3. Gate-tunability of graphene was also achieved on these samples, using a polymer electrolyte. The experimental results obtained on gate-tunable graphene-covered SiN waveguides are discussed in Sections 3.4 and 3.5, respectively a four-wave mixing and a cross-modulation experiment. In the four-wave mixing experiment (Section 3.4) the magnitude of the nonlinear waveguide parameter $|\gamma| \propto |\sigma_s^{(3)}|$ is measured. This experiment shows that the nonlinear conductivity of graphene has a sharp resonance as a function of signal-pump detuning. By tuning the Fermi energy a broad asymmetric resonance shape in the vicinity of the absorption edge $|E_\mathrm{F}| = \hbar\omega/2$ is observed. Through the cross-modulation experiment (Section 3.5), a simultaneous measurement of both the nonlinear phase and amplitude response of the graphene-covered waveguides was possible. These results show that both the nonlinear refraction of graphene (quantified by the imaginary part of its nonlinear conductivity $\mathrm{Im}(\sigma_s^{(3)})$), as well as its nonlinear absorption (quantified by $\mathrm{Re}(\sigma_s^{(3)})$) are vastly dependent on the Fermi level. Apart from the already observed peak of $|\sigma_s^{(3)}|$ in the vicinity of the absorption edge $|E_\mathrm{F}| = \hbar\omega/2$, more complex dependencies, including sign changes and strong resonances in both $\mathrm{Im}(\sigma_s^{(3)})$ and $\mathrm{Re}(\sigma_s^{(3)})$, are uncovered. As opposed to the four-wave mixing experiments, the measured nonlinear parameter is not very detuning-dependent, and reasonably large values are measured independent of pump-probe detuning.

Approximate agreement was obtained between the measurements and the model introduced in Appendix A, for both the wavelength dependence and the Fermi energy dependence, for the four-wave mixing as well as the cross-modulation results. The different behavior as a function of detuning for the four-wave mixing and cross-modulation experiment can also be understood using this model. For the cross-modulation experiment, the nonlinear effect occurs as long as the temporal changes in charge carrier distribution are able to follow the modulation of the pump power, irrespective of the probe wavelength. For the four-wave mixing however, the nonlinear effects are strong as long as the changes in carrier distribution follow the beat note between pump and signal, which will be too fast for large detunings. Purely mathematically, we are measuring $\sigma_s^{(3)}$ for different frequency arguments. Qualitative agreement was also obtained between the four-wave mixing experiment and an adapted version of previously published theory [29, 30], however quantitatively, there was still a large discrepancy. The reasons for this discrepancy should be investigated further. Improving the simple model from Appendix A could also be a future endeavour.

From an application perspective, we have shown that the nonlinear parameter γ of a graphene-covered waveguide can be both large and tunable. The magnitude, real part and the imaginary part of the measured nonlinear waveguide parameter γ can all exceed 5000 $\mathrm{m}^{-1}\mathrm{W}^{-1}$ and can be tuned to a large extent. Even sign changes in $\mathrm{Re}(\gamma)$ and $\mathrm{Im}(\gamma)$ as a function of gate voltage were measured, meaning that very different nonlinear regimes can exist. In terms of sheer strength, $|\mathrm{Re}(\gamma)|$ is more than 3 orders of magnitude larger than for a standard SiN waveguide [16]. Compared to silicon waveguides [44], the improvement is roughly one order of magnitude. Moreover, silicon suffers from two-photon absorption, effectively limiting the maximum optical power in the waveguide. As we show here graphene also exhibits nonlinear absorption, though of the opposite sign for most Fermi energies, this means that at higher pump powers the effective interaction length will increase, rather than decrease. The electrostatic tunability of the nonlinear refraction, absorption and four-wave mixing efficiency of graphene-covered waveguides indicates that such waveguides can for example be used for all-optical signal processing, where the tunability could be used for fine-tuning of the devices. Note that current experiments were performed on waveguides with a rather large cross-section, and that the graphene was located in the evanescent field. By tailoring the waveguide cross-section and going to more confined structures, the figure of merit γ/α can still be significantly increased.

There are however also potential obstacles. Firstly, graphene is very lossy, with crippling waveguide losses of about 0.05 - 0.1 dB/µm. Of course through electrostatic gating the loss can be significantly reduced, our experiments however show that at such high doping levels the nonlinearities also strongly decrease. Secondly, the limited bandwidth of the FWM-process and the good correspondence between the experiments and the model in Appendix A suggest that the nonlinearities in graphene are closely linked to the carrier dynamics, and are limited in speed by the carrier lifetime (probably in the range of 0.1 ps - 1 ps). A third potential problem is saturation of the nonlinear effects, care was taken while doing the experiments in Sections 3.4 and 3.5 to measure at relatively low powers in order to justify the use of a third order model. However many nonlinear experiments make use of notoriously high peak powers, figure 2.3 strongly suggest that a third order description will not be sufficient and that the nonlinearities will saturate. Further investigation of high-power effects will be necessary, the model in Appendix A can be a starting point for this.

In Section 3.6, the potential use of our platform for on-chip third harmonic generation is considered, be it only in theory. This was inspired by recent experimental reports of tunable third harmonic generation in graphene [42, 43]. In these papers, the authors show that also the third harmonic generation efficiency of graphene can be tuned by gating. As opposed to the effects studied in this chapter, they measure an *increase* in efficiency beyond the carrier densities where graphene becomes transparent for the fundamental wavelength. This is promising since it means that when the loss decreases, the nonlinear effects increase. Moreover, we propose a simple quasi-phase-matching scheme just by periodically patterning the graphene, which is unique to 2D-materials. Preliminary simulations were done in order to get an idea of the optical powers and detector sensitivity needed to measure these phenomena on a waveguide. Due to the large variations in published values of the third order susceptibility for third harmonic generation, it remains unclear whether this will be possible. The nonlinear susceptibility also increases for longer wavelengths [43], changing the wavelengths might be another possible route.

References

[1] K. Alexander, Y. Hu, M. Pantouvaki, S. Brems, I. Asselberghs, S.-P. Gorza, C. Huyghebaert, J. Van Campenhout, B. Kuyken, and D. Van Thourhout. *Electrically controllable saturable absorption in hybrid graphene-silicon waveguides.* In Conference on Lasers and Electro-Optics (CLEO), pages 1–2. IEEE, 2015.

[2] K. Alexander, B. Kuyken, and D. Van Thourhout. *Characterization of graphene-covered SiN waveguide using four-wave mixing.* In Proceedings Symposium IEEE Photonics Society Benelux, pages 61–64, 2016.

[3] K. Alexander, M. Mohsin, U. D. Dave, L. A. Shiramin, S. Clemmen, D. Neumaier, B. Kuyken, and D. Van Thourhout. *Electrically tunable optical nonlinearity of graphene-covered SiN waveguides.* In Conference on Lasers and Electro-Optics (CLEO), pages 1–2. IEEE, 2017.

[4] K. Alexander, N. A. Savostianova, S. A. Mikhailov, B. Kuyken, and D. Van Thourhout. *Electrically tunable optical nonlinearities in graphene-covered SiN waveguides characterized by four-wave mixing.* ACS Photonics, 4(12):3039–3044, 2017.

[5] K. Alexander, B. Kuyken, and D. Van Thourhout. *Electrically Tunable Nonlinear Refraction and Absorption in Graphene-covered SiN Waveguides.* In Conference on Lasers and Electro-Optics (CLEO), pages FF2E–3. Optical Society of America, 2018.

[6] K. Alexander, N. A. Savostianova, S. A. Mikhailov, D. Van Thourhout, and B. Kuyken. *Gate-tunable nonlinear refraction and absorption in graphene-covered silicon nitride waveguides.* ACS Photonics, 2018.

[7] Y. Hu, M. Pantouvaki, J. Van Campenhout, S. Brems, I. Asselberghs, C. Huyghebaert, P. Absil, and D. Van Thourhout. *Broadband 10 Gb/s operation of graphene electro-absorption modulator on silicon.* Laser & Photonics Reviews, 10(2):307–316, 2016.

[8] `www.graphenea.com`.

[9] H. K. Tsang, C. Wong, T. Liang, I. Day, S. Roberts, A. Harpin, J. Drake, and M. Asghari. *Optical dispersion, two-photon absorption and self-phase modulation in silicon waveguides at 1.5 μm wavelength.* Applied Physics Letters, 80(3):416–418, 2002.

[10] T. K. Liang and H. K. Tsang. *Role of free carriers from two-photon absorption in Raman amplification in silicon-on-insulator waveguides.* Applied Physics Letters, 84(15):2745–2747, 2004.

[11] C.-C. Lee, J. M. Miller, and T. R. Schibli. *Doping-induced changes in the saturable absorption of monolayer graphene.* Applied Physics B, 108(1):129–135, 2012.

[12] I. Baylam, M. N. Cizmeciyan, S. Ozharar, E. O. Polat, C. Kocabas, and A. Sennaroglu. *Femtosecond pulse generation with voltage-controlled graphene saturable absorber.* Optics Letters, 39(17):5180–5183, Sep 2014.

[13] Q. Bao, H. Zhang, Y. Wang, Z. Ni, Y. Yan, Z. X. Shen, K. P. Loh, and D. Y. Tang. *Atomic-layer graphene as a saturable absorber for ultrafast pulsed lasers.* Advanced Functional Materials, 19(19):3077–3083, 2009.

[14] B. Yao, G. Soavi, T. Ma, X. Zhang, B. Fu, D. Yoon, S. A. Hussain, A. Lombardo, D. Popa, and A. C. Ferrari. *Gate controllable ultrafast fiber lasers based on graphene.* In CLEO: Science and Innovations, pages SF3K–6. Optical Society of America, 2018.

[15] Z. Sun, T. Hasan, F. Torrisi, D. Popa, G. Privitera, F. Wang, F. Bonaccorso, D. M. Basko, and A. C. Ferrari. *Graphene mode-locked ultrafast laser.* ACS Nano, 4(2):803–810, 2010.

[16] D. J. Moss, R. Morandotti, A. L. Gaeta, and M. Lipson. *New CMOS-compatible platforms based on silicon nitride and Hydex for nonlinear optics.* Nature Photonics, 7(8):597–607, 2013.

[17] L. Abdollahi Shiramin. *Graphene-Silicon Photonic Integrated Circuits: Design, Technology and Devices.* PhD thesis, Ghent University, 2017.

[18] A. Das, S. Pisana, B. Chakraborty, S. Piscanec, S. K. Saha, U. V. Waghmare, K. S. Novoselov, H. R. Krishnamurthy, A. K. Geim, A. C. Ferrari, and A. K. Sood. *Monitoring dopants by Raman scattering in an electrochemically top-gated graphene transistor.* Nature Nanotechnology, 3:210–215, Mar 2008.

[19] V. Thareja, J.-H. Kang, H. Yuan, K. M. Milaninia, H. Y. Hwang, Y. Cui, P. G. Kik, and M. L. Brongersma. *Electrically tunable coherent optical absorption in graphene with ion gel.* Nano Letters, 15(3):1570–1576, 2015.

[20] S. A. Mikhailov. *Personal communication.*

[21] K. S. Novoselov, A. K. Geim, S. V. Morozov, D. Jiang, Y. Zhang, S. V. Dubonos, I. V. Grigorieva, and A. A. Firsov. *Electric field effect in atomically thin carbon films.* Science, 306(5696):666–669, 2004.

[22] G. Demetriou, F. Biancalana, E. Abraham, W. ji, Y. Wang, and A. K. Kar. *Negative Irradiance-Dependent Nonlinear Refraction in Single-Layer Graphene.* In Conference on Lasers and Electro-Optics, page JTu2A.115. Optical Society of America, 2018.

[23] R. W. Boyd. *Nonlinear Optics.* Academic Press, 2003.

[24] P. DelH́aye, A. Schliesser, O. Arcizet, T. Wilken, R. Holzwarth, and T. J. Kippenberg. *Optical frequency comb generation from a monolithic microresonator.* Nature, 450(7173):1214–1217, 2007.

[25] T. V. Andersen, K. M. Hilligsøe, C. K. Nielsen, J. Thøgersen, K. P. Hansen, S. R. Keiding, and J. J. Larsen. *Continuous-wave wavelength conversion in a photonic crystal fiber with two zero-dispersion wavelengths.* Optics Express, 12(17):4113–4122, 2004.

[26] U. D. Dave, B. Kuyken, F. Leo, S.-P. Gorza, S. Combrie, A. De Rossi, F. Raineri, and G. Roelkens. *Nonlinear properties of dispersion engineered InGaP photonic wire waveguides in the telecommunication wavelength range.* Optics Express, 23(4):4650–4657, 2015.

[27] H. Zhang, S. Virally, Q. Bao, L. K. Ping, S. Massar, N. Godbout, and P. Kockaert. *Z-scan measurement of the nonlinear refractive index of graphene.* Optics Letters, 37(11):1856–1858, 2012.

[28] N. Vermeulen, D. Castelló-Lurbe, J. Cheng, I. Pasternak, A. Krajewska, T. Ciuk, W. Strupinski, H. Thienpont, and J. Van Erps. *Negative Kerr nonlinearity of graphene as seen via chirped-pulse-pumped self-phase modulation.* Physical Review Applied, 6(4):044006, 2016.

[29] S. A. Mikhailov. *Quantum theory of the third-order nonlinear electrodynamic effects of graphene.* Physical Review B, 93(8):085403, 2016.

[30] J. Cheng, N. Vermeulen, and J. E. Sipe. *Third-order nonlinearity of graphene: Effects of phenomenological relaxation and finite temperature.* Physical Review B, 91(23):235320, 2015.

[31] S. D. Sarma, S. Adam, E. H. Hwang, and E. Rossi. *Electronic transport in two-dimensional graphene.* Reviews of Modern Physics, 83(2):407, 2011.

[32] Y.-W. Tan, Y. Zhang, K. Bolotin, Y. Zhao, S. Adam, E. Hwang, S. D. Sarma, H. L. Stormer, and P. Kim. *Measurement of scattering rate and minimum conductivity in graphene.* Physical Review Letters, 99(24):246803, 2007.

[33] J. J. Wathen, V. R. Pagán, and T. E. Murphy. *Simple method to characterize nonlinear refraction and loss in optical waveguides.* Optics Letters, 37(22):4693–4695, 2012.

[34] G. P. Agrawal. *Nonlinear Fiber Optics.* Springer, 2000.

[35] T. Kato, Y. Suetsugu, M. Takagi, E. Sasaoka, and M. Nishimura. *Measurement of the nonlinear refractive index in optical fiber by the cross-phase-modulation method with depolarized pump light.* Optics Letters, 20(9):988–990, 1995.

[36] C. A. Zaugg, Z. Sun, V. J. Wittwer, D. Popa, S. Milana, T. S. Kulmala, R. S. Sundaram, M. Mangold, O. D. Sieber, M. Golling, Y. Lee, A. C. Ferrari, and U. Keller. *Ultrafast and widely tuneable vertical-external-cavity surface-emitting laser, mode-locked by a graphene-integrated distributed Bragg reflector.* Optics Express, 21(25):31548–31559, 2013.

[37] N. A. Savostianova and S. A. Mikhailov. *Optical Kerr effect in graphene: Theoretical analysis of the optical heterodyne detection technique.* Physical Review B, 97(16):165424, 2018.

[38] R. Wu, Y. Zhang, S. Yan, F. Bian, W. Wang, X. Bai, X. Lu, J. Zhao, and E. Wang. *Purely coherent nonlinear optical response in solution dispersions of graphene sheets.* Nano Letters, 11(12):5159–5164, 2011.

[39] W. Chen, G. Wang, S. Qin, C. Wang, J. Fang, J. Qi, X. Zhang, L. Wang, H. Jia, and S. Chang. *The nonlinear optical properties of coupling and decoupling graphene layers.* AIP Advances, 3(4):042123, 2013.

[40] E. Dremetsika, B. Dlubak, S.-P. Gorza, C. Ciret, M.-B. Martin, S. Hofmann, P. Seneor, D. Dolfi, S. Massar, P. Emplit, and P. Kockaert. *Measuring the nonlinear refractive index of graphene using the optical Kerr effect method.* Optics Letters, 41(14):3281–3284, 2016.

[41] E. Dremetsika and P. Kockaert. *Enhanced optical Kerr effect method for a detailed characterization of the third-order nonlinearity of two-dimensional materials applied to graphene.* Physical Review B, 96(23):235422, 2017.

[42] T. Jiang, D. Huang, J. Cheng, X. Fan, Z. Zhang, Y. Shan, Y. Yi, Y. Dai, L. Shi, K. Liu, C. Zeng, J. Zi, J. E. Sipe, Y.-R. Shen, W.-T. Liu, and S. Wu. *Gate-tunable third-order nonlinear optical response of massless Dirac fermions in graphene.* Nature Photonics, 12:430–436, 2018.

[43] G. Soavi, G. Wang, H. Rostami, D. G. Purdie, D. De Fazio, T. Ma, B. Luo, J. Wang, A. K. Ott, D. Yoon, S. A. Bourelle, J. E. Muench, I. Goykhman, S. Dal Conte, M. Celebrano, A. Tomadin, M. Polini, G. Cerullo, and A. C. Ferrari. *Broadband, electrically tunable third-harmonic generation in graphene.* Nature Nanotechnology, 13:583–588, 2018.

[44] R. M. Osgood, N. C. Panoiu, J. I. Dadap, X. Liu, X. Chen, I.-W. Hsieh, E. Dulkeith, W. Green, and Y. A. Vlasov. *Engineering nonlinearities in nanoscale optical systems: physics and applications in dispersion-engineered silicon nanophotonic wires.* Advances in Optics and Photonics, 1(1):162–235, 2009.

Chapter 4

PZT on silicon nitride

The material presented in this chapter has in part been published in reference [1].

4.1 Introduction

Silicon (Si) and silicon nitride (SiN) platforms are particularly promising for integrated opto-electronics. The ability to leverage existing CMOS infrastructure and the high index contrast between silicon and its oxide, SiO_2, have enabled compact, high yield, low-cost and scalable photonics, and a route towards co-integration with electronics [2]. Recently, there has been a drive towards integrating other CMOS-compatible materials in the silicon photonics platform, with silicon nitride (SiN) at the forefront. SiN-based integrated platforms offer some added advantages in comparison with silicon-on-insulator (SOI). These include a broader transparency range [3], lower propagation losses [3, 4], significantly lower nonlinear losses [3, 5], and a much smaller thermo-optic coefficient [3].

However, certain functions are not accessible or lack in performance. A famous example is the lack of efficient light emission or amplification in these platforms, as both materials have an indirect bandgap. The nonlinear optical capabilities of these platforms are also limited. The standard materials, Si, SiN and SiO_2 are all centrosymmetric, causing the second order nonlinear susceptibility $\chi^{(2)}$ to be negligibly small [6]. Finally, solutions for optical modulation are not ideal. State-of-the-art silicon modulators rely on phase modulation through free carrier plasma dispersion in p-n [7], p-i-n [8] and MOS [9] junctions. Despite being relatively fast and efficient, these devices suffer from spurious amplitude modulation and high insertion losses. On SiN there are currently no solutions (without the introduction of other materials, see below), SiN is an insulator so plasma dispersion effects cannot be used.

To overcome these problems, new materials are being integrated into these platforms. To tackle the issue of light generation, III-V semiconductors have been integrated through wafer-bonding, transfer-printing and recently even through monolithic integration [10]. To introduce $\chi^{(2)}$-type nonlinearities in Si and SiN circuits, they can for example be combined with III-V materials [11] or highly nonlinear ferroelectric thin films such as lithium niobate [12]. Recently, solutions where an effective $\chi^{(2)}$ is induced in the silicon itself using a DC voltage have emerged as well [13]. For optical modulation, solutions on silicon are based on heterogeneous integration with III-V semiconductors [14, 15], graphene [16, 17], electro-optic organic layers [18], germanium [19] or epitaxial $BaTiO_3$ (BTO) [20–22]. On SiN photonic integrated circuits, the options for co-integration to enable modulation are much more limited. The insulating nature of the material hinders many approaches based on III-V semiconductors, graphene, and organics, which rely on the conductivity of doped waveguides. The inherent nature of deposited SiN further excludes solutions using epitaxial integration. Nonetheless, modulators on SiN exist. Using double-layer graphene, Phare *et al.* achieved high speed electro-absorption modulation [23] and using piezoelectric PZT thin films, phase modulators based on stress-optic effects [24] and geometric deformation [25] have been demonstrated, albeit with sub-MHz electrical bandwidth.

In this chapter, we discuss the co-integration of thin film lead zirconate titanate (PZT) on SiN photonic integrated circuits. PZT is a ferroelectric material known among others for its high $\chi^{(2)}$-coefficient and, in close relation to this, for its strong linear electro-optic (Pockels) effect. Co-integration of SiN with PZT creates possibilities for second order nonlinear optics and phase modulation on SiN photonic circuits. Moreover, the inherent nature of the deposition process implies that it can be used on other platforms such as Si.

In Section 4.2, we introduce the material PZT, and discuss some of its most interesting properties. In view of the experimental results presented further in this chapter, we strongly focus on the Pockels effect in PZT, and the second order nonlinear optical response of the material. These two effects are closely related but have historically been expressed using different material parameters. Expressions to relate these parameters are also derived in this section. In Section 4.3 the deposition method for the thin-film PZT used here is discussed. As an initial test, second harmonic generation (SHG) measurements were performed on thin-film PZT deposited on glass. These results are presented in Section 4.4. The remaining measurements were performed on PZT-covered SiN waveguides, the fabrication of such chips, and the obtained waveguide losses, are discussed in Section 4.5. Also on these waveguides, second harmonic generation was observed, these results are covered in Section 4.6. In the remainder of this chapter, the PZT-covered SiN waveguides are used for optical modulation. In essence these waveguides modulate phase. Direct measurement of phase modulation is discussed in Section 4.7. In specific configurations, these phase shifters can also be used for amplitude modulation. Efficient and high-speed amplitude modulators on SiN using thin-film PZT are demonstrated in Section 4.8. Strategies for further improvement of the PZT-on-SiN modulators based on geometrical optimization are discussed in Section 4.9. In Section 4.10, some conclusions and potential future steps are discussed.

4.2 PZT

PZT (chemical formula $\mathrm{PbZr}_x\mathrm{Ti}_{1-x}\mathrm{O}_3$, $0 \leq x \leq 1$) belongs to the class of perovskite materials. These are materials with the same crystal structure as CaTiO_3. Perovskites have the chemical formula ABC_3, A and B are cations of typically very different sizes, and X is an anion (often oxygen) [26]. The crystal structure of PZT becomes tetragonal below the Curie temperature [26]. The unit cell of this structure is shown in figure 4.1**a**. The O^{2-} anions and Pb^{2+} cations occupy respectively the face-centered and corner positions of the unit cell, whereas the $\mathrm{Ti}^{4+}/\mathrm{Zr}^{4+}$ cations occupy the body-centered position. The position of the $\mathrm{Ti}^{4+}/\mathrm{Zr}^{4+}$ cations is slightly shifted from the center in the tetragonal phase, giving PZT a spontaneous polarization along the crystallographic c-axis which lies at the origin of many of its interesting properties.

The spontaneous polarization of the unit cell leads to a macroscopic polarization of the crystal, this is called ferroelectricity. By applying a strong enough electric field, the polarization of the domains can be actively switched. This can for example be used to encode digital information in the polarization of these materials, which has enabled the demonstration of non-volatile random access memories [26]. Closely related are the piezoelectric properties of PZT. Piezoelectricity means that when the material is exposed to tensile or compressive stress, the induced strain generates electrical charge separation inside the material. This in turn generates an external potential difference. The inverse also occurs, an externally applied electric field induces strain in the material. Piezoelectic materials have many applications, such as micromotors, acoustic sensors, atomic force microscope cantilevers or MEMS [26]. Pyroelectricity is yet another property of PZT, this means that the polarization is dependent on the material temperature and finds its applications in for example thermal sensors [26].

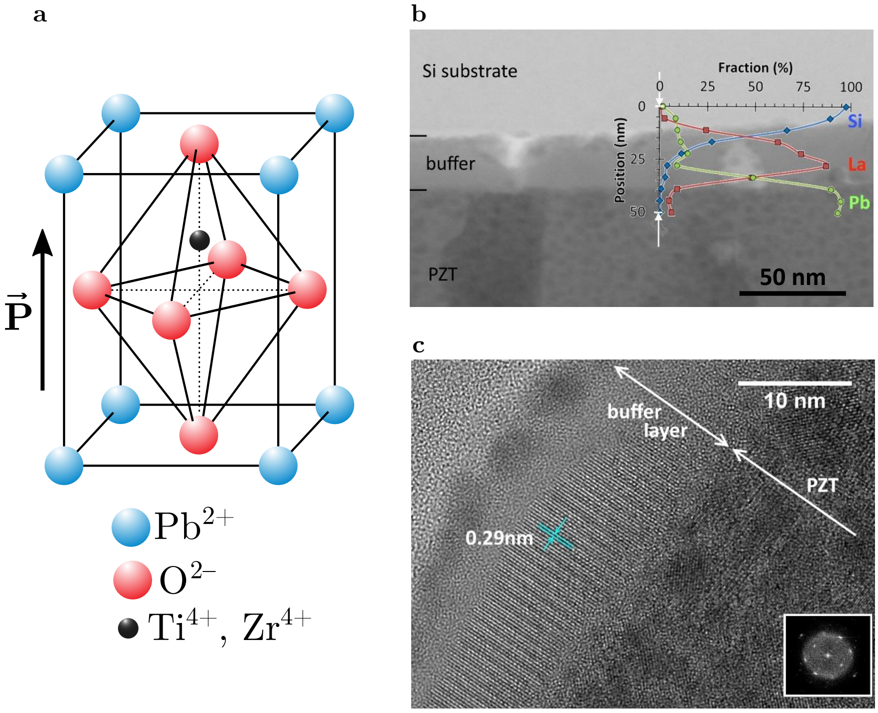

Figure 4.1: **a** PZT unit cell with a tetragonal perovskite structure (adapted from Wikipedia). **b** STEM image of the cross-section of a PZT thin film, on top of a La-based intermediate layer. The overlay shows the relative EDX signal intensity measured along the cross-section, using representative elements La, Pb and Si (image taken from the PhD thesis of John P. George [26]). **c** HRTEM image of the cross-section. The inset shows the FFT power spectrum for the PZT layer (image taken from the PhD thesis of John P. George [26]).

In this chapter however, the properties of PZT that are of interest are its strong linear electro-optic response, also called the Pockels effect, and closely related to that its strong second order nonlinear optical response. In the case of the Pockels effect, the refractive index of the material changes as an electric field **E** is applied. This is usually expressed as a linear change in the impermeability tensor $\eta = \varepsilon_r^{-1}$, where ε_r is the relative permittivity tensor [26],

$$\eta_{ij}(\mathbf{E}) = \eta_{ij}(0) + \sum_k r_{ijk}E_k, \tag{4.1}$$

here $\eta_{ij}(0)$ is the unperturbed impermeability tensor, E_k is the k^{th} component of the electric field and r_{ijk} are the Pockels coefficients. This field-induced change of the refractive index enables the adjustment of the phase velocity of electromagnetic waves and lies at the basis of voltage controlled wave-plates (Pockels cells) and electro-optic phase modulators.

In second order nonlinear optics, the material polarization is quadratically dependent on the total electric field, and the interaction is mediated by the second order susceptibility tensor $\chi^{(2)}$. When two monochromatic waves at frequencies ω_1 and ω_2 interact, then the induced material polarization contains components at the sum- and difference frequencies $\omega_1 \pm \omega_2$ (see equation (2.3) and reference [6]),

$$P_i^{(2)}(\omega_1+\omega_2) = \varepsilon_0 \sum_{jk} \chi_{ijk}^{(2)}(\omega_1+\omega_2;\omega_1,\omega_2)E_j(\omega_1)E_k(\omega_2), \tag{4.2}$$

$$P_i^{(2)}(\omega_1-\omega_2) = \varepsilon_0 \sum_{jk} \chi_{ijk}^{(2)}(\omega_1-\omega_2;\omega_1,-\omega_2)E_j(\omega_1)E_k(-\omega_2). \tag{4.3}$$

Note that in the limit $\omega_2 = 0$, both these terms just add to the *linear* polarization at frequency $\omega = \omega_1$, which becomes,

$$P_i(\omega) = \varepsilon_0 \left[\sum_j \chi_{ij}^{(1)} E(\omega) + 2\sum_{jk} \chi_{ijk}^{(2)}(\omega;\omega,0)E_j(\omega)E_k(0) \right], \tag{4.4}$$

hence this description is equivalent to a linear susceptibility which changes linearly with the applied DC electric field $\mathbf{E}$,

$$\chi_{ij}^{(1)}(\mathbf{E}) = \chi_{ij}^{(1)}(0) + 2\sum_k \chi_{ijk}^{(2)}(\omega;\omega,0)E_k. \tag{4.5}$$

In the limit of small perturbations, $\varepsilon_{r,\,ij} \gg |\Delta\varepsilon_{r,\,ij}|$ and $\eta_{ij} \gg |\Delta\eta|$ (with $\Delta\varepsilon_{r,ij} = 2\sum_k \chi_{ijk}^{(2)}(\omega;\omega,0)E_k$ and $\Delta\eta = \sum_k r_{ijk}E_k$), equations (4.1) and (4.5) describe the same physical phenomenon, being a linear variation of the dielectric constant/refractive index as a function of applied electric field. The relation between the $\chi^{(2)}$ and r follows from the observation that by definition $(\eta + \Delta\eta)(\varepsilon_r + \Delta\varepsilon_r) = \mathbf{I}$, with $\mathbf{I}$ the unit matrix. Using $\eta\varepsilon_r = \mathbf{I}$ and assuming that the second order term $\Delta\eta\Delta\varepsilon_r$ is negligible, this leads to the relation,

$$\eta\Delta\varepsilon_r = -\Delta\eta\varepsilon_r, \tag{4.6}$$

for the special case of a diagonal permittivity tensor, this eventually becomes,

$$\chi_{ijk}^{(2)}(\omega;\omega,0) = -\frac{\varepsilon_{r,ii}\varepsilon_{r,jj}}{2} r_{ijk}. \tag{4.7}$$

Material	ijk	r_{ijk} (pm/V) [27]	n [28]	$\chi^{(2)}_{ijk}(\omega;\omega,0)$ (pm/V)	$\chi^{(2)}_{ijk}(2\omega;\omega,\omega)$ (pm/V) [6]
$AgGaSe_2$	321	6.9	2.22	-84	66
CdS	333	3.2	2.55	-68	153
CdS	311	3.1	2.55	-66	-80
GaAs	321	-1.33	3.50	112	740
$LiNbO_3$	322	28	2.25	-359	-60
Quartz	111	-0.47	1.458	3.3	0.6

Table 4.1: Second order susceptibility $\chi^{(2)}_{ijk}$ of different materials. Either calculated from the Pockels coefficient using equation (4.7), or measured using second order nonlinear processes such as second harmonic generation. n is the refractive index of the material.

Note that the description borrowed from nonlinear optics using $\chi^{(2)}$ is in a sense more general, since it includes not only the Pockels effect, but also frequency-mixing effects such as second harmonic generation, sum frequency generation, optical rectification, etc. [6]. The distinction between these processes lies in the frequency arguments of the $\chi^{(2)}$-function. It is also important to note that $\chi^{(2)}$ and r are expressed in the same units, pm V^{-1}, however in materials with large dielectric constants they can have very different magnitudes. Finally, $\chi^{(2)}_{ijk}$ can be strongly frequency dependent, so different values should be expected for different phenomena, such as the Pockels effect ($\chi^{(2)}(\omega;\omega,0)$) and second harmonic generation ($\chi^{(2)}(2\omega;\omega,\omega)$). This final point is illustrated by table 4.1, which lists Pockels coefficients for several crystals (obtained at a variety of wavelengths, see reference [27]), and the corresponding second order susceptibility $\chi^{(2)}_{ijk}(\omega;\omega,0)$. The conversion was done using equation (4.7), assuming that $\varepsilon_{r,ii} = \varepsilon_{r,jj} = n^2$. On the other hand the nonlinear susceptibility $\chi^{(2)}_{ijk}(2\omega;\omega,\omega)$ quantifying second harmonic generation (also obtained at a variety of wavelengths, see reference [6]) is also given. Clearly these values are in general not the same, with differences of up to almost an order of magnitude. However a large Pockels effect and strong parametric second order nonlinear effects seem to be indicative of each other for most materials.

4.3 Thin-film PZT deposition

In this chapter, we incorporate thin-film PZT onto integrated SiN-based photonic chips. This is made possible by recent developments in the thin-film deposition of PZT by John P. George *et al.* [26], who also performed the PZT-depositions for the devices discussed in this thesis.

For the deposition of the PZT, a procedure based on chemical solution deposition (CSD) is used. This CSD method consists of several steps. First the precursor solution is prepared. This solution is then deposited onto the substrate by spincoating or aerosol deposition and dried on a hot-plate (100-200 °C). Then amorphous films are obtained by pyrolysis (“firing”) of the organic compounds (400-500 °C). The amorphous films are thereafter “annealed” at higher temperatures (600-700 °C) to obtain crystalline films of the desired perovskite phase. CSD deposition of PZT of this kind is not new and early reports date from the 1980s [29]. However high quality PZT can only be deposited on specific substrates or intermediate layers [26]. An intermediate layer has to be both an efficient template which promotes crystal growth with a strong preferential orientation, and at the same time act as a diffusion barrier. The presence of such an intermediate layer (Pt in the first reports [29]) poses large restrictions on the applications that can be envisioned. For nanophotonics, the requirements become very stringent. Preferably we want a layer with low optical loss and low thickness. For this work, the intermediate layers consist of lanthanide oxides ($La_2O_2CO_2$), which are also deposited through chemical solution deposition and have good optical transparency, result in highly oriented thin films and can be deposited as very thin ($\gtrsim$ 5 nm) layers [26]. Figure 4.1**b** shows a scanning transmission electron microscope (STEM) image of the cross-section of a PZT thin-film on Si, using a La-based intermediate layer. Through combination with energy dispersive X-ray (EDX) spectroscopy, the chemical composition could be mapped as well. The overlay shows the relative concentration of some representative elements for the different layers. Figure 4.1**c** shows a high resolution transmission electron microscope (HRTEM) image of the same cross-section, it confirms the crystalline nature of the intermediate layer and the FFT spectrum on the inset confirms that the c-axis of the PZT is oriented perpendicular to the interface. For more details of the deposition process, see the PhD thesis of John P. George [26].

4.4 Second harmonic generation on thin-film PZT

4.4.1 Measurement methodology and setup

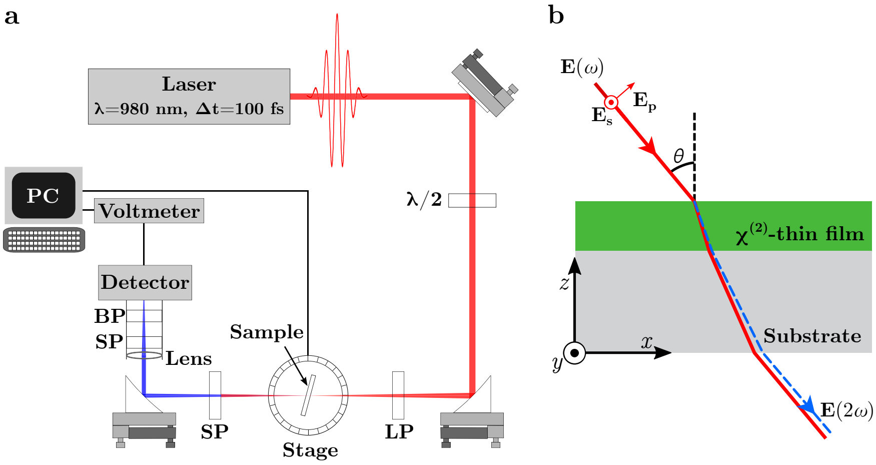

Figure 4.2: **a** Setup used for the thin-film second harmonic generation experiments. $\lambda/2$: half-wave plate, LP: longpass filter, SP: shortpass filter, BP: bandpass filter. Adapted from reference [30]. **b** Principle of the thin-film second harmonic generation experiment.

Before integrating PZT onto nanophotonic waveguides, the potential of the material was tested using a second-harmonic generation setup designed for thin-film measurements. Characterization of the second order nonlinear response of thin-films is an extensive subject by itself, more information on the method used here and related methods are summarized by Artur Hermans *et al.* in reference [30]. A schematic representation of the setup is shown in figure 4.2**a**. The light-source in these experiments is a commercial Ti:Sapphire laser (Mai Tai HP, Spectra-Physics). The pulse duration, wavelength, repetition rate and average power are respectively 100 fs, 980 nm, 80 MHz and 1 W. In the path of the beam, a half-wave plate is first used to rotate the polarization of the linearly polarized light coming from the laser. The beam is then focused onto the sample using a parabolic mirror with a focal length of 5 cm. The original beam diameter and the diameter in the focal plane ($1/e^2$) are respectively 1.2 mm and 52 µm. The depth of focus is 4.5 mm, which provides ample tolerance to place the sample close to the focal plane. Second harmonic light emerging from the sample is collimated using another identical parabolic mirror and is focused onto a femtowatt detector (Thorlabs PDF10A/M). Several filters are placed in the beam path, the first longpass filter (cutoff wavelength 800 nm) suppresses all SHG light generated on the mirrors and elsewhere in the setup, the shortpass and bandpass filters after the sample suppress the fundamental wavelength.

The setup is designed to measure the second order response of a sample as a function of incidence angle θ and, if necessary, for different excitation polarizations. The principle is sketched in figure 4.2**b**. The sample is excited at frequency ω, the incident beam can be s(TE)- or p(TM)-polarized, or a combination of the two, depending on the half-wave plate orientation. The second harmonic wave is generated in the sample and can be detected by the detector. The parameter $\chi^{(2)}$ in fact is a 3×3 tensor, consisting of 27 elements. Although the number of independent tensor elements can typically be reduced drastically using symmetry considerations, the SHG response will depend very strongly on the used excitation polarization and incidence angle. Using appropriate theoretical models the measured dependencies can then be used to derive the $\chi^{(2)}$-tensor [30]. Note that the sample in figure 4.2**b** is just an illustration, samples with much more complex layer structures can be characterized. Also note that due to momentum conservation in the x-direction, the fundamental and second harmonic will always exit the sample at the same angle as the incident beam.

4.4.2 Measurement results for thin-film PZT

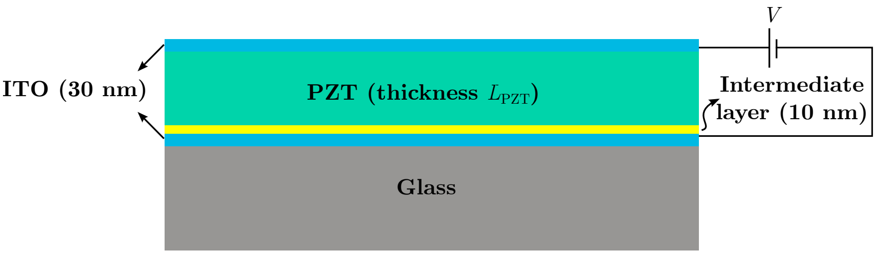
V
ITO (30 nm)
PZT (thickness L_{PZT})
Intermediate layer (10 nm)
Glass

Figure 4.3: Typical sample used for measuring the second harmonic response of thin-film PZT.

Here, we measure the $\chi^{(2)}$-tensor of a film of PZT deposited on a glass substrate. The cross-section of such a sample is shown in figure 4.3. The deposition method described in Section 4.3 is used, with an intermediate layer of about 10 nm thick, the PZT layer has variable thickness L. Figure 4.1**c** confirmed that the c-axis of the PZT crystallites is oriented in the out-of-plane direction. This however does not mean that the spontaneous dipole moment of all crystallites (see figure 4.1**a**) is oriented in the same direction. The overall second harmonic is the coherent addition of the SH generated in the different crystallites, hence we want to be able to pole the crystal. This is done using a top and bottom electrode of conductive and transparent indium tin oxide (ITO). The bottom electrode is present on the original substrate, the top electrode is deposited using e-beam evaporation and subsequent heat treatment at 300 °C [26].

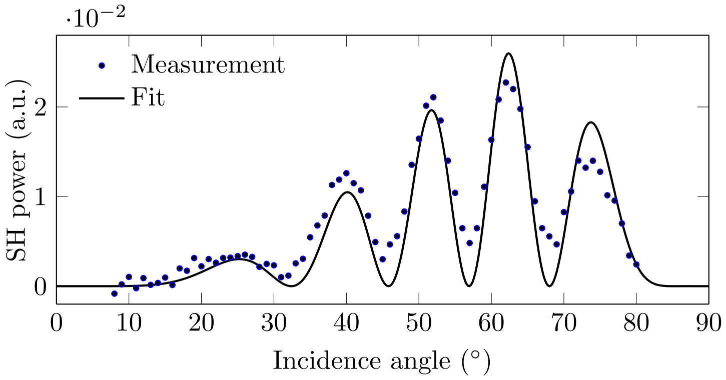

Figure 4.4: Measurement and fit for a blank BOROFLOAT® 33 substrate with known $\chi_s^{(2)}$ and thickness $L \approx 500$ µm. Used as a reference for other measurements.

Reference measurement Before performing the measurement on PZT, we do a reference measurement on a blank borosilicate glass (BOROFLOAT® 33) substrate, which has a known surface nonlinearity $\chi_s^{(2)}$, and a negligible bulk response. The surface second order susceptibility tensor of a simple interface ($C_{\infty v}$ symmetry) has only 3 independent components, $\chi^{(2)}_{s,xxz} = \chi^{(2)}_{s,yyz} = \chi^{(2)}_{s,xzx} = \chi^{(2)}_{s,yzy}$, $\chi^{(2)}_{s,zxx} = \chi^{(2)}_{s,zyy}$ and $\chi^{(2)}_{s,zzz}$. [30]. When the fundamental beam is p-polarized, the SH will also only contain a p-polarized component. To good approximation, the second harmonic electric field strength generated by a glass substrate equals [30],

$$\begin{aligned}
&E_{2\omega,\text{total}} \\
=&E_{2\omega,\text{front}} + E_{2\omega,\text{back}} \\
=&-i\frac{\omega}{2cN_\text{glass}\cos(\Theta_\text{glass})} t^2_{\text{air,glass}} T_{\text{glass,air}} E^2_{\omega,\text{in}} \\
&\left[\left(\chi^{(2)}_{s,zxx} + 2\chi^{(2)}_{s,xxz}\right)\sin(\Theta_\text{glass})\cos^2(\theta_\text{glass}) + \chi^{(2)}_{s,zzz}\sin^2(\theta_\text{glass})\sin(\Theta_\text{glass})\right] \\
&\left[\exp\left(-i\frac{2\omega N_\text{glass}\cos(\Theta_\text{glass})}{c}L\right) - \exp\left(-i\frac{2\omega n_\text{glass}\cos(\theta_\text{glass})}{c}L\right)\right].
\end{aligned} \tag{4.8}$$

This field is the result of interference between a component generated at the front ($E_{2\omega,\text{front}}$) and back ($E_{2\omega,\text{back}}$) interface. $E_{\omega,\text{in}}$ is the input fundamental field. c, ω and L are respectively the speed of light in vacuum, the fundamental frequency and the thickness of the substrate. n_{glass} and N_{glass} are the glass refractive index for respectively the fundamental and SH wavelength. θ_{glass} and Θ_{glass} are the propagation angles of respectively the fundamental and SH in the glass, which can be calculated using Snell's law from the incidence angle. $t_{i,j}$ and $T_{i,j}$ are the Fresnel transmission coefficients between medium i and j, again for the fundamental and the second harmonic wavelength, respectively. Note that this formula is approximate. The index contrast at the interface is relatively small, so reflections and potential cavity effects are not taken into account. Also lateral beam walk-off effects between the fundamental and SH due to dispersion in the glass are considered to be negligible. The model used here has been compared with more exact models by Artur Hermans *et al.* in reference [30] and is sufficiently exact for the current purpose of serving as a reference. For referencing, the $\chi_s^{(2)}$-values found in reference [31] are used; $\chi^{(2)}_{s,xxz} = 14.6 \cdot 10^{-22}$ m^2/V, $\chi^{(2)}_{s,zxx} = 7 \cdot 10^{-22}$ m^2/V and $\chi^{(2)}_{s,zzz} = 93 \cdot 10^{-22}$ m^2/V. The measurement and corresponding fit for a sample of thickness $L \approx 500$ µm are shown in figure 4.4. The fringes on this plot are due to angle-dependent interference between the light generated at different interfaces, caused by the difference in refractive index for the fundamental and SH. As these fringes were first observed by Maker *et al.*, they are often called Maker fringes [32].

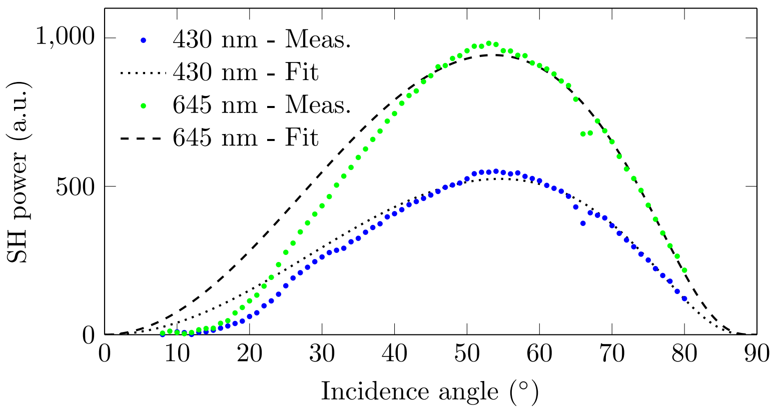

Figure 4.5: Measurements (Meas.) and fits for two different PZT-covered glass samples after out-of-plane poling using comparable electric fields (≈ 9.3 V/µm), for two different PZT thicknesses L_{PZT} (see legend).

PZT measurement The PZT-crystallites have a random in-plane orientation (if not poled in-plane, see further). Macroscopically, the thin film also has $C_{\infty v}$-symmetry with respect to the normal, and the same nonzero

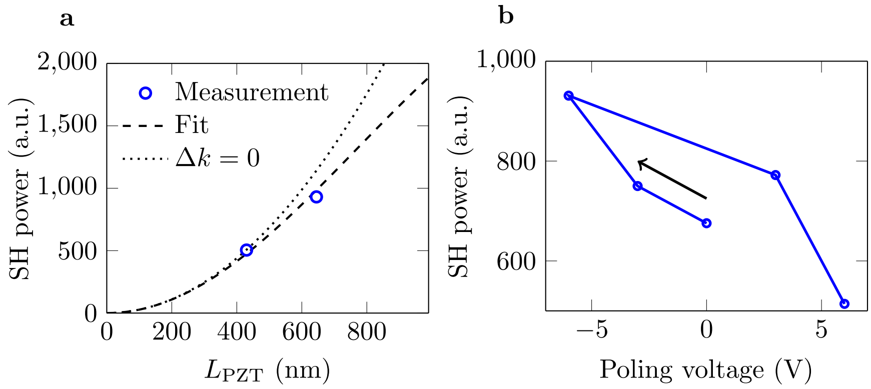

Figure 4.6: Second harmonic power at a fixed angle (48 °). **a** For two different PZT thicknesses. The dashed line is a fit based on equation (4.9). The dotted line is the theoretical curve in the absence of phase mismatch ($\Delta k = 0$), essentially a parabola. **b** After different poling steps, for $L_{\mathrm{PZT}} = 645$ nm. The arrow shows the order in which the different poling voltages are applied.

second order susceptibility tensor components as a simple air-glass interface. For the measurements performed on the PZT-covered samples, reflections within the different layers will be ignored. Though approximate, this is common practice in thin-film SHG measurements [33, 34]. Under this assumption and using p-polarized light, the SH electric field can be expressed as [30, 34],

$$\begin{aligned} &E_{2\omega,\mathrm{total}} \\ =&\frac{\omega}{2cN_{\mathrm{PZT}}\cos(\Theta_{\mathrm{PZT}})}\frac{\exp(-i\Delta k L_{\mathrm{PZT}})-1}{\Delta k}t^2_{\mathrm{air,PZT}}T_{\mathrm{PZT,glass}}T_{\mathrm{glass,air}}E^2_{\omega,\mathrm{in}} \\ &\left[\left(\chi^{(2)}_{zxx}+2\chi^{(2)}_{xxz}\right)\sin(\Theta_{\mathrm{PZT}})\cos^2(\theta_{\mathrm{PZT}})+\chi^{(2)}_{zzz}\sin^2(\theta_{\mathrm{PZT}})\sin(\Theta_{\mathrm{PZT}})\right], \end{aligned} \tag{4.9}$$

N_{PZT}, θ_{PZT} and Θ_{PZT} are defined equivalently as for the reference sample, $t_{\mathrm{air,PZT}}$ and $T_{\mathrm{PZT,glass}}$ are the full amplitude transmission functions for respectively the air-ITO-glass stack and the PZT-intermediate layer-ITO-glass stack. $\Delta k = \frac{2\omega}{c}(N_{\mathrm{PZT}} - n_{\mathrm{PZT}})$ is the phase mismatch between the SH and fundamental due to the wavelength dispersion of the PZT. The tensor components $\chi^{(2)}_{zxx}$ and $\chi^{(2)}_{xxz}$ are not observed separately in this measurement, as the second harmonic field only depends on the linear combination $\left(\chi^{(2)}_{zxx} + 2\chi^{(2)}_{xxz}\right)$. Two samples with different PZT thickness were poled and characterized. The respective PZT thicknesses L_{PZT} are 430 nm and 645 nm. To obtain similar poling fields, the samples are respectively poled by applying −4 V and −6 V. The SH response is shown in figure 4.5. For the fits, only the angles beyond 35 ° are used, since the alignment of the setup is not consistent for the whole range of incident angles. The fits result in $\chi^{(2)}_{zzz} = 39$ pm/V and $\left(\chi^{(2)}_{zxx} + 2\chi^{(2)}_{xxz}\right) = -26$ pm/V for the 430 nm thick sample, and $\chi^{(2)}_{zzz} = 42$ pm/V and $\left(\chi^{(2)}_{zxx} + 2\chi^{(2)}_{xxz}\right) = -25$ pm/V for the 645 nm thick sample. The signs of $\chi^{(2)}_{zzz}$ and $\left(\chi^{(2)}_{zxx} + 2\chi^{(2)}_{xxz}\right)$ are relative with respect to each other, the absolute sign cannot be observed using this method. In figure 4.6**a**, the SH power is plotted for a single angle (48 °), for the measurements shown in figure 4.6, as a function of PZT thickness. The theoretical fit (using average values $\chi^{(2)}_{zzz} = 40.5$ pm/V and $\left(\chi^{(2)}_{zxx} + 2\chi^{(2)}_{xxz}\right) = -25.5$ pm/V) is plotted as a dashed line. The theoretical curve in the absence of phase mismatch $((\exp(-i\Delta k L_{\mathrm{PZT}}) - 1)/\Delta k \to -iL_{\mathrm{PZT}})$ is also plotted, which is the typical parabola expected for phase-matched second harmonic generation [6]. Clearly, phase mismatch already reduces the conversion efficiency for these small thicknesses. In figure 4.6**b**, the effect of the poling voltage is shown, for the sample with $L_{\mathrm{PZT}} = 645$ nm, the SH power measured after each poling step for an angle of 48 ° is plotted, the arrow shows the order in which the voltages are applied, the measurements are performed in absence of a voltage. There are several notable features about this graph. First of all, the material has a nonzero response after deposition, meaning that the crystallites have a preferential orientatiation in the out-of plane direction, even without poling. Secondly, poling using a negative voltage strengthens the effect, from this we can conclude that a negative voltage poles more domains in the already preferred orientation. Using a positive voltage, we seem to decrease the effect, counteracting the preferred orientation after deposition. Thirdly, it seems like the voltages used here, in either polarization, have not yet caused the SH efficiency to reach saturation, *so the film is probably not poled in its most efficient way yet.* The reason for these moderate voltages is that electrostatic breakdown had occurred on comparable samples at higher voltages. In the future, more efficient poling (higher voltages,temperatures) still has to be explored. Since electrostatic breakdown is facilitated by imperfections in the crystal, this goes hand-in-hand with optimization of the thin-film quality.

4.5 PZT on silicon nitride waveguides

The remaining experiments presented in this chapter have been performed in PZT-covered integrated SiN nanophotonic circuits. In this section we describe the fabrication and losses of PZT-covered SiN waveguides.

4.5.1 Fabrication

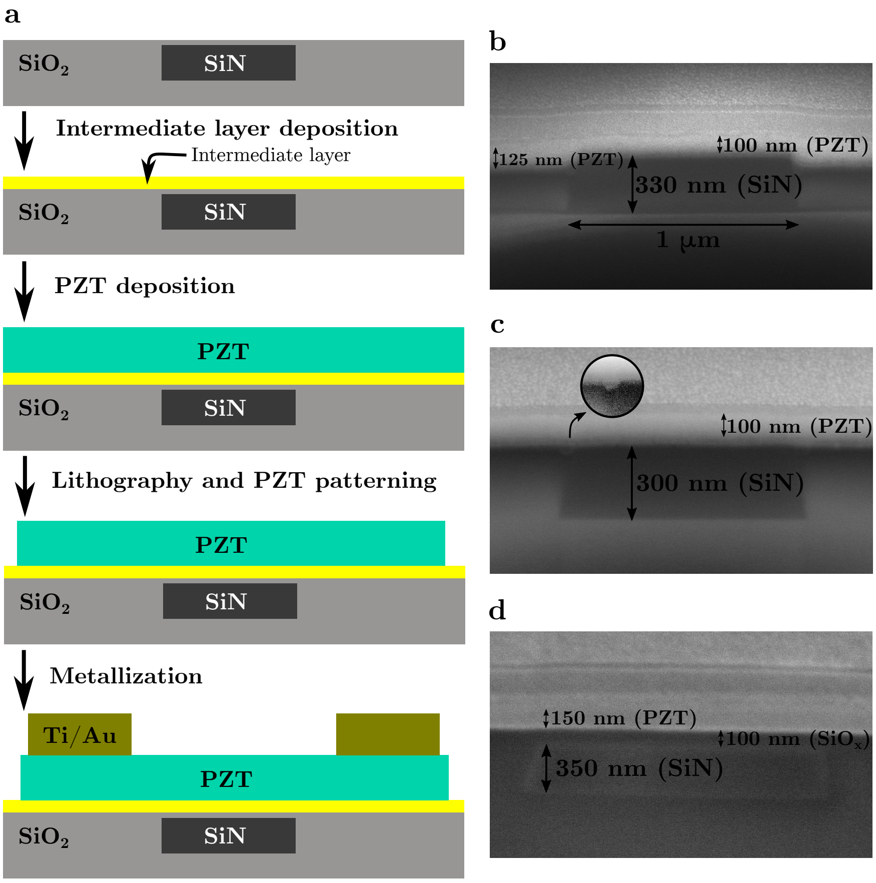
a
SiO$_2$
SiN
Intermediate layer deposition
Intermediate layer
PZT deposition
PZT
Lithography and PZT patterning
Metallization
Ti/Au
b
125 nm (PZT)
100 nm (PZT)
330 nm (SiN)
1 µm
c
100 nm (PZT)
300 nm (SiN)
d
150 nm (PZT)
100 nm (SiO$_x$)
350 nm (SiN)

Figure 4.7: **a** Fabrication steps for the PZT-on-SiN waveguides, starting from a planarized SiN chip. **b-d** Examples of SEM cross-sections of different waveguides. For **b**, **c** the planarization was done through a combination of RIE and BOE etching (see Section 3.3.1 for a more detailed description) the inset shows the trench at the waveguide edge with enhanced contrast, caused by nonuniform etch rates. For **d** the planarization was performed using CMP.

The first steps of the fabrication process are the same as for the graphene-covered SiN waveguides introduced in Section 3.3. The waveguides are patterned using 193 nm deep UV lithography in a 300-350 nm thick layer of LPCVD SiN on a 3.3 µm thick buried oxide layer, in a CMOS pilot line. Subsequently, SiO$_2$ (thickness $\approx$ 1 µm) is deposited over the devices and planarized.

The planarization is performed in two different ways, either in-house using a combination of reactive ion etching (RIE) and buffered oxide etch (BOE) wet etching (details on this method can be found in Section 3.3), or by chemical-mechanical polishing (CMP) in the CMOS foundry itself. This step is performed so that the SiN waveguide top surface and the surrounding oxide are coplanar.

The remaining steps are summarized in figure 4.7**a**. First, the La-based intermediate layer is deposited and the PZT films are deposited using the CSD methods described before. Since the samples are not always perfectly flat, relatively thick (20-30 nm) intermediate layers are typically deposited. Hereafter the PZT is patterned using an RIE recipe based on SF_6 if necessary, this is done to remove PZT on top of the grating couplers. Finally, Ti/Au electrical contacts are patterned in the vicinity of the waveguides, this is done through a sequence of photolithography (AZ 5214 E resist in image reversal), thermal evaporation of the metals and lift-off.

Figures 4.7**b** and **c** show cross-sections of two waveguides after PZT deposition, the grainy layer above the PZT is platinum deposited in the SEM to avoid charging of the sample. Both of these samples were planarized in-house using a combination of dry and wet etching. Variations in initial top oxide thickness, etch rates and exact etch times can clearly lead to a strong variation between different samples. For the case of figure 4.7**b**, overetching results in steps of several tens of nanometers around the waveguides. Moreover, the etch rates of the deposited oxide depend on the exact nitride structures underneath. As was already illustrated in figure 3.6 this can lead to trenches around the waveguides during the planarization procedure. Even in the case of a seemingly planar surface (figure 4.7**c**), trenches of several tens of nanometers can be seen next to the waveguides at enhanced contrast (see inset). Figure 4.7**d** however shows a waveguide planarized using CMP. A buffer layer of 50-100 nm of oxide is left on top of the nitride waveguide, so the obtained surface is much smoother, though at the expense of a part of the overlap of the optical mode with the PZT film.

After deposition, the PZT crystallites have one crystal plane parallel to the substrate, but no preferential orientation in the chip's plane. To obtain a significant electro-optic or second order nonlinear response for the quasi-TE optical mode, a poling step is performed by applying 60-80 V ($\approx$ 150 kV cm^{-1}) for 1 hour at room temperature, between contacts at either side of the waveguide several micrometers apart, followed by several hours of stabilization time. More details about poling are given in the following sections.

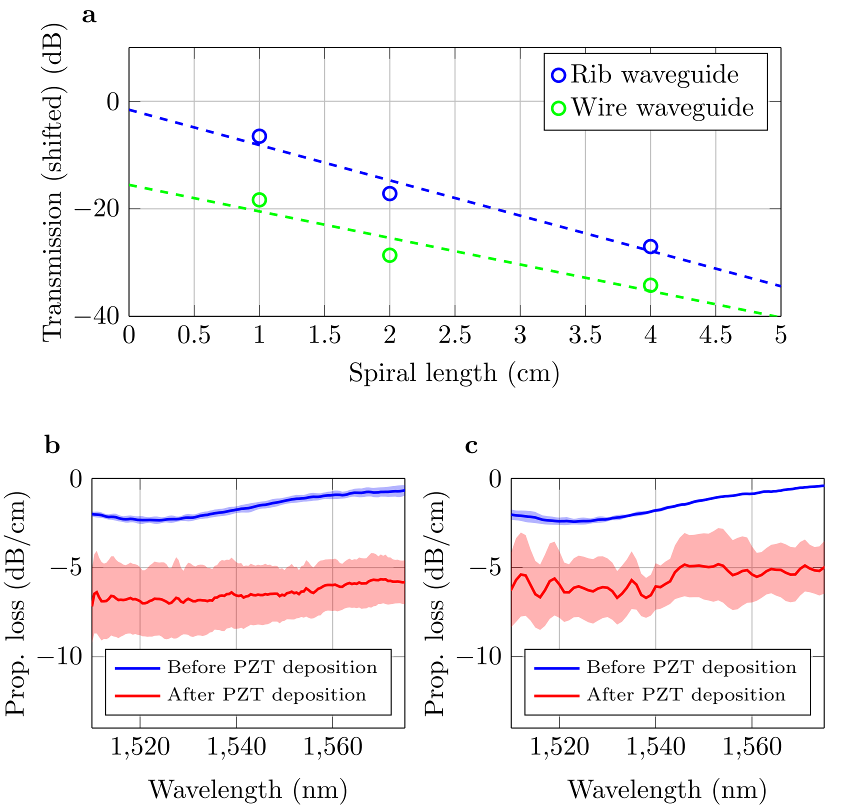

Figure 4.8: Loss measurements on samples planarized through RIE and BOE-etching. **a** Transmission versus waveguide length for a PZT-covered rib and wire waveguide, with cross-section similar to figure 4.7**b** (width = 1400 nm, wavelength = 1550 nm, PZT thickness ≈ 125 nm). **b**, **c** Propagation loss of the respective rib and wire waveguides versus wavelength, before and after PZT deposition. The shaded area shows the standard deviation on the fitted slope.

4.5.2 Waveguide losses

In figures 4.8 and 4.9, loss measurements on the different types of PZT-covered waveguide spirals are shown. These waveguides had no metallic contacts, which can also change the optical losses. Figure 4.8 summarizes loss measurements performed on waveguides planarized by etching, these measurement were moreover done around the C-band (1530 to 1565 nm in wavelength). As was clear from the previous section and figures 4.7**b** and **c**, this type of planarization typically results in steps and trenches of several tens of nanometers in the vicinity of the waveguide. Figure 4.8**a** shows the transmission versus length of both a set of rib and wire waveguide spirals.

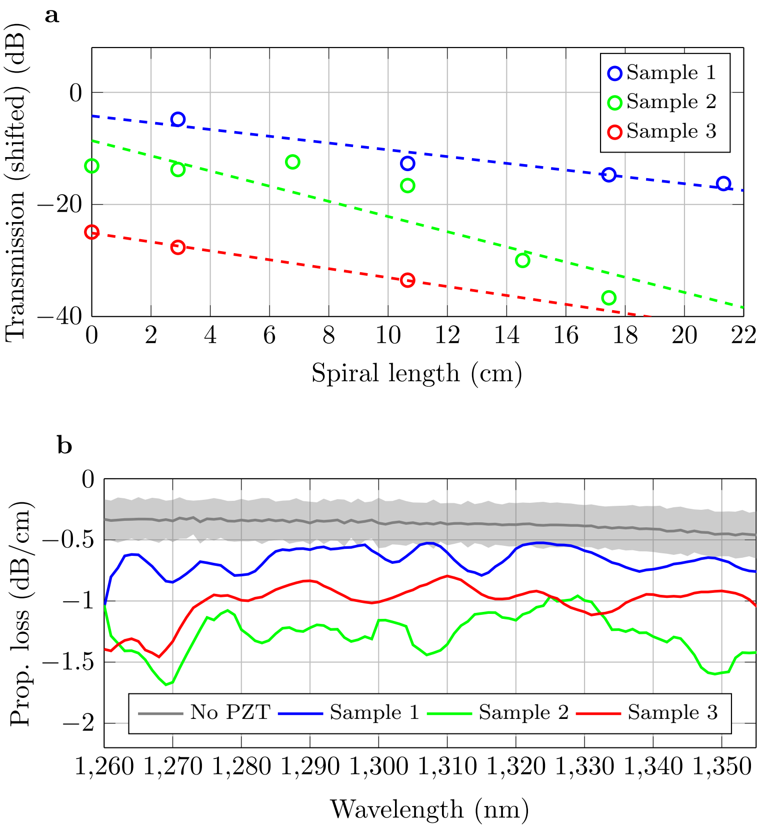

Figure 4.9: Loss measurements on samples planarized through CMP. **a** Transmission versus waveguide length for a PZT-covered waveguide, with cross-section similar to figure 4.7**d** (width = 800 nm, wavelength = 1310 nm, PZT thickness = 150 nm). Measured on 3 different samples. **b** Propagation loss versus wavelength for these waveguide sets, including a sample with no PZT.

The wire waveguides closely resemble figure 4.7**b**, the rib waveguides were defined using a partial etch of 220 nm next to the waveguide core, the influence of this on the propagation loss is only expected to be minor. Figures 4.8**b** and **c** show the respective losses of the rib and wire waveguides as a function of wavelength (red). For reference, the waveguide loss before PZT deposition is plotted in blue. The shaded zones show the standard deviations of the fit. Estimated losses of about 5 to 7 dB cm^{-1} are found. Figure 4.9 summarizes loss measurements performed on waveguides planarized by CMP, with cross-sections similar to figure 4.7**d**. These measurements were done around the O-band (1260 to 1360 nm in wavelength). Figure 4.9**a** again plots the transmission versus spiral length for 3 different samples, and figure 4.9**b** shows the propagation loss resulting from a linear fit, as a function of wavelength. The grey line shows the result for a sample without PZT (and the standard deviation of the fit is plotted in grey). Note that the propagation losses of these waveguides are in the vicinity of only 1 dB cm^{-1}. So both the total propagation losses, as well as the increase in propagation loss with respect to waveguides without PZT, are much smaller for the case of CMP planarization. It is likely that the steps and trenches that are inherent to the in-house planarization method through etching cause the thin-film quality to deteriorate and losses to increase significantly!

4.6 Second harmonic generation in PZT-covered waveguides

In Section 4.4, the second harmonic response of thin-film PZT on a glass substrate was measured, the conclusion was that the second order nonlinear response of PZT is relatively large. In Section 4.5, we discussed the fabrication of PZT-covered SiN waveguides. In this section we look at the combination of the two, we look into whether PZT can be used to achieve second harmonic generation on SiN chips. Second harmonic generation in a waveguide is more involved than on a thin-film, since phase matching becomes an issue, this is explained first, after which the experiments and some possible improvements are discussed.

4.6.1 Second harmonic generation in a waveguide

The coupled-wave equations governing second harmonic generation in a waveguide can be derived analogously to the coupled-wave equations describing third order nonlinear interactions in Section 2.5. Two optical frequencies should be considered, the fundamental ω_f, and its second harmonic $\omega_\text{SH} = 2\omega_\text{f}$. Both are in different optical modes with electric field profiles $\mathbf{e}_\text{f} \equiv \mathbf{e}(\omega_\text{f}, \mathbf{r}_\perp)$ and $\mathbf{e}_\text{SH} \equiv \mathbf{e}(\omega_\text{SH}, \mathbf{r}_\perp)$ and with slowly varying amplitudes $A_\text{f}(z) \equiv A(\omega_\text{f}, z)$ and $A_\text{SH}(z) \equiv A(\omega_\text{SH}, z)$. In most experiments, the simplifying assumption can be made that the fundamental wave carries much more power than the second harmonic and that the power in the fundamental only changes because of linear absorption. The equation describing the second harmonic can be derived from equation (2.31), with a polarization density $\mathbf{P}_\text{NL}(\omega_\text{SH}) = (\varepsilon_0/2)\chi^{(2)}(\omega_\text{SH}; \omega_\text{f}, \omega_\text{f}) \vdots \mathbf{E}_\text{f}\mathbf{E}_\text{f}$, eventually this gives the coupled wave equations,

$$\frac{\partial A_\mathrm{f}}{\partial z} = -\frac{\alpha_\mathrm{f}}{2} A_\mathrm{f}, \tag{4.10}$$

$$\frac{\partial A_\mathrm{SH}}{\partial z} = i\kappa e^{i(2\beta_\mathrm{f}-\beta_\mathrm{SH})z} A_\mathrm{f}^2 - \frac{\alpha_\mathrm{SH}}{2} A_\mathrm{SH}, \tag{4.11}$$

where the nonlinear coupling κ is given by,

$$\kappa = \frac{\omega_\mathrm{f}\varepsilon_0}{4\sqrt{\mathscr{P}_\mathrm{SH}}\mathscr{P}_\mathrm{f}} \iint_{A_\infty} \mathbf{e}_\mathrm{SH}^* \cdot \chi^{(2)}(\omega_\mathrm{SH};\omega_\mathrm{f},\omega_\mathrm{f}) \vdots \mathbf{e}_\mathrm{f}\mathbf{e}_\mathrm{f} dA. \tag{4.12}$$

From these equations it is clear that not only the overlap between the second harmonic mode and the nonlinear polarization (the integral in equation (4.12)) is important, but also that strong conversion can only be achieved when the fundamental and second harmonic mode are phase-matched. This means that $2\beta_\mathrm{f} = \beta_\mathrm{SH}$, which is equivalent to having equal effective mode indices $n_\mathrm{eff,\,f} = n_\mathrm{eff,\,SH}$. For the case of perfect phase matching the power in both the fundamental and second harmonic mode ($P_\mathrm{f}(z) \equiv |A_\mathrm{f}(z)|^2$ and $P_\mathrm{SH}(z) \equiv |A_\mathrm{SH}(z)|^2$) can be solved as,

$$P_\mathrm{f}(z) = P_\mathrm{f}(0)e^{-\alpha_\mathrm{f} z}, \tag{4.13}$$

$$P_\mathrm{SH}(z) = |\kappa|^2 (P_\mathrm{f}(0))^2 \left| \frac{e^{-\alpha_\mathrm{f} z} - e^{-\frac{\alpha_\mathrm{SH}}{2} z}}{\frac{\alpha_\mathrm{SH}}{2} - \alpha_\mathrm{f}} \right|^2. \tag{4.14}$$

Having phase matching is not trivial, and due to waveguide and material dispersion will typically not occur between two fundamental (TE00) modes. Instead the mode in which the second harmonic is generated is typically of a higher order.

4.6.2 Experimental results

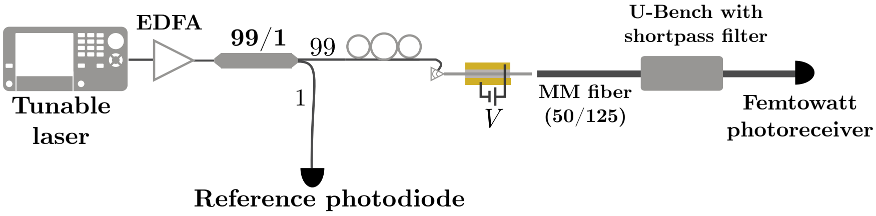

Figure 4.10: Setup used for the second harmonic generation measurements on PZT-covered waveguides. EDFA: erbium-doped fiber amplifier. The shortpass filter has a cutoff wavelength of 1000 nm.

Figure 4.10 shows the setup used for characterizing the second harmonic response of a PZT-covered SiN waveguide. Light from a tunable laser (amplified with an EDFA) is coupled into the waveguide through a grating coupler. The second harmonic, if present, can however not couple out through a grating coupler. Therefore the chip was cleaved and at the output the light was collected through a multimode fiber with a relatively high numerical aperture. The fundamental was filtered out and the second harmonic was detected using a Thorlabs PDF10A/M Detector. Second harmonic generation was observed for a fundamental wavelength near 1550 nm using a waveguide of width 2000 nm, covered with about 150 nm of PZT. The PZT was initially poled using 50 V, this step is necessary to give the PZT its nonzero nonlinear response and is explored further in Section 4.7.2.

Figure 4.11**a** shows the voltage on the detector, and the corresponding estimated second harmonic power, as a function of wavelength. The measurement is also performed for different DC voltages applied over the waveguides (see legend). Firstly, we can conclude from these graphs that the generated second harmonic only appears over a relatively narrow bandwidth, this is due to the phase-matching condition, which will only be valid within this bandwidth. Secondly, one can see that when tuning the voltage, the wavelength at which the conversion is maximum shifts. We believe that this is due to the electrooptic (Pockels) response, which is discussed in Section 4.7 and further. The Pockels effect causes the effective indices of the interacting modes to change with applied voltage. Since the shift is not expected to be the same for all modes, the phase-matching condition, $n_{\mathrm{eff,\,f}}(V) = n_{\mathrm{eff,\,SH}}(V)$, will appear at different wavelengths for different voltages. Figure 4.11**b** plots the estimated second harmonic power on the detector as a function of the reference power, the latter is proportional to the fundamental power in the waveguide. A linear fit on the (dBm-dBm)-plot shows that the relation is close to quadratic (the deviation can be due to alignment drift during the measurement, nonlinearities in the photoreceiver response and other imperfections), which is expected for second harmonic generation. Note that for the measurements in figure 4.11, mainly qualitative conclusions can be drawn with respect to the optical powers. There is a large uncertainty on the actual powers, since for example the collection efficiency of the multimode fiber for the higher-order second harmonic mode is not exactly known.

Figure 4.12 shows a camera image of the top-view of the chip. One can clearly distinguish the waveguide in which the second harmonic is generated since the scattered second harmonic light is picked up by the camera. On this image, the probe needles for applying the DC bias voltage can also be seen. The length of the waveguides with electrodes is about 1.8 mm.

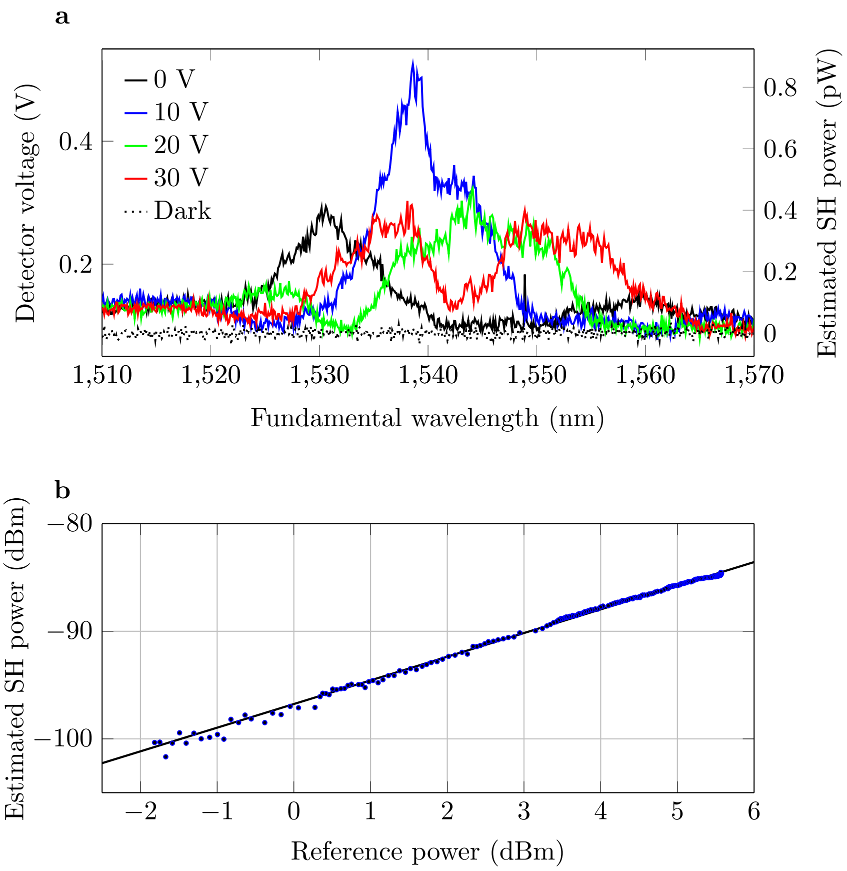

Figure 4.11: **a** Detector voltage and corresponding estimated second harmonic power on the detector, as a function of fundamental wavelength, for different voltages applied over the waveguide. The dotted line shows the dark counts of the detector. **b** Estimated second harmonic power on the detector, as a function of power on the reference photodiode. For a voltage of 10 V and a wavelength of 1540 nm. The solid line represents a fit with slope 2.19.

From this picture, a significant problem becomes apparent. The scattered SH light is quite intense in the first part of the waveguide, after which it diminishes towards the end. This is in stark contrast with the z^2-behavior that is expected for SHG in low-loss waveguides! Based on a similar camera image (although one with less background light), a rough estimate of the z-dependence of the second harmonic power in the waveguide can be made. This is done in figure 4.13. For this the assumption is made that the scattering is uniform along the waveguide length and that the camera response is linear. Then, by integrating the pixels along the waveguide in the image

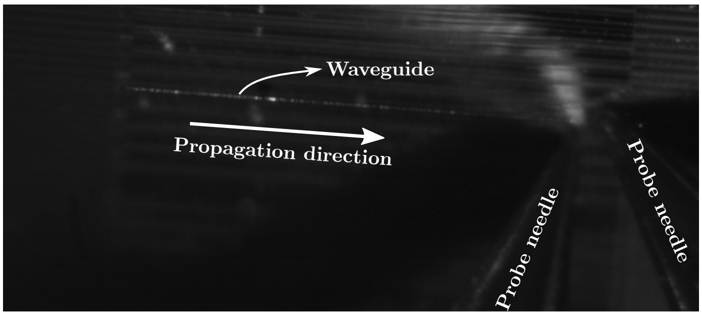

Figure 4.12: Top-view of the PZT-covered waveguide in which SHG occurs, the waveguide lights up due to the scattering of the second harmonic. The probe needels used to apply the DC voltage can also be distinguished.

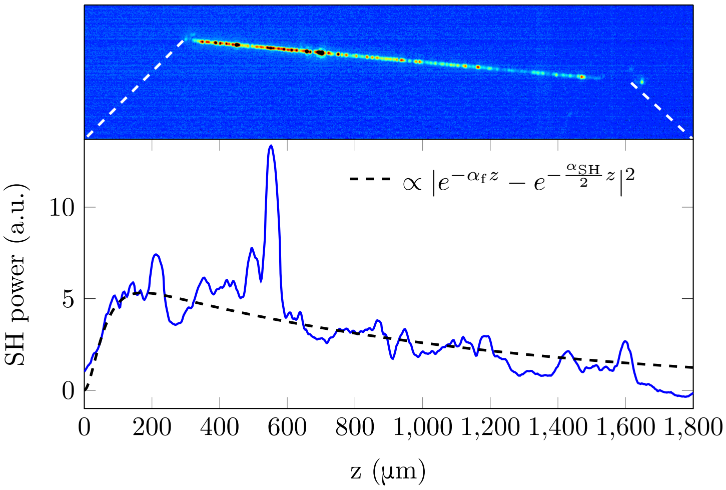

Figure 4.13: Top: camera image showing the SH light scattered from the waveguide. Bottom: estimated SH power in the waveguide based on the intensity of the scattered light observed with the camera (blue line). The dashed black line is an approximation based on equation (4.14), with $\alpha_f = 20$ dB/cm and $\alpha_{SH} = 2000$ dB/cm.

and by normalizing with respect to the dark counts of the camera, a very crude estimate of the power can be made. The blue line in the plot shows that indeed the SH power seems to rise very quickly over the first 100 - 200 μm, however over the remainder of the waveguide it seems to drop. This can be caused by very large waveguide losses. To illustrate this, the black dashed line is plotted, which is proportional to equation (4.14), for $\alpha_f = 20$ dB/cm and $\alpha_{SH} = 2000$ dB/cm.

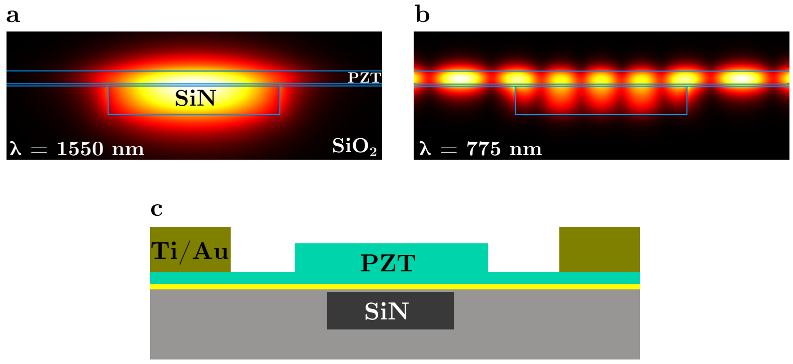

Figure 4.14: **a** TE00 mode of a PZT-covered waveguide at the fundamental wavelength (λ_f = 1550 nm). **b** Higher-order TE mode at the second harmonic wavelength (λ_{SH} = 775 nm). Both modes have an effective index of ≈ 1.83. The waveguide width, SiN thickness and PZT thickness are respectively 2000 nm, 335 nm and 150 nm. **c** Suggested solution to avoid coupling into slab modes.

Especially the loss for the second harmonic mode seems to be extremely high! We believe that this is not due to material losses, but due to coupling of the second harmonic to slab-modes in the PZT. This is illustrated in figure 4.14. Figure 4.14**a** shows the TE00 mode at a wavelength of 1550 nm, the fundamental mode in our experiment. The effective index of this mode is approximately 1.83. Hence, efficient SHG will take place to a higher order mode at about 775 nm with approximately the same index. Such a mode is given in figure 4.14**b**, as calculated using COMSOL Multiphysics®. Note that this mode is *not* well confined to the waveguide, the effective index is so low that there exist slab modes in the air-PZT-lanthanide-oxide stack with a *higher* effective index! Hence the generated second harmonic light is phase-matched to radiating slab modes (under a specific angle) which will cause enormous loss. Note that the mode in figure 4.14**b** is just an example of what the SHG mode could look like, we do not have enough information on the dispersion of the different materials to calculate the exact mode. The exact shape of the lobes outside of the waveguide core are moreover an artifact of the boundary conditions (outside of the plot).

4.6.3 Future work

It should be clear that these results can still be strongly improved. We have shown that on-chip SHG using PZT is possible, however that in the current configuration loss into slab modes is detrimental. To address this issue, an option is to etch a rib into the PZT, see figure 4.14**c**, below a certain critical thickness, no slab modes will be present and confined SH modes will exist. This is currently being explored. The loss due to radiation into the slab should then decrease, it is however unclear how the roughness of the etched surfaces of PZT will affect the mode propagation loss. It is also important that the PZT is not etched all the way through, since poling would become very difficult (PZT has a very large dielectric constant and 'expels' the poling field when not in direct contact with the electrodes). Another solution is to use a technique called quasi-phase-matching [6]. This can be achieved by periodically poling the PZT. For the right poling period, the TE00 modes of both the fundamental and second harmonic wavelength can be coupled, avoiding issues due to slab modes. It is however technologically difficult to achieve QPM on these waveguides since the material has to be periodically poled with a period of only several micrometers.

4.7 Phase modulation on a PZT-covered waveguide

4.7.1 Basic theory

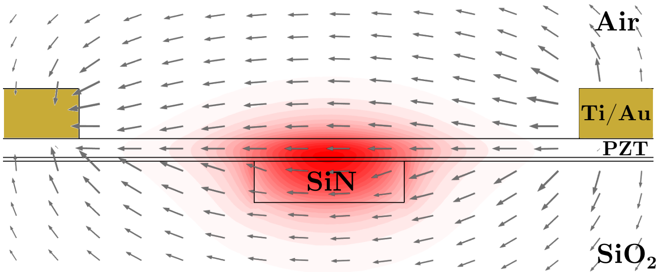

Figure 4.15: Schematic of the PZT-covered SiN waveguide used as electro-optic phase modulator, the fundamental TE optical mode at is plotted in red. The quiver plot shows the applied electric field distribution between the electrodes. PZT thickness, waveguide width and gap between the electrodes are respectively 150 nm, 1200 nm and 4 µm.

Figure 4.15 shows the cross-section of a typical PZT-on-SiN phase modulator. An electric field is applied between the in-plane electrodes, changing the refractive index in the PZT and hence the effective index of the waveguide mode. This in turn induces an extra phase shift on the optical mode upon propagation. The PZT thin films exhibit a higher refractive index ($n \approx 2.3$) than SiN ($n \approx 2$), so a significant portion of the optical mode is confined in the PZT. A grating coupler is used for in- and outcoupling, into the fundamental quasi-TE optical mode.

Mathematically this is described most intuitively by assuming the change of the PZT refractive index causes only a small perturbation. The approach is analogous to the derivation in Section 2.5. However the perturbation in equation (2.28) now does not come in the form of a nonlinear polarization density, but as a field-induced change in the dielectric susceptibility, say $\Delta\chi^{(1)}$,

$$\nabla \times \mathbf{H} = -\, i\omega\epsilon_0 n^2 \mathbf{E} - i\omega\epsilon_0 \Delta\chi^{(1)}\mathbf{E}. \tag{4.15}$$

Doing an analogous derivation, we eventually find a differential equation for the slowly varying complex amplitude of the waveguide mode A,

$$\frac{\partial}{\partial z}A(z) = i\left[\frac{\omega\epsilon_0}{4\mathscr{P}}\iint_{A_\infty}\mathbf{e}^*\cdot\Delta\chi^{(1)}\mathbf{e}dA\right]A(z) = i\Delta\beta A(z), \tag{4.16}$$

where the power normalization constant $\mathscr{P}$ is given by equation (2.20) and $\mathbf{e}$ is the electric field of the optical mode. Equation (4.16) expresses nothing more than a change in the mode propagation constant, $\Delta\beta$, and hence an equivalent change in effective mode index $\Delta n_{\text{eff}} = \Delta\beta c/\omega$.

We will now make the simplifying assumption that the electric field is applied in the in-plane-(x-)direction. As a consequence the change in susceptibility, $\Delta\chi^{(1)}$, only takes place in this direction, $\Delta\chi^{(1)}_{xx} = 2\chi^{(2)}_{\text{eff}}E^e_x$, with $\mathbf{E}^e$ the applied electric field. We will also assume that PZT is the only material with a significant Pockels coefficient in the waveguide cross-section,

$$\Delta n_{\text{eff}} = \frac{c\epsilon_0\chi^{(2)}_{\text{eff}}\iint_{\text{PZT}}|e_x|^2E^e_x dA}{\iint_{A_\infty}\text{Re}(\mathbf{e}\times\mathbf{h}^*)\cdot\hat{\text{e}}_z dA} = -\frac{c\epsilon_0 n^4_{\text{PZT}}r_{\text{eff}}\iint_{\text{PZT}}|e_x|^2E^e_x dA}{2\iint_{A_\infty}\text{Re}(\mathbf{e}\times\mathbf{h}^*)\cdot\hat{\text{e}}_z dA}, \tag{4.17}$$

where n_{PZT} is the refractive index of the PZT and r_{eff} the effective Pockels coefficient. For the final expression the relation between the second order susceptibility and Pockels coefficient in equation (4.7) was used, in the assumption that $\varepsilon_{r,xx} = n^2_{\text{PZT}}$. In this context, the concept of a confinement factor Γ is often used [21, 35, 36] to relate the effective index change with the index change in the 'active layer';

$$\Delta n_{\text{eff}} = \Gamma\Delta n_{\text{PZT}} = -\frac{1}{2}\Gamma r_{\text{eff}} n^3_{\text{PZT}}\frac{V}{g}, \tag{4.18}$$

where we have assumed that the spatial variation in Δn_{PZT} is negligible and that the electric field is uniform and equals V/g, with V the voltage difference and g the gap between the electrodes. The confinement factor is,

$$\Gamma = \frac{g}{V}\frac{c\epsilon_0 n_{\text{PZT}}\iint_{\text{PZT}}|e_x|^2E^e_x dA}{\iint_{A_\infty}\text{Re}(\mathbf{e}\times\mathbf{h}^*)\cdot\hat{\text{e}}_z dA}.^1$$

---

[1] Note that in many references, e.g. [21, 35], expressions for the confinement factor of

A very important figure-of-merit of a phase modulator is the half-wave voltage-length product $V_\pi L$. This is the voltage-length product over which the optical mode acquires an extra phase shift of $|\Delta\beta L| = |\Delta n_{\mathrm{eff}} \omega L/c| = \pi$ due to the modulation voltage. From equation (4.18) readily follows,

$$V_\pi L = \frac{\lambda g}{n_{\mathrm{PZT}}^3 \Gamma r_{\mathrm{eff}}}, \tag{4.20}$$

where λ is the free-space wavelength.

4.7.2 Preliminary phase modulation and poling

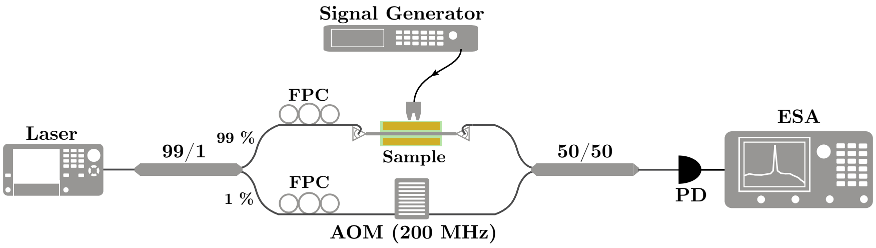

Figure 4.16: Setup used for phase modulation measurements. FPC: fiber polarization controller, AOM: acousto-optic modulator, PD: photodiode, ESA: electrical spectrum analyzer.

Directly measuring phase modulation is not straightforward, as photodiodes only measure optical intensity. In order to characterize phase modulators, it is most convenient to incorporate them into resonators or interferometers. This is done further in this chapter. It is however not impossible to characterize the phase-modulation efficiency of a simple waveguide. A method to do this is introduced here, which can be useful to do rapid proof-of principle measurements of phase modulation and poling of the deposited PZT. The setup is shown in figure 4.16. A pump laser is split into two paths, one of which is phase modulated by our device-under-test, at frequency Ω. The

---

the kind $\Gamma = \frac{g}{V} \frac{\iint_{\mathrm{PZT}} |e_x|^2 E_x^e dA}{\iint_{A_\infty} |e_x|^2 dA}$, are used. Such an expression stems from two approximations,

$$\Gamma = \frac{g}{V} \frac{c\epsilon_0 n_{\mathrm{PZT}} \iint_{\mathrm{PZT}} |e_x|^2 E_x^e dA}{\iint_{A_\infty} \mathrm{Re}(\mathbf{e} \times \mathbf{h}^*) \cdot \hat{\mathrm{e}}_z dA} \approx \frac{g}{V} \frac{n_{\mathrm{PZT}} \iint_{\mathrm{PZT}} |e_x|^2 E_x^e dA}{\iint_{A_\infty} n |e_x|^2 dA} \approx \frac{g}{V} \frac{\iint_{\mathrm{PZT}} |e_x|^2 E_x^e dA}{\iint_{A_\infty} |e_x|^2 dA},$$

the first approximation assumes that the fields closely resemble transversal electromagnetic plane waves, the second that $n(\mathrm{r}_\perp) = n_{\mathrm{PZT}}$. Both approximations are invalid in waveguides with sub-wavelength features and with high index contrast.

other path is frequency-shifted by $\Delta\omega = 200$ MHz using an acousto-optic modulator (AOM). The two paths are then combined and observed using a photodiode and an electrical spectrum analyzer (ESA). The photodiode now detects beat notes between the phase-modulated signal and the frequency-shifted signal, at frequencies $\Delta\omega$, $\Delta\omega - \Omega$ and $\Delta\omega + \Omega$. In the assumption that the phase modulation is small ($\ll \pi$) the ratio between electrical power of the beat notes at $\Delta\omega \pm \Omega$ and $\Delta\omega$ will be,

$$\frac{P_{\Delta\omega\pm\Omega}}{P_{\Delta\omega}} = \left[\frac{\pi}{\sqrt{2}}\frac{V_{\mathrm{RMS}}L}{V_\pi L}\right]^2, \tag{4.21}$$

where the square stems from the fact that electrical power scales quadratically with optical power. V_{RMS} is the root-mean-square of the voltage applied by the signal generator. This provides a good way of estimating $V_\pi L$-values of phase shifters. Preliminary tests on SiN waveguides covered with ≈ 150 nm of PZT, with gaps between the electrodes of ≈ 5 − 6 µm have been performed, showing that $V_\pi L$ values in the range of several V cm can be achieved. Figure 4.17**a** shows an example of an electrical spectrum as measured on the ESA, for $\Omega = 5$ MHz. Figure 4.17**b** shows how the measured $V_\pi L$ varies when a series of poling voltages is applied (for this a bias-T is added in parallel with the signal generator). Initially, the modulation is very inefficient, upon applying increasingly larger poling voltages, the $V_\pi L$ drops sharply. At 42 V, the poling voltage is maintained for 30 minutes.

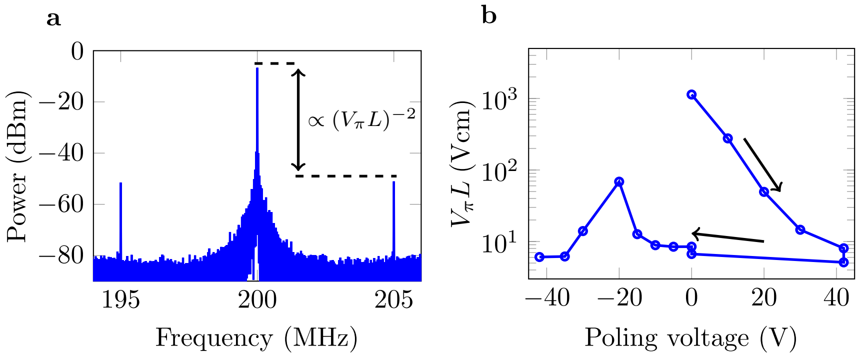

Figure 4.17: **a** Example of an RF power spectrum used for preliminary characterization of a PZT-on-SiN phase modulator. **b** Estimated $V_\pi L$ value while applying a sequence of different poling voltages. The arrows show the order in which the voltages were applied. At 42 V the poling voltage is applied for 30 minutes (hence the two points, before and after). At 0 V, the same is done for 60 minutes. Waveguide width = 2400 nm, PZT thickness ≈ 150 µm, wavelength = 1550 nm, phase shifter length = 165 µm, electrode gap ≈ 6 µm, $\Omega = 10$ MHz.

There is a clear drop in $V_\pi L$ over this period. After poling, the voltage is brought back down to 0 V, and two measurements are performed with a 60 minute delay. A small decrease in modulation efficiency is observed. Upon applying negative voltages the poling can be undone and the $V_\pi L$ briefly increases around -20 V, after which it drops again, this corresponds to the coercive fields at which the poling of the crystals gets reversed. From this we can conclude that poling voltages of several tens of volts (here limited by the specifications of the bias-T, however on other devices voltages of 60-80 V have been successfully used) should be used for the poling of the PZT, and that the voltage should be applied for at least a couple of tens of minutes. Note that the $V_\pi L$-values given in this section are only to be used for order-of-magnitude estimations and relative comparisons between different measurements, as a relatively large error can be induced by the nonlinearity of the photoreceiver (Thorlabs PDB480C-AC). The increase of $V_\pi L$ at 0 V over time will be the subject of the discussion in Section 4.8.3.

4.8 Electro-optic amplitude modulators on SiN

A phase modulator can be used for amplitude modulation when incorporated in a photonic resonator or interferometer. Two types of such devices, ring resonator modulators and Mach-Zehnder modulators, were fabricated, these devices and their performance are discussed in this section.

4.8.1 Modulator types

In figure 4.18, top views and cross-sections of three different modulators are shown, in figure 4.19, the transmission curves of these devices are shown. All these devices are designed for the fundamental TE mode.

Figures 4.18**a** and **b** show a ring modulator designed for the C-band (1530 nm - 1565 nm). A more detailed cross-section of the phase-shifter of this device can be found in figure 4.7**b**. The ring radius R, the length of the phase shifter L and the electrode spacing g are respectively 100 µm, 524 µm and 4.4 µm. This device is fabricated on a SiN chip which was planarized in-house, through a combination of dry and wet etching (see Section 4.5). As discussed before, this can result in significant steps between the waveguide core and the surrounding oxide, causing the PZT to have slight variations in thickness. Figure 4.19**a** shows the transmission spectrum of this device. The ring has a loaded Q factor of 2230 and a free-spectral range (FSR) $\Delta\lambda_{\mathrm{FSR}} \approx 1.7$ nm. The combined loss of a grating coupler and the transition loss between a bare and PZT-covered waveguide section is ≈ 12 dB at the

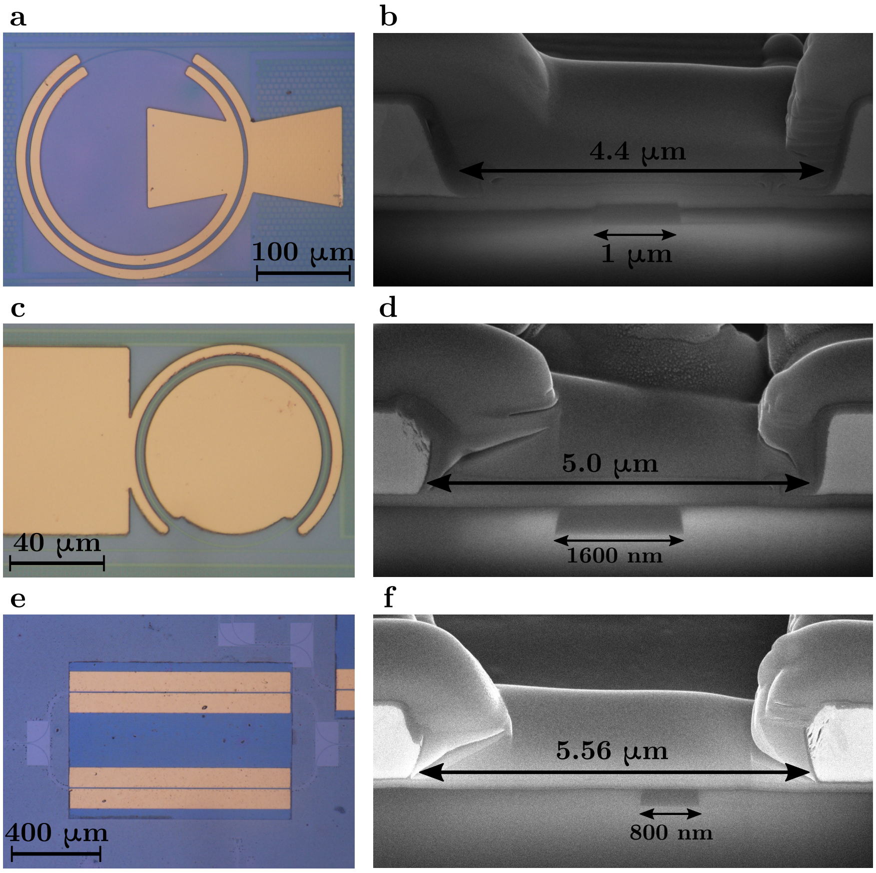

Figure 4.18: **a** Top view of a C-band ring modulator. **b** Cross-section of a C-band ring modulator. **c** Top view of an O-band ring modulator. **d** Cross-section of an O-band ring modulator. **e** Top view of a C-band MZI modulator. **f** Cross-section of a C-band MZI modulator. The nominal thickness of the intermediate lanthanide layer (below the PZT) is 24 nm in all devices.

optimum, however this is currently not optimized and can still be improved by design.

From these numbers, it is possible to estimate the losses in the ring resonator. Using the expressions in reference [37], and by assuming that the ring is critically coupled (which is a good approximation considering the deep resonance dips), we can relate the single pass amplitude transmission a to the FSR and the Q factor,

$$Q \approx \frac{\pi \lambda a}{\Delta\lambda_{\mathrm{FSR}}(1-a^2)}. \tag{4.22}$$

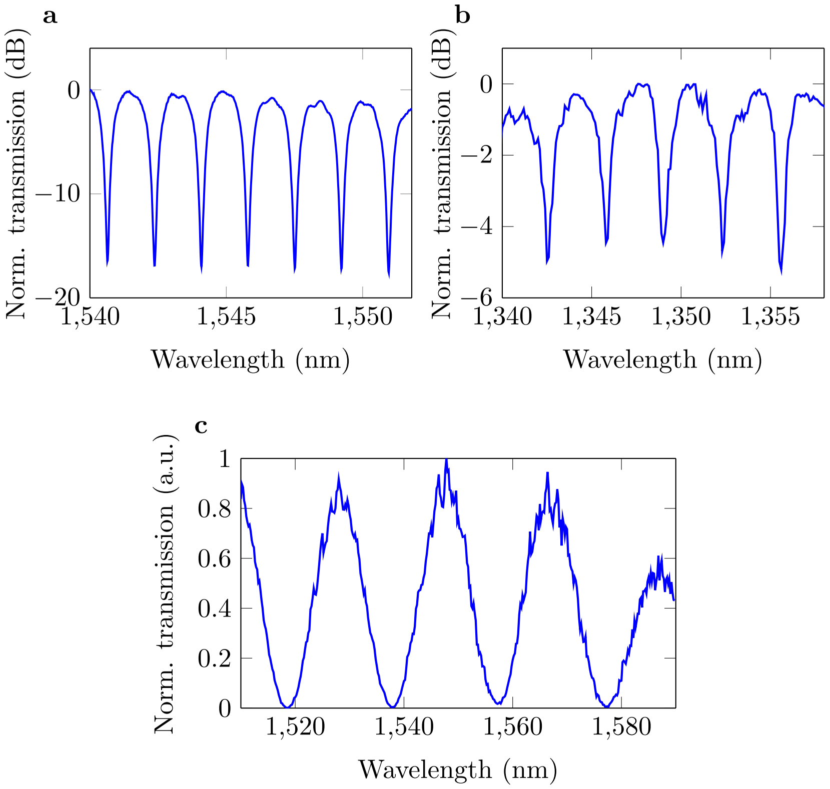

Figure 4.19: Normalized transmission spectra of a C-band ring modulator (**a**), an O-band ring modulator (**b**) and a C-band MZI modulator (**c**).

The average propagation loss per unit length then equals $20 \log_{10}(a)/(2\pi R) \approx$ 83 dB cm^{-1}. Notably, this is about an order of magnitude larger than the propagation losses measured on spirals with no electrical contacts (Section 4.5.2). We believe that this is due to misalignment of the electrodes. Figure 4.20**a** shows a microscope image of such misalignment, which can easily amount to 1 µm or more. In figure 4.20**b**, the simulated loss contribution (using Lumerical FDTD) due to the electrodes is plotted, as a function of misalignment. For a wavelength of 1550 nm, a bend radius of 100 µm, a waveguide width of 1 µm and a PZT thickness of 120 nm, with an intermediate layer of 24 nm thick. Note that the extra losses for electrode spacings in the range of 4 - 5 µm can be of the order of 100 dB cm^{-1} or more, which can easily explain the *average* loss for the whole ring circumference to be $\approx$ 80 dB cm^{-1}. For this ring, the estimated power coupling of the

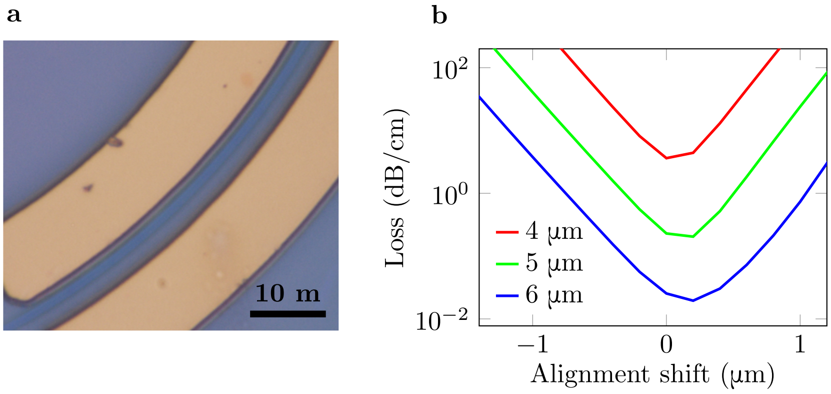

Figure 4.20: **a** Example of a slightly misaligned electrode pattern on a ring modulator, the misalignment is ≈ 1 μm. **b** Electrode-induced loss as a function of electrode misalignment, for different electrode spacings (see legend). For a wavelength of 1550 nm, a bend radius of 100 μm, a waveguide width of 1 μm and a PZT thickness of 120 nm, with an intermediate layer of 24 nm thick. Simulated with Lumerical FDTD.

directional coupler that is estimated based on the transmission spectrum equals $k^2 = 1 - a^2 \approx 0.7$. This explains why we found approximate critical coupling for rings with relatively small directional coupling gaps (200 nm). Estimates based on supermode theory have shown that for these gaps power coupling coefficients on the order of 0.7 - 0.8 are indeed realistic.

Figures 4.18**c** and **d** show the respective top-view and cross-section of a ring modulator designed for the O-band (1260 nm - 1360 nm). A more detailed cross-section of the phase-shifter of this device can be found in figure 4.7**d**. For this device, the planarization was done in the CMOS foundry through CMP (see Section 4.5). Figure 4.19**b** shows the transmission. The ring has a Q-factor of 1820 and a FSR of 3.27 nm. The ring radius is 40 μm, with a phase shifter length L of 195 μm.

The second modulator type is a Mach-Zehnder Interferometer (MZI). For this device, the incoming light is split using multimode interferometer (MMI) into two different arms, in which the light acquires different phase delays. The output field is then the result of interference in a second MMI combining light from these two arms. For an MZI with equal loss over the two arms, the output power is proportional to $1 + \cos(\Delta\varphi)$, with $\Delta\varphi$ the phase difference between the two arms. In figures 4.18**e** and **f**, such an MZI modulator designed for the C-band is shown. A more detailed cross-section can be found in figure 4.7**c**, the planarization was again done in-house. The electrodes have a length of 1 mm. The static transmission spectrum of this device is shown in figure 4.19**d**.

4.8.2 Static modulation

The transmission spectra of the modulators can be measured for different DC-voltages applied across the PZT layer. In figure 4.21**a**, this is done for the C-band ring resonator. The voltage-induced change in effective index clearly shifts the resonance. In figure 4.21**b**, the resonance wavelength shift is plotted as a function of voltage, the slope of the linear fit corresponds to a tuning efficiency $\Delta\lambda/\Delta V \approx -13.4$ pm V^{-1}. From this slope, it is possible to estimate the $V_\pi L$ of the phase shifter in the ring modulator. We can do this using the simple observation that when the phase change in the ring, $|\pi\frac{\Delta V L}{V_\pi L}|$, equals 2π, that the wavelength shift is exactly $|\Delta\lambda| = \Delta\lambda_{\mathrm{FSR}}$. This leads to the relation $V_\pi L = |L\lambda_{\mathrm{FSR}}\Delta V/(2\Delta\lambda)|$. For the C-band ring modulator, this yields a half-wave voltage-length product of $V_\pi L \approx 3.3$ Vcm.

Figures 4.21**c** and **d** show the transmission spectra for the O-band ring resonator for different applied voltages, and the resonance shift as a function of voltage. The linear fit on figure 4.21**c** shows a resonance tuning efficiency of $\Delta\lambda/\Delta V \approx -10$ pm V^{-1}. From this we can estimate, $V_\pi L = |L\lambda_{\mathrm{FSR}}\Delta V/(2\Delta\lambda)| \approx 3.19$ Vcm.

In figure 4.21**e** the transmission spectrum of the C-band MZI modulator is plotted, for different voltages applied to a *single* arm of the MZI. As was mentioned before, the transmission spectrum of an MZI is proportional to $1 + \cos(\Delta\varphi)$, with $\Delta\varphi$ the phase difference between the two arms. To good approximation (assuming that the relative phase difference is linear with the wavelength), we can fit this sinusoidal function to the curves in figure 4.21**e**. The relative phase differences between the fitted curves then correspond to the relative changes in optical phase along the phase-modulated arm. These relative phase shifts are plotted in figure 4.21**f**, as a function of voltage. From the slope of the linear fit, we can estimate $\frac{\partial\varphi}{\partial V} = 0.021\pi$ rad/V. We can now estimate $V_\pi L = (\pi L)/(\frac{\partial\varphi}{\partial V}) \approx 4.76$ Vcm.

From the measured $V_\pi L$-values, it is possible to estimate the Pockels coefficient of the PZT. For this we can use equation (4.20), provided that we can make a good estimate of the electro-optic confinement factor Γ. This can be done by calculating the optical mode using a COMSOL Multiphysics®-model, using an as accurate waveguide cross-section as possible and equation (4.19). The used waveguide models are based on the SEM-images of figure 4.7**b-d**. For the C-band ring, the C-band MZI and the O-band ring, the respective estimated Pockels coefficients r_{eff} are 61, 70 and 67 pm V^{-1}. The respective simulated confinement factors were 0.27, 0.22 and 0.28.

Variations in the measured $V_\pi L$ values are mainly due to variations in

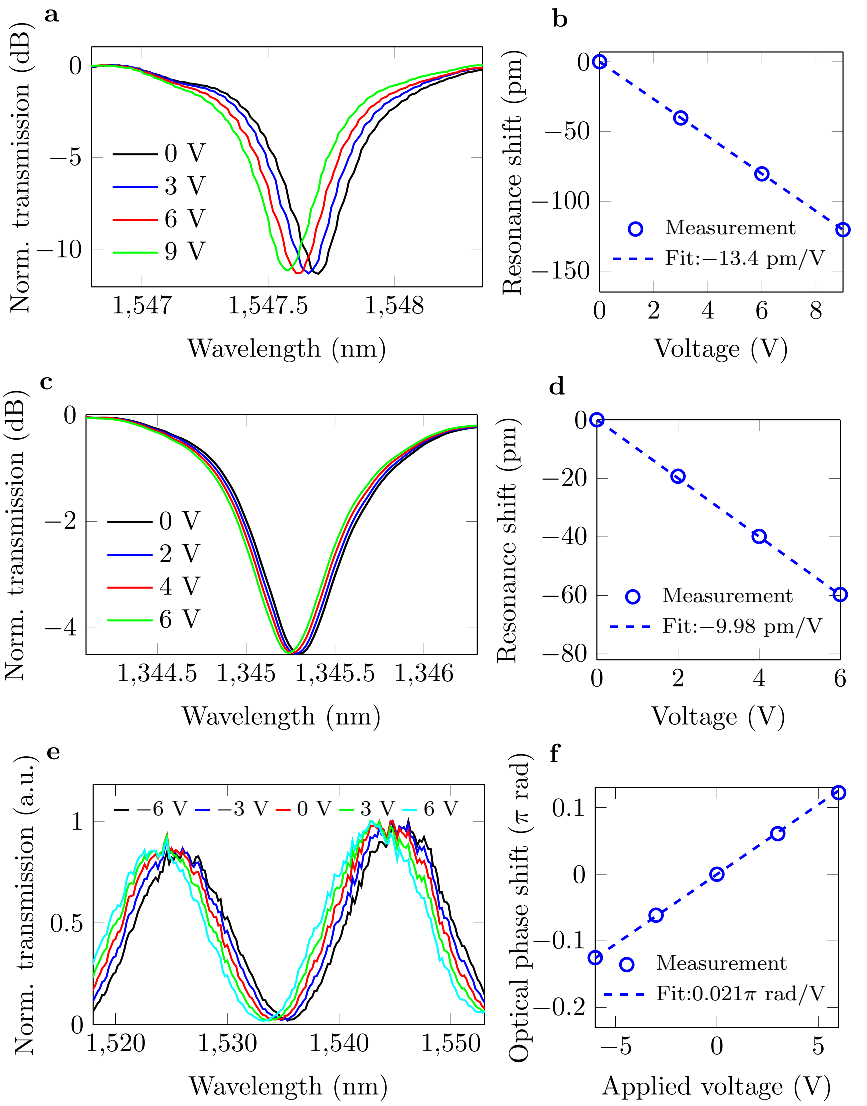

Figure 4.21: **a** Normalized transmission spectra for different DC voltages of the C-band ring modulator. **b** Resonance wavelength shift of the C-band ring versus voltage, including a linear fit. **c** Normalized transmission spectra for different DC voltages of the O-band ring modulator. **d** Resonance wavelength shift of the O-band ring versus voltage, including a linear fit. **e** Normalized transmission spectra for different DC voltages of the C-band MZI modulator. **f** Optical phase shift as a function of voltage, including linear fit.

the waveguide cross-sections, electrode spacings and the used wavelengths (C-band versus O-band), see equation (4.20). Extracted electro-optic coefficients r_{eff} also vary somewhat, differences can in part be due to variations in film quality on different samples, but mainly stem from small uncertainties on the exact cross-section dimensions.

4.8.3 Poling stability

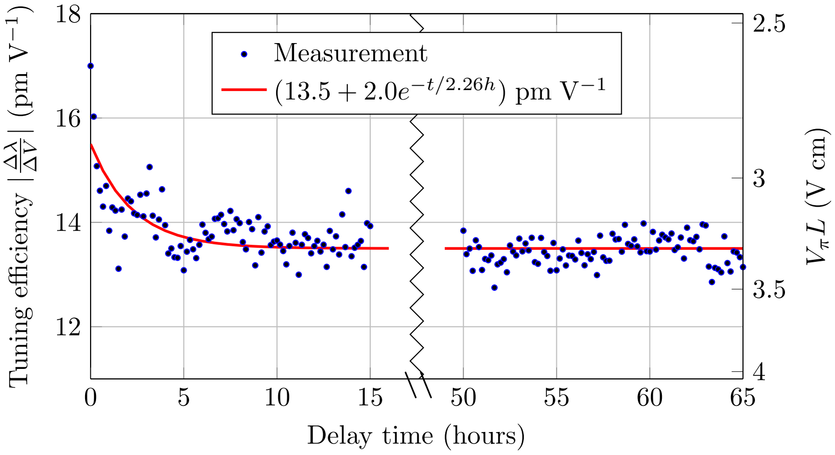

Figure 4.22: Tuning efficiency (in absolute value) of a C-band ring as a function of time after poling. The axis on the right shows the estimated corresponding $V_\pi L$.

It was clear from the preliminary phase modulation measurements discussed in Section 4.7.2 that the response of the PZT is negligible right after deposition. To become electro-optically active, the material has to be poled first. During this poling step, the material is exposed to high voltages (60-80 V), typically for about an hour. After the poling voltage is removed, the material (partly) retains its Pockels coefficient. This is advantageous, as for similar demonstrations, for example using BTO, a constant bias has to be maintained [20–22].

However, as was already clear from the measurement shown in figure 4.17**b**, the Pockels-coefficient decreases over time after the poling step. To investigate this further, a measurement of the tuning efficiency of a ring was performed over time after the poling step. The results are shown in figure 4.22. The PZT on a C-band ring modulator was poled prior to the measurement, after which no bias voltage was used. The DC tuning efficiency was periodically measured (sweeping the voltage over [-2,+2] V) over a total time of almost three days. The resulting tuning efficiency $\Delta\lambda/\Delta V$ is plotted as a function of time. On the right-hand axis, the corresponding $V_\pi L$ is plotted. $\Delta\lambda/\Delta V$ decays towards a stable value of about -13.5 pmV^{-1} over the course of several hours (see the exponential fit). Within the time-frame of the measurement, the poling stabilized and there have been no indications of decay over much longer periods of time.

4.8.4 High-speed characterization

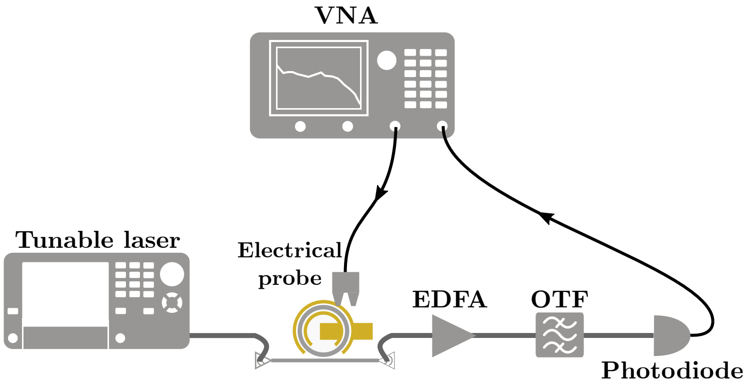

Figure 4.23: Sketch of the setup used for the small signal measurements. VNA: vector network analyzer, EDFA: erbium-doped fiber amplifier, OTF: optical tunable filter.

For many applications, high-speed operation is essential. For this, first the small-signal response of our devices was characterized. In figure 4.24, the setup used for the small-signal characterization is shown. Light coming from a tunable laser is coupled into the modulator. For a ring resonator, the laser is tuned to the edge of the resonance dip, hence applying a voltage between the contacts will shift the resonance position (see for example figures 4.21**a** and **c**) and modulate the transmitted laser power. For an MZI, the laser is tuned to one of the slopes in the transmission curve (figure 4.21**e**). The out-coupled light is amplified using an erbium doped fiber amplifier (EDFA) (only for C-band measurements, not for O-band) to facilitate detection and the amplified spontaneous emission (ASE) is filtered out using an optical tunable filter (OTF). The power is then detected using a high-speed photodiode (Discovery Semiconductors DSC10H Optical Receiver). The modulator is driven by an Agilent PNA-X N5247A vector network analyzer (VNA) through a high-speed probe. The VNA measures the S_{21} parameter of the system as a function of modulation frequency. $|S_{21}|$ corresponds the ratio of the amplitudes of the received and transmitted modulated voltage.

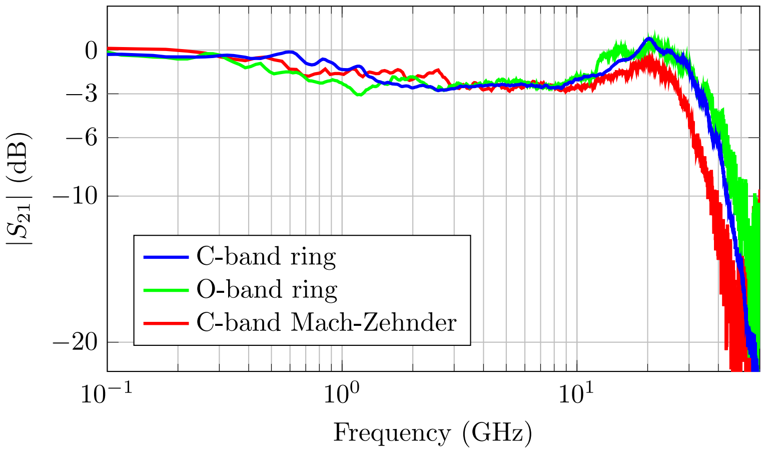

Figure 4.24: Electro-optic small signal ($|S_{21}|$ parameter) measurement of several modulators.

On figure 4.24, the $|S_{21}|$ measurements for different modulators are plotted. The measured 3 dB bandwidths of both rings are around 33 GHz, the Mach-Zehnder has a bandwidth of 27 GHz. The bandwidths are not limited by the intrinsic material response of PZT, but by device design and/or characterization equipment, as the dominating contributions to the Pockels effect are expected to have a bandwidth which is almost two-orders of magnitude larger [38, 39]. Note that the plotted S-parameter is a ratio between the electrical powers. If one would look at the point where the modulation of the optical power is half of that at low frequencies, one would have to look at the 6 dB bandwidths (due to the quadratic dependence between electrical and optical power caused by the photodiode), which lie at approximately 40, 42 and 32 GHz for respectively the C-band ring, the O-band ring and the C-band Mach-Zehnder modulator.

We furthermore demonstrate that our platform can be used for high-speed data transmission. In figure 4.25, a setup to measure eye diagrams is sketched. The setup is very similar to the small signal setup in figure 4.23, however the VNA is now replaced by an arbitrary waveform generator (AWG - Keysight AWG M8195A) and RF amplifier (SHF S807) to drive the modulator and an oscilloscope (Keysight 86100D) to detect the modulated signal. The photodiode used for this experiment is a Discovery Semiconductors DSC-R409 PIN-TIA Optical Receiver. The AWG and RF amplifier apply a pseudorandom non-return-to-zero (NRZ) binary sequence to the

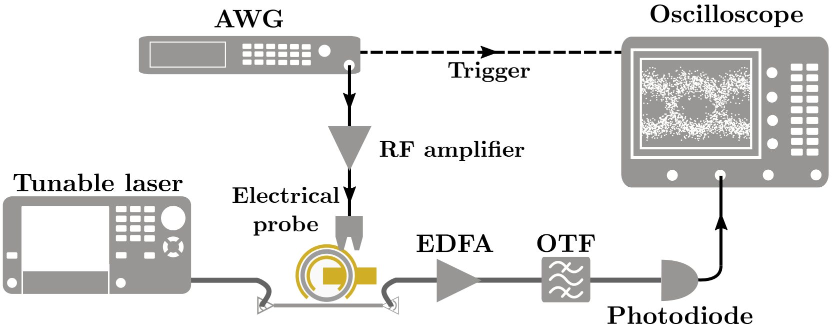
AWG
Oscilloscope
Trigger
RF amplifier
Tunable laser
Electrical probe
EDFA
OTF
Photodiode

Figure 4.25: Sketch of the setup used for the eye diagram measurements. AWG: arbitrary waveform generator, EDFA: erbium-doped fiber amplifier, OTF: optical tunable filter.

modulator (about 4.2 V peak-to-peak), the eye diagrams can be visualized on the oscilloscope.

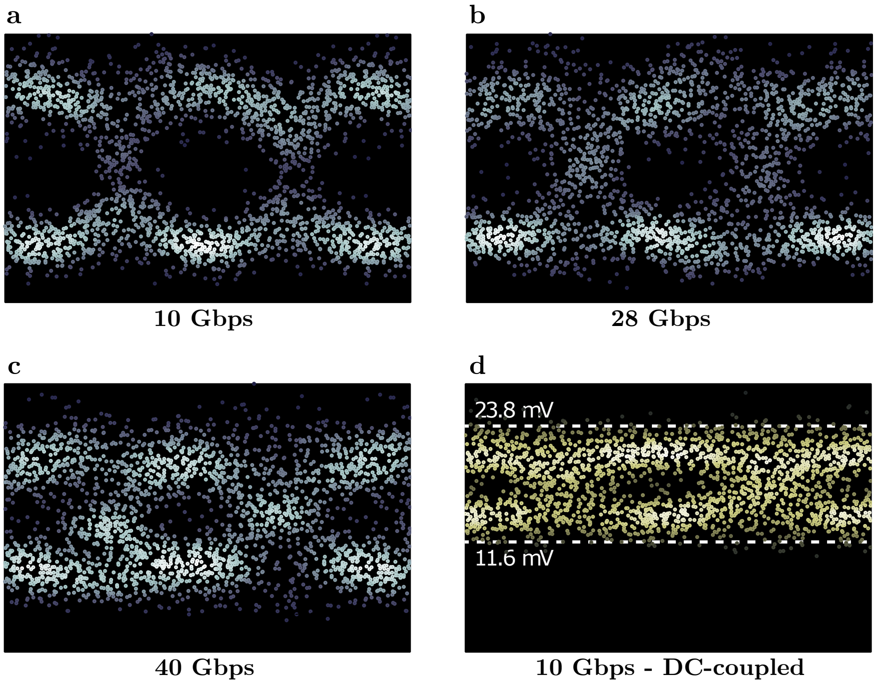

Figure 4.26: **a-c** Eye diagrams of a C-band ring modulator, measured with a non-return-to-zero scheme (2^9-1 pseudorandom binary sequence) and a peak-to-peak drive voltage of 4.2 V. Using respective modulation speeds of 10, 28 and 40 Gbps. **c** Eye diagram at 10Gbps, obtained using a DC-coupled optical receiver.

In figures 4.26**a-c**, eye diagrams obtained for the C-band ring modulator are plotted for different bitrates. The eye remains open up until about 40 Gbps, this is likely limited by the AWG, which has a bandwidth of 25 GHz and automatically decreases its voltage swing when the bandwidth of the generated signal exceeds the AWG bandwidth to maintain signal integrity.

The eye diagrams in figures 4.26**a-c** only show the modulated component of the optical power, to estimate the extinction ratio and link this to the static measurements, a measurement was performed of both the DC and modulated component. The eye diagram shown in figure 4.26**d** was obtained using a DC-coupled Tectronix 80 C02-CR optical receiver with a sampling oscilloscope (Tektronix CSA 8000). Since the measured voltage scales with the total optical power, we can estimate the extinction ratio to be about $10 \cdot \log_{10}(P_{\mathrm{max}}/P_{\mathrm{min}})$ dB $\approx \log_{10}(23.8/11.6)$ dB $= 3.12$ dB. This corresponds well with a simple ball-park estimate based on the observed transmission spectrum and static DC-shift (figures 4.19**a** and 4.21**a**, **b**), since the extinction ratio in DC can be estimated as $\Delta T \approx |\left[\frac{dT}{d\lambda}\right]_{\mathrm{max}} \cdot \frac{d\lambda}{dV} \cdot V_{\mathrm{pp}}| \approx$ 60 dB nm^{-1} $\cdot$ 13.5 pm V^{-1} $\cdot$ 4.2 V = 3.4 dB, where T is the transmission expressed in dB and $\left[\frac{dT}{d\lambda}\right]_{\mathrm{max}} \approx$ 60 dB nm^{-1} is essentially the peak of the derivative of the transmission spectrum (for example the curves in figure 4.21**a**). This ball-park comparison shows that the static measurements, and the measurements performed at high-speed, are quantitatively reasonably consistent.

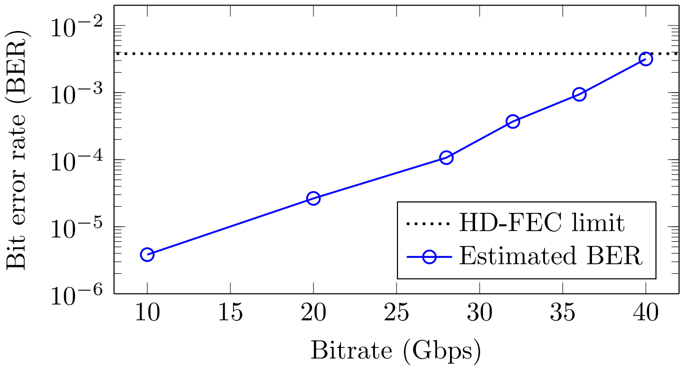

Figure 4.27: Bit error rates estimated on the basis of measured eye diagrams, the horizontal dotted line represents the HD-FEC limit with 7% overhead.

Finally, the measured eye diagrams can also be used to make a rough estimate of the bit-error rate (BER). To do this, a sum of two Gaussian distributions is fitted to the density of points as a function of voltage within a limited region around the center of the eyes. The Gaussian distributions are centered around the top (1) and bottom (0) levels of the eye diagram. The standard deviations of the distributions are representative for the fluctuations of the measured points around their average values, and can be linked to how often a 1-bit will be detected as a 0-bit, and vice versa. The detailed mathematics of this method can be found in reference [40]. The results of this analysis are plotted in figure 4.27. Note that this is only an approximate method for estimating the BER, it assumes the noise is Gaussian and the fit is performed on a limited number of points in a chosen 'time interval around the center of the eye'. However the trend is clear, as can be seen on the plot, the estimated BER increases very rapidly with bitrate. As a reference, the hard-decision forward error coding (HD-FEC) limit with 7% overhead of $3.8 \cdot 10^{-3}$ is also shown (an admittedly very forgiving limit, although commonly used in practice, see for example references [41, 42]). All measured bitrates give an estimated BER below this limit. It is also important to note that the BER is not inherent to the platform, if the extinction ratio of the modulator would for example increase, by using a ring with a higher Q factor or by applying a larger voltage swing, the BER would automatically decrease.

4.9 Further optimization of PZT-on-SiN phase modulators

The devices studied in this chapter were not fully optimized in terms of electro-optic modulation parameters. For example, the PZT thickness was rather low in order to reduce deposition times and to limit bend losses and coupling losses into PZT covered waveguide sections. However such limitations can be alleviated by design.

In this section, a PZT-on-SiN phase shifter is optimized with respect to the PZT thickness, the electrode spacing and the width of the waveguide, all calculations are performed using a COMSOL model of the phase shifter cross-section. Two important parameters are calculated using this model. Firstly, the waveguide propagation loss is estimated, the loss is assumed to consist of two contributions, one caused by the electrodes, $\alpha_{\text{electrodes}}$, and an intrinsic contribution, $\alpha_{\text{intrinsic}}$, caused by material/scattering losses in the remainder of the waveguide cross-section. The electrode contribution can be estimated by appropriately modelling the metals in the mode solver and by simply using the imaginary part of the calculated effective mode index κ_{eff}, $\alpha_{\text{electrodes}} = \frac{4\pi}{\lambda}\kappa_{\text{eff}}$. The intrinsic contribution can not be modelled in a straightforward way, since we do not know to which extent the different materials and interfaces contribute to the waveguide loss. Hence $\alpha_{\text{intrinsic}}$ is assumed to have a constant value of 1 dB cm^{-1}, a realistic value if the

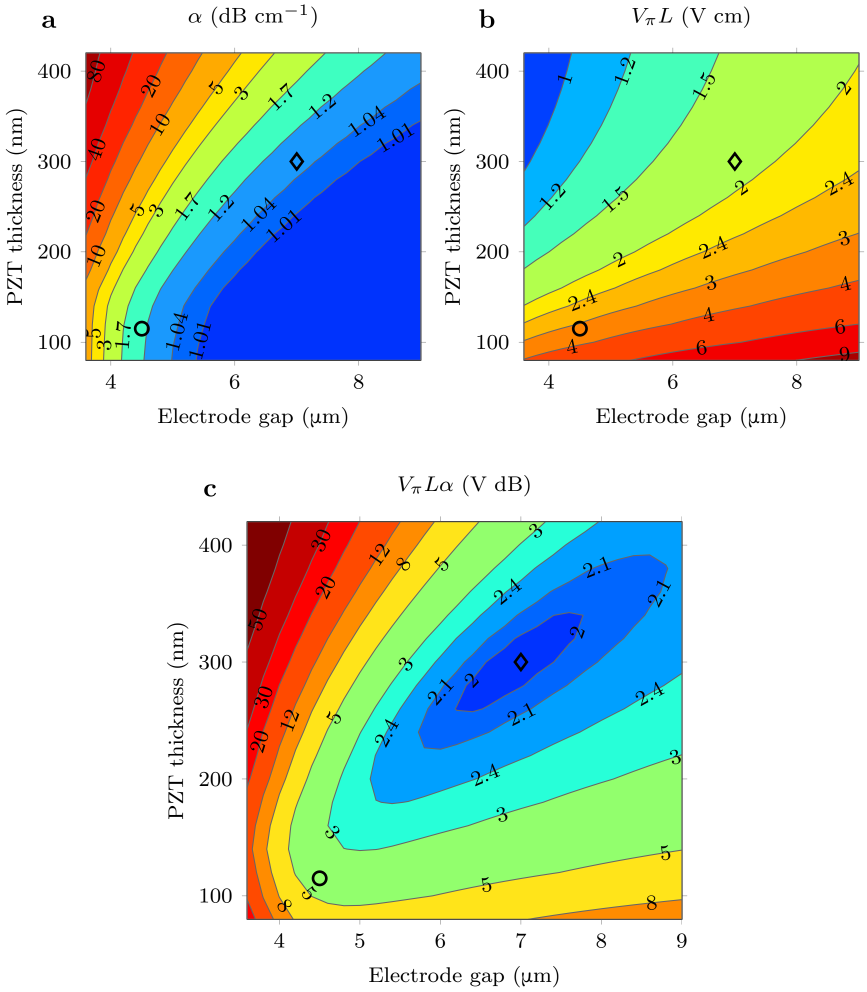

Figure 4.28: Simulation of the waveguide loss α (**a**), the half-wave voltage-length product $V_\pi L$ (**b**) and their product $V_\pi L\alpha$ (**c**) of a PZT-covered SiN waveguide modulator of the type shown in figure 4.15, for a wavelength of 1550 nm. Waveguide height, width and intermediate layer thickness are respectively 300 nm, 1.2 µm and 20 nm. The intrinsic waveguide loss (in the absence of electrodes) was taken to be 1 dB cm^{-1}, the effective electro-optic Pockels coefficient 67 pm V^{-1}. The circles show the approximate parameters used in this work, the diamonds show the optimal point with respect to $V_\pi L\alpha$.

samples are planarized using CMP. Secondly, the half-wave voltage length product $V_\pi L$ is estimated, using equations (4.19) and (4.20). In figure 4.28,

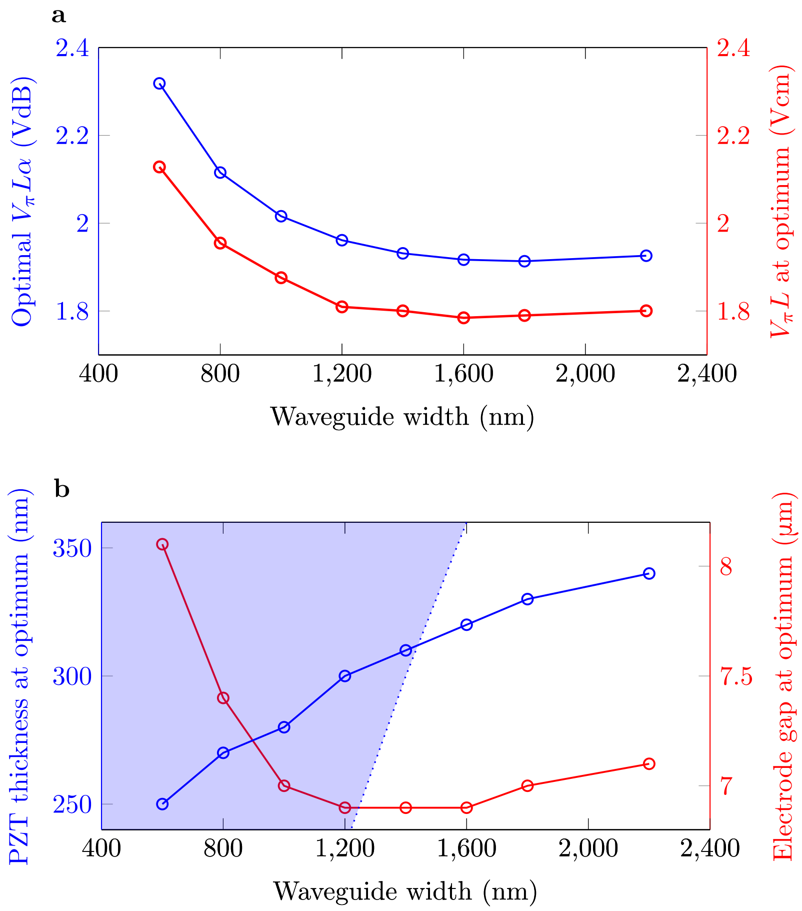

Figure 4.29: Optimization of the waveguide loss times the half-wave voltage-length product $V_\pi L\alpha$ of a PZT-covered SiN waveguide modulator as a function of waveguide width. **a** For each waveguide width $V_\pi L\alpha$ is minimized as function of both electrode spacing and PZT thickness (blue line). The red line plots the calculated $V_\pi L$ at this optimum. **b** Electrode spacing (blue) and PZT thickness (red) at the optimum. The light blue area shows the waveguide width/PZT thickness combinations for which the waveguide only supports a single TE mode. Wavelength, SiN height and intermediate layer thickness are respectively 1550 nm, 300 nm and 20 nm. The intrinsic waveguide loss (in the absence of electrodes) was taken to be 1 dB cm^{-1}, the effective electro-optic coefficient 67 pm V^{-1}.

the results of such a simulation are plotted as a function of the PZT layer thickness and of the electrode spacing. The waveguide height, width and the wavelength are respectively 300 nm, 1.2 µm and 1550 nm. Figure 4.28**a** shows the estimated waveguide loss. Intuitively, the dependence of the loss on the electrode spacing can be understood as follows, the loss converges to the intrinsic loss of 1 dB cm^{-1} when the electrodes are far away, when they come closer, the overlap of the optical mode with the metal exponentially increases, adding a strongly increasing term to optical loss with decreasing spacing. The loss also increases with PZT thickness, this is due to the increasing overlap of the mode with the PZT, rather than with the SiN and oxide underneath. As a result of this, the lateral index contrast decreases and the mode expands towards the electrodes. Figure 4.28**b** shows the simulated $V_\pi L$. With increasing PZT thickness, the $V_\pi L$ decreases due to the increasing confinement Γ of the mode in the PZT. $V_\pi L$ also increases with electrode spacing, due to the decrease in electric field for a given voltage.

From figures 4.28**a** and **b**, one can see the the loss α and the modulation efficiency characterized by the $V_\pi L$ can not be both optimized at the same time. In fact the very change in parameters that would decrease the loss (increase in electrode spacing and/or decrease in PZT thickness), would make the modulator less efficient, and vice versa. These are however not the only relevant figures of merit. Arguably the most important figure of merit for many applications is the product $V_\pi L\alpha$ [25], which expresses a trade-off between the necessary drive voltage and total optical loss that has to be tolerated ($V_\pi L$ rather represents a trade-off between drive voltage and device footprint). The simulated values for $V_\pi L\alpha$ are plotted in figure 4.28**c**. As opposed to α and $V_\pi L$, $V_\pi L\alpha$ does have a minimum for the parameters space that was investigated, of ≈ 2 VdB, approximately for a PZT thickness of 300 nm and an electrode spacing of 7 µm (see the diamonds in figure 4.28). The circles in figure 4.28 represent the approximate geometrical parameters used in the experiments discussed before.

In the simulations in figure 4.28, a sweep of the electrode spacing and PZT thickness was performed, since these can be easily tailored in post-processing. This was done for a fixed waveguide width of 1.2 µm. One can however also optimize the waveguide width, such an optimization is given in figure 4.29. At each width, a sweep of $V_\pi L\alpha$ as a function of PZT thickness and electrode gap of the kind shown in figure 4.28 was performed. Figure 4.29**a** shows the values of $V_\pi L\alpha$ and the $V_\pi L$ at the optimum (where the $V_\pi L\alpha$ reaches a minimum). Figure 4.29**b** shows the PZT thickness and electrode spacing corresponding to this optimum. The light blue area shows the waveguide width/PZT thickness combinations for which the waveguide only supports a single TE mode. In figure 4.28, a width of 1.2 µm was chosen in order to minimize $\min(V_\pi L\alpha)$ whilst still having single-mode behavior at the optimal point.

Note that some of the assumptions made in these simulations are optimistic, especially an intrinsic loss value of 1 dB cm^{-1} assumes that the planarization is performed through CMP. For the current devices planarized through CMP, a residual oxide thickness of 50-100 nm is present (see figure 4.7**d**). This is not taken into account in our simulations in the assumption that the process can get optimized. The electrode alignment is also assumed to be perfect, in the current devices extra losses are induced due to misalignment of the electrodes (see figure 4.20). On the other hand, values such as the PZT Pockels coefficent are based on current measurements, it is not unrealistic to think that this parameter can still be improved, for example when poling at higher temperatures or changing the PZT composition.

4.10 Conclusions and future prospects

To conclude, we have explored some promising possibilities of thin film lead zirconate titanate (PZT) on photonic integrated circuits, for nonlinear optics and electro-optic modulation. The material itself was introduced in Section 4.2. PZT has very interesting properties, such as ferroelectricity, piezoelectricity and pyroelectricity. However for the applications discussed here, the strong Pockels effect and second order optical nonlinearity are of most interest. The specific thin-film deposition method used in this thesis, chemical solution deposition with an intermediate lanthanide layer, is introduced in Section 4.3. This method is absolutely crucial for the optical applications pursued here, as both the PZT layer and the intermediate layer are of high quality and are, most importantly, transparent over a large wavelength range. PZT and the intermediate layer are both transparent beyond $\approx$ 370 nm [43, 44]. This enables us to bring the thin-film in close proximity of integrated optical waveguides without significantly compromising the loss.

In Section 4.4, a second harmonic generation experiment on thin-film PZT on glass was discussed. This experiment gave an initial idea of the strength of the second order nonlinearity of PZT. Out-of-plane second order susceptibility components on the order of $\chi^{(2)}_{zzz} \approx 40$ pm/V were measured, however due to breakdown issues the samples were probably not poled to their full extent. More efficient poling of these films is something that can be investigated further. The ultimate goal is to harness the properties of PZT on an integrated photonic platform. Hence the other experiments in this chapter were performed on PZT-covered SiN waveguides. The fabrication of these waveguides is discussed in Section 4.5. Waveguide losses can be as low as $\approx$ 1 dB/cm. This however strongly depends on the way the chips are planarized before thin-film deposition and low losses are only achieved on samples planarized by CMP in the CMOS foundry. Using in-house planarization methods, the losses are rather on the order of $\approx$ 6 dB/cm. In

Section 4.6, we demonstrated that also in these waveguides second harmonic generation can be observed. These measurements are preliminary and can still be heavily improved. Although some assets of the platform are immediately clear, despite the high losses and poor collection, the second harmonic can clearly be observed, moreover by applying a DC voltage across the material we can fine-tune the phase-matching wavelength using the Pockels effect. Strategies for moving forward are also discussed, in the near future, a ridge can be etched in the PZT layer to confine the second harmonic mode and decrease its losses. On the longer term, strategies for periodic poling of the PZT can be explored. Periodic poling is difficult from a fabrication perspective since very small poling periods would be required, however it would enable us to do efficient SHG between two TE00 modes which could be used for optical parametric amplifiers or oscillators, quantum applications (parametric downconversion for photon pair generation), etc.

Electro-optic modulation is the application in which the PZT-on-SiN platform has truly started to show its colors. In Section 4.7, we discussed the basic theory behind phase modulation in these waveguides. In summary, two parameters are important, the Pockels coefficient of the material, as well as the confinement of the optical mode within the PZT. Furthermore a method for basic characterization of phase modulation in a simple PZT-covered waveguide is introduced. These measurements indicate that efficient modulation is possible, and also give an idea of the poling voltages needed to induce a nonzero electro-optic response in the thin-film PZT. In ball-park a voltage of about 50 V for an electrode spacing of about 5 µm, applied over 30 minutes to one hour, should be sufficient. Voltages exceeding 100 V have lead to electrical breakdown for such electrode spacings. When used in a Mach-Zehnder interferometer, or in a ring resonator, PZT-covered SiN waveguides can be used for amplitude modulation. This is demonstrated in Section 4.8. In this section we demonstrated efficient and high-speed modulation, in the absence of a bias voltage, both in the O- and C- telecommunication bands. Our static measurements show half-wave voltage-length products $V_\pi L$ down to 3.2 Vcm and stable poling of the material for periods of at least several days. Our high-speed measurements show modulation bandwidths exceeding 33 GHz in both the O- and C-bands, and data rates up to 40 Gbps using C-band ring modulators. The modulators on which the modulation experiments were performed were moreover not fully optimized. In Section 4.9, a simple optimization already shows that significant improvements are possible. Our approach is also unique in its versatility, as the PZT film can be deposited on any sufficiently flat surface. This could enable the incorporation of the electro-optic films onto other guided-wave platforms.

The modulation results are very promising, though future work is still required. Firstly, other platforms such as SOI are currently also being investigated. On silicon also phase modulation can be achieved, however some things are quite different. For example the ratios between the different refractive indices, SiN has a *smaller* index than PZT (≈ 2 versus ≈ 2.3), this implies that when depositing increasingly thicker PZT layers on the waveguides, the mode will be significantly more confined into the PZT itself. This leads to some subtle dependencies (see Section 4.9). On one hand the increased confinement in the active material is good for the overall electro-optic effect, on the other hand the lateral index contrast also decreases, and the interaction of the mode with the electrodes causes more and more loss. For Si, this is not true, the silicon has a significantly higher index (≈ 3.4) and the PZT can be considered a cladding layer within the evanescent field of the optical mode. Secondly, the poling and poling stability is explored to a certain extent in this thesis, but further tests are needed, such as tests for longer periods of time and under harsh environmental conditions. Also, the Pockels coefficients measured here ($r_{\text{eff}} \approx 60 - 70$ pm/V) are lower than the ones measured in the thesis of John P. George (230 pm/V) through ellipsometry on thin-films [26] . This is not too surprising, since the measurements by George *et al.* are performed on samples poled using ITO electrodes below and above the PZT film. Hence the poling is performed along the c-axis of the PZT crystallites after deposition. In this work, the PZT is poled in-plane, which is likely much more inefficient. This means that improving the poling efficiency is a potential avenue to improve our modulators. For example poling at elevated temperatures should be investigated. Thirdly, the modulator design can be improved significantly. In Section 4.9, we demonstrate that by numerical optimization of the cross-section, figures of merit like $V_\pi L$ and $V_\pi L\alpha$ can be significantly reduced. The current amplitude modulators can also be improved by for example reducing the losses and increasing the Q factors of the rings, this can increase the extinction ratio and reduce bit-error rates. On the longer term, MZI modulators with longer phase shifters can be developed. The design of such modulators is quite involved since phase matching between both the optical and the RF wave has to be considered. Optical losses in the transition sections between PZT-covered and bare waveguides can be reduced by clever design. An example of how this can be done by tapering the waveguides can be found in reference [45]. Finally, the performance of this platform at other wavelength ranges can still be explored.

References

[1] K. Alexander, J. P. George, J. Verbist, K. Neyts, B. Kuyken, D. Van Thourhout, and J. Beeckman. *Nanophotonic Pockels modulators on a silicon nitride platform.* Nature Communications, 9(1):3444, 2018.

[2] C. Sun, M. T. Wade, Y. Lee, J. S. Orcutt, L. Alloatti, M. S. Georgas, A. S. Waterman, J. M. Shainline, R. R. Avizienis, S. Lin, B. R. Moss, R. Kumar, F. Pavanello, A. H. Atabaki, H. M. Cook, A. J. Ou, J. C. Leu, Y.-H. Chen, K. Asanovic, R. J. Ram, M. A. Popovic, and V. M. Stojanovic. *Single-chip microprocessor that communicates directly using light.* Nature, 528:534–538, 2015.

[3] A. Rahim, E. Ryckeboer, A. Z. Subramanian, S. Clemmen, B. Kuyken, A. Dhakal, A. Raza, A. Hermans, M. Muneeb, S. Dhoore, Y. Li, U. Dave, P. Bienstman, N. L. Thomas, G. Roelkens, D. V. Thourhout, P. Helin, S. Severi, X. Rottenberg, and R. Baets. *Expanding the silicon photonics portfolio with silicon nitride photonic integrated circuits.* Journal of Lightwave Technology, 35(4):639–649, 2017.

[4] J. F. Bauters, M. J. Heck, D. John, D. Dai, M.-C. Tien, J. S. Barton, A. Leinse, R. G. Heideman, D. J. Blumenthal, and J. E. Bowers. *Ultra-low-loss high-aspect-ratio Si_3N_4 waveguides.* Optics Express, 19(4):3163–3174, 2011.

[5] D. J. Moss, R. Morandotti, A. L. Gaeta, and M. Lipson. *New CMOS-compatible platforms based on silicon nitride and Hydex for nonlinear optics.* Nature Photonics, 7(8):597–607, 2013.

[6] R. W. Boyd. *Nonlinear Optics.* Academic Press, 2003.

[7] G. T. Reed, D. J. Thomson, F. Y. Gardes, Y. Hu, J.-M. Fedeli, and G. Z. Mashanovich. *High-speed carrier-depletion silicon Mach-Zehnder optical modulators with lateral PN junctions.* Frontiers in Physics, 2:77, 2014.

[8] Q. Xu, B. Schmidt, S. Pradhan, and M. Lipson. *Micrometre-scale silicon electro-optic modulator.* Nature, 435(7040):325–327, 2005.

[9] A. Liu, R. Jones, L. Liao, D. Samara-Rubio, D. Rubin, O. Cohen, R. Nicolaescu, and M. Paniccia. *A high-speed silicon optical modulator based on a metal–oxide–semiconductor capacitor.* Nature, 427(6975):615–618, 2004.

[10] Z. Wang, A. Abbasi, U. Dave, A. Groote, S. Kumari, B. Kunert, C. Merckling, M. Pantouvaki, Y. Shi, B. Tian, K. Gasse, J. Verbist, R. Wang, W. Xie, J. Zhang, Y. Zhu, J. Bauwelinck, X. Yin, Z. Hens, J. Campenhout, B. Kuyken, R. Baets, G. Morthier, D. Thourhout, and G. Roelkens. *Novel light source integration approaches for silicon photonics.* Laser & Photonics Reviews, 11(4):1700063, 2017.

[11] U. D. Dave. *Nonlinear optics in a-Si: H-on-insulator and InGaP-on-insulator waveguide circuits.* PhD thesis, Ghent University, 2017.

[12] A. Rao, M. Malinowski, A. Honardoost, J. R. Talukder, P. Rabiei, P. Delfyett, and S. Fathpour. *Second-harmonic generation in periodically-poled thin film lithium niobate wafer-bonded on silicon.* Optics Express, 24(26):29941–29947, 2016.

[13] E. Timurdogan, C. V. Poulton, M. Byrd, and M. Watts. *Electric field-induced second-order nonlinear optical effects in silicon waveguides.* Nature Photonics, 11(3):200, 2017.

[14] T. Hiraki, T. Aihara, K. Hasebe, K. Takeda, T. Fujii, T. Kakitsuka, T. Tsuchizawa, H. Fukuda, and S. Matsuo. *Heterogeneously integrated III–V/Si MOS capacitor Mach–Zehnder modulator.* Nature Photonics, 11(8):482–485, 2017.

[15] J.-H. Han, F. Boeuf, J. Fujikata, S. Takahashi, S. Takagi, and M. Takenaka. *Efficient low-loss InGaAsP/Si hybrid MOS optical modulator.* Nature Photonics, 11(8):486–490, 2017.

[16] M. Liu, X. Yin, E. Ulin-Avila, B. Geng, T. Zentgraf, L. Ju, F. Wang, and X. Zhang. *A graphene-based broadband optical modulator.* Nature, 474(7349):64–67, 2011.

[17] V. Sorianello, M. Midrio, G. Contestabile, I. Asselberghs, J. Van Campenhout, C. Huyghebaert, I. Goykhman, A. K. Ott, A. C. Ferrari, and M. Romagnoli. *Graphene–silicon phase modulators with gigahertz bandwidth.* Nature Photonics, 12(1):40–44, 2018.

[18] L. Alloatti, R. Palmer, S. Diebold, K. P. Pahl, B. Chen, R. Dinu, M. Fournier, J.-M. Fedeli, T. Zwick, W. Freude, and C. Koos. *100 GHz silicon–organic hybrid modulator.* Light: Science & Applications, 3(5):e173, 2014.

[19] A. Srinivasan, M. Pantouvaki, S. Gupta, H. T. Chen, P. Verheyen, G. Lepage, G. Roelkens, K. Saraswat, D. Van Thourhout, P. Absil, and J. Van Campenhout. *56 Gb/s germanium waveguide electro-absorption modulator.* Journal of Lightwave Technology, 34(2):419–424, 2016.

[20] S. Abel, T. Stöferle, C. Marchiori, C. Rossel, M. D. Rossell, R. Erni, D. Caimi, M. Sousa, A. Chelnokov, B. J. Offrein, and J. Pompeyrine. *A strong electro-optically active lead-free ferroelectric integrated on silicon.* Nature Communications, 4:1671, 2013.

[21] C. Xiong, W. H. Pernice, J. H. Ngai, J. W. Reiner, D. Kumah, F. J. Walker, C. H. Ahn, and H. X. Tang. *Active silicon integrated nanophotonics: ferroelectric* $BaTiO_3$*-devices.* Nano Letters, 14(3):1419–1425, 2014.

[22] F. Eltes, M. Kroh, D. Caimi, C. Mai, Y. Popoff, G. Winzer, D. Petousi, S. Lischke, O. J. E., C. L., Z. L., F. J., and A. S. *A novel 25 Gbps electro-optic Pockels modulator integrated on an advanced Si photonic platform.* IEEE International Electron Devices Meeting (IEDM), 2017.

[23] C. T. Phare, Y.-H. D. Lee, J. Cardenas, and M. Lipson. *Graphene electro-optic modulator with 30 GHz bandwidth.* Nature Photonics, 9(8):511–514, 2015.

[24] N. Hosseini, R. Dekker, M. Hoekman, M. Dekkers, J. Bos, A. Leinse, and R. Heideman. *Stress-optic modulator in TriPleX platform using a piezoelectric lead zirconate titanate (PZT) thin film.* Optics Express, 23(11):14018–14026, 2015.

[25] W. Jin, R. G. Polcawich, P. A. Morton, and J. E. Bowers. *Piezoelectrically tuned silicon nitride ring resonator.* Optics Express, 26(3):3174–3187, Feb 2018.

[26] J. P. George. *Integration of ferroelectric thin films on silicon for electro-optic devices.* PhD thesis, Ghent University, 2016.

[27] M. J. Weber. *Handbook of optical materials.* CRC press, 2002.

[28] *`RefractiveIndex.INFO`.*

[29] S. Dey, K. Budd, and D. Payne. *Thin-film ferroelectrics of PZT of sol-gel processing.* IEEE transactions on ultrasonics, ferroelectrics, and frequency control, 35(1):80–81, 1988.

[30] A. Hermans, C. Kieninger, K. Koskinen, A. Wickberg, E. Solano, J. Dendooven, M. Kauranen, S. Clemmen, M. Wegener, C. Koos, and R. Baets. *On the determination of* $\chi^{(2)}$ *in thin films: a comparison of one-beam second-harmonic generation measurement methodologies.* Scientific Reports, 7:44581, 2017.

[31] F. J. Rodriguez, F. X. Wang, and M. Kauranen. *Calibration of the second-order nonlinear optical susceptibility of surface and bulk of glass.* Optics Express, 16(12):8704–8710, 2008.

[32] P. Maker, R. Terhune, M. Nisenoff, and C. Savage. *Effects of dispersion and focusing on the production of optical harmonics.* Physical Review Letters, 8(1):21, 1962.

[33] S. Clemmen, A. Hermans, E. Solano, J. Dendooven, K. Koskinen, M. Kauranen, E. Brainis, C. Detavernier, and R. Baets. *Atomic layer deposited second-order nonlinear optical metamaterial for back-end integration with CMOS-compatible nanophotonic circuitry.* Optics Letters, 40(22):5371–5374, 2015.

[34] T. Ning, H. Pietarinen, O. Hyvärinen, J. Simonen, G. Genty, and M. Kauranen. *Strong second-harmonic generation in silicon nitride films.* Applied Physics Letters, 100(16):161902, 2012.

[35] C. Xiong, W. H. Pernice, and H. X. Tang. *Low-loss, silicon integrated, aluminum nitride photonic circuits and their use for electro-optic signal processing.* Nano Letters, 12(7):3562–3568, 2012.

[36] S. Koeber, R. Palmer, M. Lauermann, W. Heni, D. L. Elder, D. Korn, M. Woessner, L. Alloatti, S. Koenig, P. C. Schindler, H. Yu, W. Bogaerts, L. R. Dalton, W. Freude, J. Leuthold, and C. Koos. *Femtojoule electro-optic modulation using a silicon-organic hybrid device.* Light: Science & Applications, 4:e255, Feb 2015.

[37] W. Bogaerts, P. De Heyn, T. Van Vaerenbergh, K. De Vos, S. Kumar Selvaraja, T. Claes, P. Dumon, P. Bienstman, D. Van Thourhout, and R. Baets. *Silicon microring resonators.* Laser & Photonics Reviews, 6(1):47–73, 2012.

[38] P. Günter. *Electro-optical effects in dielectric crystals.* In Electro-optic and Photorefractive Materials, pages 2–17. Springer, 1987.

[39] S. Abel and J. Fompeyrine. *Electro-Optically Active Oxides on Silicon for Photonics.* In Thin Films On Silicon: Electronic And Photonic Applications, pages 455–501. World Scientific, 2017.

[40] G. P. Agrawal. *Fiber-optic communication systems.* John Wiley & Sons, 2012.

[41] J. Cho, C. Xie, and P. J. Winzer. *Analysis of soft-decision FEC on non-AWGN channels.* Optics Express, 20(7):7915–7928, 2012.

[42] R. Asif. *Advanced and flexible multi-carrier receiver architecture for high-count multi-core fiber based space division multiplexed applications.* Scientific Reports, 6:27465, 2016.

[43] S. Pandey, A. James, R. Raman, S. Chatterjee, A. Goyal, C. Prakash, and T. Goel. *Structural, ferroelectric and optical properties of PZT thin films.* Physica B: Condensed Matter, 369(1-4):135–142, 2005.

[44] W. Gu, Y. Song, J. Liu, and F. Wang. *Lanthanum-Based Compounds: Electronic Bandgap-Dependent Electro-Catalytic Materials toward Oxygen Reduction Reaction.* Chemistry-A European Journal, 2017.

[45] P. O. Weigel, J. Zhao, K. Fang, H. Al-Rubaye, D. Trotter, D. Hood, J. Mudrick, C. Dallo, A. T. Pomerene, A. L. Starbuck, , and C. T. DeRose. *Hybrid Silicon Photonic-Lithium Niobate Electro-Optic Mach-Zehnder Modulator Beyond 100 GHz.* arXiv preprint arXiv:1803.10365, 2018.

Chapter 5

Nonlinear optics in MoS_2

5.1 Introduction

In this chapter we take a look at second order nonlinear optics in molybdenum disulfide (MoS_2). MoS_2 is a 2D material belonging to the class of the transition metal dichalcogenides (TMDCs or TMDs). Also being two-dimensional, these materials are in a sense structurally similar to graphene (Chapters 2 and 3). However as opposed to graphene, TMDC monolayers are not centrosymmetric. Hence they have a nonzero second order nonlinear susceptibility, which means that we can expect nonlinear optical phenomena similar to the ones observed in PZT (Chapter 4). In this chapter we will explore second order nonlinear optical effects in TMDCs, borrowing concepts from both these parts of the thesis.

In Section 5.2, TMDCs and some other notable 2D materials beyond graphene are introduced. The focus of this chapter lies on second harmonic generation in MoS_2. The fundamentals and state-of-the-art of nonlinear optics in MoS_2, and by extension the whole family of TMDCs, are discussed in Section 5.3. Section 5.4 talks about the actual SHG experiment. The goal is to combine these materials with integrated optics for on-chip nonlinear applications. Section 5.5 focuses on some initial steps in this direction.

5.2 2D materials beyond graphene

In Chapter 2, the increasingly important role of graphene in photonics and optoelectronics was discussed. The first isolation of single layer graphene was however not only the start of an enormous amount of graphene research, it was also the start of the broader field of 2D material research in general. Some of the other 2D materials, such as MoS_2, were already known in their many-layered bulk form, and were for example used as dry lubricants, however the advent of graphene science triggered scientists to isolate and study also monolayers of these materials [1].

All 2D materials have some common qualities. The quantum confinement in the direction perpendicular to the 2D crystals leads to interesting electronic properties such as strong excitonic effects and light-matter interaction. The surfaces of a 2D crystal are also intrinsically passivated, with no dangling bonds. This facilitates integration with photonic and electronic structures [1, 2].

Despite these common features we can find 2D materials with very different properties. The most prevalent example, graphene, is a gapless semimetal. It is very conductive and interacts strongly with electromagnetic radiation with wavelengths ranging from the microwave to the ultraviolet. Though the absence of a bandgap makes it unsuitable for light emission. Another class of 2D materials are the transition metal dichalcogenides (TMDCs), which have the chemical formula MX_2, with M a transition metal (Mo, W...) and X a chalcogen (S, Se...) [1, 2]. Monolayer TMDCs possess direct band gaps in the visible to near-IR wavelength range [1]. These materials are candidates for future detectors and light sources, such as LEDs, low-threshold lasers or even single-photon emitters [2]. Lack of inversion symmetry in TMDC monolayers also gives rise to direct bandgaps at two different corners of the Brillouin zone (K and K') [1]. Carriers in these valleys have for example different orbital angular momentum and can be selectively pumped using circularly polarized light, this has lead to the emerging field of "valleytronics" [1]. Hexagonal boron nitride, hBN, is yet another 2D material with a very large bandgap (≈ 6 eV), hBN makes an excellent dielectric. As a final example there is black phosphorus (BP), a material with a direct bandgap which is strongly correlated to the number of layers (0.3 eV for bulk to 2 eV for the monolayer) [1]. This "library" of 2D materials opens up the door to many new applications. The study of heterostructures, where 2D crystals are stacked to make junctions and engineer the overall electronic and optical properties, opens up the design space even more.

5.3 Nonlinear optics in TMDCs

Apart from the potential applications mentioned before, TMDCs have also been investigated for their nonlinear properties. Namely, the second order nonlinear susceptibility of monolayer MoS_2 was first reported on in 2013 by Kumar *et al.* [4]. In this first work, a second order bulk susceptibility $\chi_b^{(2)} \sim 10^{-7}$ m/V (corresponding to a sheet susceptibility on the order of $\chi_s^{(2)} = \chi_b^{(2)}\delta \sim 10^{-16}$ m^2/V, with $\delta \approx 0.62$ nm [5] being the thickness

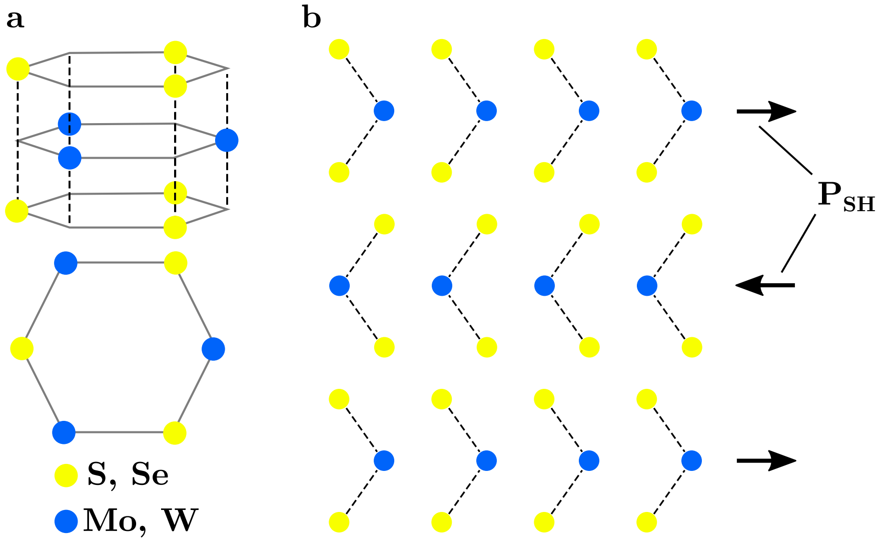

Figure 5.1: **a** Structure of a monolayer TMDC, side view and top view. From the top it looks like a honeycomb structure with broken inversion symmetry (adapted from reference [2]). **b** Schematic of the side-view of 2H-MoS$_2$, adjacent layers have antiparallel orientations, restoring the inversion symmetry. The second order polarizations generated in different layers in a SHG experiment will destructively interfere (adapted from reference [3]).

of the monolayer) was reported. This is between three and four orders of magnitude higher than some popular bulk materials for nonlinear optics, such as LiNbO$_3$ [6]. Even considering the sub-nanometer thickness of MoS$_2$, such a value would imply tremendous potential for nonlinear applications, Pockels modulation, etc. Other publications followed within months [5, 7–9], however these works consistently report respective peak bulk and surface second order susceptibilities on the order of $\chi_b^{(2)} \sim 10^{-10}$ m/V and $\chi_s^{(2)} \sim 10^{-19}$ m^2/V, none of them confirming the large values reported by Kumar *et al.* [4]. It was moreover quickly experimentally confirmed that the second harmonic generation efficiency is strongly wavelength dependent, showing strong peaks when the second harmonic is in the vicinity of one of the excitonic resonances (A-, B- and C-excitons at respective wavelengths of 675 nm, 625 nm and 440 nm in monolayer MoS$_2$) [7, 10]. All the aforementioned values were measured in the vicinity of the C-exciton. From the perspective of potential applications these resonantly enhanced values are not the most interesting, since they occur at wavelengths with strong reabsorption of the generated SH. Clark *et al.* reported off-resonant values (fundamental wavelength of 1600 nm) of $\chi_b^{(2)} \approx 7 \cdot 10^{-12}$ m/V or $\chi_s^{(2)} \approx 4.3 \cdot 10^{-21}$ m^2/V, Woodward *et al.* reported slightly higher values of $\chi_b^{(2)} \approx 3.2 \cdot 10^{-11}$ m/V or $\chi_s^{(2)} \approx 2 \cdot 10^{-20}$ m^2/V, for a pump at 1560 nm [11]. Reports on the second order susceptibility of other TMDCs (MoSe2, WS2 and WSe2) have lead to the similar conclusions with respect to resonant enhancement and similar order-of magnitude values for the nonlinear parameters. Seyler *et al.* moreover demonstrated that the strength of the SH in the vicinity of the A-exciton of WSe_2 can be tuned strongly by electrostatic doping in a field-effect transistor [12].

Figure 5.1**a** schematically shows the atomic structure of a monolayer of a TMDC, both from the side and from the top. The material consists of a single layer of transition metal atoms, between two layers of chalcogen atoms in trigonal prismatic structure [2]. The monolayer has D_{3h} symmetry, and lacks inversion symmetry. This lack of inversion symmetry lies at the core of the second order nonlinear response of these materials, as centrosymmetric materials have no second order response [6]. Figure 5.1**b** shows the most common arrangement of TMDC layers in bulk or few-layer materials, the 2H polytype [3]. In this arrangement, adjacent layers have antiparallel orientiation, restoring the overall inversion symmetry. The bulk material has D_{6h}-symmetry and has a negligible second order response, this is illustrated by the second order polarizations $\mathbf{P}_{\mathrm{SH}}$ in figure 5.1**b**, which cancel each other out. For few-layer TMDCs, a nonzero response is only expected for an odd number of layers [3, 5]. Recently, several groups have studied arrangements of TMDCs where the layers are stacked with identical orientation, this is called the 3R polytype and is equally stable but less commonly studied [3, 13]. In these materials, constructive interference of the second harmonic dipoles leads to much stronger second harmonic powers when going from monolayer to bulk.

5.4 Second harmonic generation in MOCVD-grown MoS_2

We have access to large area MoS_2, synthesized at imec (Leuven, Belgium) using metal-organic chemical vapor deposition (MOCVD) on a sapphire substrate. MOCVD growth of TMDCs is not a self-limiting process, so having control over the deposited number of layers is hard [14]. In general samples are covered with a patchwork of areas with a different number of layers (for example monolayer, bilayer and trilayer). However significant steps toward having more control of the layer number have been made recently by Chiappe *et al.* [14], who provided the samples used in this work. For the samples used here, a combination of MOCVD deposition with a thermal etching step to remove bi- and trilayer patches was used to obtain a monolayer. One potential application of this material is to use it for on-chip nonlinear optics or electro-optic modulation. As a first step, we investigate the second order nonlinear material response of the available material transferred to an unprocessed substrate, and compare it with literature values. The transfer was done by first spin-coating poly(methyl methacrylate) (PMMA) on the $\mathrm{MoS_2}$-covered sapphire substrate and using thermal tape to transfer the PMMA-$\mathrm{MoS_2}$ stack to the target substrate [14].

Figure 5.2**a** shows the setup used for the $\mathrm{MoS_2}$ SHG measurement. This is in essence the same setup used for the measurements on thin film PZT layers, see figure 4.2**a**. However two features are added, firstly, the half-wave plate is mounted on a rotating stage, connected to the computer. Through this, we can automatically sweep the polarization angle φ of the fundamental beam. A second added feature is the analyzer, which is a polarizer either selecting the horizontally or vertically polarized component of the generated second harmonic. On figure 5.2**b**, the measurement on an $\mathrm{MoS_2}$ covered substrate is sketched. The incidence angle θ is 0 ° (perpendicular incidence), but the polarization direction of the linearly polarized beam is rotated using the half-wave plate. The second harmonic generated in the $\mathrm{MoS_2}$ is passed through the analyzer, either passing the vertically polarized light (polarized along y), or the horizontally polarized light (polarized along x). For this measurement, the $\mathrm{MoS_2}$ was transferred to a $\mathrm{SiO_2}$-on-Si substrate. The $\mathrm{SiO_2}$ has a thickness of approximately 85 nm. It is also important to note that the second order susceptibility tensor $\chi_s^{(2)}$ is defined within the reference frame of the crystal. For the $\mathrm{MoS_2}$ sample provided, this reference frame is typically not aligned with the 'lab' frame of reference. Figure 5.2**c** shows how the two relate, X and Y are respectively defined as the 'armchair' and 'zigzag' directions of the $\mathrm{MoS_2}$-crystal [7]. The angle between the x-axis of the lab frame and the armchair direction of the crystal is defined as α.

Based on its symmetry, it is known that the second order scuspetibility tensor of $\mathrm{MoS_2}$ has only a single nonzero tensor element: $\chi^{(2)}_{s,\,\mathrm{MoS_2}} \equiv \chi^{(2)}_{s,\,XXX} = -\chi^{(2)}_{s,\,XYY} = -\chi^{(2)}_{s,\,YYX} = -\chi^{(2)}_{s,\,YXY}$ [7]. Hence the second harmonic field can be expressed as,

$$\begin{aligned}\mathbf{E}(2\omega) &= C\chi_s^{(2)} : \mathbf{E}(\omega)\mathbf{E}(\omega)\\ &= C\chi^{(2)}_{s,\,\mathrm{MoS_2}}\left[(E_X^2(\omega) - E_Y^2(\omega))\hat{e}_X - 2E_X(\omega)E_Y(\omega)\hat{e}_Y\right],\end{aligned} \tag{5.1}$$

where ω and 2ω are the fundamental and SH frequency. C is a proportionality constant determined by the local dielectric environment and $\hat{e}_{X,\,Y}$ are unit vectors in the respective directions. When changing between reference frames by using the substitutions $E_X(\omega) = |\mathbf{E}|\cos(\varphi - \alpha)$, $E_Y(\omega) =$

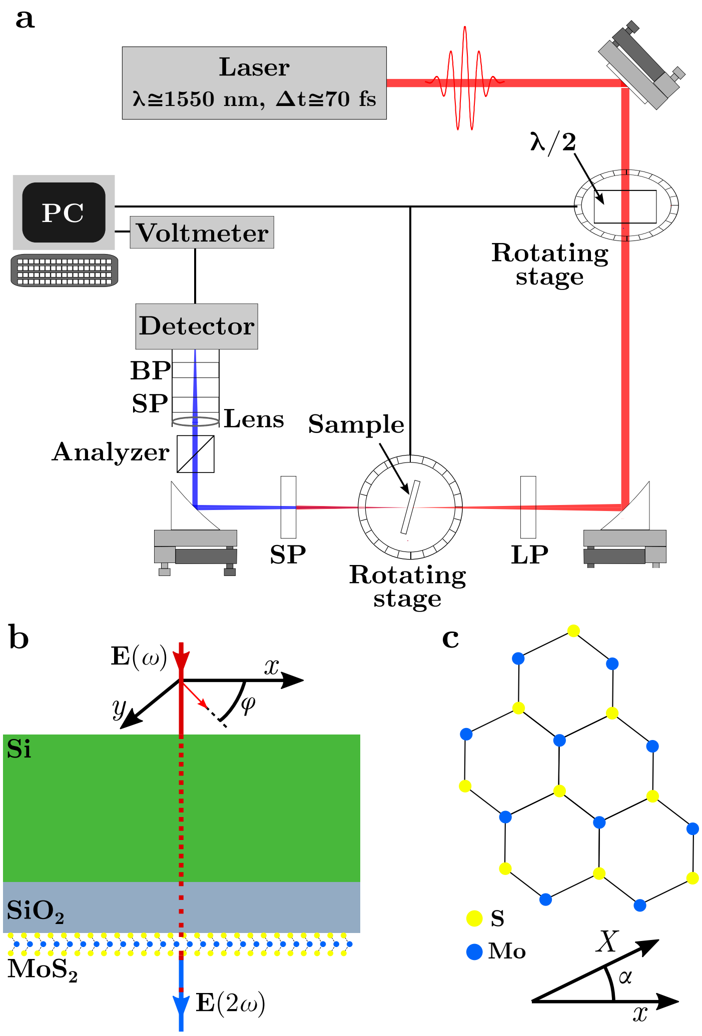
a
Laser
λ≅1550 nm, Δt≅70 fs
λ/2
PC
Voltmeter
Rotating stage
Detector
BP
SP
Lens
Sample
Analyzer
SP
Rotating stage
LP
b
E(ω)
x
y
φ
Si
SiO₂
MoS₂
E(2ω)
c
S
Mo
X
α
x

Figure 5.2: **a** Setup used for the second harmonic generation experiments. $\lambda/2$: half-wave plate, LP: longpass filter, SP: shortpass filter, BP: bandpass filter. Adapted from reference [15]. The half-wave plate is mounted on a rotating stage in the vertical direction, the sample is mounted on a horizontally rotating stage. **b** Sketch of a measurement on an MoS_2 monolayer transferred to a silica-on-silicon substrate. **c** Sketch of the orientation of the MoS_2 monolayer on the substrate, x, y and z represent the 'lab' reference frame, X, Y and $Z = z$ the conventional reference frame of the MoS_2.

$|\mathbf{E}|\sin(\varphi-\alpha)$, $\hat{e}_X = \hat{e}_x\cos(\alpha)+\hat{e}_y\sin(\alpha)$ and $\hat{e}_Y = \hat{e}_y\cos(\alpha)-\hat{e}_x\sin(\alpha)$, this eventually yields,

$$\mathbf{E}(2\omega) = C\chi^{(2)}_{s,\ \mathrm{MoS_2}}|\mathbf{E}|^2\left[\cos(2\varphi - 3\alpha)\hat{e}_x - \sin(2\varphi - 3\alpha)\hat{e}_y\right]. \tag{5.2}$$

Hence the detected powers for respectively the vertically and horizontally polarized components of the SH scale as $\sin^2(2\varphi - 3\alpha)$ and $\cos^2(2\varphi - 3\alpha)$ [1]. The exact calculation of the proportionality factor C is rather complicated for a multilayered substrate of the kind used here (see figure 5.2**b**). Due to the large index of silicon multiple reflections and resonance effects should be included, both for the fundamental and the generated SH. D. S. Bethune has developed a transfer matrix method for the general problem of harmonic generation in multilayer media, in this method, the linear problem for the fundamental wave is solved first, hereafter the nonlinear polarization and generated nonlinear fields are calculated [16]. For our measurement, this method was implemented in MATLAB by Artur Hermans. The measurements shown here were referenced using a Barium Borate sample, using the second order susceptibility measured by Shoji *et al.* [17].

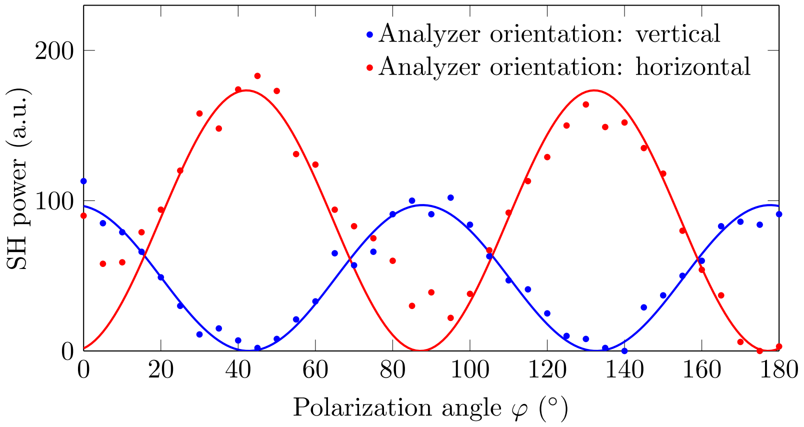

Figure 5.3: Measured SH power for the MoS$_2$-covered substrate, for respectively the analyzer selecting the s-(blue) and p-polarizations (red). The solid lines are the theoretical fits.

In figure 5.3, the measurement results are shown, for the analyzer selecting either the vertically or horizontally polarized component of the SH. Note that there is an offset between the two measurements, this indicates that there is a change in the alignment and the collection efficiency of the setup when rotating the analyzer. The solid lines on the plot represent the theoretical fit. The fitted surface second order susceptibilities for the respective vertical and horizontal orientations of the analyzer are $\chi_s^{(2)} = 4.0 \cdot 10^{-21}$ m^2/V and $\chi_s^{(2)} = 5.4 \cdot 10^{-21}$ m^2/V. Note that despite the large difference in detected powers, the difference in the fitted susceptibilities is still acceptable (due to the square relation between the two). For both measurements, the fitted angle α is about 28 degrees.

---

[1] Note that in most other experimental works, the detected SH scales as $\cos^2[3(\varphi - \alpha)]$ this is because generally the analyzer and the incident polarization are aligned in parallel, here the analyzer orientation is fixed for a single measurement.

These values are reasonably close to what was reported by Clark *et al.* ($4.3 \cdot 10^{-21}$ m^2/V) and Woodward *et al.* ($2 \cdot 10^{-20}$ m^2/V) for similar wavelengths. Using a thickness of 0.62 nm, we can estimate the corresponding bulk susceptibilities to be $\chi_b^{(2)} = 6.5 \cdot 10^{-12}$ m/V and $\chi_b^{(2)} = 8.7 \cdot 10^{-12}$ m/V for the respective fits. This is not exceptionally large compared to typical bulk nonlinear crystals, and comes with the additional caveat that we are limited to subnanometer thick monolayers. Note that in our setup, we focus the fundamental beam with a $1/e^2$-beam waist of 52 µm. This means that we probe the *average* value of the second order response of the film within this spot [2]. As was mentioned before, MOCVD processes do not result in perfect monolayers, rather in a patchwork of monolayers, bilayer islands and maybe even uncovered areas [14]. This is another possible reason of a reduced $\chi^{(2)}$-value, and improving layer-number control is a potential way of getting more control over the second order nonlinear response. In the next sections we will assess some of the possibilities of MoS$_2$-covered integrated waveguides.

5.5 MoS$_2$ on integrated SiN waveguides

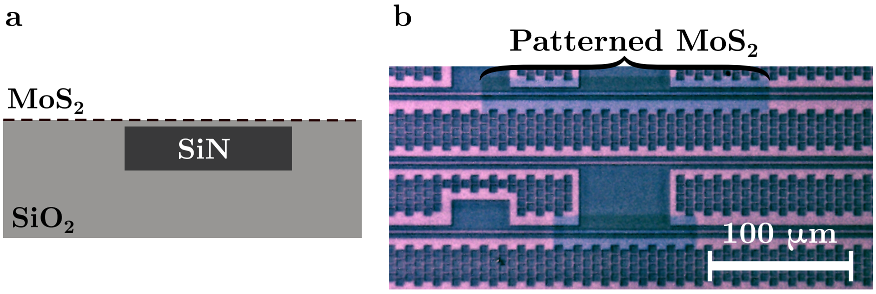

Figure 5.4: **a** Sketch of the cross-section of an MoS$_2$-covered SiN waveguide. **b** Microscope image of a set of waveguides covered with MoS$_2$ after patterning. The contrast was enhanced to make the MoS$_2$-patches clearly visible.

---

[2] Most of the cited references use a second harmonic microscope setup which can probe a spot smaller than a single monolayer flake.

In analogy to the graphene-covered silicon nitride waveguides first introduced in Section 3.3, we covered similar waveguides with MoS_2. A typical cross-section of such a waveguide is shown in figure 5.4**a**. Up until the transfer of the 2D material, the sample preparation is identical to the fabrication of graphene-covered waveguides, see figure 3.5. The top oxide is etched back using both reactive ion etching and HF wet etching. Then the MoS_2 is transferred to the sample using the same tape-assisted transfer method described above, and patterned using optical lithography and CF_4 reactive ion etching for 60 seconds (at a power of 25 W, flow of 50 sccm and pressure of 50 mTorr). Figure 5.4**b** shows the top view of the sample after patterning, the MoS_2-patches of different length are clearly visible.

5.5.1 Optical losses

Using the waveguides covered with different lengths of MoS_2, we performed cut-back loss measurements. The results are summarized in figure 5.5, for 3 different waveguide widths (1200 nm, 1600 nm and 2400 nm), the thickness of the SiN is approximately 300 nm. Figure 5.5**a** shows the overall fiber-to-fiber loss between for the different waveguide widths and for a wavelength of 1550 nm. A linear fit to these measurements can be used to estimate the coupling loss (grating coupler loss) and the propagation loss of the MoS_2-covered waveguide sections. In figure 5.5**b**, the thus estimated waveguide propagation losses are plotted as a function of wavelength. The estimated grating coupler losses are plotted in figure 5.5**c**. It is clear from the figure that the propagation losses are quite high, within the range of 20-25 dB/cm. This is about an order of magnitude larger than for similar SiN waveguides without MoS_2, see for example figure 4.8**c** (blue plot). The high loss here is not fully understood, and might be linked to quality of the MoS_2-film, for example through the presence of grain boundaries or bilayer areas. Further improving the deposition process of the material might strongly reduce these losses. Other groups have reported on similar TMDC-covered (using WS_2) waveguides with losses below 6 dB/cm [18]. Hence this is a property which still can be optimized.

5.5.2 SHG on MoS_2-covered SiN waveguides

Here, we will use the measured second order susceptibility and waveguide losses from the previous sections to assess whether large-area TMDCs can be used for on-chip second harmonic generation when combined with integrated SiN waveguides, and to which extent the platform still needs to be improved.

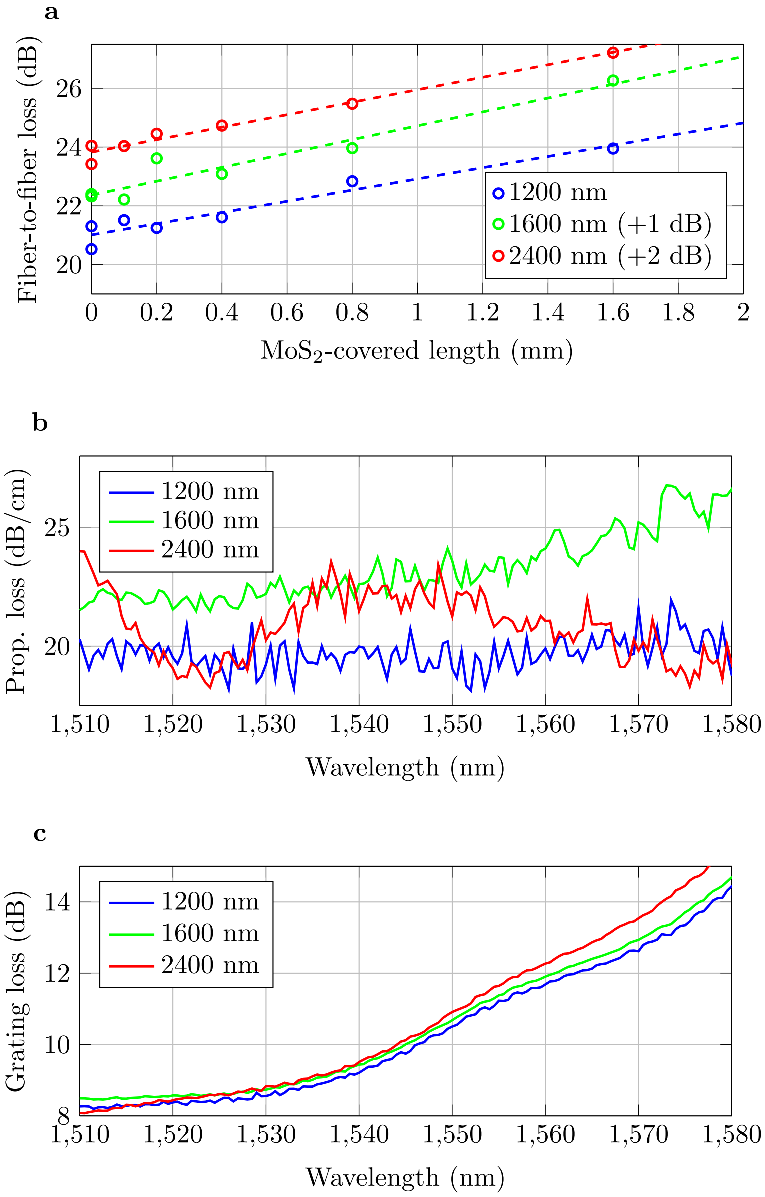

Figure 5.5: **a** Fiber-to-fiber loss for the MoS$_2$-covered waveguides, for different lengths of MoS$_2$. The measurements were performed on waveguides of different widths, see legend. The dashed lines show the linear fits. The wavelength is 1550 nm. **b** Estimated propagation loss of the MoS$_2$-covered section as a function of wavelength, from the linear fits. **c** Grating coupler loss as a function of wavelength.

For second harmonic generation, the equations (4.10), (4.11) and (4.12) derived for bulk materials such as PZT can be rewritten for 2D materials. The coupled-wave equations for the fundamental and second harmonic amplitude (A_f and A_SH) are still (in the assumption that downconversion from the second harmonic back to the fundamental can be ignored),

$$\frac{\partial A_\mathrm{f}}{\partial z} = -\frac{\alpha_\mathrm{f}}{2} A_\mathrm{f}, \tag{5.3}$$

$$\frac{\partial A_\mathrm{SH}}{\partial z} = i\kappa e^{i(2\beta_\mathrm{f}-\beta_\mathrm{SH})z} A_\mathrm{f}^2 - \frac{\alpha_\mathrm{SH}}{2} A_\mathrm{SH}, \tag{5.4}$$

where the nonlinear coupling κ is given by,

$$\kappa = \frac{\omega_\mathrm{f}\varepsilon_0}{4\sqrt{\mathscr{P}_\mathrm{SH}}\mathscr{P}_\mathrm{f}} \int_{2\mathrm{D}} \mathbf{e}_\mathrm{SH}^* \cdot \chi_s^{(2)} : \mathbf{e}_\mathrm{f}\mathbf{e}_\mathrm{f} d\ell, \tag{5.5}$$

where the line integral is taken over the intersection between the 2D-material and the waveguide cross-section. $\mathbf{e}_{\mathrm{f},\,\mathrm{SH}}$ is the electric field profile of the respective optical mode and $\mathscr{P}_{\mathrm{f},\,\mathrm{SH}}$ are normalization constants calculated using equation (2.20). From equation (5.4) it is clear that phase-matching is an important issue for on-chip second harmonic generation. A possible way to tackle this is quasi-phase-matching, where the nonlinear response of the waveguide is modulated along its length with a period Λ [6]. With $K \equiv 2\pi/\Lambda = |2\beta_\mathrm{f} - \beta_\mathrm{SH}|$. In that case the nonlinear coupling $\kappa(z)$ can be written as a Fourier series [6]:

$$\kappa(z) = \sum_{m=-\infty}^{\infty} k_m e^{imKz}. \tag{5.6}$$

Equation (5.4) can be directly solved as $A_\mathrm{f}(z) = A_{\mathrm{f},0} e^{-\frac{\alpha_\mathrm{f} z}{2}}$, after which the solution of equation (5.4) becomes (with $\Delta\beta \equiv 2\beta_\mathrm{f} - \beta_\mathrm{SH}$),

$$\begin{aligned} A_\mathrm{SH}(z) &= \sum_{m=-\infty}^{\infty} ik_m A_{\mathrm{f},0}^2 e^{-\frac{\alpha_\mathrm{SH}}{2} z} \int_0^z e^{[\frac{1}{2}(\alpha_\mathrm{SH}-2\alpha_\mathrm{f})+i(\Delta\beta+mK)]z'} dz' \\ &= \sum_{m=-\infty}^{\infty} ik_m A_{\mathrm{f},0}^2 \frac{e^{[-\alpha_\mathrm{f}+i(\Delta\beta+mK)]z} - e^{-\frac{\alpha_\mathrm{SH}}{2} z}}{\frac{1}{2}(\alpha_\mathrm{SH} - 2\alpha_\mathrm{f}) + i(\Delta\beta + mK)}. \end{aligned} \tag{5.7}$$

Most of the terms in this series expansion will oscillate with a period comparable to or smaller than Λ. Only one term, with $m = -1$ or 1 (depending on the sign of $\Delta\beta$), will grow coherently.

We propose the phase-matching scheme illustrated by figure 5.6, half of each period is covered with the 2D material, and the other half is not. This can be achieved by patterning the monolayer of the TMDC using optical

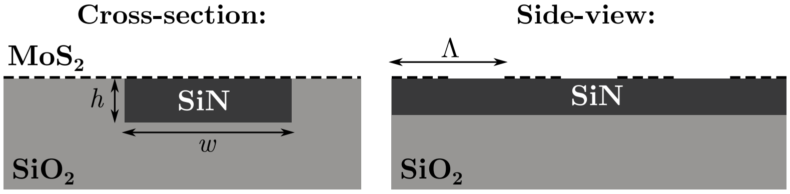

Figure 5.6: Proposed waveguide structure for on-chip quasi-phase-matched second harmonic generation using MoS_2 and other TMDCs.

lithography. For this case the first order terms of the Fourier expansion become $k_{\pm1} = \kappa_{\max}/\pi$. With $\kappa_{\max}$ calculated using equation (5.6). For this scheme the power conversion from fundamental to SH will be, if we ignore all the fast oscillating terms in equation (5.7),

$$\frac{P_{\mathrm{SH}}(L)}{P_{\mathrm{f}}(0)^2} \approx \frac{|\kappa_{\max}|^2}{\pi^2}\left|\frac{e^{-\alpha_{\mathrm{f}} z} - e^{-\frac{\alpha_{\mathrm{SH}}}{2} z}}{\frac{\alpha_{\mathrm{SH}}}{2} - \alpha_{\mathrm{f}}}\right|^2 . \tag{5.8}$$

Based on these equations, we can make some initial estimates of what would be the nonlinear conversion efficiency of the phase-matching scheme. The results are summarized in figure 5.7. Figure 5.7**a** shows the simulated phase matching period for different waveguide widths w and thicknesses h. The necessary period is always in the vicinity of 3 µm. This means that feature sizes on the order of 1.5 µm are necessary. This can be achieved with optical lithography. Figure 5.7**b** displays the calculated nonlinear coupling κ, calculated using equation (5.6). The dotted lines represent the currently available waveguide parameters. The diamonds represent the waveguide parameter with the highest calculated κ ($0.173\ \mathrm{m}^{-1}\mathrm{W}^{-\frac{1}{2}}$). in figure 5.7**c** the calculated nonlinear conversion $\frac{P_{\mathrm{SH}}(L)}{P_{\mathrm{f}}(0)^2}$ is plotted. The blue line uses values roughly in line with what we currently measured, $\kappa = 0.1\ \mathrm{m}^{-1}\mathrm{W}^{-\frac{1}{2}}$ and $\alpha_{\mathrm{f}} = \alpha_{\mathrm{SH}} = \frac{1}{2} \cdot 25$ dB/cm. The factor $\frac{1}{2}$ in the loss comes from the fact that only half of the period is covered with the monolayer. The loss for the second harmonic was taken identical to the loss for the fundamental, this is somewhat of a stab in the dark. However one should note that the overlap of the second harmonic mode with the 2D monolayer is significantly smaller than for the fundamental mode, since it is much more confined within the waveguide core, *if* the material loss at the second harmonic wavelength is not significantly larger than for the fundamental, this guess should be quite safe. The green line represents a calculation for more optimistic parameters ($\kappa = 0.17\ \mathrm{m}^{-1}\mathrm{W}^{-\frac{1}{2}}$ and $\alpha_{\mathrm{f}} = \alpha_{\mathrm{SH}} = \frac{1}{2} \cdot 5$ dB/cm, in line with the loss measured for WS_2-covered waveguides by Datta *et al.* [18]). The optimal conversion efficiencies range from 10^{-9} to just over $10^{-7}\ \mathrm{W}^{-1}$. These values

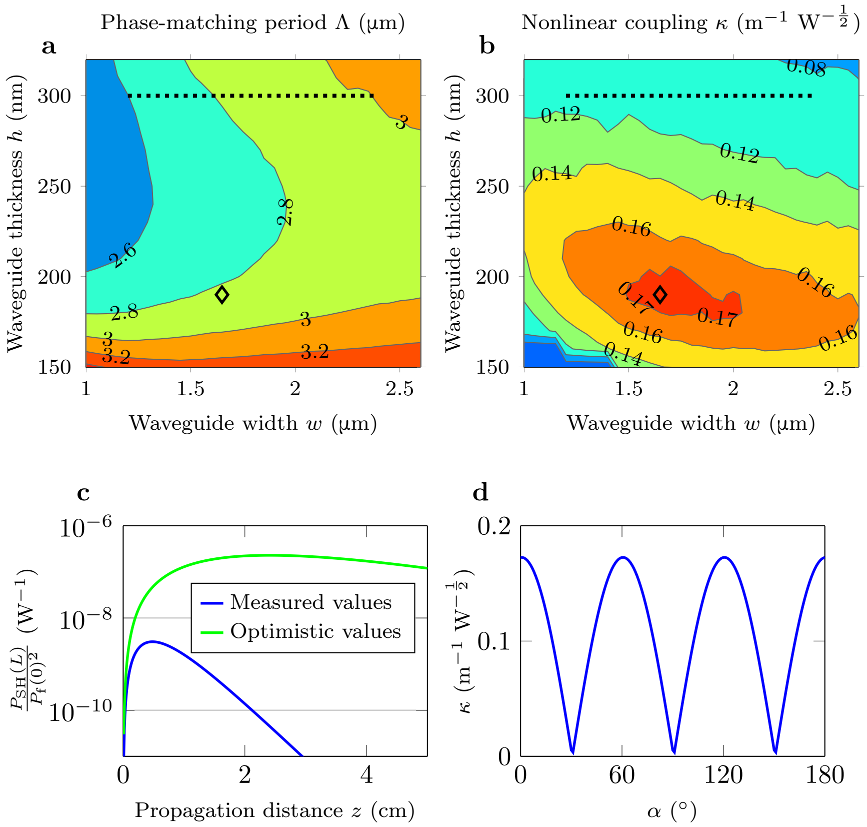

Figure 5.7: Simulation results for quasi-phase-matched second harmonic generation using an MoS_2-covered SiN-waveguide, see figure 5.6. **a** Phase matching period for a fundamental wavelength of 1550 nm, as a function of waveguide thickness h and width w. **b** Calculated nonlinear coupling κ (using equation (5.6)), as a function of waveguide thickness h and width w, for $\chi^{(2)} = 5 \cdot 10^{-21}$ m^2/V. The dotted lines on figures **a** and **b** represent the approximate parameters of the currently available waveguides, the diamonds represent the point with optimal κ. **c** Calculated nonlinear conversion $\frac{P_{SH}(L)}{P_f(0)^2}$, for the values in line with what was measured ($\kappa = 0.1$ m^{-1} $W^{-\frac{1}{2}}$, propagation losses of 12.5 dB/cm for both fundamental and second harmonic) and for more optimistic values ($\kappa = 0.17$ $m^{-1}W^{-\frac{1}{2}}$, propagation losses of 2.5 dB/cm), respectively in blue and green. **d** Nonlinear coupling κ versus relative orientation of the MoS_2 crystal with respect to the waveguide, α is the angle between the waveguide cross-section plane and the ‘armchair’ (X) direction of the MoS_2 (see figure 5.2**c**), for $w = 1.65$ µm and $h = 190$ nm.

are measurable using low repetition rate pulsed sources[3]. However they are not practically useful, for example for efficient frequency doubling. Figure 5.7**d** shows another potential complication. It is a simulation of the nonlinear coupling as a function of the $\mathrm{MoS_2}$ crystal orientation, with α being the angle between the waveguide cross-section plane and the 'armchair' (X) direction of the $\mathrm{MoS_2}$. Due to the symmetry of the crystal, the nonlinear conversion will change significantly with this angle as well.

5.6 Conclusions and future prospects

In this chapter we discussed some preliminary measurements on $\mathrm{MoS_2}$, a 2D material belonging to the class of the transition metal dichalcogenides (TMDCs). First (Section 5.2) we introduced TMDCs, with a strong focus on second harmonic generation in these materials. In Section 5.4 we characterize the second harmonic response of large area $\mathrm{MoS_2}$ grown through metal-organic chemical vapor deposition. We measure values in line with what has been reported in literature for similar wavelengths. Our second harmonic measurements are performed for a fundamental wavelength around 1550 nm. As a result the value of the nonlinear susceptibility is lower than what some groups have reported, since those measurements typically take place in the vicinity of an excitonic resonance. The wavelength we used is more relevant when working towards nonlinear applications. In Section 5.5, we show some initial measurements on $\mathrm{MoS_2}$-covered waveguides. Waveguide losses exceeding 20 dB/cm are measured. This is relatively high and should be further investigated. An estimate of conversion efficiencies for on-chip second harmonic generation is done, based on theoretical simulations. For this a quasi-phase-matching scheme unique to 2D materials is proposed. Our conclusion is that this type of SHG can probably be demonstrated, however that the conversion efficiencies would not be of an order of magnitude which is useful. Other options, such as the use of optical resonators to enhance the effects, should be investigated in the future. Improvement of the material quality by improving the growth process can also still have a big impact. Another interesting avenue that can be explored, is to bring the electrostatic tuning of the nonlinear response of TMDCs, as first demonstrated by Seyler *et al.* [12], to a chip.

---

[3] Assume for example a pulsed source generating 1 mW of average power on-chip, with a pulse duration of 1 ns and a repetition rate of 10 MHz, for $\frac{P_{\mathrm{SH}}(L)}{P_{\mathrm{f}}(0)^2} = 10^{-7}\ \mathrm{W}^{-1}$ this gives an on-chip avarage SH power of 1 nW.

References

[1] F. Xia, H. Wang, D. Xiao, M. Dubey, and A. Ramasubramaniam. *Two-dimensional material nanophotonics.* Nature Photonics, 8(12):899–907, 2014.

[2] K. F. Mak and J. Shan. *Photonics and optoelectronics of 2D semiconductor transition metal dichalcogenides.* Nature Photonics, 10(4):216–226, 2016.

[3] M. Zhao, Z. Ye, R. Suzuki, Y. Ye, H. Zhu, J. Xiao, Y. Wang, Y. Iwasa, and X. Zhang. *Atomically phase-matched second-harmonic generation in a 2D crystal.* Light: Science & Applications, 5(8):e16131, 2016.

[4] N. Kumar, S. Najmaei, Q. Cui, F. Ceballos, P. M. Ajayan, J. Lou, and H. Zhao. *Second harmonic microscopy of monolayer* MoS_2. Physical Review B, 87(16):161403, 2013.

[5] Y. Li, Y. Rao, K. F. Mak, Y. You, S. Wang, C. R. Dean, and T. F. Heinz. *Probing symmetry properties of few-layer* MoS_2 *and h-BN by optical second-harmonic generation.* Nano Letters, 13(7):3329–3333, 2013.

[6] R. W. Boyd. *Nonlinear Optics.* Academic Press, 2003.

[7] L. M. Malard, T. V. Alencar, A. P. M. Barboza, K. F. Mak, and A. M. de Paula. *Observation of intense second harmonic generation from* MoS_2 *atomic crystals.* Physical Review B, 87(20):201401, 2013.

[8] D. J. Clark, V. Senthilkumar, C. T. Le, D. L. Weerawarne, B. Shim, J. I. Jang, J. H. Shim, J. Cho, Y. Sim, M. J. Seong, S. H. Rhim, A. J. Freeman, K. H. Chung, and Y. S. Kim. *Strong optical nonlinearity of CVD-grown* MoS_2 *monolayer as probed by wavelength-dependent second-harmonic generation.* Physical Review B, 90(12):1–5, 2014.

[9] W.-T. Hsu, Z.-A. Zhao, L.-J. Li, C.-H. Chen, M.-H. Chiu, P.-S. Chang, Y.-C. Chou, and W.-H. Chang. *Second harmonic generation from artificially stacked transition metal dichalcogenide twisted bilayers.* ACS Nano, 8(3):2951–2958, 2014.

[10] D. Clark, C. Le, V. Senthilkumar, F. Ullah, H.-Y. Cho, Y. Sim, M.-J. Seong, K.-H. Chung, Y. Kim, and J. Jang. *Near bandgap second-order nonlinear optical characteristics of* MoS_2 *monolayer transferred on transparent substrates.* Applied Physics Letters, 107(13):131113, 2015.

[11] R. Woodward, R. Murray, C. Phelan, R. de Oliveira, T. Runcorn, E. Kelleher, S. Li, E. de Oliveira, G. Fechine, G. Eda, and C. J. S. De Matos. *Characterization of the second-and third-order nonlinear optical susceptibilities of monolayer* MoS_2 *using multiphoton microscopy.* 2D Materials, 4(1):011006, 2016.

[12] K. L. Seyler, J. R. Schaibley, P. Gong, P. Rivera, A. M. Jones, S. Wu, J. Yan, D. G. Mandrus, W. Yao, and X. Xu. *Electrical control of second-harmonic generation in a* WSe_2 *monolayer transistor.* Nature Nanotechnology, 10(5):407, 2015.

[13] X. Fan, Y. Jiang, X. Zhuang, H. Liu, T. Xu, W. Zheng, P. Fan, H. Li, X. Wu, X. Zhu, and Q. Zhang. *Broken symmetry induced strong nonlinear optical effects in spiral* WS_2 *nanosheets.* ACS Nano, 11(5):4892–4898, 2017.

[14] D. Chiappe, J. Ludwig, A. Leonhardt, S. El Kazzi, A. N. Mehta, T. Nuytten, U. Celano, S. Sutar, G. Pourtois, M. Caymax, and K. Paredis. *Layer-controlled epitaxy of 2D semiconductors: bridging nanoscale phenomena to wafer-scale uniformity.* Nanotechnology, 29:29425602, 2018.

[15] A. Hermans, C. Kieninger, K. Koskinen, A. Wickberg, E. Solano, J. Dendooven, M. Kauranen, S. Clemmen, M. Wegener, C. Koos, and R. Baets. *On the determination of* $\chi^{(2)}$ *in thin films: a comparison of one-beam second-harmonic generation measurement methodologies.* Scientific Reports, 7:44581, 2017.

[16] D. Bethune. *Optical harmonic generation and mixing in multilayer media: extension of optical transfer matrix approach to include anisotropic materials.* JOSA B, 8(2):367–373, 1991.

[17] I. Shoji, H. Nakamura, K. Ohdaira, T. Kondo, R. Ito, T. Okamoto, K. Tatsuki, and S. Kubota. *Absolute measurement of second-order nonlinear-optical coefficients of* β*-*BaB_2O_4 *for visible to ultraviolet second-harmonic wavelengths.* JOSA B, 16(4):620–624, 1999.

[18] I. Datta, S. H. Chae, G. R. Bhatt, B. Li, Y. Yu, L. Cao, J. Hone, and M. Lipson. *Giant electro-refractive modulation of monolayer* WS_2 *embedded in photonic structures.* In CLEO: Science and Innovations, pages STu4N–7. Optical Society of America, 2018.

Chapter 6

Conclusions and future perspectives

6.1 Conclusions on the presented work

The goal of this work was to look for ways of enhancing the nonlinear optical functionality of CMOS-compatible nanophotonic platforms, mainly focusing on silicon nitride and to a lesser extent on silicon. The motivation for this was that these platforms are in many respects superior for the fabrication of integrated photonics circuits. Especially silicon nitride stands out from the crowd, being a CMOS-compatible platform with low linear and nonlinear losses, a relatively high index contrast, large transparency range, etc. However despite this, active functions such as light generation, detection and manipulation are only partly (on silicon) or not at all (on nitride) available. Integrating other materials onto these platforms is an attractive way of improving the functionality. In this work, we specifically looked into the integration of materials which have (or are expected to have) strong optical nonlinearities. Nonlinear optical effects can pave the way to several applications, such as light generation at specific wavelengths, electro-optical phase modulation, or more exotic things like all-optical signal processing and entangled photon pair generation. Several materials were considered, in the choice of which we focused on materials which were expected to show high optical nonlinearities and could be integrated in a relatively straightforward and cheap way onto chips fabricated in the CMOS fab.

Graphene Graphene was initially considered because of several reasons. Firstly it is these days quite readily available and can easily be integrated onto nanophotonic structures. Secondly some studies on graphene nonlinear optics that were around when this project started were very optimistic, and stated very high values for its third order optical nonlinearity. In Chapter 2, a short review of some experimental studies available at the time of writing (August 2018) is given. Here it becomes clear that the situation is quite a bit more complicated and nuanced. The general conclusion is that the field of graphene nonlinear optics is very scattered, both in terms of the different descriptions used to quantify the optical nonlinearity as well as in terms of the vastly different nonlinear coefficients that have been published. In Chapter 3, this is investigated experimentally. In a first experiment, saturable absorption is measured on graphene-covered silicon waveguides (Section 3.2). This is a well-known property of graphene and we demonstrate that the saturation of the absorption is strongly dependent on the Fermi energy. For a second experiment (Section 3.4), we integrated graphene onto silicon nitride waveguides and measured degenerate four-wave mixing. We conclude that also this nonlinear phenomenon is strongly dependent on the Fermi energy $|E_{\mathrm{F}}|$. The nonlinear response has a strong peak around the absorption edge ($|E_{\mathrm{F}}| = \hbar\omega/2$), and for higher doping the nonlinear response drops sharply. Another observation is that the four-wave mixing response is relatively narrow-band, decreasing drastically when the pump and probe are detuned by even a couple of nanometers. Finally, a cross-modulation experiment was conducted on graphene-covered silicon nitride waveguides (Section 3.5). The cross-phase and cross-amplitude modulation between a pump and a probe were measured. This measurement revealed even more complex dependencies of the third order nonlinear optical response of graphene. With very strong resonances and even sign changes of both the real and imaginary part of the third order optical conductivity in the vicinity of the absorption edge. We moreover matched the four-wave mixing and cross-modulation experiments with a simple phenomenological model based on heating of the charge carrier distribution under strong illumination (Appendix A). In conclusion, these experiments have given more insight in some of the nonlinear optical processes that occur in graphene. The correspondence with the simple model shows that these phenomena are mainly induced by carrier heating, and not by the electronic contributions which dominate in dielectrics [1]. The strong dependencies on Fermi energy and wavelength can also in part explain the discrepancies between different values of the third order nonlinear coefficients published elsewhere. From an application perspective, one has to note that under specific circumstances the measured nonlinear coefficients are indeed very large. However the carrier-based nature means that these effects are relatively narrow-band, and that they occur when the linear absorption of the material is also very high. Another potential problem is the saturation of the nonlinear response. A noteworthy advantage of graphene is however the demonstrated tunability of the nonlinearity, which could enable electrically tunable nonlinear devices, or be used as a tool to achieve phase-matching, etc.

PZT Lead zirconate titanate (PZT) is the material with which perhaps the most promising results were obtained in terms of applications. One of the motivations for studying this material were the known strong electro-optic response and second order optical nonlinear response. Though the main reason was the thin-film deposition method developed in the Department of Electronics and Information Systems at our university. We are in a unique position in that we can deposit high quality thin films on top of any sufficiently flat surface using an *optically transparent* intermediate layer. This enabled us to perform measurements of second harmonic generation on thin film PZT-on-glass substrates, and later on PZT-covered silicon nitride waveguides using modal phase-matching. Despite the preliminary nature of the latter experiment, and the issues of high loss of the second harmonic due to coupling to slab modes, this seems to be very promising. Even more significant are the demonstration of high-speed modulation using the Pockels effect in PZT-covered silicon nitride waveguides. Using ring resonators and Mach-Zehnder interferometers, we showed bias-free modulation in both the C-band and the O-band, with bandwidths beyond 33 GHz and data rates of 40 Gbps. We also showed low propagation losses (down to 1 dB/cm) and a half-wave voltage-length product of the phase shifters as low as 3.2 Vcm. A simple optimization of the waveguide cross-section also showed that the modulation efficiency still can be improved.

Transition metal dichalcogenides (TMDCs) Finally, we studied some properties of MoS_2, a 2D-material of the family of the TMDCs. Through our collaborators in imec (Leuven, Belgium), we have access to large area monolayer MoS_2. For TMDCs, relatively large values values of second order optical nonlinearities have been published (with one excessively large value which no one has reproduced [2]). Similar to graphene these materials are relatively easy to integrate on nanophotonic chips, which was a strong trigger to look in to their nonlinearity. Using a setup dedicated to measuring the second harmonic response of thin films, we measured the surface second order susceptibility for a fundamental wavelength of 1550 nm. Since most literature values are obtained with the second harmonic frequency in the vicinity of an excitonic resonance, we measured values which were significantly lower. As a matter of fact, when expressed as a bulk nonlinear susceptibility the value was lower than in for example lithium niobate, with the added caveat that the high nonlinearity is only present in a subnanometer thick monolayer. As a second experiment we covered silicon nitride waveguides with the MoS_2 monolayers. The optical loss of the covered waveguides was relatively high and should still be further investigated.

Finally, a quasi-phase-matching scheme which involves periodic patterning of the 2D material is proposed. Our conclusion is that for the current loss and nonlinearity values on-chip SHG can probably be demonstrated, however that the conversion efficiencies would not be of an order of magnitude which is useful.

6.2 Future perspectives

While this work contains several new insights and results concerning nonlinear optics in graphene, TMDCs and PZT, this is not the end of the road and many avenues are left to explore.

Graphene The results on gate tunable saturable absorption could be a valuable starting point for the design of integrated mode-locked lasers using graphene as a saturable absorber. Recently, similar gate-tunability of graphene was used to adjust the operational regime of a modelocked fiber laser [3], such opportunities can also be explored for integrated lasers. When it comes to Kerr-like phenomena, or four-wave mixing, the gate-tunability and potentially very high optical nonlinearities are strong advantages. On the other hand, there are some concerns that need to be sorted out. The high linear loss seems for example to be hard to avoid. Saturation of the optical nonlinearity seems to be another major concern which was not yet addressed in detail in this work [4]. Having the nonlinearity decrease at high illumination intensities is commonly recognized as a strong disadvantage. In a recent publication, Vermeulen *et al.* describe a similar saturation process in the context of picosecond pulse broadening [5]. The authors however inverse the argument and argue that a higher nonlinear optical response at a low power (read: saturation at higher powers) is an advantage and leads to “exponential-like bandwidth growth” [5] of pulses. However in the current demonstration, the spectral broadening is still very limited and the exponential-like growth (as a function of waveguide length) is achieved due to a particular interplay between the pulse spectral shape, the high absorption of graphene and the waveguide lengths used in the experiment. In the current incarnation of this experiment, neither increasing the pulse power, nor the interaction length is expected to further increase the spectral broadening significantly, so there is no evidence pointing in the direction of “frequency-comb and supercontinuum generation at record-low input power levels”, as envisaged in reference [5]. Some other recent studies however show that third harmonic generation in graphene can also be tuned by gating [6, 7]. As opposed to Kerr-like effects and four-wave mixing, the efficiency of this effect increases when graphene becomes transparent for the fundamental wavelength. This means that when the loss decreases, the nonlinear response increases, which is definitely a reason to look further into this. We also propose a simple quasi-phase-matching scheme just by periodically patterning the graphene, which is unique to 2D materials.

PZT In terms of on-chip second harmonic generation, efforts are ongoing to improve the efficiency by reducing the loss of the second harmonic. This would be done by etching a ridge in the PZT-layer, so that both the fundamental and second harmonic optical mode are properly confined. On the longer term it seems best to explore periodic poling of the PZT for quasi-phase-matching. This is difficult in terms of fabrication since relatively small poling periods would be required, but it would enable coupling between the TE00 modes of the fundamental and of the second harmonic frequency. This is far more convenient than modal phase matching and can for example lead to optical parametric amplifiers or oscillators, quantum applications (parametric downconversion for photon pair generation), etc. For optical modulation, still quite some work can be done. For example, the potential improvements to the waveguide cross-section suggested in this thesis are not yet tested experimentally. The poling also remains stable for at least a couple of days at room temperature, as was demonstrated in this thesis. However more extensive reliability tests should still be done. Effective Pockels coefficients extracted from the measurements in this work are still much lower than values measured through ellipsometry on thin-films (in reference [8]). This means that by improving the poling procedure, for example by going to higher temperatures, the modulation efficiency might still significantly increase. The phase-shifters used in the modulators here are all quite short. If one wants to go to lower drive voltages longer Mach-Zehnder-type modulators will have to be used. The design of such modulators is quite involved since phase matching between both the optical and the RF wave has to be considered. A key advantage of the Pockels effect is its optically broadband nature. Hence another future direction can be the demonstration of efficient modulation at other wavelengths, from the visible to the mid infrared. Yet another future avenue worth exploring is the use of PZT on other integrated platforms, such as silicon, since one of the main advantages is the versatility of the deposition process. Finally, some recent reports have shown that other ferroelectric materials, such as $BaTiO_3$, can have higher Pockels coefficients than PZT [9]. It has been demonstrated that also this material can be deposited through a similar method as is used for our thin-film PZT [8], which is also worth exploring.

Transition metal dichalcogenides As was clear from the previous section, the results of the preliminary measurements were not spectacular. However some future avenues can still be explored. First en foremost understanding the optical losses, and hopefully reducing them, is something that should be looked into, also in vue of other potential applications such as luminescence or even lasing. Secondly, a strong wavelength dependency of the nonlinear effects has been demonstrated by other groups. Maybe it's worth the effort looking into other wavelengths, or other materials of the TMDC class. Another interesting path that can be explored, is to look into bringing the electrostatic tuning of the nonlinear response of TMDCs, which was demonstrated in reference [10], to a chip.

References

[1] R. W. Boyd. *Nonlinear Optics.* Academic Press, 2003.

[2] N. Kumar, S. Najmaei, Q. Cui, F. Ceballos, P. M. Ajayan, J. Lou, and H. Zhao. *Second harmonic microscopy of monolayer MoS_2.* Physical Review B, 87(16):161403, 2013.

[3] B. Yao, G. Soavi, T. Ma, X. Zhang, B. Fu, D. Yoon, S. A. Hussain, A. Lombardo, D. Popa, and A. C. Ferrari. *Gate controllable ultrafast fiber lasers based on graphene.* In CLEO: Science and Innovations, pages SF3K–6. Optical Society of America, 2018.

[4] G. Demetriou, F. Biancalana, E. Abraham, W. ji, Y. Wang, and A. K. Kar. *Negative Irradiance-Dependent Nonlinear Refraction in Single-Layer Graphene.* In Conference on Lasers and Electro-Optics, page JTu2A.115. Optical Society of America, 2018.

[5] N. Vermeulen, D. Castelló-Lurbe, M. Khoder, I. Pasternak, A. Krajewska, T. Ciuk, W. Strupinski, J. Cheng, H. Thienpont, and J. Van Erps. *Graphenes nonlinear-optical physics revealed through exponentially growing self-phase modulation.* Nature Communications, 9(1):2675, 2018.

[6] T. Jiang, D. Huang, J. Cheng, X. Fan, Z. Zhang, Y. Shan, Y. Yi, Y. Dai, L. Shi, K. Liu, C. Zeng, J. Zi, J. E. Sipe, Y.-R. Shen, W.-T. Liu, and S. Wu. *Gate-tunable third-order nonlinear optical response of massless Dirac fermions in graphene.* Nature Photonics, 12:430–436, 2018.

[7] G. Soavi, G. Wang, H. Rostami, D. G. Purdie, D. De Fazio, T. Ma, B. Luo, J. Wang, A. K. Ott, D. Yoon, S. A. Bourelle, J. E. Muench, I. Goykhman, S. Dal Conte, M. Celebrano, A. Tomadin, M. Polini, G. Cerullo, and A. C. Ferrari. *Broadband, electrically tunable third-harmonic generation in graphene.* Nature Nanotechnology, 13:583–588, 2018.

[8] J. P. George. *Integration of ferroelectric thin films on silicon for electro-optic devices.* PhD thesis, Ghent University, 2016.

[9] F. Eltes, M. Kroh, D. Caimi, C. Mai, Y. Popoff, G. Winzer, D. Petousi, S. Lischke, O. J. E., C. L., Z. L., F. J., and A. S. *A novel 25 Gbps electro-optic Pockels modulator integrated on an advanced Si photonic platform.* IEEE International Electron Devices Meeting (IEDM), 2017.

[10] K. L. Seyler, J. R. Schaibley, P. Gong, P. Rivera, A. M. Jones, S. Wu, J. Yan, D. G. Mandrus, W. Yao, and X. Xu. *Electrical control of second-harmonic generation in a* WSe_2 *monolayer transistor*. Nature Nanotechnology, 10(5):407, 2015.

Appendix A

Phenomenological model for graphene nonlinear optics

A.1 Introduction

In order to explain the observed dependencies of the third order conductivity $\sigma^{(3)}(=\sigma_s^{(3)}$, we will drop the subscript 's' in this appendix for convenience) values measured in the four-wave mixing experiment in Section 3.4 and the cross-modulation experiment in Section 3.5, we apply a simple phenomenological model which takes into account the heating of the electron-hole gas by the incident electromagnetic radiation and its cooling due to interaction with the environment. In Section A.4, we also use this model to assess within which range of intensities a third-order description of the optical nonlinearity in graphene is valid, the limited validity of such a description has been subject of recent experimental investigations [1].

The derivation below is based on the stringent assumption that, at all times, the carrier distribution in the graphene can be described by a Fermi-Dirac distribution. This limits the applicability of this approach to experiments where variations in the total optical intensity are slower than the typical time-scales needed to reach such an equilibrium (several 100s of femtoseconds [2–7]). **In practice this limits this model to self- and cross-modulation experiments using CW sources or pulses of ps or longer durations, and to four-wave-mixing experiments where the signal-pump detuning is limited to a couple of nanometer.**

This model was devised by Sergey A. Mikhailov and Nadja A. Savostianova in the context of the cross-modulation experiment described in Section 3.5. The expansion to include four-wave mixing and the calculations in Section A.4 were done by myself.

For completeness, we start by giving the expressions for the *linear* conductivity of graphene.

A.2 Linear conductivity of graphene

The linear conductivity of graphene, assuming chemical potential μ and electron temperature T, is given by $\sigma^{(1)}(\omega,\mu,T) = \sigma^{(1)}_{\text{intra}}(\omega,\mu,T) + \sigma^{(1)}_{\text{inter}}(\omega,\mu,T)$. It consists of the intra- and inter-band contributions [8–10]. For the intraband conductivity we use the standard Drude formula,

$$\sigma^{(1)}_{\text{intra}}(\omega,\mu,T) = \frac{e^2}{4\hbar^2}\frac{i}{\pi k_{\text{B}}T}\int_0^\infty \frac{EdE}{\omega + i\gamma_{\text{intra}}(E)}\left(\frac{1}{\cosh^2\left(\frac{E-\mu}{2k_{\text{B}}T}\right)} + \frac{1}{\cosh^2\left(\frac{E+\mu}{2k_{\text{B}}T}\right)}\right), \tag{A.1}$$

with k_{B} the Boltzmann constant and γ_{intra} the intraband scattering rate[1] For the inter-band conductivity we use the expression (see for example references [8–10]),

$$\sigma^{(1)}_{\text{inter}}(\omega,\mu,T) = \frac{e^2}{4\hbar}\frac{-i}{\pi}\int_0^\infty dE\frac{\sinh(E/k_{\text{B}}T)}{\cosh(\mu/k_{\text{B}}T) + \cosh(E/k_{\text{B}}T)}\frac{\hbar(\omega + i\gamma_{\text{inter}})}{E^2 - [\hbar(\omega + i\gamma_{\text{inter}})/2]^2}, \tag{A.2}$$

and assume that the inter-band scattering rate is negligibly small, $\gamma_{\text{inter}} \to 0$; a finite γ_{inter} does not influence the final result under the condition $\hbar\gamma_{\text{inter}} \ll k_{\text{B}}T$ which is typically satisfied in experiments.

A.3 Nonlinear conductivity of graphene

In equilibrium (without irradiation and at room temperature T_0) the electron/hole distribution over quantum states in the conduction and valence bands is described by the Fermi-Dirac function $f_0(E,\mu_0,T_0)$, where the chemical potential $\mu_0 = \mu(T_0)$ is determined by the equilibrium electron or hole density controlled by the gate voltage. Under strong irradiation, electrons are excited from the valence to the conduction band and their distribution function changes. The relaxation processes taking place after a strong short excitation of electrons have been studied in many papers, e.g. references [2–7]. It was shown that, due to the very frequent ($\tau_{ee} \simeq 10-20$ fs) electron-electron intra-band and inter-band scattering processes, quasi-equilibrium Fermi-Dirac-type electron distributions are established in the conduction and valence bands shortly after the pulse excitation, with a new electron temperature T and new chemical potential(s) which may in general be different for electrons (μ_e) and holes (μ_h). We assume here for simplicity that in our case the electron distribution can be described by the formula

---

[1] It has been demonstrated that the scattering γ_{intra} is energy-dependent and follows the relation $\hbar\gamma_{\text{intra}}(E) = E_i^2/E$, for $E \gtrsim E_i$, with $E_i \approx 0.36\frac{e^2}{\kappa}\sqrt{\pi N_i}$, where N_i is the density of impurities and κ is the dielectric constant of the environment [11]. In our simulations we use the value $E_i \sim 0.1$ eV, however the exact value has only a minor influence on the outcome.

$$f(E,\mu,T) = \frac{1}{1+\exp\left(\frac{E-\mu}{k_\mathrm{B}T}\right)}, \tag{A.3}$$

with a single chemical potential $\mu \neq \mu_0$ and temperature $T > T_0$.

In order to find the quasi-equilibrium distribution parameters μ and T we use two equations. The first one,

$$n_h(\mu,T) - n_e(\mu,T) = -\frac{\mathrm{sgn}(E_\mathrm{F})E_\mathrm{F}^2}{\pi(\hbar v_\mathrm{F})^2}, \tag{A.4}$$

is the **electroneutrality condition**, in which the 2D densities of holes n_h and electrons n_e are calculated with the electron distribution, equation (A.3), $E_\mathrm{F} = \mu(T=0)$ is the Fermi energy and $v_\mathrm{F} \approx 10^6$ m/s is the Fermi velocity. The carrier densities can be calculated as

$$n_e(\mu,T) = \int_0^\infty f(E,\mu,T)\rho(E)dE, \tag{A.5}$$

$$n_h(\mu,T) = \int_{-\infty}^0 \left[1 - f(E,\mu,T)\right]\rho(E)dE, \tag{A.6}$$

where $\rho(E) = 2|E|/\pi(\hbar v_\mathrm{F})^2$ equals the density of states in graphene [12].

The second equation is the **energy balance condition**. It expresses how the total energy $\mathcal{E}(\mu,T) = \mathcal{E}_e(\mu,T) + \mathcal{E}_h(\mu,T)$ of the electron and hole gasses evolves over time,

$$\frac{\partial\mathcal{E}(\mu,T)}{\partial t} = -\frac{\mathcal{E}(\mu,T) - \mathcal{E}(\mu_0,T_0)}{\tau_\mathcal{E}} + P_\mathrm{abs}, \tag{A.7}$$

the first term on the right-hand side expresses the rate at which energy relaxes to the environment, $\tau_\mathcal{E}$ is the phenomenological energy relaxation time. The second term expresses the rate at which wave energy gets absorbed, which typically can be expressed as $P_\mathrm{abs} = \frac{1}{2}\mathrm{Re}\{\sigma^{(1)}(\mu,T)\}|E_\mathrm{opt}|^2$, with $|E_{\mathrm{opt}}|$ the optical field strength. The total energy in the electron and hole gasses is given by

$$\mathcal{E}_e = \int_0^\infty E f(E,\mu,T)\rho(E)dE, \tag{A.8}$$

$$\mathcal{E}_h = \int_{-\infty}^0 (-E)\left[1 - f(E,\mu,T)\right]\rho(E)dE. \tag{A.9}$$

It is clear how this model can describe optical nonlinearities in the system. Enforcing the energy balance and electroneutrality condition for different optical intensities $\propto |E_{\mathrm{opt}}|^2$ (and optical frequencies), will yield intensity dependent chemical potentials μ and electron temperatures T. These in turn change the optical response quantified by the linear conductivity $\sigma^{(1)}$, resulting in optical nonlinearities.

Cross-modulation

In the cross-modulation experiment (section 3.5), a strong modulated pump and a weaker probe were used, respectively at frequencies ω_{pump} and ω_{probe}. Moreover, the pump is modulated at GHz frequencies, much slower than the relaxation rate $1/\tau_{\mathcal{E}}$. Hence the energy balance condition (equation A.7) yields,

$$\mathcal{E}(\mu,T) \approx \mathcal{E}(\mu_0,T_0) + \frac{\tau_{\mathcal{E}}}{2}\mathrm{Re}\{\sigma^{(1)}(\omega_{\mathrm{pump}},\mu,T)\}|E_{\mathrm{pump}}|^2. \tag{A.10}$$

Numerically solving equations (A.7) and (A.10) we obtain the chemical potential μ and the electron temperature T as functions of the field E_{pump}. After $\mu(E_{\mathrm{pump}})$ and $T(E_{\mathrm{pump}})$ have been found we consider the linear response of the system to the weak probe wave. It is determined by the conductivity $\sigma^{(1)}[\omega_{\mathrm{probe}},\mu(E_{\mathrm{pump}}),T(E_{\mathrm{pump}})]$.

At sufficiently low local intensities we can use the Taylor expansion,

$$\begin{aligned}\sigma^{(1)}[\omega_{\mathrm{probe}},\mu(E_{\mathrm{pump}}),T(E_{\mathrm{pump}})] \equiv& \sigma^{(1)}(\omega_{\mathrm{probe}},|E_{\mathrm{pump}}|^2)\\ =&\sigma^{(1)}(\omega_{\mathrm{probe}},0)\\ &+\frac{\partial\sigma^{(1)}(\omega_{\mathrm{probe}},0)}{\partial|E_{\mathrm{pump}}|^2}|E_{\mathrm{pump}}|^2\\ &+\frac{1}{2}\frac{\partial^2\sigma^{(1)}(\omega_{\mathrm{probe}},0)}{\partial(|E_{\mathrm{pump}}|^2)^2}|E_{\mathrm{pump}}|^4\\ &+\dots\end{aligned} \tag{A.11}$$

In order to find the higher order conductivity functions ($\sigma^{(3)}$, $\sigma^{(5)}$, $\sigma^{(7)}$, etc.) we equate the expansion (equation (A.11)) with the following power series:

$$\begin{aligned} j_{\omega_{\text{probe}},\,x} =& \sigma^{(1)}_{xx}[\mu(E_{\text{pump}}),T(E_{\text{pump}})]E_{\text{probe}} \\ \equiv& \sigma^{(1)}_{xx}(\omega_{\text{probe}},\mu_0,T_0)E_{\text{probe}} \\ &+\frac{3}{2}\sigma^{(3)}_{xxxx}(\omega_{\text{probe}};\omega_{\text{probe}},\omega_{\text{pump}},-\omega_{\text{pump}},\mu_0,T_0)|E_{\text{pump}}|^2E_{\text{probe}} \\ &+\frac{15}{8}\sigma^{(5)}_{x\ldots x}(\omega_{\text{probe}};\ldots,\mu_0,T_0)|E_{\text{pump}}|^4E_{\text{probe}} \\ &+\frac{35}{16}\sigma^{(7)}_{x\ldots x}(\omega_{\text{probe}};\ldots,\mu_0,T_0)|E_{\text{pump}}|^6E_{\text{probe}} \\ &+\ldots \end{aligned} \tag{A.12}$$

We assume the fields to be linearly polarized in the x-direction. The higher order conductivities can then be found as:

$$\sigma^{(3)}_{xxxx}(\omega_{\text{probe}};\omega_{\text{probe}},\omega_{\text{pump}},-\omega_{\text{pump}}) = \frac{2}{3}\frac{\partial\sigma^{(1)}_{xx}(\omega_{\text{probe}})}{\partial(|E_{\text{pump}}|)^2}, \tag{A.13}$$

$$\sigma^{(5)}_{xxxxxx}(\omega_{\text{probe}};\omega_{\text{probe}},\omega_{\text{pump}},-\omega_{\text{pump}},\omega_{\text{pump}},-\omega_{\text{pump}}) = \frac{4}{15}\frac{\partial^2\sigma^{(1)}_{xx}(\omega_{\text{probe}})}{\partial(|E_{\text{pump}}|^2)^2}, \tag{A.14}$$

$$\sigma^{(7)}_{x\ldots x}(\omega_{\text{probe}};\ldots) = \frac{8}{105}\frac{\partial^3\sigma^{(1)}_{xx}(\omega_{\text{probe}})}{\partial(|E_{\text{pump}}|^2)^3}, \tag{A.15}$$

$$\ldots,$$

where we omitted the μ_0 and T_0-arguments for clarity. Note that following the conventions used in nonlinear optics [13], the degeneracy factors for cross-modulation and self-modulation are different. Hence for the degenerated case where $\omega_{\text{probe}} = \omega_{\text{pump}} = \omega$, the prefactor 3/2 in equation (A.12) becomes 3/4. Yielding a nonlinear conductivity of

$$\sigma^{(3)}_{xxxx}(\omega;\omega,\omega,-\omega) = \frac{4}{3}\frac{\partial\sigma^{(1)}_{xx}(\omega)}{\partial(|E_\omega|)^2}. \tag{A.16}$$

Four-wave mixing

In the four-wave mixing experiment (section 3.4), nonlinear frequency mixing was considered between two wavelengths, the pump and signal, respectively at frequencies ω_{p} and ω_{s} with electric fields E_{p} and E_{s}. We specifically look at the generation of light at a third frequency, called the idler

$\omega_\mathrm{i} = 2\omega_\mathrm{p} - \omega_\mathrm{s}$. To take into account frequency mixing, we have to look at the beat note between the pump and the idler. The absorbed power is now:

$$P_\mathrm{abs}(t) = \frac{1}{2}\mathrm{Re}\{\sigma^{(1)}(\mu,T)\}\{|E_\mathrm{p}|^2 + |E_\mathrm{s}|^2 + \frac{2E_\mathrm{p}E_\mathrm{s}^* e^{-i\Delta\omega t} + \mathrm{c.c.}}{2}\}, \quad \text{(A.17)}$$

where c.c. stands for 'complex conjugate', we assume that the detuning $\Delta\omega = \omega_\mathrm{p} - \omega_\mathrm{s}$ is small, so that $\sigma^{(1)}(\mu,T) = \sigma^{(1)}(\omega_\mathrm{p},\mu,T) \approx \sigma^{(1)}(\omega_\mathrm{s},\mu,T)$. To solve equation (A.7), we propose the following solutions for the total energy $\mathcal{E}$ and $\sigma^{(1)}$:

$$\mathcal{E}(t) \approx \mathcal{E}_\mathrm{const.} + \frac{\Delta\mathcal{E}e^{-i\Delta\omega t} + \mathrm{c.c.}}{2}, \quad \text{(A.18)}$$

$$\sigma^{(1)}(t) \approx \sigma^{(1)}_\mathrm{const.} + \frac{\Delta\sigma^{(1)}e^{-i\Delta\omega t} + \mathrm{c.c.}}{2}. \quad \text{(A.19)}$$

The constant (const.) terms can be found by solving the elecroneutrality condition (equation (A.4)) and the energy balance condition for the constant term in equation (A.17).

Substituting equations (A.17 – A.19) into the energy balance condition (equation (A.7)) and isolating the terms with time-dependence $e^{-i\Delta\omega t}$,

$$\begin{aligned}(\tau_\mathcal{E}^{-1} - i\Delta\omega)\Delta\mathcal{E} &= \mathrm{Re}(\sigma^{(1)}_\mathrm{const.})E_\mathrm{p}E_\mathrm{s}^* + \frac{1}{2}\mathrm{Re}(\Delta\sigma^{(1)})(|E_\mathrm{p}|^2 + |E_\mathrm{s}|^2) \\ &\approx \mathrm{Re}(\sigma^{(1)}_\mathrm{const.})E_\mathrm{p}E_\mathrm{s}^*.\end{aligned} \quad \text{(A.20)}$$

For the last equation we have assumed that $\Delta\sigma^{(1)} \ll \sigma^{(1)}_\mathrm{const.}$, which is realistic in the limit of weak illumination (well below the saturation power). Using the same assumption, we can now approximate $\Delta\sigma^{(1)}$,

$$\Delta\sigma^{(1)} \approx \frac{\partial\sigma^{(1)}}{\partial\mathcal{E}}\Delta\mathcal{E} \approx \frac{\partial\sigma^{(1)}}{\partial\mathcal{E}}\frac{\mathrm{Re}(\sigma^{(1)}_\mathrm{const.})}{\tau_\mathcal{E}^{-1} - i\Delta\omega}E_\mathrm{p}E_\mathrm{s}^*. \quad \text{(A.21)}$$

The current density, $j(t) = \sigma^{(1)}(t)\cdot(E_\mathrm{p}e^{-i\omega_\mathrm{p}t} + E_\mathrm{s}e^{-i\omega_\mathrm{s}t} + \mathrm{c.c.})/2$, now contains a frequency component at frequency ω_i, with complex amplitude,

$$\begin{aligned}j_{\omega_\mathrm{i}} &= \frac{1}{2}\Delta\sigma^{(1)}E_\mathrm{p} \\ &\approx \frac{1}{2}\frac{\partial\sigma^{(1)}}{\partial\mathcal{E}}\frac{\mathrm{Re}(\sigma^{(1)}_\mathrm{const.})}{\tau_\mathcal{E}^{-1} - i\Delta\omega}E_\mathrm{p}^2E_\mathrm{s}^*.\end{aligned} \quad \text{(A.22)}$$

Equating the last term to the expression using the nonlinear conductivity, $(3/4)\sigma^{(3)}(\omega_\mathrm{i};\omega_\mathrm{p},\omega_\mathrm{p},-\omega_\mathrm{s})E_\mathrm{p}^2E_\mathrm{s}^*$, we get,

$$\sigma^{(3)}(\omega_\mathrm{i};\omega_\mathrm{p},\omega_\mathrm{p},-\omega_\mathrm{s}) \approx \frac{2}{3}\frac{\partial\sigma^{(1)}}{\partial\mathcal{E}}\frac{\mathrm{Re}(\sigma^{(1)}_\mathrm{const.})}{\tau_\mathcal{E}^{-1} - i\Delta\omega}. \quad \text{(A.23)}$$

On the other hand, equation (A.16) yields the nonlinear conductivity expressing self-modulation at frequency ω (with field ampitude E_ω),

$$\begin{aligned}\sigma^{(3)}(\omega;\omega,\omega,-\omega) &= \frac{4}{3}\frac{\partial\sigma^{(1)}(\omega,\mu_0,T_0)}{\partial(|E_\omega|)^2} \\ &= \frac{4}{3}\frac{\partial\sigma^{(1)}(\omega,\mu_0,T_0)}{\partial\mathcal{E}}\frac{\partial\mathcal{E}}{\partial(|E_\omega|)^2} \\ &= \frac{2\tau_{\mathcal{E}}}{3}\frac{\partial\sigma^{(1)}(\omega,\mu_0,T_0)}{\partial\mathcal{E}}\mathrm{Re}[\sigma^{(1)}(\omega,\mu_0,T_0)].\end{aligned} \tag{A.24}$$

where for the last step we have used equation (A.10). If we assume the perturbation caused by the irradiation is small, $\sigma^{(1)}_{\text{const.}} \approx \sigma^{(1)}(\omega_\text{p},\mu_0,T_0)$, from equations (A.23) and (A.24) we get,

$$\sigma^{(3)}(\omega_\text{i};\omega_\text{p},\omega_\text{p},-\omega_\text{s}) \approx \sigma^{(3)}(\omega_\text{p};\omega_\text{p},\omega_\text{p},-\omega_\text{p})\frac{\tau_{\mathcal{E}}^{-1}}{\tau_{\mathcal{E}}^{-1}-i\Delta\omega}. \tag{A.25}$$

This implies that the four-wave mixing efficiency, which scales as $|\sigma^{(3)}|^2$, has a Lorenzian lineshape with damping rate $\tau_{\mathcal{E}}^{-1}$.

A.4 High intensity behavior

In the above section, the assumption was made that the linear conductivity $\sigma^{(1)}$ can be expanded as a Taylor series as function of the optical intensity (expressed as the square of the electric field magnitude). Interpreting the experiments in Sections 3.4 and 3.5, we also assumed that the third-order nonlinearity is dominant, this is a common approach in literature. One might question what the limits are of this assumption. We can calculate $\sigma^{(1)}(|E_\omega|^2)$ as a function of optical field strength E_ω. For this we solve the time-independent energy balance condition (equation A.10) and electroneutrality condition (equation (A.4)) for a range of field strengths. Note that if we take $\tau_{\mathcal{E}}|E_\omega|^2$ to be an 'effective' power, there are no fitting parameters in our equations. Figures A.1**a** and A.1**b** show respectively the calculated real and imaginary parts of the intensity-dependent linear conductivity $\sigma^{(1)}$, the dashed lines show the approximation $\sigma^{(1)}(|E_\omega|^2) = \sigma^{(1)}(0) + \frac{3}{2}\sigma^{(3)}|E_\omega|^2$.

From these figures it is very clear that the third order approximation, which is essentially a linearization of the linear conductivity as a function of optical intensity, is only valid at low intensities. From figure A.1 it is hard to judge what the limits are of this approximation. Figure 2.3 of the main text shows the *variation* in linear conductivity as a function of electric field strength. From these figures it is clear that the linearized $\sigma^{(3)}$-based model is a reasonably good representation for $\tau_{\mathcal{E}}|E_\omega|^2 \lesssim 1$ sV^2/m^2,

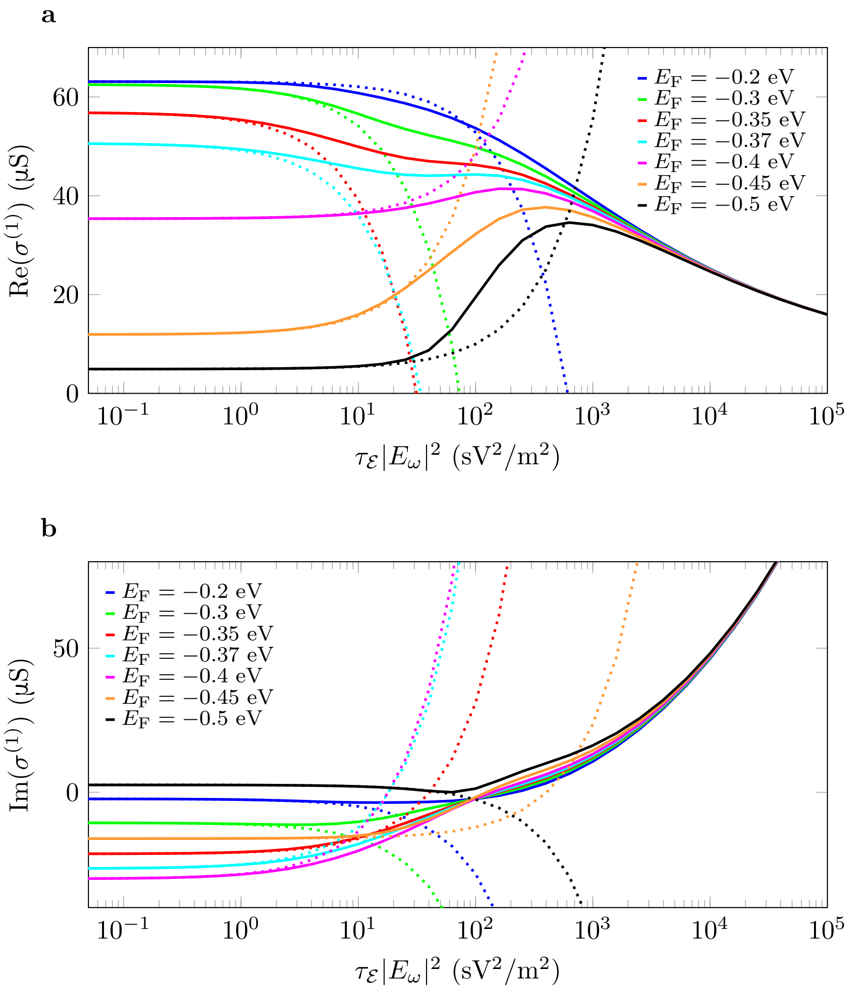

Figure A.1: **a** Real part of the intensity-dependent linear conductivity $\sigma^{(1)}$, as a function of $\tau_{\mathcal{E}}|E_\omega|^2$. The dotted lines represents the approximation using only the third order conductivity $\sigma^{(3)}$; $\sigma^{(1)}(|E_\omega|^2) = \sigma^{(1)}(0) + \frac{3}{2}\sigma^{(3)}|E_\omega|^2$. **b** Imaginary part of the power-dependent linear conductivity $\sigma^{(1)}$, the dotted lines again express the $\sigma^{(3)}$-based approximation.

for increasing intensities, the linearization starts to deviate strongly from the exact calculations, for $\tau_{\mathcal{E}}|E_\omega|^2 > 10\ \mathrm{sV^2/m^2}$, even order-of-magnitude estimates become problematic.

For the experiments performed in Sections 3.4 and 3.5, on-chip input pump powers were kept below ≈ 10 mW, for this power, mode profile calculations show that the average electric-field squared in the graphene is on the order of 10^{12} $\mathrm{V^2/m^2}$, yielding $\tau_{\mathcal{E}}|E_\omega|^2 \lesssim 1$ ($\mathrm{sV^2/m^2}$) for realistic $\tau_{\mathcal{E}}$-values in the range of 0.1-1 ps.

In many experiments in literature however, high optical powers are used, while at the same time still using a model based on the third order conductivity. Approximately, $\tau_{\mathcal{E}}|E_\omega|^2 = 1$ $\mathrm{sV^2/m^2}$ corresponds to an intensity of $I = \frac{n}{2}\varepsilon_0 c|E_\omega|^2 \approx \mathcal{O}(10^{10})$ $\mathrm{Wm^{-2}}$, with n the material refractive index [13]. As can be seen in table 2.1, many experiments are using peak powers that are orders of magnitude higher. Note that these conclusions are only fair for cross-and self-phase modulation experiments (labeled in green in table 2.1), as well as four-wave mixing experiments (labeled in red in table 2.1) with small signal-pump detuning. The model developed here is unable to make any predictions for other experiments such as third harmonic generation (blue in table 2.1), for these experiments using high peak powers might not cause any problems.

References

[1] G. Demetriou, F. Biancalana, E. Abraham, W. ji, Y. Wang, and A. K. Kar. *Negative Irradiance-Dependent Nonlinear Refraction in Single-Layer Graphene.* In Conference on Lasers and Electro-Optics, page JTu2A.115. Optical Society of America, 2018.

[2] T. Winzer, A. Knorr, and E. Malic. *Carrier multiplication in graphene.* Nano Letters, 10(12):4839–4843, 2010.

[3] E. Malic, T. Winzer, E. Bobkin, and A. Knorr. *Microscopic theory of absorption and ultrafast many-particle kinetics in graphene.* Physical Review B, 84(20):205406, 2011.

[4] T. Winzer and E. Malić. *Impact of Auger processes on carrier dynamics in graphene.* Physical Review B, 85(24):241404, 2012.

[5] D. Brida, A. Tomadin, C. Manzoni, Y. J. Kim, A. Lombardo, S. Milana, R. R. Nair, K. S. Novoselov, A. C. Ferrari, G. Cerullo, and M. Polini. *Ultrafast collinear scattering and carrier multiplication in graphene.* Nature Communications, 4:1987, 2013.

[6] A. Tomadin, D. Brida, G. Cerullo, A. C. Ferrari, and M. Polini. *Nonequilibrium dynamics of photoexcited electrons in graphene: Collinear scattering, Auger processes, and the impact of screening.* Physical Review B, 88(3):035430, 2013.

[7] I. Gierz, J. C. Petersen, M. Mitrano, C. Cacho, I. C. E. Turcu, E. Springate, A. Stöhr, A. Köhler, U. Starke, and A. Cavalleri. *Snapshots of non-equilibrium Dirac carrier distributions in graphene.* Nature Materials, 12(12):1119–1124, 2013.

[8] T. Ando, Y. Zheng, and H. Suzuura. *Dynamical conductivity and zero-mode anomaly in honeycomb lattices.* Journal of the Physical Society of Japan, 71(5):1318–1324, 2002.

[9] L. A. Falkovsky and V. A. A. *Space-time dispersion of graphene conductivity.* The European Physical Journal B, 56(4):281–284, 2007.

[10] L. A. Falkovsky and S. S. Pershoguba. *Optical far-infrared properties of a graphene monolayer and multilayer.* Physical Review B, 76(15):153410, 2007.

[11] E. H. Hwang and S. D. Sarma. *Screening-induced temperature-dependent transport in two-dimensional graphene.* Physical Review B, 79(16):165404, 2009.

[12] S. Dröscher, P. Roulleau, F. Molitor, P. Studerus, C. Stampfer, K. Ensslin, and T. Ihn. *Quantum capacitance and density of states of graphene.* Applied Physics Letters, 96(15):152104, 2010.

[13] R. W. Boyd. *Nonlinear Optics.* Academic Press, 2003.